

Transactions of the ASME

FLUIDS ENGINEERING DIVISION

Technical Editor
FRANK M. WHITE (1989)
Executive Secretary
L. T. BROWN (1989)
Calendar Editor
M. F. ACKERSON

Associate Editors

Fluid Machinery
WIDEN TABAKOFF (1988)
RICHARD F. SALANT (1987)
Fluid Measurements
ALEXANDER DYBBS (1987)
Fluid Mechanics
J. A. MILLER (1987)
HUGH W. COLEMAN (1987)
STANLEY F. BIRCH (1988)
WILLIAM W. DURGIN (1988)
Fluid Transients
FREDERICK J. MOODY (1989)
Numerical Methods
PATRICK J. ROACHE (1988)
Multiphase Flow
M. C. ROGO (1988)
GEORGES L. CHAHINE (1986)
Review Articles
K. N. GHIA (1988)

BOARD ON COMMUNICATIONS

Chairman and Vice President
K. N. REID, Jr.

Members-at-Large

W. BEGELL
J. T. COKONIS
M. FRANKE
W. G. GOTTENBERG
M. KUTZ
F. LANDIS
J. R. LLOYD
T. C. MIN
R. E. NICKELL
R. E. REDER
F. W. SCHMIDT

President, **N. D. FITZROY**
Executive Director
PAUL ALLMENDINGER
Treasurer,
ROBERT A. BENNETT

PUBLISHING STAFF

Mng. Dir. Publ., **J. J. FREY**
Dep. Mng. Dir. Publ.,
JOS. SANSONE
Managing Editor,
CORNELIA MONAHAN
Editorial Production Assistant,
MARISOL ANDINO

Transactions of the ASME, The Journal of Fluids Engineering (ISSN 0098-2202) is published quarterly (Mar., June, Sept., Dec.) for \$105 per year by The American Society of Mechanical Engineers, 345 East 47th Street, New York, NY 10017. Second class postage paid at New York, NY and additional mailing offices. POSTMASTER: Send address changes to The Journal of Fluids Engineering, c/o THE AMERICAN SOCIETY OF MECHANICAL ENGINEERS, 22 Law Drive, Box 2300, Fairfield, NJ 07007-2300.

CHANGES OF ADDRESS must be received at Society headquarters seven weeks before they are to be effective. Please send old label and new address.

PRICES: To members, \$24.00, annually; to nonmembers, \$105. Add \$8.00 for postage to countries outside the United States and Canada.

STATEMENT from By-Laws

The Society shall not be responsible for statements or opinions advanced in papers or printed in its publications (B7.1, Par. 3).

COPYRIGHT © 1987 by The American Society of Mechanical Engineers. Reprints from this publication may be made on condition that full credit be given the TRANSACTIONS OF THE ASME, JOURNAL OF FLUIDS ENGINEERING and the author, and date of publication be stated.

INDEXED by Engineering Information

Journal of Fluids Engineering

Published Quarterly by The American Society of Mechanical Engineers

VOLUME 109 • NUMBER 1 • MARCH 1987

- 1 Fluids Engineering Calendar
- 3 Fluid Motion Within the Cylinder of Internal Combustion Engines—The 1986 Freeman Scholar Lecture
John B. Heywood
- 36 Improvement of Unstable Characteristics of an Axial Flow Fan by Air-Separator Equipment
Y. Miyake, T. Inaba, and T. Kato
- 41 Calculation of Three Dimensional Boundary Layers on Rotating Turbine Blades
O. L. Anderson
- 51 Performance Characteristics of a Multiple-Disk Centrifugal Pump
P. J. Roddy, R. Darby, G. L. Morrison, and P. E. Jenkins
- 58 Dynamics of Liquid Sloshing in Upright and Inverted Bladdered Tanks
F. T. Dodge and D. D. Kana
- 64 Drop Size Distribution and Air Velocity Measurements in Air Assist Swirl Atomizer Sprays
C.-P. Mao, V. Oechsle, and N. Chigier
- 70 Suppression of Sheet Cavitation Inception by Water Discharge Through Slit
Hiroharu Kato, Hajime Yamaguchi, Shinzo Okada, Kohei Kikuchi, and Masaru Miyanaga

Technical Brief

- 75 Further Studies on Laminar Flow About a Rotating Sphere in an Axial Stream
M. A. I. El-Shaarawi, M. M. Kemry, and S. A. El-Bedeawi
 - 78 1986 Journal of Fluids Engineering Index
 - 79 Discussion on Previously Published Papers
- ## Announcements and Special Notices
- 50 Call for Papers—Forum on Unsteady Flow, 1987 WAM
 - 74 Transactions Change of Address Form
 - 82 Conference Report—Conference on Laser Anemometry
 - 83 ASME Prior Publication Notice
 - 83 Submission of Papers
 - 83 Statement of Experimental Uncertainty

Fluid Motion Within the Cylinder of Internal Combustion Engines—The 1986 Freeman Scholar Lecture

John B. Heywood

Professor of Mechanical Engineering,
Director, Sloan Automotive Laboratory,
Massachusetts Institute of Technology,
Cambridge, Mass. 02139

The flow field within the cylinder of internal combustion engines is the most important factor controlling the combustion process. Thus it has a major impact on engine operation. This paper reviews those aspects of gas motion into, within, and out of the engine cylinder that govern the combustion characteristics and breathing capabilities of spark-ignition engines and compression-ignition or diesel engines.

Necessary background information on reciprocating engine operating cycles, the primary effect of piston motion and the spark-ignition and diesel engine combustion processes is first summarized. Then the characteristics of flow through inlet and exhaust valves in four-stroke cycle engines, and through ports in the cylinder liner in two-stroke cycle engines are reviewed. These flows govern the airflow through the engine, and set up the in-cylinder flow that controls the subsequent combustion process. The essential features of common in-cylinder flows—the large scale rotating flows set up by the conical intake jet, the creation and development of swirl about the cylinder axis, the flows produced during compression due to combustion chamber shape called squish, flow during the combustion process, and two-stroke scavenging flows—are then described. The turbulence characteristics of these flows are then defined and discussed. Finally, flow phenomena which occur near the walls, which are important to heat transfer and hydrocarbon emissions phenomena, are reviewed.

The primary emphasis is on developing insight regarding these important flow phenomena which occur within the cylinder. To this end, results from many different research techniques—experimental and computational, established and new—have been used as resources. It is the rapidly increasing convergence of engine flow information from these many sources that make this an exciting topic with promise of significant practical contributions.

1 Introduction

Internal combustion engines—both spark-ignition and compression-ignition types—are distinct from most other power producing and propulsion systems in the following important way. The working fluid undergoes the processes essential for the production of power—compression, fuel energy release by combustion, and expansion—within a single chamber: in almost all internal combustion engines this is the engine's cylinders. The flow field within the cylinder is the most important factor controlling the combustion process. It governs the flame propagation rate in homogeneous charge spark-ignition engines; it controls the fuel-air mixing and burning rates in diesels. It influences the mechanisms by which many of the important emissions form. This flow pattern also

governs the rate of heat transfer to the cylinder walls. Creation of the specific, highly turbulent, flow field required for combustion affects the breathing capacity of the engine and hence its maximum power. These flows are extremely complex: they are turbulent, unsteady, and three dimensional. When liquid fuel is injected into the cylinder, phase change is also involved. A good understanding of the fluid motion in internal combustion engines is critical to developing engine designs with the most attractive operating and emissions characteristics. This paper reviews those features of the air, unburned mixture and burned gas motion within the cylinder of internal combustion engines which have an important influence on engine operation.

Why is such a review appropriate now? Many of the fluid-mechanic diagnostic and analytical tools that have been developed and applied to internal combustion engines over the past ten years have led to substantial progress in our

Contributed by the Fluids Engineering Division for publication in the JOURNAL OF FLUIDS ENGINEERING. Manuscript received by the Fluids Engineering Division September 11, 1986.

understanding of the flow field inside the engine cylinder. Information has come from two types of experiments: flow visualization studies in engines and special engine-like rigs; and measurements of gas velocities at specific locations in engine cylinders. While laser doppler anemometry (LDA)—the preferred velocity measurement technique [1]—can define the flow field details locally, within the engine cylinder, an understanding of the overall character of the flow pattern derived from flow visualization studies aids the interpretation of detailed data substantially. Computer based flow models also promise to be a major new analysis tool. Much flow information has come from modeling activities, through: (i) use of computational fluid mechanic models to predict how in-cylinder gas motion develops and changes during the engine cycle; (ii) use of various types of combustion models to predict flame development in engines; (iii) development of techniques for predicting the behavior of vaporizing liquid-fuel sprays. The status of fluid-dynamic based engine-flow computer models has been summarized in several recent review papers (e.g., [2]–[4]). These “multidimensional” flow models solve the unsteady mass, momentum, and energy conservation equations in one, two, or three dimensions, in discretized form, using models or equations to describe the turbulence phenomena. While only limited validation of these codes to date has been accomplished, the recent extension of these codes to three-dimensions so that real engine flow processes can be examined promises to increase their value in a major way. It is the combination of these techniques that is leading to dramatic improvements in our understanding of internal combustion engine flows. Results from all these “flow-defining resources” will be used in this review.

There are two broad objectives of internal combustion engine flow processes: (i) filling the cylinder with as much fresh air as possible; (ii) achieving a fast enough combustion process to release the fuel’s chemical energy in a short time interval centered at the beginning of the power producing stroke. Maximum engine power is airflow limited: only as much fuel can be burned as there is oxygen available. The impact of the flow on the combustion process is more subtle, however, and is different for spark-ignition and compression-ignition engines. The goal of this review is to structure the information now available on engine flows so that the important features of gas flow into, within, and out of the cylinder with respect to these two goals are identified and explained. The precise focus is to describe the gas motion within the cylinder set up by the flow through the intake and exhaust valves or ports during the intake and exhaust processes, and how that in-cylinder motion is modified by the movement of the piston once the valves or ports have been closed. It is, of course, the gas flow pattern within the cylinder at the end of the engine compression process that sets the scene for combustion in both spark-ignition and diesel engines. The intent is a review that is both an introduction and a reference resource on this topic, which brings together both the fundamental and pragmatic aspects of our understanding of engine flows.

The paper is arranged as follows. First, necessary background information on reciprocating engine operating cycles, the primary effect of piston motion, and the nature of the spark-ignition and diesel engine combustion processes is reviewed. Then the flow through inlet and exhaust valves in four-stroke cycle engines, and flow through ports in the cylinder liner in two-stroke cycle engines, are discussed. These flows govern the amount of air that enters the engine cylinder each cycle, and set up the in-cylinder flow pattern that later in the cycle will control the rate of energy release in the combustion process. Next the nature of the bulk flow pattern within the cylinder is examined. The character of the intake-valve generated flow, creation of swirl about the cylinder axis, compression produced flows, the exhaust flow and scavenging process flows are reviewed. The turbulence characteristics of

these flows are then defined and discussed. Finally, aspects of the flow behavior near the walls of the engine combustion chamber which can be substantially different from the bulk fluid motion are described. The review concludes with a discussion of critical research issues.

The behavior of the liquid fuel injected as one or more jets into the diesel engine cylinder just before combustion starts will not be reviewed. While the development of these initially liquid jets, and the atomization, vaporization, and fuel-air mixing processes that occur are critical to the diesel engine combustion process, these jet phenomena constitute a major separate topic beyond the scope of this paper. References [5] and [6] will introduce the reader to the literature on engine fuel spray phenomena.

2 IC Engine Operation

2.1 Engine Operating Cycles and Geometry.

This review is about reciprocating engines, where a piston moves back and forth in a cylinder and transmits power through a connecting rod and crank mechanism to the drive shaft as shown in Fig. 1. The steady rotation of the crank produces a cyclical piston motion. The piston comes to rest at the top-center (TC) crank position and bottom-center (BC) crank position when the cylinder volume is a minimum or maximum, respectively. The ratio of maximum volume to minimum is the compression ratio, r_c . Typical values of r_c are 8 to 12 for spark-ignition (SI) engines and 12 to 24 for compression-ignition (CI) or diesel engines.

The majority of reciprocating engines operate on the *four-stroke cycle*. Each cylinder requires four strokes of its piston—two revolutions of the crankshaft—to complete the sequence of events which produces one power stroke. This cycle comprises:

An intake stroke, which starts with the piston at TC and ends with the piston at BC, which draws fresh mixture into the cylinder. To increase the mass inducted, the inlet valve opens shortly before the stroke starts and closes after it ends.

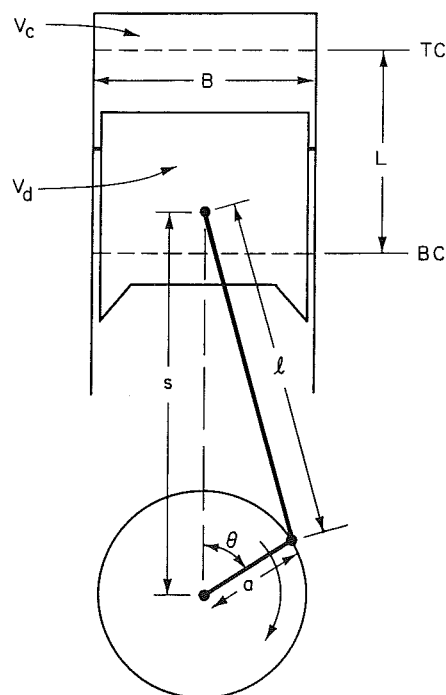


Fig. 1 Basic geometry of the reciprocating internal combustion engine. V_c and V_d indicate clearance and displaced volumes. B = bore, L = stroke, θ = crank angle, h = clearance height, l = connecting rod length, s = wrist pin axis to crank axis distance.

A *compression stroke*, when both valves are closed, and the mixture inside the cylinder is compressed to a small fraction of its initial volume. Toward the end of the compression stroke, combustion is initiated and the cylinder pressure rises more rapidly.

A *power stroke*, or expansion stroke, that starts with the piston at TC and ends at BC as the high temperature, high pressure, gases push the piston down and force the crank to rotate. Combustion is completed in the early part of the power stroke. As the piston approaches BC the exhaust valve opens to initiate the exhaust process, and drop the cylinder pressure to close to the exhaust pressure.

An *exhaust stroke*, where the remaining burned gases exit the cylinder; first because the cylinder pressure may be substantially higher than the exhaust pressure, then as they are swept out by the piston as it moves toward TC. As the piston approaches TC the inlet valve opens. Just after TC the exhaust valve closes, and the cycle starts again.

An alternative operating cycle is the *two-stroke* cycle where ports in the cylinder liner opened and closed by the piston motion (and sometimes valves in the cylinder head), control the exhaust and inlet flows while the piston is close to BC. The two-strokes are:

A *compression stroke*, where piston motion first closes the inlet ports and the exhaust ports (or the exhaust valves close), and then compresses the cylinder contents. As the piston approaches TC, combustion is initiated.

A *power or expansion stroke*, similar to that in the four-stroke cycle until the piston approaches BC when first the exhaust ports (or valves) are opened and then the intake ports are uncovered. Most of the burnt gases exit the cylinder in an exhaust blowdown process. When the inlet ports are uncovered, previously compressed fresh charge flows into the cylinder, displacing much of the remaining burned gases and scavenging the cylinder.

The above discussion of operating cycles identifies an important aspect of engine processes: piston position and velocity are key variables in determining what is happening inside the cylinder. Thus *crank angle* (θ in Fig. 1) is a useful independent variable since it defines piston position and cylinder volume, and because engine processes occupy almost constant crank angle intervals over a wide range of engine speeds. Rate of change of crank angle and engine geometry define the instantaneous piston speed S_p via the relation:

$$\frac{S_p}{\bar{S}_p} = \frac{\pi}{2} \sin \theta \left[1 + \frac{\cos \theta}{(R^2 - \sin^2 \theta)^{1/2}} \right] \quad (1)$$

where \bar{S}_p is the mean piston speed ($= 2LN$, where N is the crankshaft rotational speed in rev/s), $R = l/a$ and L , l , and a are defined in Fig. 1. Figure 2 shows the variation in piston speed for a typical value of R over the stroke. Piston speed is important because piston motion is the forcing function for many of the flow processes which take place within the engine. For example, a simple gas displacement model for flow through any cross-section in the intake system during the intake stroke gives the local inlet velocity v_i :

$$v_i = S_p (\pi B^2/4)/A_i \quad (2)$$

where B is the cylinder bore and A_i is the effective intake flow area at the location. Or, during the compression stroke, the mean axial velocity of the gas in the cylinder is

$$\bar{v}_z = S_p (z/h) \quad (3)$$

where z is distance from the cylinder head and h is the instantaneous clearance height. It is clear from these simple gas displacement models that the mean piston speed \bar{S}_p will be the important scaling velocity for all gas velocities driven by the piston motion.

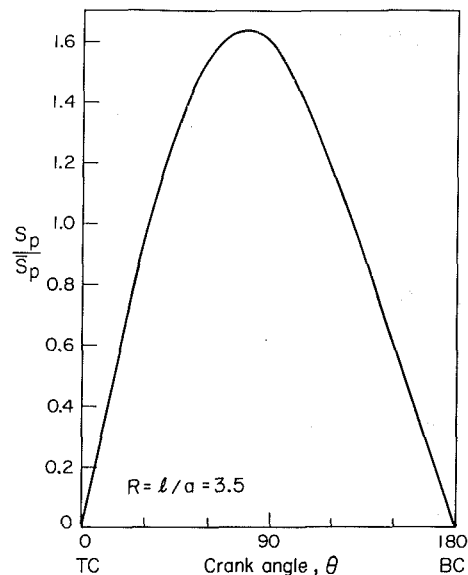


Fig. 2 Instantaneous piston speed S_p divided by mean piston speed \bar{S}_p as a function of crank angle

2.2 Spark-Ignition Engine Combustion Processes. In a conventional spark-ignition engine the fuel and air are mixed together in the intake system, inducted through the intake valve into the cylinder where mixing with residual gas takes place, and then compressed. Under normal operating conditions, combustion is initiated towards the end of the compression stroke at the spark-plug by an electric discharge. Following inflammation, a flame develops, propagates through this essentially premixed fuel, air, burned-gas, mixture until it reaches the combustion chamber walls, and then extinguishes. The combustion process takes place in a turbulent flow field which is produced by the high shear flows set up during the intake process and modified during compression. The importance of the turbulence to the engine combustion process was recognized long ago through experiments where the intake event, and the turbulence it generates, was eliminated and the rate of flame propagation decreased substantially.

Insight into this flame propagation process can be obtained from photographs taken with techniques which are sensitive to density changes in the flow field, such as schlieren and shadowgraph. Detailed observations have been made of flame structure from ignition, to flame extinguishing at the far cylinder wall in special visualization engines with glass walls (e.g., [7]). The flame develops initially from the spark discharge which causes ignition as a spherical kernel which starts to grow at the laminar flame speed (Fig. 3(a)). As this developing sheet-like flame grows it interacts with the turbulent flow field in the vicinity of the spark plug as seen in Fig. 3(b): the flame outer surface becomes increasingly convoluted, and the flame center can be convected away from the plug in a direction and with a velocity that can vary substantially cycle-by-cycle. The structure of the flame continues to develop as it propagates across the chamber (Fig. 3(c)). Early in the burning process the flame is a thin, moderately wrinkled but simply connected, front or reaction sheet between unburned and burned gas. As the flame propagates across the chamber, the thickness of the reaction sheet front remains roughly constant, the flame front becomes more convoluted and the scale of the wrinkles tends to decrease with time [8]. Further insight into the structure of the developed engine flame can be obtained from enlarged photographs of the leading and trailing edges of the flame, obtained with the schlieren or shadowgraph technique. Figure 4(a) shows the front of the flame 40 deg after spark when it has propagated

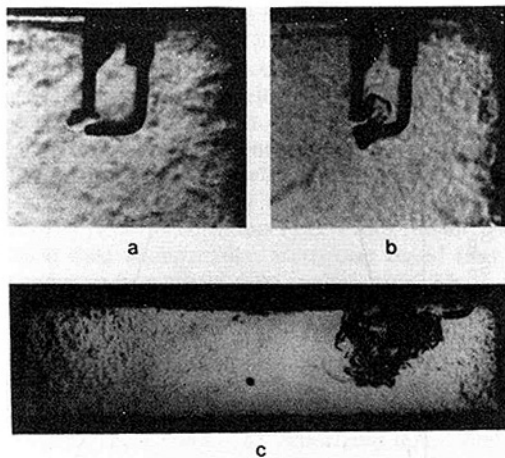


Fig. 3 Schlieren photos of developing spark-ignition engine flame: (a) 1 deg after start of spark discharge; (b) 5 deg after spark; (c) 25 deg after spark. Each photo from different cycle. Spark plug wires 0.8 mm diameter. 1400 rev/min; 0.5 atm inlet pressure; propane fuel; fuel-air equivalence ratio 0.9; spark advance 45 deg BTC [7].

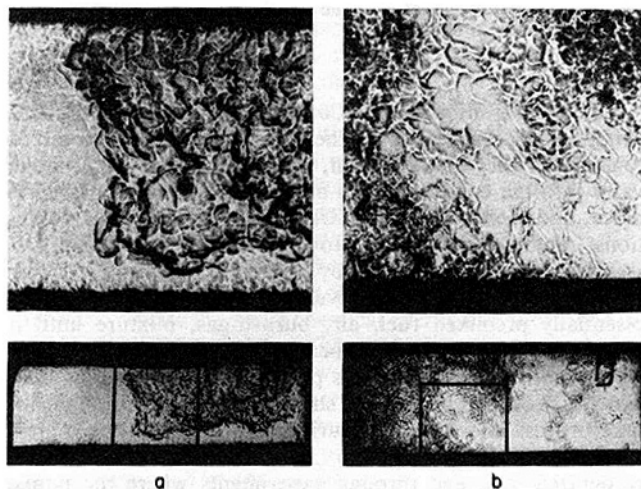


Fig. 4 Enlarged schlieren photos of flame front (a) and flame back (b) in square cross-section cylinder engine with two glass side walls. Same conditions as Fig. 3 [7].

about half way across the chamber. It shows the irregular but smoothly curved surfaces which comprise the leading edge of the flame. Figure 4(b) shows the back of the flame 70 deg after the spark, when the front of the flame has just reached the wall of the combustion chamber farthest from the spark plug. It shows large clear regions of burned gas behind the flame, and smaller clear regions connected by a lace-like structure within which the remaining regions of unburned mixture are being consumed. The analogy with a crumpled sheet of paper is appropriate. Finally, the flame front reaches the far wall and flame propagation ceases; the final combustion phase where mixture within the flame burns out to complete the process then occurs.

The above described features of the developing and propagating flame are common to almost all engine geometries and operating conditions. Figure 5 shows shadowgraph photographs of the flame, at fixed crank angle intervals after ignition, taken through a transparent cylinder head with different geometric and flow configurations [9]. The approximately spherical development of the flame from the vicinity of the spark plug except where it intercepts the chamber walls is evident for side and center ignition with one plug, and from both plugs, in the absence of any intake-generated swirl. With normal levels of swirl, the flame center is convected with the

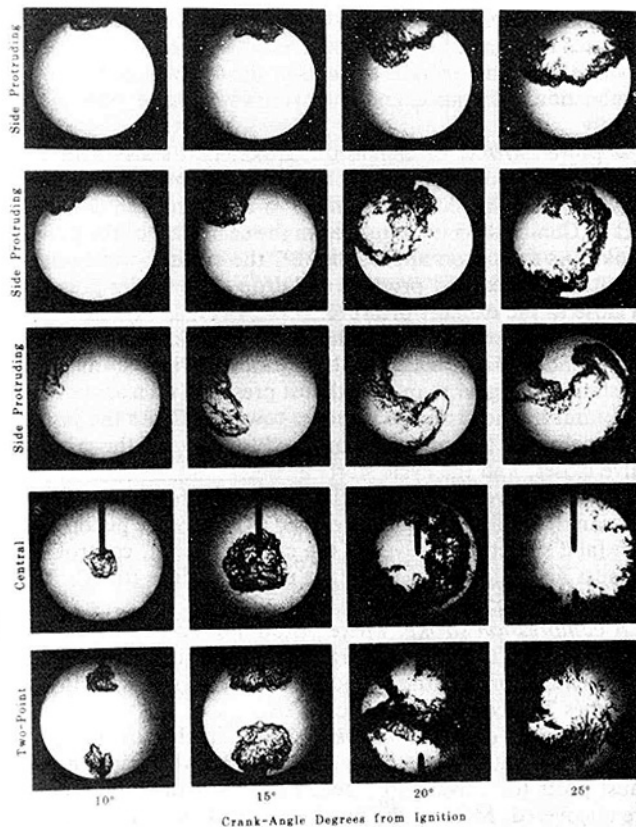


Fig. 5 Laser shadowgraph photographs of SI engine combustion in engine with transparent cylinder head. From top to bottom: side plug without swirl; side plug with moderate swirl; side plug with high swirl; central plug without swirl; two plugs without swirl [9].

swirling flow, but the flame front as it grows is still approximately spherical in shape. With unusually high levels of swirl, and aerodynamic stabilization of the flame at the spark-plug location, the flame can become stretched out and distorted by the flow in a major way.

The flame development and subsequent propagation vary significantly, cycle-by-cycle. This is because flame growth depends on local mixture composition and motion. These quantities vary in successive cycles in any given cylinder, and may vary cylinder-to-cylinder. Especially important are mixture composition and motion in the vicinity of the spark plug at time of spark discharge since these govern the early stages of flame development. Mixture burning rate is strongly influenced by engine speed. It is well established that the duration of combustion in crank angle degrees only increases slowly with increasing engine speed [10]. The burning rate throughout the combustion process increases almost, though not quite, as rapidly as engine speed. All the above summarized evidence indicates that developed turbulent flames in spark-ignition engines, under normal operating conditions are highly wrinkled and probably multiply connected thin reaction sheets [11].

What is needed during combustion in a spark-ignition engine, therefore, is a sufficiently turbulent flowfield to ensure rapid flame development and propagation. It is important also that the mixture burning rate vary little from one cycle to the next; thus the flow pattern should exhibit low cycle to cycle variability. The resistance to flow into and out of the cylinder must also be as low as possible to give high engine output. Thus, excessive mixture motion and turbulence beyond that required to achieve the desired burning rate is undesirable; it results in higher than necessary air flow penalty, and excessive heat losses to the combustion chamber walls.

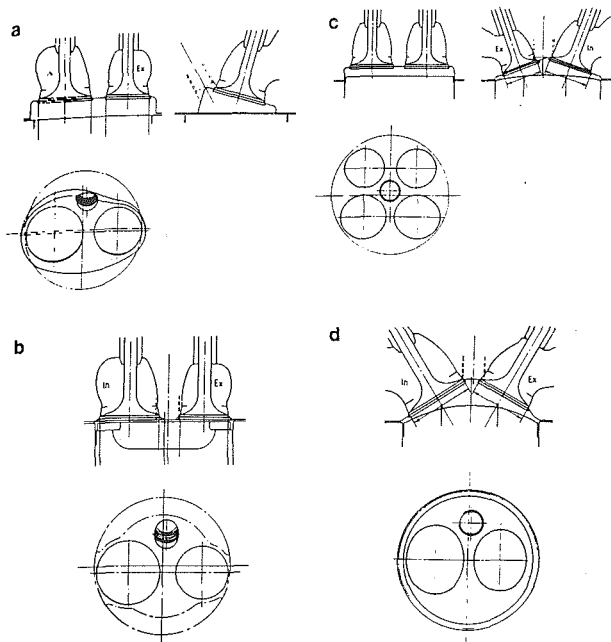


Fig. 6 Common spark-ignition engine combustion chamber shapes: (a) wedge or bathtub; (b) bowl-in-piston; (c) four-valve, pent-roof; (d) hemispherical [14]

While the disk-shaped combustion chamber shown in Fig. 1 is sometimes used for research experiments, production spark-ignition engines usually have more complex chamber shapes. The optimum chamber design is a balance between achieving a fast combustion process which is repeatable cycle-by-cycle for high efficiency and good emission control, large valve effective flow areas for maximum power, low wall surface area for a given displaced volume to minimize heat losses, and achieving a low fuel octane requirement by avoiding knock [12]. Geometry constraints due to manufacturing considerations often limit chamber design too.

There are a large number of options for cylinder head and piston crown shape, spark plug location, size and number of valves, and intake port design [13]. Figure 6 shows examples of common combustion chamber shapes. Current practice favors more open chambers such as the two-valve hemispherical and four-valve pent-roof designs for their larger valve flow area and lower surface-to-volume ratio. These more complex shapes than the simple disk chamber obviously have an impact on the flow inside the cylinder.

2.3 Diesel Engine Combustion. The essential features of the compression-ignition diesel combustion process can be summarized as follows. Fuel is injected by the fuel-injector into the engine cylinder towards the end of the compression stroke, just before the desired start-of-combustion. The liquid fuel, usually injected at high velocity as one or more jets, atomizes into small drops and penetrates into the combustion chamber. The fuel vaporizes and mixes with the high-temperature high-pressure cylinder air, and since the air temperature and pressure are above the fuel's ignition point, spontaneous ignition of portions of the already mixed fuel and air occurs after a delay period of a few crank angle degrees. The cylinder pressure increases as combustion of fuel-air mixture occurs. The consequent compression of the unburned portion of the charge shortens the delay before ignition for the fuel and air which has mixed to within combustible limits, which then burns rapidly. It also reduces the evaporation time of the remaining liquid fuel. Injection continues until the desired amount of fuel has entered the cylinder. Atomization, vaporization, fuel-air mixing and combustion continue until

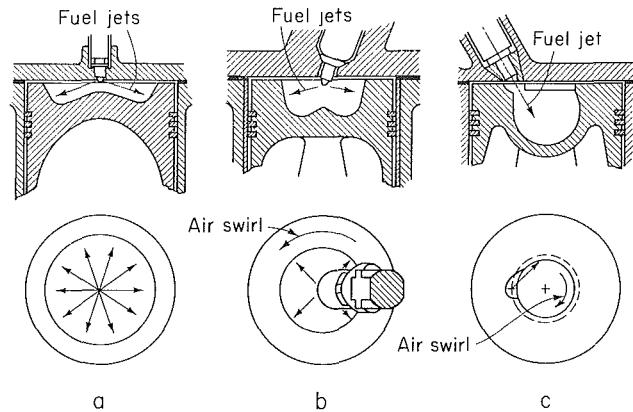


Fig. 7 Common types of direct-injection compression-ignition or diesel engine combustion systems: (a) quiescent chamber with multi-hole nozzle typical of larger engines; (b) bowl-in-piston chamber with swirl and multi-hole nozzle; (c) bowl-in-piston chamber with swirl and single-hole nozzle. (b) and (c) used in medium to small DI engine range.

essentially all the fuel has passed through each process. In addition, mixing of air remaining in the cylinder with burning and already burned gases continues throughout the combustion and expansion processes [15]. The details of the process depend on the characteristics of the fuel, the design of the combustion chamber and fuel injection system, and on the engine's operation conditions. It is an unsteady, heterogeneous, three-dimensional combustion process. While an adequate conceptual understanding of diesel combustion has been developed to date, an ability to describe many of the important individual processes in a quantitative manner is lacking.

The major problem in diesel combustion chamber design is achieving sufficiently rapid mixing between the injected fuel and the air in the cylinder to complete combustion in the appropriate crank angle interval close to top center. The fuel-air mixing rate is the primary factor controlling the fuel burning rate. The practical diesel engine size range is substantial with cylinder bores varying from about 70 to 900 mm. The mean piston speed at maximum rated power is approximately constant over this size range so the maximum rated engine speed will be inversely proportional to the stroke. For a fixed crank angle interval for combustion (of order 50° to maintain high cycle thermal efficiency), the time available for combustion will, therefore, scale with the stroke. Thus, at the small end of the diesel size range, the mixing between the injected fuel and the air must take place on a time scale some 10 times shorter than in engines at the large end of the range. It would be expected, therefore, that the design of the engine combustion chamber and the fuel injection system would have to change substantially over this size range to provide the fuel and air motion inside the cylinder required to achieve the desired fuel-air mixing rate. As engine size decreases, more vigorous air motion is required while less fuel jet penetration is necessary. It is this logic, primarily, that leads to the different diesel combustion chamber designs (and their different air flow patterns) found in practice over the engine size range.

In the largest size engines, where mixing rate requirements are least stringent, quiescent direct-injection systems of the type shown in Fig. 7(a) are used. The momentum and energy of the injected fuel jets are sufficient to achieve adequate fuel distribution and rates-of-mixing with the air; additional organized air motion is not required. The combustion chamber shape is usually a shallow bowl in the crown of the piston, and a central multi-hole injector nozzle is used.

As engine size decreases, increasing amounts of air swirl are used to achieve faster fuel-air mixing rates. Air swirl—rotational motion about the cylinder axis—is generated by suitable

design of the inlet port. The air swirl rate is then increased as the piston approaches TC by forcing the air towards the cylinder axis, into the cup or bowl-in-piston combustion chamber. Two types of DI engine with swirl are in common use. Figure 7(b) shows a DI engine with swirl, with a centrally located multi-hole injector nozzle. Here the design goal is to hold the amount of fuel which impinges on the piston cup walls to a minimum. Figure 7(c) shows the M.A.N. "M system" with its single-hole fuel-injection nozzle, oriented so that much of the fuel is deposited on the piston cup wall. These two types of designs are used in medium size diesels.

Inlet generated air swirl, despite amplification in the piston cup, does not provide sufficiently high fuel-air mixing rates for the small high-speed diesels used in automobiles. Indirect-injection or divided-chamber engine systems have been used instead, where the vigorous charge motion required during injection is generated during the compression stroke. Two broad classes of IDI systems can be defined: (i) swirl chamber systems, and (ii) prechamber systems, as illustrated in Figs. 8(a) and (b), respectively. During compression, air is forced from the main chamber above the piston into the auxiliary chamber, through the nozzle or orifice (or set of orifices). Thus, toward the end of compression, a vigorous flow in the auxiliary chamber is set up. In swirl chamber systems the connecting passage and chamber are shaped so that this flow within the auxiliary chamber rotates rapidly. Fuel is usually injected at lower pressure than is typical of DI systems through a pintle nozzle as a single spray. Combustion starts in the auxiliary chamber; the pressure rise associated with combustion forces fluid back into the main chamber where the jet issuing from the nozzle entrains and mixes with the main chamber air. The glow plug shown in Figs. 8(a,b) is a cold starting aid. The plug is heated prior to starting the engine to ensure ignition of fuel early in the engine cranking process.

The fluid dynamic aspects of these diesel injection and combustion processes can be illustrated with photographs. Figure 9 shows schlieren pictures of diesel fuel sprays prior to onset of combustion in a swirling airflow. The photo on the left, taken with high sensitivity, shows the outer vapor boundaries

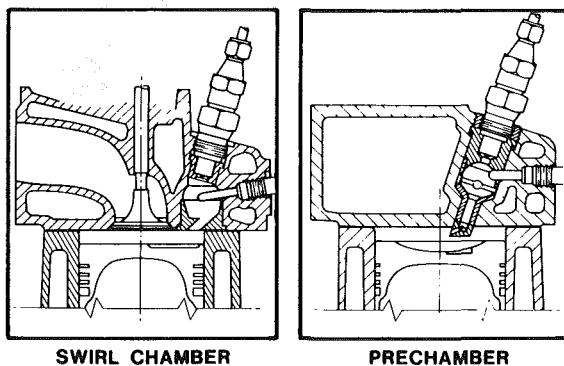


Fig. 8 Two common types of small indirect-injection diesel engine combustion system: (a) swirl chamber; (b) prechamber

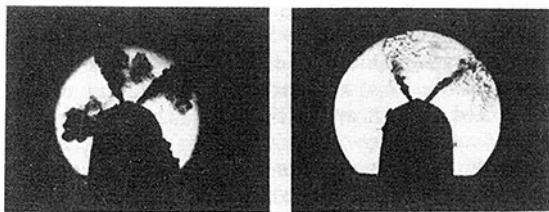


Fig. 9 Schlieren photos of diesel engine fuel jets in a swirling airflow. Photo on left at high sensitivity shows the extent of the fuel vapor outer region of each jet; photo on right at low sensitivity shows the liquid fuel core of each jet [16].

of the evaporating turbulent fuel jet; that on the right, at lower sensitivity, shows the liquid fuel core of the jet (dark) surrounded by the fuel vapor regions of the jet [16]. Figure 10 shows the structure of the flame in a direct-injection engine at different stages in the combustion process [17]. The close linking of the flame shape with that of the fuel jet is apparent. While the jet and flame behavior is different in the different types of diesel combustion systems shown in Figs. 7 and 8, similar jet-type fluid mechanic features are present in all of them.

3 Flows Through Valves and Ports

The purpose of the exhaust and inlet processes in four-stroke cycle engines, or of the scavenging process in two-stroke cycle engines, is to remove the burned gases at the end of the power stroke and admit the fresh charge for the next cycle. The indicated power of an internal combustion engine at a given speed is proportional to the mass flow rate of air. Thus, inducing the maximum air mass at wide open throttle or full load, and retaining that mass within the cylinder, is one major goal of the gas exchange processes. An additional goal of the intake process is the setting up of the appropriate flow within the cylinder. The effectiveness of these gas exchange processes is defined by overall parameters such as volumetric efficiency

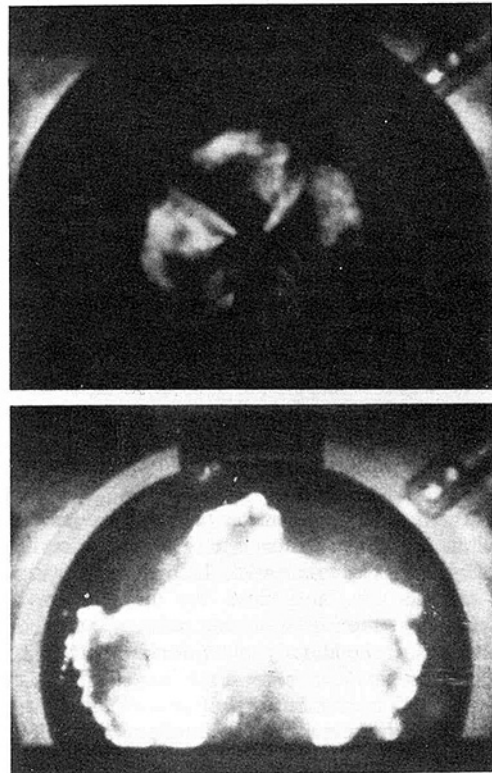
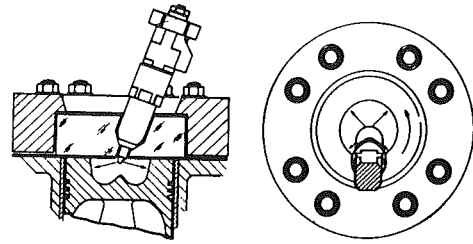


Fig. 10 Photographs of flame in direct-injection diesel engine [17]. Engine geometry shown at top. Upper photos shows flame early in combustion process, at the outer edge of the fuel sprays within the piston bowl. Lower photo shows flame later as gases expand out of the bowl into the region between piston crown and cylinder head.

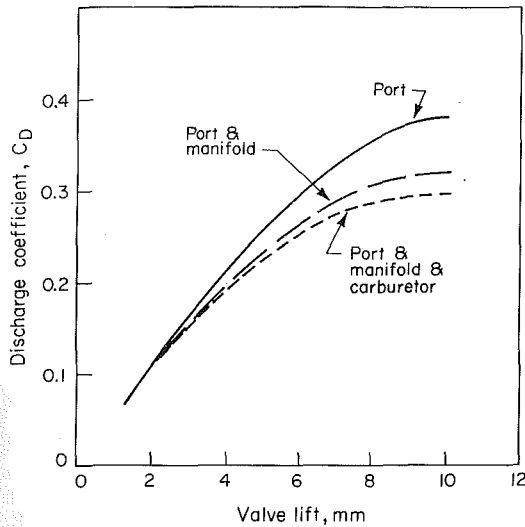


Fig. 11 Discharge coefficients for inlet port and valve, port valve and manifold, port valve manifold and carburetor, as a function of valve lift [18]

(for four-stroke cycles), and scavenging efficiency and trapping efficiency (for two-stroke cycles). These overall parameters depend on the flow characteristics of engine intake and exhaust systems, and especially the valves or ports.

3.1 Flow Through Valves. The valve, or valve and its port together, is the most important flow restriction in the intake and the exhaust system of 4-stroke cycle engines. Figure 11 shows how the discharge coefficient (effective area divided by a reference geometric area) for the intake system, which defines the flow resistance, is dominated by the valve and port in an automobile spark-ignition engine [18].

3.1.1 Poppet Valve Geometry and Timing. Figure 12 shows the proportions of typical inlet and exhaust valves and ports, relative to the valve inner seat diameter D . The inlet port is generally circular, or nearly so, and the cross-sectional area is no larger than is required to achieve the desired power output. For the exhaust port, the importance of good valve seat and guide cooling, with the shortest length of exposed valve stem, leads to a different design. Although a circular cross-section is still desirable, a rectangular or oval shape is often essential around the guide boss area. Typical valve head sizes for different shape combustion chambers in terms of cylinder bore B are given in Table 1 [14]. Each of these chamber shapes imposes different constraints on valve size. Larger valve sizes (or four valves compared with two) allow higher maximum airflows for a given cylinder displacement. Typical valve timing, valve lift profiles and valve open areas for a four-stroke cycle spark-ignition engine are shown in Fig. 13.

The instantaneous valve flow area depends on valve lift and the geometric details of the valve head, seat and stem. There are three separate stages to the flow area development as valve lift increases [20], as shown in Fig. 13(b). For low valve lifts, the minimum flow area corresponds to a frustum of a right circular cone where the conical face between the valve and the seat, which is perpendicular to the seat, defines the flow area. For this stage:

$$\frac{w}{\sin\beta\cos\beta} > L_v > 0$$

and the minimum area is:

$$A_m = \pi L_v \cos\beta \left(D_v - 2w + \frac{L_v}{2} \sin 2\beta \right) \quad (4)$$

β is the valve seat angle, L_v is the valve lift, D_v is the valve

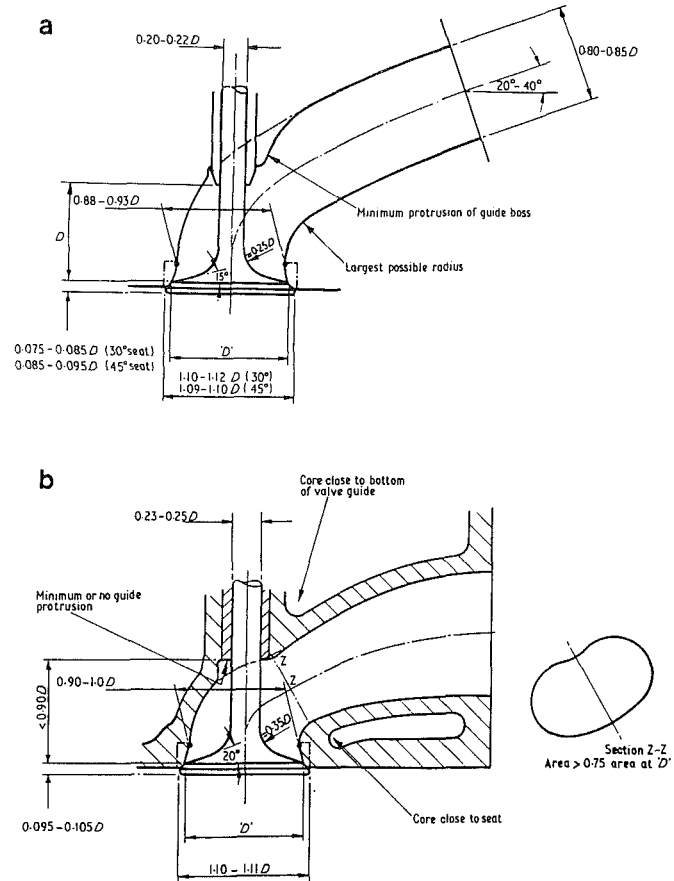


Fig. 12 Shape, proportions, and critical design areas of typical inlet (top) and exhaust (bottom) valves and ports [14]

Table 1 Valve head diameter in terms of cylinder bore, B [14]

Combustion chamber shape*	Inlet	Exhaust	Approx mean piston speed at max power, m/s
Wedge or bathtub	0.43-0.46 B	0.35-0.37 B	15
Bowl-in-piston	0.42-0.44 B	0.34-0.37 B	14
Hemispherical	0.48-0.5 B	0.41-0.43 B	18
Four-valve pent-roof	0.35-0.37 B	0.28-0.32 B	20

*See Fig. 6.

head diameter (the outer diameter of the seat), and w is the seat width (difference between inner and outer seat radii).

For the second stage, the minimum area is still the slant surface of a frustum of a right circular cone, but this surface is no longer perpendicular to the valve seat. The base angle of the cone increases from $(90 - \beta)$ deg toward that of a cylinder, 90 deg. Thus for this stage:

$$\left[\left(\frac{D_p^2 - D_s^2}{4D_m} \right) - w^2 \right]^{1/2} + w \tan\beta \geq L_v > \frac{w}{\sin\beta\cos\beta}$$

and

$$A_m = \pi D_m [(L_v - w \tan\beta)^2 + w^2]^{1/2} \quad (5)$$

D_p is the port diameter, D_s is the valve stem diameter, D_m is the mean seat diameter ($D_v - w$).

Finally, when the valve lift is sufficiently large, the minimum flow area is no longer between the valve head and seat; it is the port flow area minus the sectional area of the valve stem. Thus, for

$$L_v > \left[\left(\frac{D_p^2 - D_s^2}{4D_m} \right)^2 - w^2 \right]^{1/2} + w \tan \beta,$$

$$A_m = \frac{\pi}{4} (D_p^2 - D_s^2) \quad (6)$$

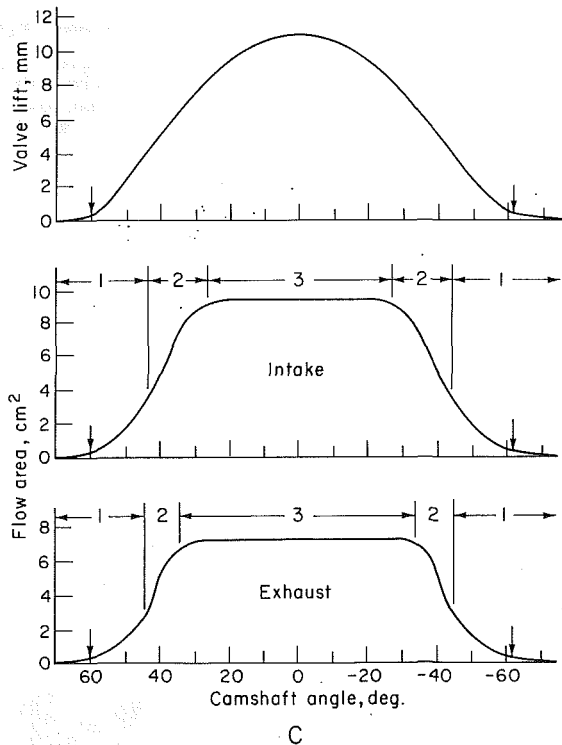
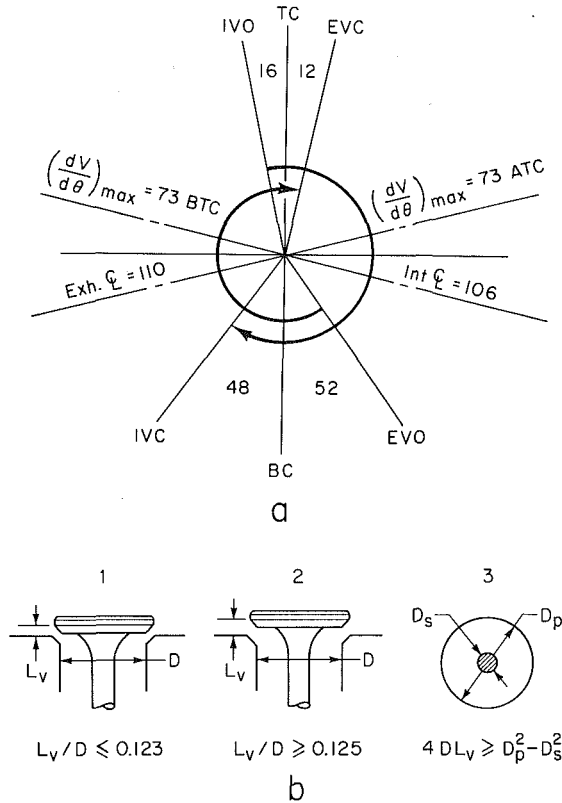


Fig. 13(a) Typical valve timing diagram for high speed 2.2 l 4-cylinder spark-ignition engine; (b) Schematic showing three stages of valve lift; (c) valve lift curve and corresponding minimum intake and exhaust valve open areas as a function of cam shaft angle. Inlet and exhaust valve diameters are 3.6 and 3.1 cm, respectively [19].

Intake and exhaust valve open areas corresponding to a typical valve lift profile are plotted versus camshaft angle in Fig. 13(c). These three different flow regimes are indicated. The maximum valve lift is normally about 12 percent of the cylinder bore. Note from the timing diagram (Fig. 13(a)) that the crank angles of maximum valve lift and maximum piston velocity (Fig. 2) do not coincide.

The effect of valve geometry and timing on airflow can be illustrated conceptually by dividing the rate of change of cylinder volume by the instantaneous minimum valve flow area to obtain a *pseudo flow velocity* v_{ps} for each valve [19]:

$$v_{ps} = \frac{1}{A_m} \frac{dV}{d\theta} = \frac{\pi B^2}{4A_m} \frac{ds}{d\theta} \quad (7)$$

V is the cylinder volume, B the cylinder bore, s is the distance between wrist pin and crank axis (see Fig. 1), and A_m is the valve area given by equations (4), (5), or (6). Instantaneous pseudo flow velocity profiles for the exhaust and intake strokes of a four-stroke four-cylinder engine are shown in Fig. 14. Note the appearance of two peaks in the pseudo flow velocity, for both the exhaust and intake strokes. The broad peaks occurring at maximum piston velocity reflect the fact that valve flow area is constant at this point. The peaks close to TC result from the exhaust valve closing and intake valve opening profiles. The peak at the end of the exhaust stroke is important since it indicates there is a high pressure drop across the valve at this point, which will result in higher trapped residual mass. The value of this exhaust stroke pseudo velocity peak depends strongly on the timing of exhaust valve closing. The pseudo velocity peak at the start of the intake stroke is much less important. That the pseudo velocities early in the exhaust stroke and late in the intake stroke are low indicates that phenomena other than quasi-steady flow govern the flow rate. These are the periods when exhaust blowdown, and ram and tuning effects in the intake, are most important.

3.1.2 Flow Rate, Discharge Coefficients and Flow Patterns.

The mass flow rate through a poppet valve is usually described by the equation for compressible flow through a flow restriction. This equation is derived from a one-dimensional isentropic flow analysis, and real gas flow effects are included by means of an experimentally-determined discharge coefficient C_D . The air flow-rate is related to the upstream stagnation pressure p_0 and stagnation temperature T_0 , static pressure just downstream of the flow restriction (assumed equal to the

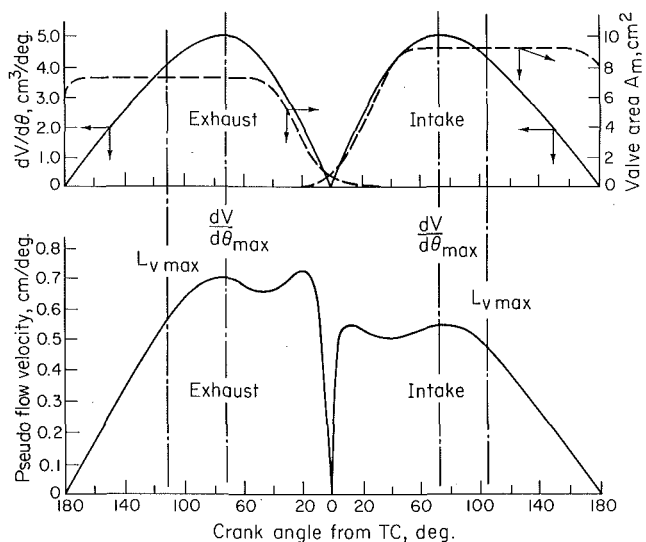


Fig. 14 Rate of change of cylinder volume $dV/d\theta$, valve minimum flow area A_m and pseudo flow velocity as a function of crank angle for exhaust and inlet valves of Fig. 13 [19]

pressure at the restriction, p_T , and a reference area A_R characteristic of the valve design:

$$\dot{m} = \frac{C_D A_R p_0}{\sqrt{RT_0}} \left(\frac{p_T}{p_0} \right)^{1/\gamma} \left\{ \frac{2\gamma}{\gamma-1} \left[1 - \left(\frac{p_T}{p_0} \right)^{(\gamma-1)/\gamma} \right] \right\}^{1/2} \quad (8)$$

When the flow is choked, i.e., $p_T/p_0 \leq [2/(\gamma+1)]^{\gamma/(\gamma-1)}$, the appropriate equation is

$$\dot{m} = \frac{C_D A_R p_0}{\sqrt{RT_0}} \gamma^{1/2} \left(\frac{2}{\gamma+1} \right)^{(\gamma+1)/2(\gamma-1)} \quad (9)$$

For flow into the cylinder through an intake valve, p_0 is the intake manifold pressure p_i , and p_T is the cylinder pressure. For flow out of the cylinder through an exhaust valve, p_0 is the cylinder pressure and p_T is the exhaust manifold pressure.

The value of C_D and the choice of reference area are linked together: their product, $C_D A_R$, is the effective flow area of the valve assembly, A_e . Several different reference areas have been used. These include the valve head area $\pi D_v^2/4$ [21], the port area at the valve seat $\pi D_p^2/4$ [22], the geometric minimum flow area (equations (4), (5), and (6)) and the curtain area $\pi D_v L_v$ [23] where L_v is the valve lift. The choice is arbitrary, through some of the above allow easier interpretation than others. As has been shown above, the geometric minimum flow area is a complex function of valve and valve seat dimensions. The most convenient reference area in practice is the so-called valve curtain area:

$$A_C = \pi D_v L_v \quad (10)$$

since it varies linearly with valve lift and is simple to determine.

Figure 15 shows the results of steady flow tests on a typical inlet valve configuration with a sharp-cornered valve seat [23]. The discharge coefficient based on the valve curtain area is a discontinuous function of the valve lift to diameter ratio. The three segments shown correspond to different flow regimes as indicated. At very low lifts, the flow remains attached to the valve head and seat giving high values for the discharge coefficient. At intermediate lifts, the flow separates from the valve head at the inner edge of the valve seat as shown. An abrupt decrease in discharge coefficient occurs at this point. The discharge coefficient then increases with increasing lift since the size of the separated region remains approximately constant while the minimum flow area is increasing. At high lifts, the flow separates from the inner edge of the valve seat, as well [20, 24]. Typical maximum values of L_v/D_v are 0.25.

An important question is whether these steady flow data are representative of the dynamic flow behavior of the valve in an operating engine. There is some evidence that the "change points" between different flow regimes shown in Fig. 15 occur at slightly different valve lifts under dynamic operation than under steady flow operation. Also, the pressure upstream of the valve varies significantly during the intake process. However, it has been shown that over the normal engine speed range, steady-flow discharge-coefficient results can be used to predict dynamic performance with reasonable precision [20] [25].

In addition to valve lift, the performance of the inlet valve assembly is influenced by the following factors: valve seat width, valve seat angle, rounding of the seat corners, port design, cylinder head shape. In many engine designs the port and valve assembly are used to generate a rotational motion (swirl) inside the engine cylinder during the induction process. Or, the cylinder head can be shaped to restrict the flow through one side of the valve open area to generate swirl. Swirl generation significantly reduces the valve and port flow coefficient. Swirl production is discussed later. Changes in seat width affect the L_v/D_v at which the shifts in flow regimes illustrated in Fig. 15 occur. C_D increases as seat width decreases. The seat angle β affects the discharge coefficient in

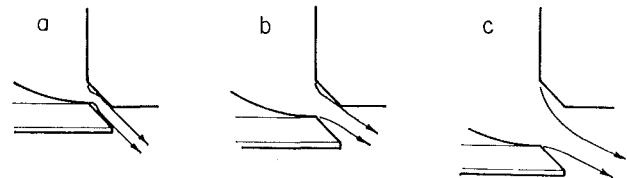
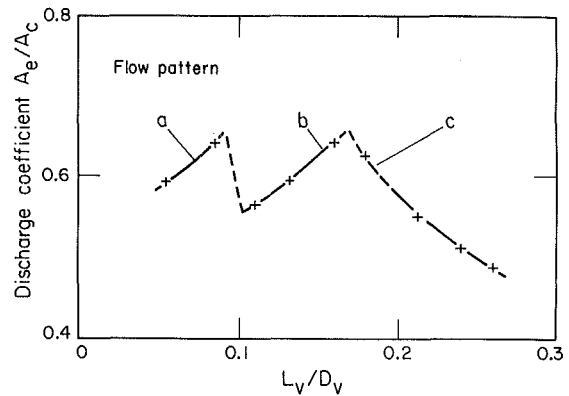


Fig. 15 Discharge coefficient of typical inlet poppet valve (effective flow area/valve curtain area) as a function of valve lift. Different segments correspond to flow regimes indicated [23].

the low-lift regime in Fig. 15. Rounding the upstream corner of the valve seat reduces the tendency of the flow to break away, thus increasing C_D at higher lifts. At low valve lifts, when the flow remains attached, increasing the Reynolds number decreases the discharge coefficient. Once the flow breaks away from the wall, there is no Reynolds number dependence of C_D [23].

For well-designed ports (e.g., Fig. 12) the discharge coefficient of the port and valve assembly need be no lower than that of the isolated valve (except when the port is used to generate swirl). However, if the cross-sectional area of the port is not sufficient or the radius of the surface at the inside of the bend is too small, a significant reduction in C_D for the assembly can result [23].

At high engine speeds, unless the inlet valve is of sufficient size, the inlet valve during part of the induction process can become choked (i.e., reach sonic velocity) at the minimum valve flow area. Choking substantially reduces volumetric efficiency. Various definitions of inlet Mach number have been used to identify the onset of choking. Taylor and coworkers [21] correlated volumetric efficiencies measured on a range of engine and inlet valve designs with an inlet Mach index Z formed from an average gas velocity through the inlet valve:

$$Z = A_p \bar{S}_p / (C_i A_i a) \quad (11)$$

where A_i is the nominal inlet valve area ($\pi D_v^2/4$), C_i is a mean valve discharge coefficient based on the area A_i , and a is the sound speed. From the method used to determine C_i , it is apparent that $C_i A_i$ is the average effective open area of the valve (it is the average value of $C_D \pi D_v L_v$). Z corresponds closely, therefore, to the mean Mach number in the inlet valve throat. Taylor's correlations show that η_v decreases rapidly for $Z \geq 0.5$. An alternative equivalent approach to this problem has been developed, based on the average flow velocity through the valve during the period the valve is open [26]. A mean inlet Mach number was defined:

$$\bar{M}_i = v_i / a \quad (12)$$

where v_i is the mean inlet flow velocity during the valve open period. \bar{M}_i is related to Z via

$$\bar{M}_i = Z(\eta_v/100)180/(\theta_{IVC} - \theta_{IVO}) \quad (13)$$

This mean inlet Mach number correlates volumetric efficiency characteristics better than the Mach index. For a series of modern small 4-cylinder engines, when \bar{M}_i approaches 0.5 the volumetric efficiency decreases rapidly, due to the flow becoming choked during part of the intake process. This relationship can be used to size the inlet valve for the desired volumetric efficiency at maximum engine speed. Also, if the inlet valve is closed too early, volumetric efficiency will decrease gradually with increasing \bar{M}_i , for $\bar{M}_i < 0.5$, even if the valve open area is sufficiently large [26].

Because the flow in the intake port and valve is inherently three-dimensional realistic predictions of the flow field in the port with fluid dynamic computer codes have only recently become feasible. They promise to be extremely useful for improving port and valve designs to give the desired velocity profile at inlet valve exit with minimum pressure drop across the valve and port, thus providing maximum airflow. The results in Fig. 16 illustrate the potential for these types of calculations [27]. The flow pattern within a helical-shaped inlet port is shown. The grid used to model the port geometry is indicated in the upper right of the figure. The other three parts of the figure show the traces of selected gas particles in three orthogonal planes. Helical shaped intake ports (see Fig. 33 and Section 4.2) are used to generate a swirling in-cylinder flow pattern, by forcing the flow in the port above the valve to rotate about the valve stem. The predicted velocity vector maps and particle traces indicate how this flow pattern within the port is achieved.

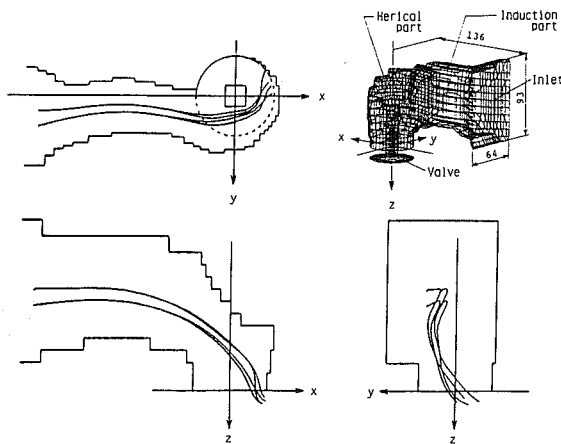


Fig. 16 Results of three-dimensional calculation of flow through helical inlet port and valve. Mesh used to model passage shown upper right. Cross sections show calculated traces of gas particles as they flow through port and valve [27].

When the exhaust valve opens toward the end of the expansion stroke, the cylinder pressure is usually substantially higher than the exhaust system pressure. A blowdown process results as burned gases exit the cylinder rapidly, usually choking the flow at the exhaust valve minimum area until the cylinder pressure drops below the critical valve. An extremely vigorous in-cylinder gas flow toward the exhaust valve occurs during this process which generates in-cylinder velocities up to several times the mean piston speed [28]. As the blowdown process ends, the gas velocities near the exhaust valve decrease. Piston motion has little effect on this blowdown process, which at low to moderate engine speeds ends at about BC. The motion of the piston then displaces gas out of the cylinder. Figure 17 shows schlieren photographs of the exhaust stroke flow taken in a square cross-section engine with two transparent quartz walls. The nonuniform density and turbulent character of the flow into the exhaust valve annular opening are apparent. A recirculation zone was observed beneath the open valve. Note how the upward motion of the piston scrapes the boundary layer off the cylinder wall and rolls it into a vortex during the exhaust stroke [28]. This flow in the cylinder-liner piston-face corner is discussed more fully in Section 6.2

In studies of the flow from the cylinder through an exhaust poppet valve, different flow regimes at low and high lift occur, as shown in Fig. 18. Values of C_D based on the valve curtain area, for several different exhaust valve and port combinations, are given in Fig. 19. A sharp-cornered isolated poppet valve (i.e., straight pipe downstream, no port) gives the best performance. At high lifts, $L_v/D_v \geq 0.2$, the breakaway of the flow reduces the discharge coefficient. (At $L_v/D_v = 0.25$ the effective area is about 90 percent of the minimum geometric area. For $L_v/D_v < 0.2$ it is about 95 percent [23].) The port design significantly affects C_D at higher valve lifts as indicated by the data from four port designs in Fig. 19. Good designs can approach the performance of isolated valves, however. Exhaust valves operate over a wide range of pressure

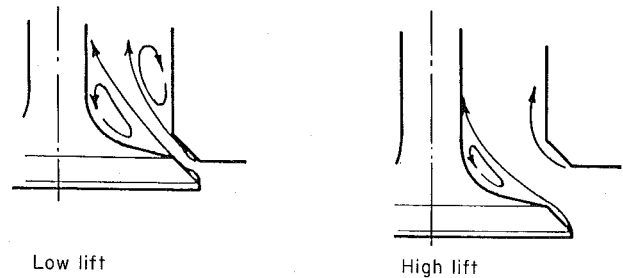


Fig. 18 Flow pattern through exhaust valve at low and high lift [23]

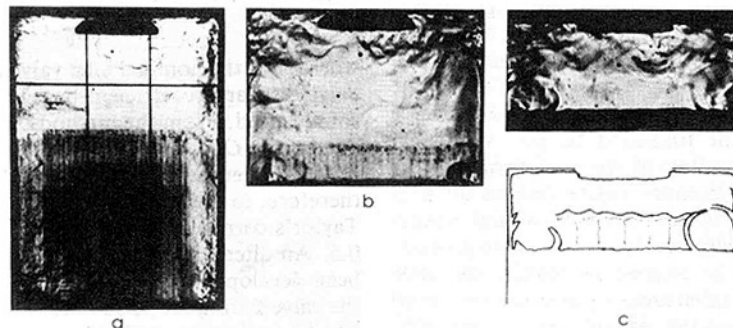


Fig. 17 Schlieren photographs of cylinder of square cross-section visualization spark-ignition engine during the exhaust stroke at (a) 120 deg, (b) 60 deg and (c) 20 deg before TC [28]. Character of turbulent flow toward exhaust valve is evident. Photos and schematic also show vortex in piston-crown cylinder-wall corner, discussed in Section 6.2.

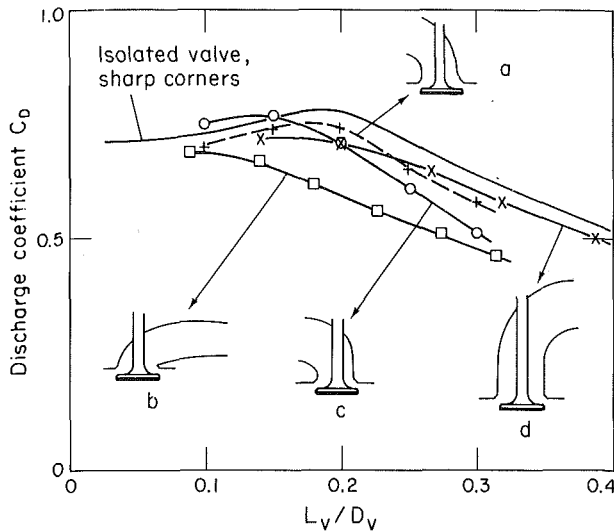


Fig. 19 Discharge coefficient as function of valve lift for several exhaust valve and port designs [23]: a [29]; b [22]; c [29]; d [30]

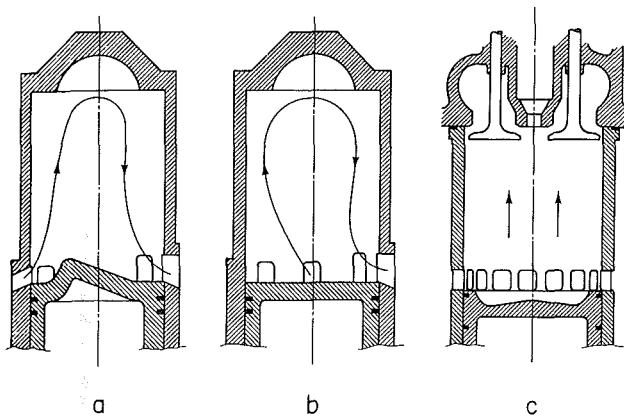


Fig. 20 Cross-scavenged (A), loop-scavenged (B), and uniflow-scavenged (C) two-stroke cycle flow configurations

ratios (1 to 5). For pressure ratios greater than about 2 the flow will be choked, but the effect of pressure ratio on discharge coefficient is small and confined to higher lifts (e.g., ± 5 percent at $L_v/D_v = 0.3$) [22].

3.2 Flow Through Cylinder-Liner Ports

3.2.1 Two-Stroke Cycle Port Configurations. In two-stroke cycle engines, each outward stroke of the piston is a power stroke. To achieve this operating cycle, the fresh charge must be supplied to the engine cylinder at a high enough pressure to displace the burned gases from the previous cycle. Raising the pressure of the intake mixture is done in a separate pump or blower or compressor. The operation of clearing the cylinder of burned gases and filling it with fresh mixture (or air)—the combined intake and exhaust process—is called scavenging. However, air capacity is just as important as in the four-stroke cycle; an equivalent or greater air mass flow rate must be achieved for the same output power.

The different categories of two-stroke cycle scavenging flows, and the port (and valve) arrangements that produce them are illustrated in Figs. 20 and 21. Scavenging arrangements are classified into: (a) *cross-scavenged*; (b) *loop-scavenged*; and (c) *uniflow scavenged*. The location and orientation of the scavenging ports control the scavenging process, and the most common arrangements are indicated. Cross and loop scavenging systems use exhaust and inlet ports in the

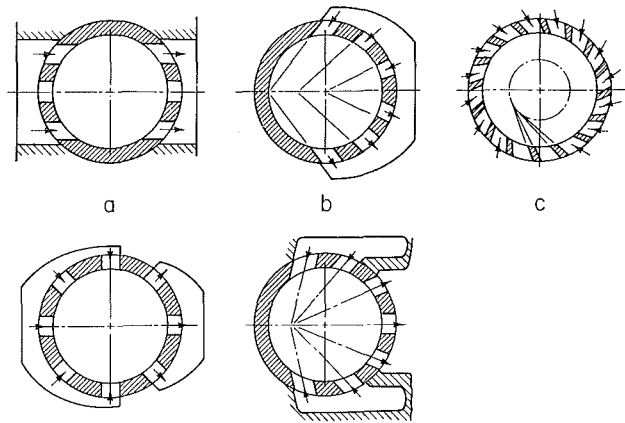


Fig. 21 Common porting arrangements that go with cross-scavenged (A), loop-scavenged (B), and uniflow-scavenged (C) configurations

cylinder wall, uncovered by the piston as it approaches BC. The uniflow system may use inlet ports with exhaust valves in the cylinder head, or inlet and exhaust ports with opposed pistons. Despite the different flow patterns obtained with each cylinder geometry, the general operating principles are similar. Air in a diesel, or fuel-air mixture in a spark-ignition engine, must be supplied to the inlet ports at a pressure higher than the exhaust-system pressure.

The scavenging process (for a uniflow engine design) proceeds as follows. Early in the second half of the expansion or power stroke, the exhaust valve opens, and a blowdown discharge process commences. Initially, the pressure ratio across the exhaust valve exceeds the critical value and the flow at the valve will be sonic. As the cylinder pressure decreases, the pressure ratio drops below the critical value. The discharge period up to the time of scavenging port opening is called the blowdown (or free exhaust) period. The scavenging ports open between 70–45 deg before BC when the cylinder pressure slightly exceeds the scavenging pump pressure. Because the burned gas flow is towards the exhaust valves, which now have a large open area, the exhaust flow continues and no backflow occurs. When the cylinder pressure falls below the inlet pressure, air enters the cylinder and the scavenging process starts. This flow continues as long as the inlet ports are open and the inlet total pressure exceeds the pressure in the cylinder. As the cylinder pressure rises above the exhaust pressure, the fresh charge flowing into the cylinder displaces the burned gases; however a part of the fresh charge mixes with the burned gases and is expelled with them. The exhaust valves close at the same time as, or before, the inlet ports close. Since the exhaust valve open area is less than that of the scavenging ports, additional charging can be obtained. Proper flow patterns for the fresh charge are extremely important for good scavenging and charging of the cylinder. The in-cylinder scavenging flow is discussed in more detail in Section 4.5.

3.2.2 Port Flow Processes. The crank angle at which the ports open, the size, number, geometry, and location of the ports around the cylinder circumference, and the direction and velocity of the jets issuing from the ports into the cylinder all affect the scavenging flow. A summary of the information available on flow through piston controlled ports can be found in Annand and Roe [23]. Both the flow resistance of the inlet and exhaust port configurations, as well as the details of the flow pattern produced by the port system inside the cylinder during scavenging are important. Figure 22 defines the essential geometrical characteristics of inlet ports. Rectangular ports make best use of cylinder wall area and give precise timing control. Ports can be tapered, and may have axial and tangential inclination as shown.

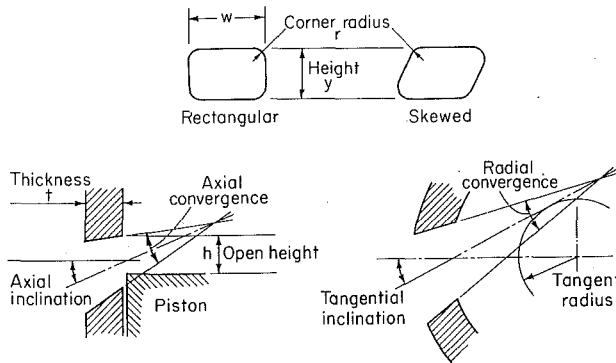


Fig. 22 Parameters which define geometry of inlet ports [23]

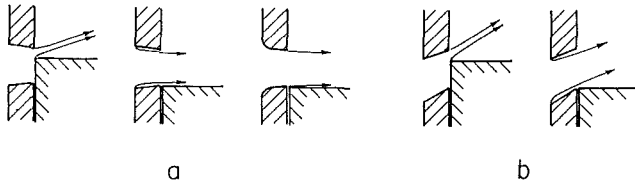


Fig. 23 Flow pattern through piston-controlled inlet ports: (a) port axis perpendicular to wall; small opening, and large opening with sharp and rounded entry" (b) port axis inclined [23]

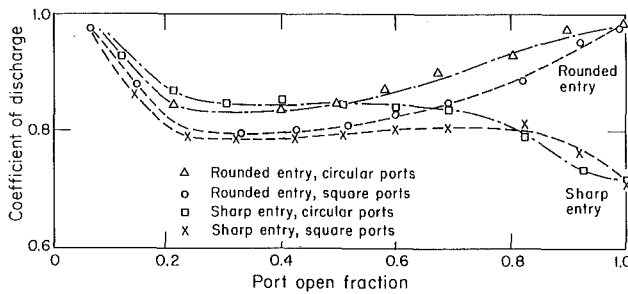


Fig. 24 Discharge coefficients as a function of port open fraction (uncovered height/port height) for different inlet port designs. Pressure ratio across port = 2.35 [29].

Figure 23 illustrates the flow patterns expected downstream of piston-controlled inlet ports. For small openings, the flow remains attached to the port walls. For fully open ports with sharp corners the flow detaches at the upstream corners. Both a rounded entry and converging taper to the port help prevent flow detachment within the port. Discharge coefficients for ports have been measured as a function of the open fraction of the port, pressure ratio across the port, and port geometry and inclination (see [23] for a detailed summary). The most appropriate reference area for evaluating the discharge coefficient is the open area of the port (see Fig. 22). For the open height h less than $(Y-r)$ but greater than r this is

$$A_R = wh - 0.43 r^2 \quad (14)$$

where Y is the port height, w the port width and r the corner radius. For $h = Y$, the reference area is

$$A_R = wY - 0.86 r^2 \quad (15)$$

The effect of variations in geometry and operating conditions on the discharge coefficient C_D can usually be interpreted by reference to the flow patterns illustrated in Fig. 23. Effects of inlet port open fraction and port geometry on C_D are shown in Fig. 24: geometry effects are most significant at small and large open fraction [29]. C_D varies with pressure ratio, increasing as pressure ratio increases. Empirical relations which predict this variation with pressure ratio have been developed [31].

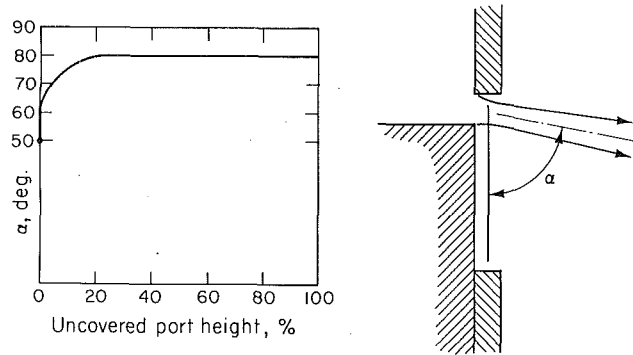


Fig. 25 Angle of jet exiting exhaust port as a function of uncovered port height [32]

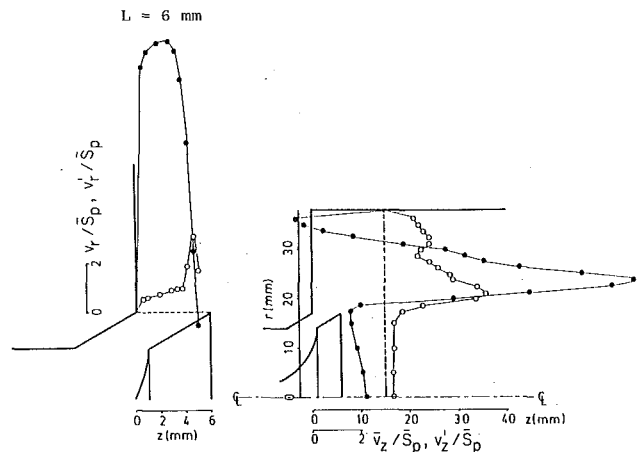


Fig. 26 Radial mean velocity \bar{v}_r , and root-mean-square (rms) velocity fluctuations v_r' at the valve exit plane, and axial mean velocity \bar{v}_z and rms velocity fluctuation v_z' 15 mm below the cylinder head at 36 deg ATC, in model engine operated at 200 rev/min. Valve lift = 6 mm. Velocities normalized by mean piston speed: • mean; ° rms [25].

Tangentially inclined inlet ports are used when swirl is desired to improve scavenging, or when jet focussing or impingement within the cylinder off the cylinder axis is required (see Section 4.5). The discharge coefficient decreases as the jet tangential inclination increases. The jet angle and the port angle can deviate significantly from each other depending on the details of the port design and the open fraction [32].

In piston controlled exhaust ports, the angle of the jet from a thin walled exhaust port increases as indicated in Fig. 25 [32]. In thick ports, the walls are usually tapered to allow the outward flow to diffuse. The pressure ratio across the exhaust ports varies substantially during the exhaust process. The pressure ratio has a significant effect on exhaust port discharge coefficient. The changes in exit jet angle and separation point explain the effects of increasing open fraction and pressure ratio. The discharge coefficient also increases modestly with increasing gas temperature [33].

4 Bulk Flow Within the Cylinder

4.1 Intake Jet Flow. The engine intake process governs many important aspects of the flow within the cylinder. In four-stroke cycle engines, the inlet valve is the minimum area for the flow so gas velocities at the valve throat are the highest velocities set up during the intake process. The gas issues from the valve opening into the cylinder as a conical jet, and the velocities in the jet are about 15 times the mean piston speed. Figure 26 shows the radial and axial velocity components close to the valve exit, measured during the intake process, in a motored model engine with transparent walls and single valve

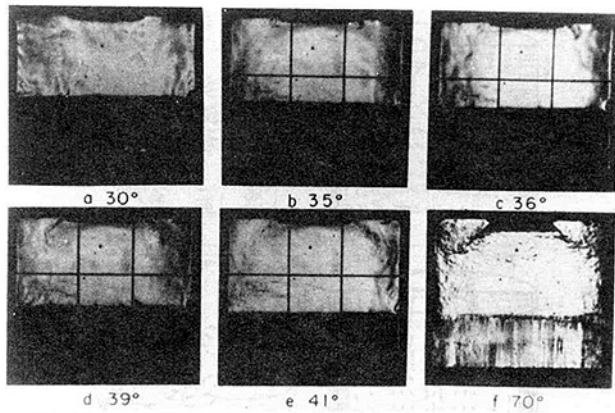


Fig. 27 Sequence of schlieren photos of intake jet as it develops during intake stroke. Numbers are crank angle degrees after TC [28].

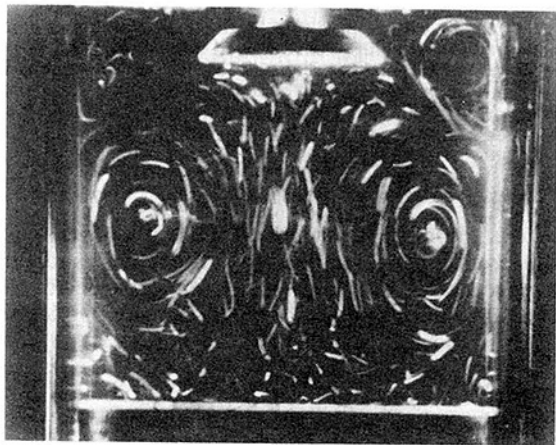


Fig. 28 Large scale rotating flow pattern set up within the cylinder by the intake jet. Photo shows streak lines of particles in thin illuminated plane which includes cylinder axis, in water flow into model engine with axisymmetric valve [34].

located on the cylinder axis, using laser doppler anemometry [25]. The jet separates from the valve seat and lip, producing shear layers with large velocity gradients, which generate turbulence. This separation of the jet sets up recirculation regions beneath the valve head, and in the corner between cylinder wall and cylinder head.

The motion of the intake jet within the cylinder is shown in the schlieren photographs taken in a transparent engine, in Fig. 27. This engine had a square cross section with the cylinder made up of two quartz walls and two steel walls, to permit easy optical access [28]. The schlieren technique makes regions with density gradients in the flow show up as lighter or darker regions on the film. The engine was throttled to one-half an atmosphere intake pressure, so the jet starts after the intake stroke has commenced, at 35 deg ATC, following backflow of residual gas into the intake manifold. The front of the intake jet can be seen propagating from the valve to the cylinder wall at several times the mean piston speed. Once the jet reaches the wall ($\theta > 41$ deg ATC), the wall deflects the major portion of the jet downwards toward the piston; however, a substantial fraction flows upward toward the cylinder head. The highly turbulent nature of the jet is evident.

The interaction of the intake jet with the wall produces large scale rotating flow patterns within the cylinder volume. These are easiest to visualize where the engine geometry has been simplified so the flow is axisymmetric. The photo in Fig. 28, of a water analog of an engine intake flow, was taken in a transparent model of an engine cylinder and piston [34]. The valve is located in the center of the cylinder head, and the flow

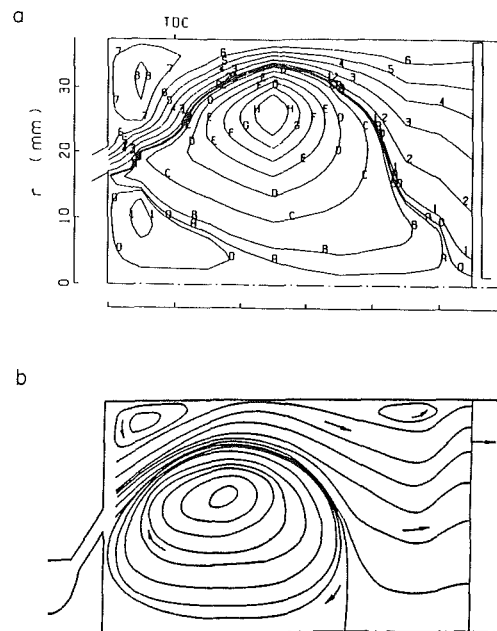
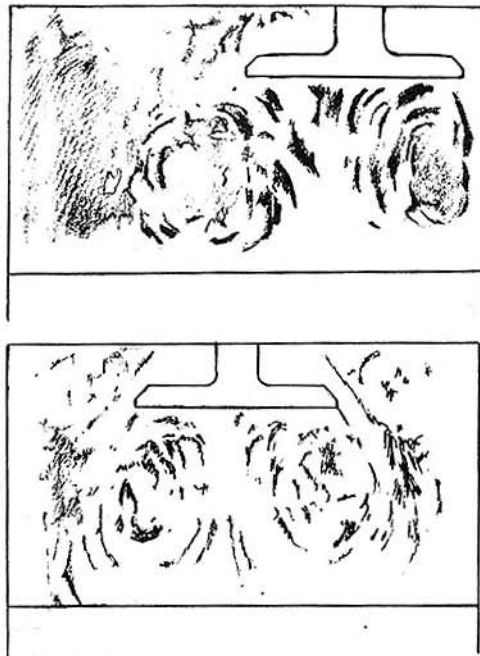


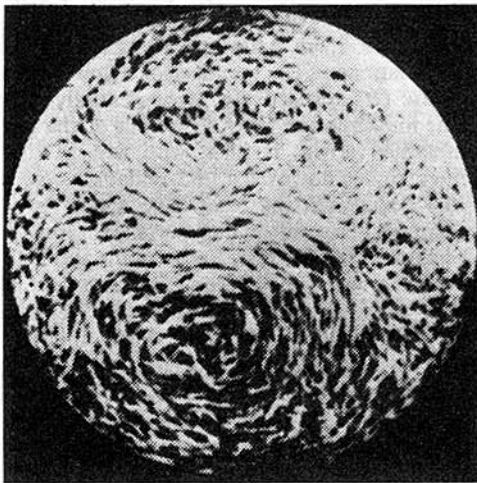
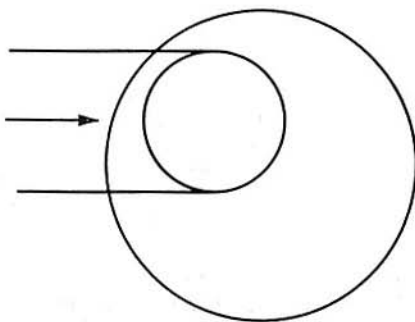
Fig. 29(a) Streamlines deduced from LDA measurements of velocity field 90 deg ATC during intake stroke in motored model engine [35]; (b) streamline contours 90 deg ATC predicted with axisymmetric CFD calculation of intake stroke flow [36]

into the valve is along the cylinder axis. The experimental parameters have been scaled so that the appropriate dimensionless numbers which govern the flow, the Reynolds and Strouhal numbers, were maintained constant. The photo shows the major features of the intake-generated flow in a thin illuminated plane through the cylinder axis. The streaks are records of the paths of tracer particles in the flow, during the period the camera shutter is open. Streamline patterns based on velocity profiles measured during the intake stroke with LDA, within a motored transparent plexiglass engine with air flowing through an axisymmetric valve [35], and streamline contours obtained from axisymmetric computational fluid dynamic calculations of the intake stroke flow [36], shown in Fig. 29(a) and (b), respectively, give essentially identical pictures of this intake-stroke flow. The bulk of the cylinder, as the piston moves down, is filled with a large ring vortex, whose center moves downward and remains about half way between the piston and the head. The upper corner of the cylinder contains a second smaller vortex, rotating in the opposite direction. These vortices persist until about the end of the intake stroke, when they became unstable and break up.

With inlet valve location and inlet port geometry more typical of normal engine practice, the flow within the cylinder generated by flow is more complex. However, the presence of large scale rotating flow patterns can still be discerned. Figure 30(a) shows the effect of off-axis valve location (with the flow into the valve still parallel to the cylinder and valve axis). During the first half of the inlet stroke, at least, a flow pattern similar in character to that in Figs. 28 and 29 is evident. The vortices are now displaced to one side, however, and the planes of their axes of rotation are no longer perpendicular to the cylinder axis but are tipped at an angle to it. The vortices become unstable and break up earlier in the intake stroke than was the case with the axisymmetric flow [34]. With an offset valve, and a normal inlet port configuration which turns the flow through 50–70 deg (see Fig. 12), photos of the flow pattern in a diametral plane show an additional large-scale rotation. Figure 30(b) shows streak photographs taken in a water-flow model of the cylinder with the illuminating thin beam of light 30 mm (one-third of the bore) from the cylinder head,



a



b

Fig. 30(a) Sketches from streak photographs of in-cylinder rotating flow in axial plane in water analog of intake process in model engine with offset inlet valve, at 90 deg ATC [34]; (b) Streak photographs of flow in diametral plane, 30 mm below cylinder head, with intake port and valve geometry shown, with steady water flow into cylinder. Bore = 88 mm; Valve lift = 4 mm [37].

with a standard inlet port design. The direction of flow with this vortex pair is towards the left across the center of the cylinder. This flow pattern occurs because the cylinder wall closest to the valve impedes the flow out of the valve, and

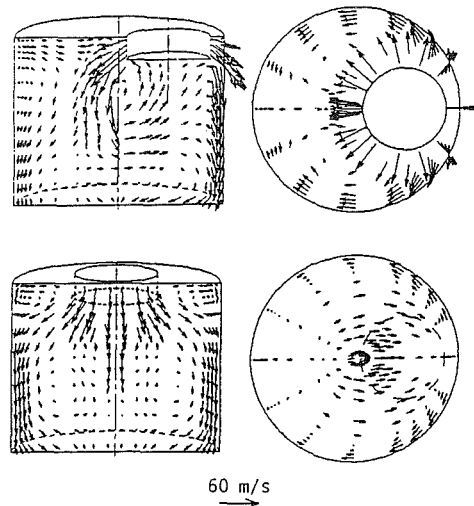


Fig. 31 Velocity vectors predicted by three-dimensional calculations of intake-stroke flow with offset valve, at 90 deg after TC, in two orthogonal axial planes and two diametral planes (top picture one-eighth and bottom picture five-eighths of distance from cylinder head to piston crown below the cylinder head). Uniform inlet velocity around the valve curtain area was assumed [38].

forces the flow on either side of the plane passing through the valve and cylinder axes to circulate around the cylinder in opposite directions. Three-dimensional computations of the in-cylinder flow during intake, with off-center valve locations, such as the velocity vector plots shown in Fig. 31 [38], predict similar flow patterns to those seen in the water analog visualization studies. Here uniform flow into the cylinder, through the valve curtain area was assumed for the inlet boundary condition. The details of this intake-generated in-cylinder flow depend on the port design, valve stem orientation and the valve lift. With suitable port and/or cylinder head design, it is possible to develop a single vortex flow aligned with the cylinder. The production and characteristics of such "swirling" flows are reviewed in Section 4.2.

The jet-like character of the intake flow, interacting with the cylinder walls and moving piston, creates large scale rotating flow patterns within the cylinder. The details of this flow are strongly dependent on the inlet port, valve and cylinder head geometry. These flows appear to become unstable, either during the intake or the compression process, and break down into three-dimensional turbulent motions. Recirculating flows of this type are usually sensitive to small variations in the flow: hence one would expect substantial cycle-by-cycle flow variations [39].

4.2 Swirl. Swirl is defined as organized rotation of the charge about the cylinder axis. Swirl is created by bringing the intake flow into the cylinder with an initial angular momentum. While some decay in swirl due to friction occurs during the engine cycle, intake-generated swirl usually persists through the compression, combustion and even the expansion processes. In engine designs with bowl-in-piston combustion chambers, the rotational motion set up during intake is substantially modified during compression. Swirl is used in diesels and some stratified-charge engine concepts to promote more rapid mixing between the inducted air charge and the injected fuel. Swirl is also used to increase the turbulent intensity, and thereby speed up the combustion process, in spark-ignition engines. In two-stroke engines it is used to improve scavenging. In some designs of prechamber engines, organized rotation about the prechamber axis is also called swirl. In prechamber engines where swirl within the precombustion chamber is important, the flow into the prechamber during the

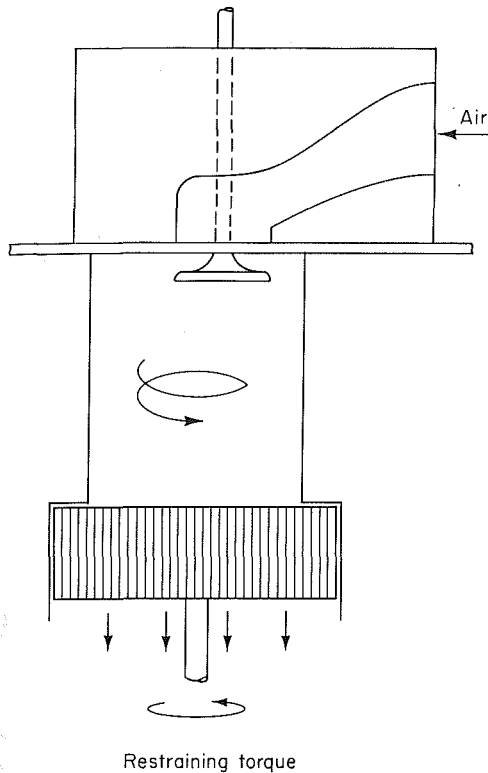


Fig. 32 Schematic of steady-flow impulse torque swirl-meter [40]

compression process creates the rotating flow. Prechamber flows are discussed in Section 4.4.

4.2.1 Swirl Measurement. The details of the swirling flow in an actual operating engine are complex and extremely difficult to determine. Accordingly, steady flow tests are often used to characterize the swirl. Air is blown steadily through the inlet port and valve assembly in the cylinder head into an appropriately located equivalent of the cylinder. A common technique for characterizing the swirl within the cylinder has been to use a light paddle wheel, pivoted on the cylinder center line, mounted between 1 and 1.5 bore diameters down the cylinder. The paddle wheel diameter is close to the cylinder bore. The rotation rate of the paddle wheel is used as a measure of the air swirl. Since this rotation rate depends on the location of the wheel and its design, and the details of the swirling flow, this technique is being superceded by the impulse swirl meter shown in Fig. 32. A honeycomb flow straightener replaces the paddle wheel: it measures the total torque exerted by the swirling flow. This torque equals the flux of angular momentum through the plane coinciding with the flow straightener upstream face.

For each of these approaches, a *swirl coefficient* is defined which essentially compares the flow's angular momentum with its axial momentum. For the paddle wheel, the swirl coefficient is defined by:

$$C_s = \omega_p B / v_0 \quad (16)$$

where ω_p is the paddle wheel angular velocity, and the bore B has been used as the characteristic dimension. The characteristic velocity, v_0 , is derived from the pressure drop across the valve using an incompressible flow equation:

$$v_0 = \{2(p_0 - p_c) / \rho\}^{1/2} \quad (17)$$

or a compressible flow equation:

$$v_0 = \left\{ \frac{2\gamma}{(\gamma-1)} \frac{p_0}{\rho_0} \left[1 - \left(\frac{p_c}{p_0} \right)^{\frac{\gamma-1}{\gamma}} \right] \right\}^{1/2} \quad (18)$$

where subscripts 0 and c refer to upstream stagnation and cylinder values, respectively. The difference between equations (17) and (18) is usually small. With the impulse torque meter, characteristic velocity and length scales must also be introduced. Several swirl parameters have been defined [40] [41]. The simplest is:

$$C_s = 8T / (\dot{m} v_0 B) \quad (19)$$

where T is the torque, and \dot{m} the air mass flowrate. The velocity v_0 , defined by equation (17) or (18), and the bore have again been used to obtain a dimensionless coefficient. Note that for solid body rotation of the fluid within the cylinder at the paddle wheel speed ω_p , equations (16) and (19) give identical swirl coefficients. In practice, because the swirling flow is not solid body rotation, and because the paddle wheel usually lags the flow due to slip and friction, the impulse torque meter gives higher swirl coefficients [41]. When swirl measurements are made in an operating engine, a *swirl ratio* is normally used to define the swirl. It is defined as the angular velocity of a solid body rotating flow ω_s which has equal angular momentum to the actual flow, divided by the crankshaft angular rotational speed:

$$R_s = \omega_s / (2\pi N) \quad (20)$$

During the induction stroke in an engine the flow and the valve open area, and consequently the angular momentum flux into the cylinder, vary with crank angle. Whereas in rig tests the flow and valve open area are fixed and the angular momentum passes down the cylinder continuously, in the engine intake process the momentum produced under corresponding conditions of flow and valve lift remains in the cylinder. Steady-state impulse-torque-meter flow-rig data can be used to estimate engine swirl in the following manner [41]. Assuming that the port and valve retain the same characteristics under the transient conditions of the engine as on the steady flow rig, the equivalent solid body angular velocity ω_s , at the end of the intake process, is given by

$$\omega_s = \frac{8}{B^2} \left(\int_{\theta_1}^{\theta_2} T d\theta \right) / \left(\int_{\theta_1}^{\theta_2} \dot{m} d\theta \right) \quad (21)$$

where θ_1 and θ_2 are crank angles at the start and end of the intake process, and the torque T and mass flow rate \dot{m} are evaluated at the valve lift corresponding to the local crank angle. Using equation (19) for T , equation (8) for \dot{m} , assuming v_0 and ρ are constant throughout the intake process, and introducing volumetric efficiency η_v based on intake manifold conditions, it can be shown that

$$R_s = \frac{\omega_s}{2\pi N} = \pi \eta_v B L \left[\int_{\theta_1}^{\theta_2} (A_v C_d) C_s d\theta \right] / \left[\int_{\theta_1}^{\theta_2} (A_v C_D) d\theta \right]^2 \quad (22)$$

where $A_v C_D$ is the effective valve open area at each crank angle. Except for its (weak) dependence on η_v , equation (22) gives R_s independent of operating conditions directly from rig test results and engine geometry.

The relationship between steady flow rig tests (which are frequently used because of their simplicity) and actual engine swirl patterns is not fully understood. Steady flow tests adequately describe the swirl generating characteristics of the intake port and valve (at fixed valve lift), and are used extensively for this purpose. However, the swirling flow set up in the cylinder during intake can change significantly during compression.

4.2.2 Swirl Generation During Induction. There are two broad approaches to generating swirl during the induction process. In one, the flow is discharged into the cylinder tangentially towards the cylinder wall, where it is deflected sideways and downward in a swirling motion. In the other, the

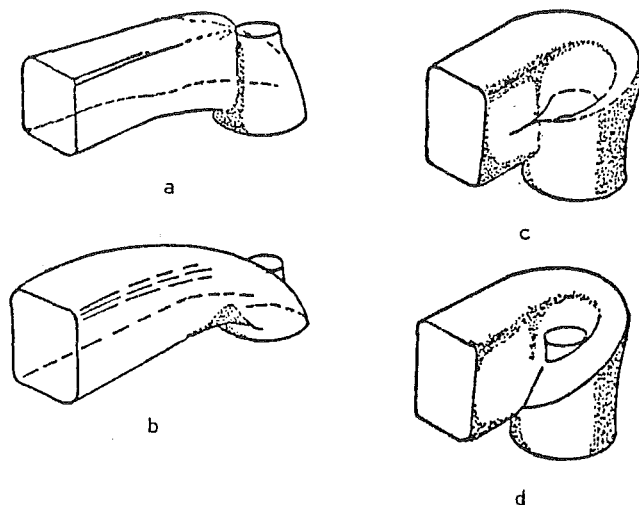


Fig. 33 Different types of swirl-generating inlet ports: (a) deflector wall; (b) directed; (c) shallow ramp helical; (d) steep ramp helical [42]

swirl is largely generated within the inlet port: the flow is forced to rotate about the valve axis *before* it enters the cylinder. The former type of motion is achieved by forcing the flow distribution around the circumference of the inlet valve to be nonuniform, so that the inlet flow has a substantial net angular momentum about the cylinder axis. The directed port and deflector-wall port in Fig. 33 are two common ways of achieving this result. The directed port brings the flow towards the valve opening in the desired tangential direction. Its passage is straight, which due to other cylinder head requirements restricts the flow area and results in a relatively low discharge coefficient. The deflector-wall port uses the port inner side wall to force the flow preferentially through the outer periphery of the valve opening, in a tangential direction. Since only one wall is used to obtain a directional effect, the port areas are less restrictive.

Flow rotation about the cylinder axis can also be generated by *masking off or shrouding part of the peripheral inlet valve open area*. Use is often made of a mask or shroud on the valve in research engines because changes can readily be made. In production engines, the added cost and weight, problems of distortion, the need to prevent valve rotation and reduced volumetric efficiency make masking the valve an unattractive approach. The more practical alternative of building a mask on the cylinder head, around part of the inlet valve periphery, is used in some production spark-ignition engines to generate swirl. It can easily be incorporated in the cylinder head casting process.

The second broad approach is to generate swirl within the port, about the valve axis, prior to the flow entering the cylinder. Two examples of such *helical ports* are shown in Fig. 33. Usually, with helical ports, a higher flow discharge coefficient at equivalent levels of swirl is obtained, since the whole periphery of the valve open area can be utilized. A higher volumetric efficiency results. Also, helical ports are less sensitive to position displacements, such as can occur in casting, since the swirl generated depends mainly on the port geometry above the valve, and not the position of the port relative to the cylinder axis.

Figure 34 compares steady-state swirl-rig measurements of examples of the ports in Fig. 33. The rig swirl number increases with increasing valve lift, reflecting the increasing impact of the port shape and decreasing impact of the flow restriction between valve head and seat. Helical ports normally impart more angular momentum at medium lifts than do directed ports [41] [43]. The swirl ratios for these ports calculated from this rig data using equations (19) and (22) are:

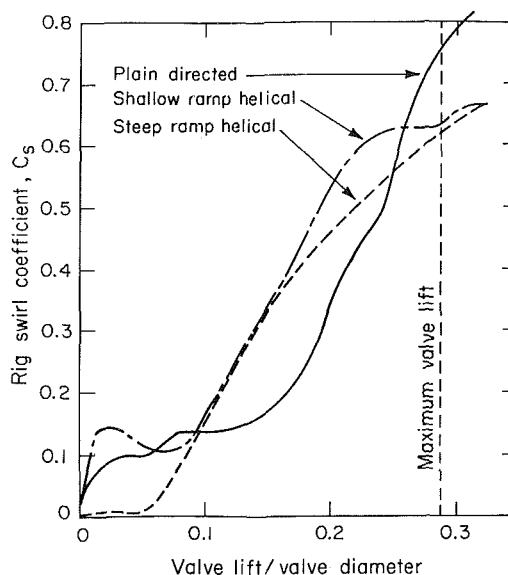


Fig. 34 Steady-state torque-meter swirl-measurements of directed, shallow ramp and steep ramp helical ports as a function of inlet valve lift to diameter ratio [41]

2.5 for the directed port, 2.9 for the shallow ramp helical, and 2.6 for the steep ramp helical. Vane swirl-meter swirl-ratios were about 30 percent less. These impulse-swirl-meter derived "engine swirl" results are within about 20 percent of the solid body rotation which has equal angular momentum to that of the cylinder charge determined from tangential velocity measurements made within the cylinder of an operating engine with the port, at the end of the induction process [41].

Directed and deflector-wall ports, and masked valve or head designs produce a tangential flow into the cylinder by increasing the flow resistance through that part of the valve open area where flow is not desired. A highly nonuniform flow through the valve periphery results and the flow into the cylinder has a substantial v_θ velocity component in the same direction about the cylinder axis. In contrast, helical ports produce the swirl in the port upstream of the valve, and the velocity components v_r , and v_z through the valve opening, and v_θ about the valve axis, are relatively uniform around the valve open area. Figure 35 shows velocity data measured at the valve exit plane in steady-flow rig tests with examples of these two types of port. The valve and cylinder wall locations are shown. In Fig. 35(a), the directed character of the flow set up by the port deflector wall effectively prevents any significant flow around half the valve periphery [44]. In contrast, in Fig. 35(b) with the helical port, the air flows into the cylinder around the full valve open area. The radial and axial velocities are essentially uniform around the valve periphery, except where the cylinder wall impedes the flow. The swirl velocity about the valve axis (anticlockwise when viewed from above) for this helical port is also relatively uniform and is about half the magnitude of the radial and axial velocities [45]. At low valve lifts, with the deflector-wall or tangential port, the directed character of the valve exit flow is much less apparent because the minimum flow area is at the valve seat and any port flow effects are significantly reduced. Velocity profiles around the valve are a strong function of valve lift. The velocity profiles around the valve curtain area at a fixed valve lift, normalized by a characteristic flow velocity, have been shown to be essentially independent of the flow rate [46].

The swirling airflow within the cylinder of an operating engine is not uniform. The velocities generated at the valve at each point in the induction process depend on the valve open area and piston velocity. The velocities are highest during the

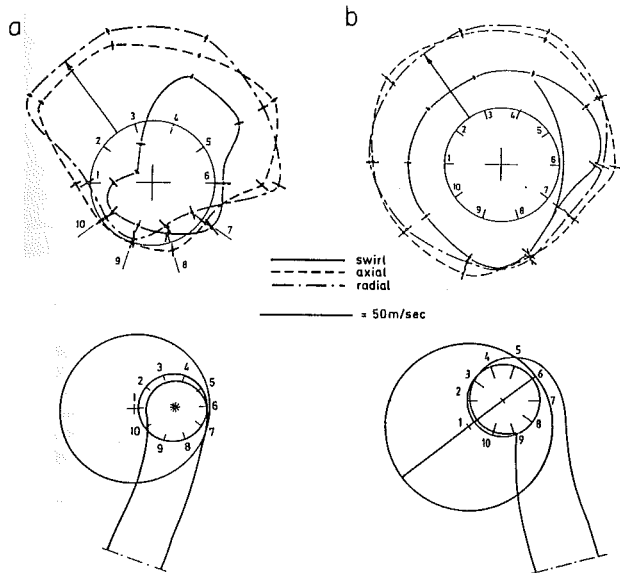


Fig. 35 Swirl, axial, and radial velocities measured 2 mm from cylinder head around the valve circumference for (a) tangential deflector-wall port and (b) helical port; magnitude of velocity is given by the distance along a radial line (from valve axis, from valve outline to the respective curve scaled by the reference length (examples of radial velocity indicated by two arrows); valve lift = 12.8 mm [44, 45]

first half of the intake process as indicated in Fig. 14. Thus, the swirl velocities generated during this portion of the induction stroke are higher than the swirl generated during the latter half of the stroke: there is swirl stratification. Also, the flow pattern close to the cylinder head during induction is comparatively disorganized, and not usually close to a solid body rotation. It consists of a system of vortices, created by the high velocity tangential or spiraling intake jet. Further down the cylinder, the flow pattern is closer to solid body rotation with the swirl velocity increasing with increasing radius [41] [42]. This more ordered flow directly above the piston produces higher swirl velocities in that region of the cylinder. As the piston velocity decreases during intake, the swirl pattern redistributes, with swirl speeds close to the piston decreasing and swirl speeds in the center of the cylinder increasing [45]. Note that the axis of rotation of the in-cylinder gases may not exactly coincide with the cylinder axis.

Figure 36 illustrates the complexity of such intake-generated swirling flows. The trajectories of six particles, initially uniformly spaced around the valve curtain area at top center, were calculated as part of a three-dimensional computational fluid dynamic analysis of the intake stroke flow until bottom center piston position. A marker is shown on the trace every 5 crank angle degrees. The irregularity of the flow in the upper half of the cylinder, and the stronger swirling flow in the lower half of the cylinder are apparent [38].

4.2.3 Swirl Modification Within the Cylinder. The angular momentum of the air which enters the cylinder at each crank angle during induction decays throughout the rest of the intake process and during the compression process due to friction at the walls and turbulent dissipation within the fluid. Typically one-quarter to one-third of the initial moment of momentum about the cylinder axis will be lost by top center at the end of compression. However, swirl velocities in the charge can be substantially increased during compression by suitable design of the combustion chamber. In many designs of direct-injection diesel, air swirl is used to obtain much more rapid mixing between the fuel injected into the cylinder and the air, than would occur in the absence of swirl. The tangential velocity of the swirling airflow set up inside the cylinder

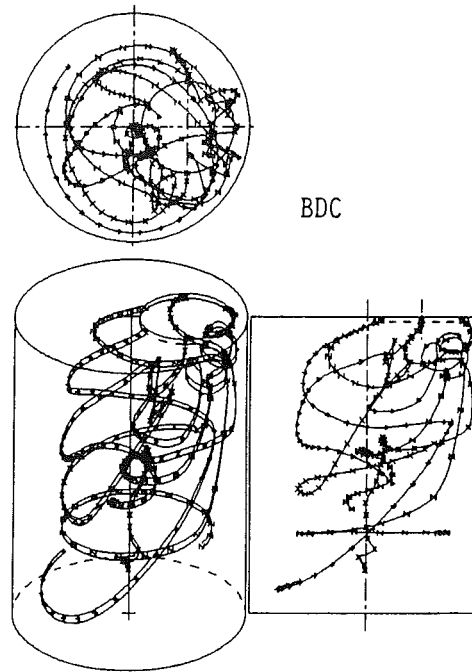


Fig. 36 Traces of paths followed by six particles during the intake stroke. Initially particles were uniformly placed around the valve circumference at TC. Marks on particle traces indicate every five degrees. Velocity through the inlet valve has initial net tangential velocity typical of directed inlet port. Complexity of swirling flowfield is evident [38].

during induction is substantially increased by forcing most of the air into a compact bowl-in-piston combustion chamber, usually centered on the cylinder axis, as the piston approaches its top center position. Neglecting the effects of friction, angular momentum is conserved, and as the moment of inertia of the air is decreased its angular velocity must increase.

However, the total angular momentum of the charge within the cylinder does decay due to friction at the chamber walls. The angular momentum of the charge Γ_c changes with time according to the moment of momentum conservation equation:

$$\frac{d\Gamma_c}{dt} = J_i - T_f \quad (23)$$

where J_i is the flux of angular momentum into the cylinder and T_f is the torque due to wall friction. The actual angular momentum within the cylinder at the end of induction will be less than the entering angular momentum, due to wall friction during the intake process. Friction continues through the compression process so the total charge angular momentum at the end of compression is further reduced.

There is friction on the cylinder wall, cylinder head and piston crown (including any combustion chamber surfaces within the crown). This friction can be estimated using friction formulas developed for flow over a flat plate, with suitable definition of characteristic length and velocity scales. Friction on the cylinder wall can be estimated from the wall shear stress

$$\tau = \frac{1}{2} \rho (\omega_s B/2)^2 C_F \quad (24)$$

where ω_s is the equivalent solid body swirl. The friction factor, C_F , is given by the flat plate formula

$$C_F = 0.037\lambda(\text{Re}_B)^{-0.2} \quad (25)$$

where λ is an empirical constant introduced to allow for differences between the flat plate and cylinder wall ($\lambda \approx 1.5$ [47]), and Re_B is the equivalent of the flat plate Reynolds number ($\text{Re}_B = \rho(B\omega_s/2)(\pi B)/\mu$). Friction on the cylindrical walls of a piston cup or bowl can be obtained from the above

expressions with D_B , the bowl diameter, replacing the bore. Friction on the cylinder head, piston crown, and piston bowl floor can be estimated from expressions similar to equations (24) and (25). However, since the tangential velocity v_θ at the wall varies with radius, the shear stress should be evaluated at each radius and integrated over the surface [48]. An alternative approximate approach is to evaluate these components of the wall shear stress at the mean radius [47].

Next, consider the effects on swirl of radially inward displacement of the air charge during compression. The most common example of this phenomenon occurs with the bowl-in-piston combustion chamber design of medium and high-speed direct-injection diesels (see Figs. 7(b) and (c)). However, in spark-ignition engines where swirl is used to increase the burning rate, the shape of the combustion chamber close to top center can also force radially inward motion of the charge.

Given a swirling-in-cylinder flow at the end of induction and neglecting the effects of friction, as the moment of inertia of the air about the cylinder axis is decreased, its angular velocity must increase to conserve angular momentum. For example, for solid body rotation of the cylinder air charge of mass m_c , the initial angular momentum $\Gamma_{c,i}$ and solid body rotation $\omega_{s,i}$ are related at bottom center by:

$$\Gamma_{c,i} = I_c \omega_{s,i}$$

where I_c is the moment of inertia of the charge about the cylinder axis. For a disc shaped combustion chamber, $I_c = m_c B^2/8$ and is constant. For a bowl-in-piston combustion chamber,

$$I_c = \frac{m_c B^2}{8} \left[\frac{z}{h_B} + \left(\frac{D_B}{B} \right)^4 \right] / \left[\frac{z}{h_B} + \left(\frac{D_B}{B} \right)^2 \right] \quad (26)$$

where D_B and h_B are the diameter and depth of the bowl, respectively, and z is the distance of the piston crown from the cylinder head. At TC crank position, $z \approx 0$ and $I_c \approx m_c D_B^2/8$. At the end of induction, $I_c \approx m_c B^2/8$. Thus, in the absence of friction ω_s would increase by $(B/D_B)^2$, usually a factor of about 4.

In an operating engine with this bowl-in-piston chamber design, the observed increase in swirl in the bowl is less; it is usually about a factor of 2 to 3 [41, 43]. This is because of wall friction, dissipation in the fluid due to turbulence and velocity gradients, and the fact that a fraction of the fluid remains in the clearance height above the piston crown. The loss in angular momentum due to these effects will vary with geometric details, initial swirl flow pattern, and engine speed. Figure 37 shows measurements and predictions of this increase in tangential or swirl velocity within the bowl-in-piston combustion chamber, during the compression process. The axisymmetric cylindrical bowl was 40 mm in diameter and 22.5 mm deep, the cylinder bore was 83 mm. The measurements of instantaneous swirl velocity at a radius of 16 mm and 5.3 mm below the top of the piston crown increase to about 3 times their value at start-of-compression. The computations with an axisymmetric flow code of mean swirl velocity shown with ± 2 times the turbulent intensity which should encompass 95 percent of the instantaneous values show good agreement [49]. Sometimes the bowl axis is offset from the cylinder axis and some additional loss in swirl amplification results [43].

Swirl velocity distributions in the cylinder at the end of induction show the tangential velocity increasing with radius, except close to the cylinder wall where friction causes the velocity to decrease. While the velocity distribution is not exactly that of a solid body rotation, depending on port design and operating conditions it is often close to solid body rotation [41, 43]. Departures from the solid body velocity distribution are greater at higher engine speeds, suggesting that the flow pattern in the cylinder at this point in the cycle is still developing with time [41, 50]. In the absence of radially in-

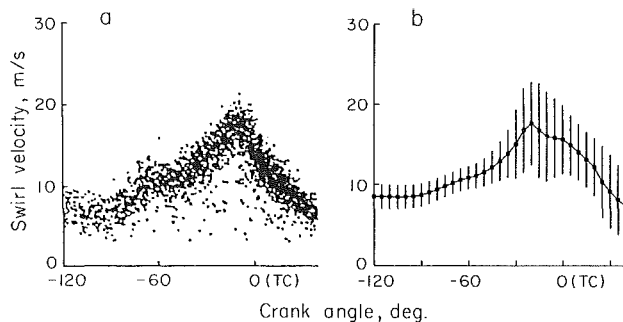


Fig. 37(a) Instantaneous swirl velocity measured by LDA, and (b) mean swirl velocity (dots) and $\pm 2 \times$ turbulent intensity (bars) predicted with two-dimensional code, at the outer edge of the piston bowl in typical high-swirl diesel combustion chamber. Bore = 83 mm, bowl diameter = 40 mm, bowl depth = 22.5 mm. Measurement and prediction location is 16 mm radius, 5.3 mm below bowl lip. Good agreement between measurement and predictions is obtained [49].

ward gas displacement during compression, the flow pattern continues to develop toward a solid body distribution throughout the compression stroke [43]. Swirl ratios of 3 to 5 at top center can be achieved with the ports shown in Fig. 33, with flat-topped pistons (i.e., in the absence of any swirl amplification during compression) [41, 43].

With combustion chambers where the chamber radius is less than the cylinder bore, such as the bowl-in-piston, the tangential velocity distribution with radius will change during compression. Even if the solid body rotation assumption is reasonable at the end of induction, the profile will distort as gas moves into the piston bowl. Neglecting the effects of friction, the angular momentum of each fluid element will remain constant as it moves radially inward. Thus the increase in tangential velocity of each fluid element as it moves radially inward is proportional to the change in the reciprocal of its radius. Measurements of the swirl velocity distribution within the cylinder of bowl-in-piston engine designs support this description. The rate of displacement of gas into the bowl depends on the bowl volume V_B , cylinder volume V , and piston speed S_p , at that particular piston position:

$$\frac{dm_B}{dt} = \frac{m_c}{L} \left(\frac{V_B}{V} \right) \left(\frac{V_d}{V} \right) S_p \quad (27)$$

The gas velocity into the bowl will therefore increase rapidly toward the end of the compression stroke and reach a maximum just before TC (see Section 4.3 where this radial "squish" motion is discussed more fully). Thus, there is a rapid increase in v_θ in the bowl as crank angle approaches TC. The lower layers of the bowl rotate slower than the upper layers because that gas entered the bowl earlier in the compression process [41, 43].

Velocity measurements illustrating the development of this radial distribution in tangential velocity are shown in Fig. 38. These measurements were made by analyzing the motion of burning carbon particles in the cylinder of an operating diesel engine, from movies of the combustion process. The figure shows the engine geometry, and the data compared with a model based on gas displacement and conservation of angular momentum in each element of the charge as it is displaced inwards. Different swirl velocity profiles exist within and outside the bowl as the piston approaches TC. Swirl velocities within the bowl increase as TC is approached roughly as predicted by the ideal model. Outside the bowl, the swirl velocity decreases with increasing radius due to the combined effects of friction and inward gas displacement as the clearance height decreases [51].

4.3 Squish. Squish is the name given to the radially inward or transverse gas motion that occurs toward the end of the

compression stroke when a portion of the piston face and cylinder head approach each other closely. Figure 39 shows how gas is thereby displaced into the combustion chamber, in a typical wedge-shaped SI engine combustion chamber and a bowl-in-piston diesel combustion chamber. The amount of squish is often defined by the *percentage squish area*: i.e., the percentage of the piston area, $\pi B^2/4$, which closely approaches the cylinder head (the shaded areas in Fig. 39). Squish generated gas motion results when a compact combustion chamber geometry is used.

A theoretical squish velocity can be calculated from the instantaneous displacement of gas across the inner edge of the squish region (across the dashed lines in the upper two drawings in Fig. 40), required to satisfy mass conservation. Ignoring the effects of gas dynamics (nonuniform pressure), friction, leakage past the piston rings and heat transfer, expressions for the squish velocity are:

(a) *bowl-in-piston chamber* (Fig. 40(a)) [52]

$$\frac{v_{sq}}{S_p} = \frac{D_B}{4z} \left[\left(\frac{B}{D_B} \right)^2 - 1 \right] \left[\frac{V_B}{A_c z + V_B} \right] \quad (28)$$

where V_B is the volume of the piston bowl, A_c is the cross-sectional area of the cylinder ($\pi B^2/4$), S_p is the instantaneous piston speed, equation (1), and z is the distance between piston crown top and the cylinder head ($z = c + Z$, where $Z = l + a - s$; see Fig. 1).

(b) *simple wedge chamber* (Fig. 40(b)) [53]

$$\frac{v_{sq}}{S_p} = \frac{A_s}{B(Z+c)} \left(1 - \frac{Z+c}{C+Z} \right) \quad (29)$$

where A_s is the squish area, and $C = Z/(r_c - 1)$ evaluated at the end of induction.

The theoretical squish velocity for a bowl-in-piston engine, normalized by the mean piston speed \bar{S}_p , is shown in Fig. 41 for different ratios of D_B/B and clearance heights c [54]. The maximum squish velocity occurs at about 10 deg before TC. After TC, v_{sq} is negative; in the absence of combustion, a reverse squish motion equal in magnitude to the forward motion occurs as gas flows out of the bowl into the clearance height region.

These models omit the effects of gas inertia, friction, gas leakage past the piston rings, and heat transfer. Gas inertia and friction effects have been shown to be negligible. The effects of gas leakage past the piston rings, and of heat transfer, are more significant. The squish velocity decrement Δv_L due to leakage is proportional to mean piston speed and a dimensionless leakage number

$$N_L = A_{E,L} \sqrt{\gamma R T_{IVC}} / (N V_d) \quad (30)$$

where $A_{E,L}$ is the effective leakage area, T_{IVC} is the temperature of the cylinder gases at inlet valve closing.

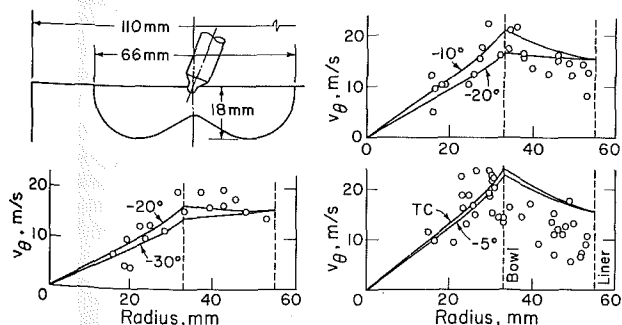


Fig. 38 Velocity measurements as a function of radius across the combustion chamber of a firing bowl-in-piston direct-injection diesel engine. Schematic shows the chamber geometry. Solid lines are calculations based on assumption of constant angular momentum for fluid elements as they move radially inward [51].

Leakage was modeled as a choked flow through the effective leakage area. Values of $\Delta v_L/v_{sq}$ are shown in Fig. 42 [54]. The effect of leakage on v_{sq} is small for normal gas leakage rates. A decrement in squish velocity due to heat transfer, Δv_H , has

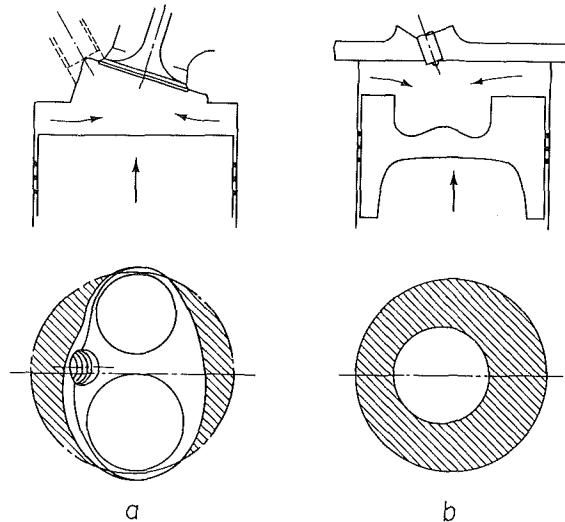


Fig. 39 Schematics of how piston motion during compression stroke generates squish: (a) wedge-shaped SI engine combustion chamber; (b) bowl-in-piston direct-injection diesel combustion chamber

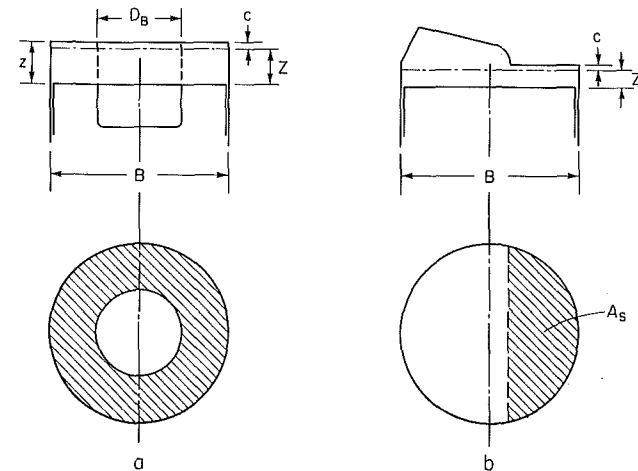


Fig. 40(a) Schematic of axisymmetric bowl-in-piston chamber for equation (28); (b) schematic of wedge chamber with transverse squish for equation (29)

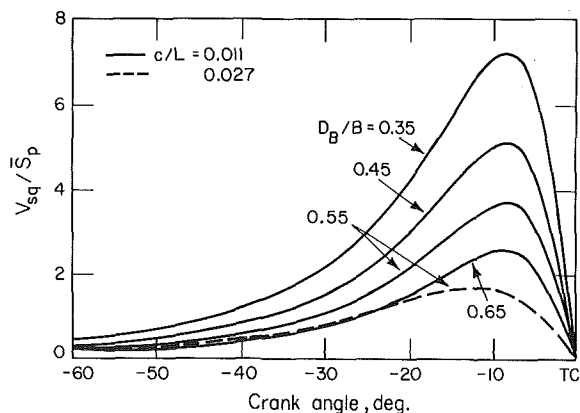


Fig. 41 Theoretical squish velocity divided by mean piston speed for bowl-in-piston chambers, for different D_B/B and c/L (clearance height/stroke). $B/L = 0.914$, $V_B/V_d = 0.056$, crank radius/connecting rod length = 3.76 [54].

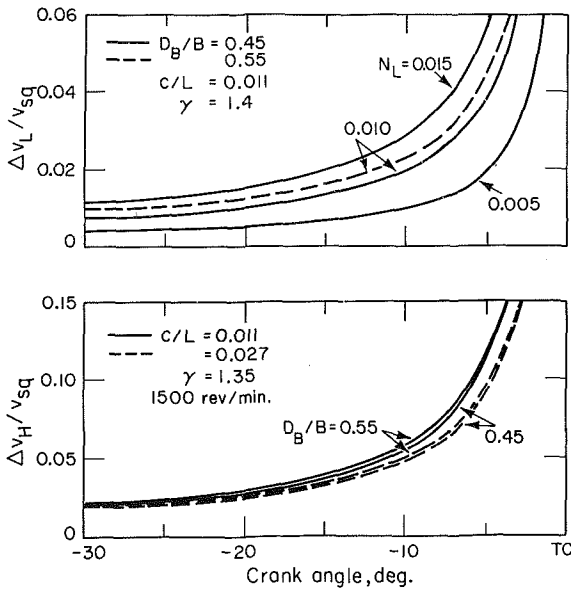


Fig. 42 Values of squish velocity decrement due to leakage Δv_L and heat transfer Δv_H , normalized by the ideal squish velocity, as function of crank angle [54]

also been derived, using standard engine heat-transfer correlations [55]. Values of $\Delta v_H/v_{sq}$ are also shown in Fig. 42. Again the effects are small in the region of maximum squish, though they become more important as the squish velocity decreases from its maximum value as the piston approaches TC.

Velocity measurements in engines provide good support for the above theory. The ideal theory adequately predicts the dependence on engine speed [56]. With appropriate corrections for leakage and heat transfer effects, the above theory predicts the effects of bowl diameter to bore ratio and clearance height on squish velocity (see Fig. 43). The change in direction of the radial motion as the piston moves through TC has been demonstrated under motored engine conditions. Under firing conditions, the combustion generated gas expansion in the open portion of the combustion chamber substantially increases the magnitude of the reverse squish motion after TC [57].

The flow patterns set up within the bowl-in-piston combustion chamber of DI diesel engines by these squish flows have been studied in some detail because they control the fuel-air mixing process. In the absence of swirl, the strong radially inward flow out of the squish region at the bowl circumference sets up a torroidal flow within the bowl as one would expect. Figure 44(a) and (b) show schematics of this squish created flow in the absence of swirl in axisymmetric piston bowls, with cylindrical and re-entrant shapes, based on LDA velocity measurements within the bowl [50]. With swirl, however, the squish and swirl flows interact forcing a redistribution of the flow's angular momentum. The centrifugal forces associated with swirl oppose the radially inward squish flow, causing it to turn into the bowl earlier; thus the vortex flow set up in the bowl now rotates in the opposite direction to the vortex in the no-swirl case, as shown in Figs. 44(c) and (d). One consequence of this swirl-squish interaction is that the flow in the core of the bowl is less disturbed from its initial almost solid-body swirling structure. This may explain why increasing swirl above an optimum level in this type of DI diesel results in reduced fuel-air mixing and burning rates [3].

The complexity of the flow within the piston bowl combustion chamber, with practical bowl shapes and an off-axis bowl (often required due to geometric constraints on injector location) is illustrated in Fig. 45 by the velocity vector plots obtained from three-dimensional computations at 10 deg before TC (when the magnitude of the squish flow reaches a maximum)

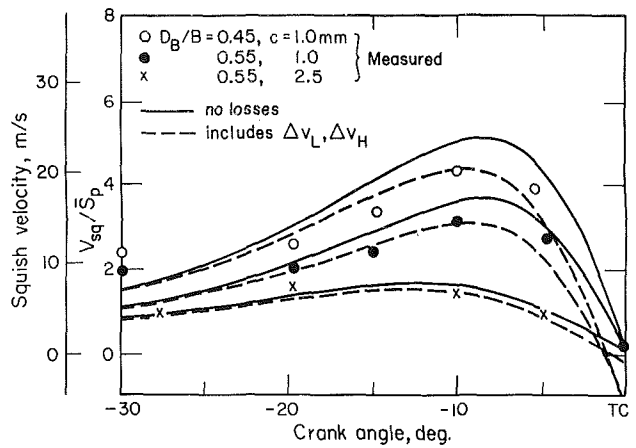


Fig. 43 Comparison of measured squish velocities in bowl-in-piston combustion chambers, with different bowl diameter to bore ratios and clearance heights, to calculated ideal squish velocity (solid lines) and calculations corrected for leakage and heat transfer (dashed lines) [54]

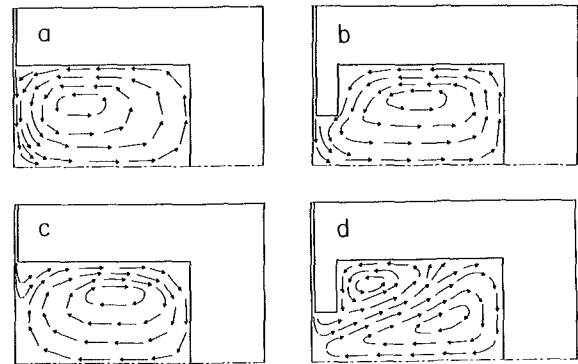


Fig. 44 Schematics of air flow pattern in cylindrical and reentrant bowl-in-piston combustion chambers, derived from LDA velocity measurements in a model engine. a and b with no swirl; c and d with swirl [50].

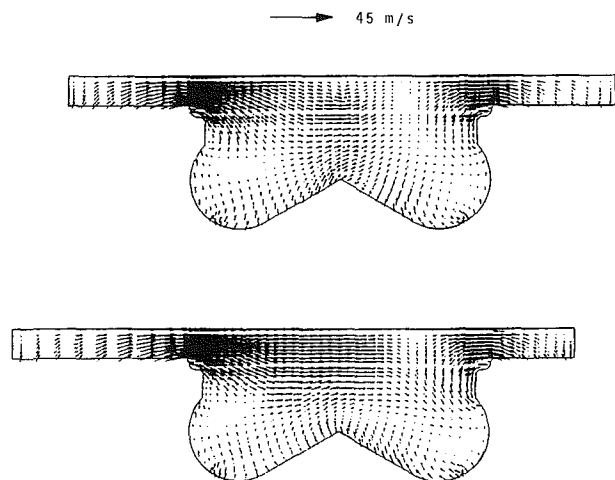


Fig. 45 Velocity vectors predicted by three-dimensional flowfield calculation in a DI diesel with off-cylinder-axis bowl-in-piston combustion chamber, at 20 deg before TC on the compression stroke. Two orthogonal planes through the bowl axis are shown. Complex nonsymmetric character of the flow is evident [58].

[58]. The initial swirl ratio was 2, a typical practical value. The flow in the bowl is dominated by swirl with velocities which are four times greater than the radial or axial values. However, the eccentricity of the bowl results in an asymmetric vortex flow with stagnation regions between the incoming squish flow and upward directed flow near the bowl center.

4.4 Prechamber Engine Flows. Small high-speed diesel engines use an auxiliary combustion chamber, or prechamber, to achieve adequate fuel-air mixing rates. The prechamber is connected to the main combustion chamber above the piston via a nozzle, passageway, or one or more orifices. Flow of air through this restriction into the prechamber during the compression process sets up high velocities in the prechamber at the time the fuel injection process commences. This results in the required high fuel-air mixing rates. Figure 8 shows the two most common examples of these prechamber or indirect-injection diesels: (a) the swirl chamber design, where the flow through the passageway enters the chamber tangentially producing rapid rotation within the chamber; (b) the prechamber design with one or more connecting orifices which produce a highly turbulent flow but no ordered motion within the chamber. Auxiliary chambers are sometimes used in spark-ignition engines. The torch-ignition three-valve stratified-charge engine is one such concept [59]. The prechamber is used to create a rich turbulent mixture in the vicinity of the spark plug to promote rapid flame development.

The most critical phase of flow into the prechamber occurs towards the end of compression. While this flow is driven by the pressure difference between the main chamber above the piston and the auxiliary chamber, this pressure difference is small, and the mass flow rate and velocity at the nozzle, orifice or passageway can be estimated using a simple gas displacement model. Assuming the gas density throughout the cylinder is uniform (an adequate assumption towards the end of compression—the most critical period), the mass in the prechamber, m_p , is given by $m_c(V_p/V)$, where m_c is the cylinder mass, V the cylinder volume, and V_p the prechamber volume. The mass flow rate through the throat of the restriction is, therefore:

$$\dot{m} = \frac{dm_p}{dt} = -\frac{m_c V_p}{V^2} \frac{dV}{dt} \quad (31)$$

Using the relations $dV/dt = -(\pi B^2/4)S_p \dot{V}_d$ where S_p is the instantaneous piston speed, $\dot{V}_d = \pi B^2 L/4$, and $\dot{S}_p = 2NL$, equation (31), can be written

$$\frac{\dot{m}}{m_c N} = 2(r_c - 1) \left(\frac{V_p}{V_c}\right) \left(\frac{S_p}{\dot{S}_p}\right) \left(\frac{V_c}{V}\right)^2 \quad (32)$$

where V_c is the clearance volume, S_p/\dot{S}_p is given by equation (1) and V/V_c is obtained from the engine geometry. The gas velocity at the throat V_T can be obtained from \dot{m} via the relation $\rho V_T A_T = \dot{m}$, the density $\rho = m_c/V$ and equation (32):

$$\frac{V_T}{\dot{S}_p} = \left(\frac{V_p}{V_c}\right) \left(\frac{\pi B^2/4}{A_T}\right) \left(\frac{S_p}{\dot{S}_p}\right) \left(\frac{V_c}{V}\right) \quad (33)$$

where A_T is the effective cross-section area of the throat. The variation of $\dot{m}/(m_c N)$ and V_T/\dot{S}_p with crank angle during the compression process for values of r_c , V_p/V_c and $A_T/(\pi B^2/4)$ typical of a swirl prechamber diesel are shown in Fig. 46. The velocity reaches its peak value about 20 deg before TC: very high gas velocities, an order of magnitude or more larger than the mean piston speed, can be achieved depending on the relative effective throat area. Note that as the piston approaches TC, first the nozzle velocity, and then the mass flow rate, decrease to zero. After TC, in the absence of combustion, an equivalent flow in the reverse direction out of prechamber would occur. Combustion in the prechamber diesel usually starts just before TC, and the pressure in the prechamber then rises significantly above the main chamber pressure. The outflow from the prechamber is then governed by the development of the combustion process, and the above simple gas displacement model no longer describes the flow.

The velocity field set up inside the prechamber during compression is strongly dependent on the details of the nozzle and prechamber geometry. Measured velocities have been shown

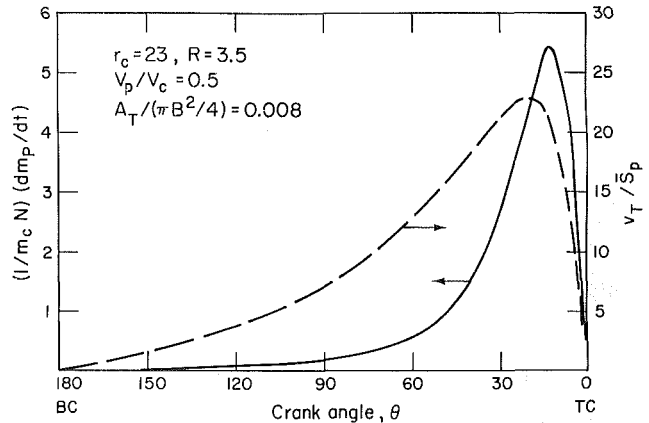


Fig. 46 Mean velocity, and mass flow rate, at the prechamber throat during compression stroke for a typical small swirl prechamber automotive diesel

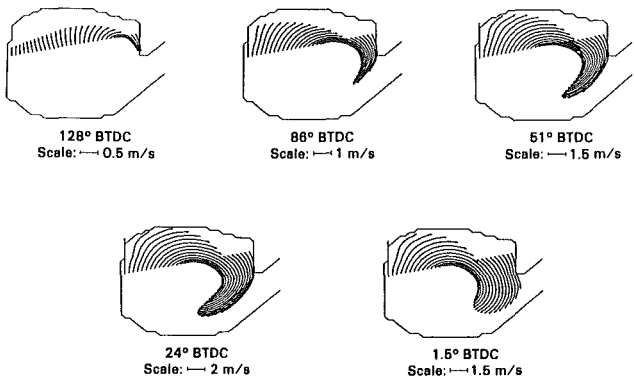


Fig. 47 Calculations of developing flow field in (two-dimensional) swirl prechamber during compression process. Lines are instantaneous flow streamlines, analogous to streak photographs of flow field [61].

to vary linearly with mean piston speed [60]. In swirl prechambers, the nozzle flow sets up a vortex within the chamber. Figure 47 shows calculations of this developing flow field: instantaneous flow streamlines have been drawn in, with the length of the streamlines indicating how the particles of fluid move relative to each other [61]. The velocities increase with increasing crank angle as the compression process proceeds, and reach a maximum about 20 deg before TC. Then, as the piston approaches TC and the flow through the passageway decreases to zero, the vortex in the swirl chamber expands to fill the entire chamber and mean velocities decay. Very high swirl rates can be achieved just before TC: local swirl ratios of up to 60 at intermediate radii, and up to 20 at the outer radius have been measured. These high swirl rates produce large centrifugal accelerations, which result in high fuel-air, and burned-gas unburned-gas, mixing rates.

4.5 Two-Stroke Scavenging Processes. Several methods have been used to determine what occurs in actual two-stroke cycle engine cylinder scavenging processes [62]. Flow visualization experiments [63–65] in liquid analogs of the cylinder, flow velocity mapping techniques [32], and multidimensional modeling studies [66] [67] have proved useful in providing a clearer picture of the scavenging flow field and identifying problems such as fresh mixture short-circuiting directly from the intake to the exhaust system, and dead volumes which do not get scavenged.

Figure 48 illustrates a loop-scavenged flow with a sequence of frames from a flow visualization movie of one liquid scavenging another in a model of a large two-stroke cycle loop-scavenged diesel [64]. The physical variables were scaled

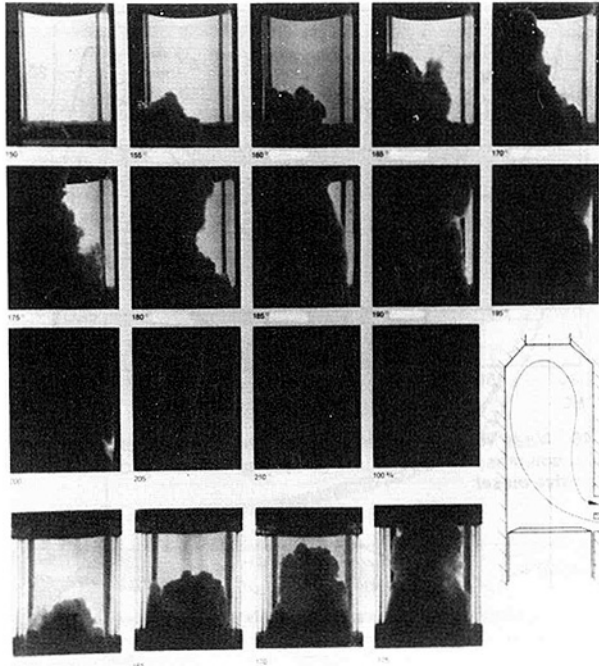


Fig. 48 Photos of one fluid scavenging another in liquid analog experiments in model loop-scavenged engine cylinder. Top three rows show view perpendicular to the scavenging loop: dark denser fluid displaces light less dense fluid. Bottom row shows orthogonal view. Crank angles are values after top center, starting toward the end of the expansion stroke [64].

to maintain the same values of the appropriate dimensionless numbers for the liquid analog flow and the real engine flow. The density of the liquid representing air (dyed to appear dark) was twice the density of the liquid representing burned gas (which is clear). Early in the scavenging process, the fresh air jets penetrate into the burned gas and displace it first towards the cylinder head, and then towards the exhaust ports (the schematic gives the location of the ports). During this initial phase, the outflowing gas contains no air; pure displacement of the burned gas from the cylinder is being achieved. Then short-circuiting losses start to occur, due to the damming-up or build-up of fresh air on the cylinder wall opposite the exhaust ports. These short-circuiting flows occur directly between the scavenge ports and the exhaust ports above them. Since this damming-up of the inflowing fresh air back toward the exhaust ports continues, short-circuiting losses will also continue. While the scavenging front remains distinct as it traverses the cylinder, its turbulent character indicates that mixing between burned gas and air across the front is taking place. For both these reasons (short-circuiting and mixing at the front), the outflowing gas, once the "displacement" phase is over, contains an increasing amount of fresh air.

Engine tests confirm these results from model studies. Initially, the exhausted gas contains no fresh air or mixture; only burned gas is being displaced from the cylinder. However, within the cylinder both displacement and mixing at the interface between burned gas and fresh gas is occurring. The departure from perfect scavenging behavior is evident when fresh mixture first appears in the exhaust. The mixing that occurs is short-range mixing, not mixing throughout the cylinder volume.

It is important that the jets from the inlet ports slow down significantly once they enter the cylinder. Otherwise the scavenging front will reach the exhaust ports or valves too early. The jets are frequently directed to impinge on each other, or against the cylinder wall. The most desirable type of loop-scavenging flow is illustrated in Fig. 49. The scavenging jets

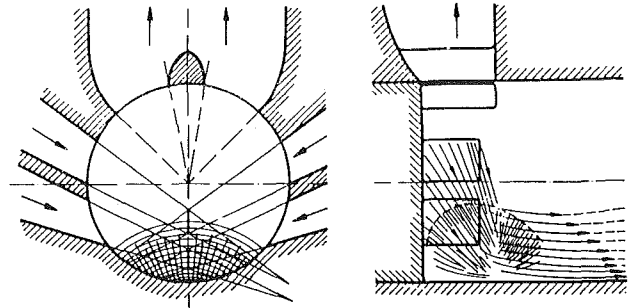


Fig. 49 Desirable airflow in loop-scavenged engine: air from the entering jets impinges on far cylinder wall and flows toward the cylinder head [32]

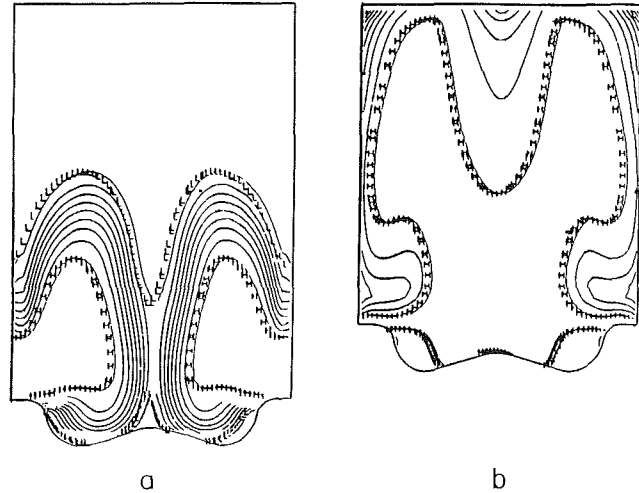


Fig. 50 Air purity contours during scavenging process of uniflow scavenged large two-stroke diesel engine, predicted with two-dimensional flow code [67]. (a) at 169 deg after TC at end of expansion stroke; (b) at 121 deg before TC at time inlet ports close. Maximum purity line (H) corresponds to 90 percent fresh air; minimum purity line (L) in (a) corresponds to 10 percent air. These boundaries define the extent of mixing at the interface.

enter symmetrically with sufficient velocity to fill up about half the cylinder cross-section, and thereafter flow at lower velocity along the cylinder wall towards the cylinder head. By proper direction of the scavenging jets it is possible to achieve almost no outflow in the direction of the exhaust from the cross-hatched stagnation zone on the opposite cylinder wall. In fact, measurement of the velocity profile in this region is a good indicator of the effectiveness of the scavenging flow. If the flow along the cylinder wall towards the head is stable, that is if its maximum velocity occurs near the wall and the velocity is near zero on the plane perpendicular to the axis of symmetry of the ports (which passes through the cylinder axis), the scavenging flow will follow the desired path. If there are "tongues" of scavenging flow towards the exhaust port, either in the center of the cylinder or along the walls, then significant short-circuiting will occur [32].

Multidimensional model analysis of two-stroke cycle scavenging flows shows promise of defining the flow field details with sufficient precision to provide guidance for inlet and exhaust port design optimization [66-68]. In addition to computing the velocity distribution, such calculations also define air and burned gas concentration contours. Figure 50 shows the calculated air purity contours (fraction of the local mixture which is fresh mixture) during the early part of the scavenging process (191 deg before TC), and at the end of the exhaust process (121 deg before TC). The engine is a uniflow design, with inlet ports located around the full circumference

at the bottom of the cylinder liner directed to give swirl to the incoming flow, and with four exhaust valves in the cylinder head [67]. The extent of short range mixing across the burned-gas fresh-air interface is apparent. The front shape is a consequence of the flow generated by the interaction of incoming air jets on the cylinder axis, and the turning upwards and outwards of this flow. This flow sets up two recirculating flow regions, one just above the inlet port location, and the other in the upper regions of the cylinder on the axis. The poor scavenging of these regions, and of the upper corners of the cylinder, is apparent. This study was able to show how increasing the amount of swirl affects the size of these regions, and leads overall to an improvement in scavenging and trapping efficiencies.

5 Turbulence Characteristics of In-cylinder Flows

5.1 Definitions. The bulk engine flow processes are turbulent. In the engine cylinder, as has been explained above, the flow involves a complicated combination of turbulent shear layers, recirculating regions and boundary layers. The flow is unsteady, and may exhibit substantial cycle-to-cycle fluctuations. Both large-scale and small-scale turbulent motions are important factors governing the overall behavior of the flow [39].

An important characteristic of a turbulent flow is its irregularity or randomness and statistical methods are necessary to define the flow field. The quantities normally used are: the mean velocity, the fluctuating velocity about the mean, and several length and time scales. In a steady turbulent flow, the instantaneous local fluid velocity U (in a specific direction) is written:

$$U(t) = \bar{U} + u(t) \quad (34)$$

For steady flow, the mean velocity \bar{U} is the time average of $U(t)$:

$$\bar{U} = \lim_{\tau \rightarrow \infty} \frac{1}{\tau} \int_{t_0}^{t_0 + \tau} U(t) dt \quad (35)$$

The fluctuating velocity component u is characterized by its root-mean-square value, the turbulent intensity, u' :

$$u = \lim_{\tau \rightarrow \infty} \left(\frac{1}{\tau} \int_{t_0}^{t_0 + \tau} u^2 dt \right)^{1/2} \quad (36)$$

In engines, the application of these velocity definitions is complicated by the fact that the flow pattern changes during the engine cycle. Also, while the overall features of the flow repeat each cycle, the details do not because the mean flow can vary significantly from one engine cycle to the next. There are both cycle-to-cycle variations in the mean or bulk flow at any point in the cycle, as well as turbulent fluctuations about that specific cycle's mean flow.

One approach used in periodic flows such as that which occurs in the engine cylinder, is *ensemble-averaging* or *phase-averaging*. Usually, velocity measurements are made over many engine cycles, and over a range of crank-angles. The instantaneous velocity, at a specific crank-angle position θ in a particular cycle i , can be written as

$$U(\theta, i) = \bar{U}(\theta, i) + u(\theta, i) \quad (37)$$

The ensemble or phase-average velocity, $\bar{U}(\theta)$, is defined as the average of values at a specific phase or crank-angle in the basic cycle. Figure 51 shows this approach applied schematically to the velocity variation during an engine cycle, with small and large cycle-to-cycle variations. The ensemble-average velocity is the average over a large number of measurements taken at the same crank angle (two such points are indicated by dots):

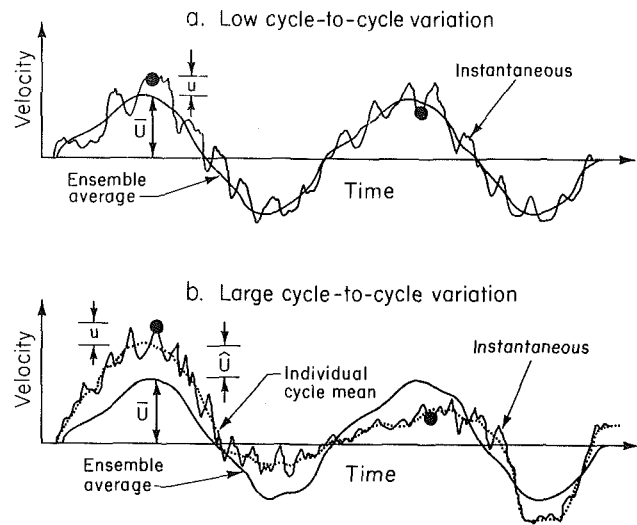


Fig. 51 Schematic of velocity variation with crank angle at a fixed location in the cylinder during two consecutive cycles of an engine. Dots indicate measurements of instantaneous velocity at the same crank angle. Ensemble or phase average velocity obtained by averaging over a large number of such measurements shown as solid smooth line. (a) Low cycle-to-cycle mean flow variations. Here the individual cycle mean velocity and ensemble average velocity are closely comparable. (b) Large cycle-to-cycle mean flow variations. Here the individual cycle mean velocity (dotted line) is different from the ensemble average mean by \bar{U} . The turbulent fluctuation u is then defined in relation to the individual cycle mean. Developed from [39].

$$\bar{U}_{EA}(\theta) = \frac{1}{N_c} \sum_{i=1}^{N_c} U(\theta, i) \quad (38)$$

where N_c is the number of cycles for which data is available. By repeating this process at many crank-angle locations, the ensemble-average velocity profile over the complete cycle is obtained.

The ensemble-average mean velocity is only a function of crank-angle since the cyclic variation has been averaged out. The difference between the mean velocity in a particular cycle and the ensemble-average mean velocity over many cycles is defined as the cycle-by-cycle variation in mean velocity $\hat{U}(\theta, i)$:

$$\hat{U}(\theta, i) = \bar{U}(\theta, i) - \bar{U}_{EA}(\theta) \quad (39)$$

Thus the instantaneous velocity, given by equation (37), can be split into three components [1]:

$$U(\theta, i) = \bar{U}_{EA}(\theta) + \hat{U}(\theta, i) + u(\theta, i) \quad (40)$$

Figure 51 illustrates this breakdown of the instantaneous velocity at a particular point in space into an ensemble-average component, an individual cycle mean velocity and a component which randomly fluctuates in time about the individual cycle mean. This last component is the conventional definition of the turbulent velocity fluctuation. Whether this differs significantly from the fluctuations about the ensemble-average velocity depends on whether the cycle-to-cycle mean flow fluctuations are small or large. The figure indicates these two extremes.

There is considerable debate as to whether the two fluctuating components of the velocity $U(\theta, i)$ defined by equation (40) (cyclic fluctuations in the mean velocity, and fluctuations in time about the individual cycle mean) are physically distinct phenomena. High-frequency fluctuations in velocity are accepted as "turbulence". Low-frequency fluctuations are generally accepted as corresponding to the variations in the mean flow between individual cycles, a phenomenon which is well established. Whether this distinction remains valid at intermediate frequencies is unclear.

Thus, it is necessary to analyze engine velocity data on an individual cycle basis as well as using ensemble-averaging techniques. The basic definitions for obtaining velocities which characterize the flow will now be developed. The ensemble average velocity \bar{U}_{EA} has already been defined by equation (38).

The ensemble-average fluctuation intensity $u'_{F,EA}$ is given by:

$$u'_{F,EA}(\theta) = \left\{ \frac{1}{N_c} \sum_{i=1}^{N_c} [u(\theta, i)]^2 \right\}^{1/2} \\ = \left\{ \frac{1}{N_c} \sum_{i=1}^{N_c} [U(\theta, i)^2 - \bar{U}_{EA}(\theta)^2] \right\}^{1/2} \quad (41)$$

Use of equations (38) and (41) requires values for U and u at each specific crank angle under consideration. While some measurement techniques (e.g., hot-wire anemometry) provide this, the preferred velocity measurement method (laser doppler anemometry) provides an intermittent signal. With laser doppler anemometry (LDA), interference fringes are produced within the small volume created by the intersection of two laser beams, within the flow field. When a small particle passes through this volume, it scatters light at a frequency proportional to the particle velocity. By seeding the flow with particles small enough to be carried without slip by the flow, and collecting this scattered light, the flow velocity is determined [69]. A signal is only produced when a particle moves through the measurement volume; thus one collects data as velocity crank-angle pairs. It is necessary, therefore, to perform the ensemble averaging over a finite crank-angle window $\Delta\theta$ around the specific crank angle of interest, $\bar{\theta}$. The ensemble-average velocity equation becomes:

$$\bar{U}_{EA}(\bar{\theta}) = \frac{1}{N_t} \sum_{i=1}^{N_c} \sum_{j=1}^{N_i} U_{i,j} \left(\bar{\theta} \pm \frac{\Delta\theta}{2} \right) \quad (42)$$

where N_i is the number of velocity measurements recorded in the window during the i th cycle, N_c is the number of cycles, and N_t is the total number of measurements.¹ The corresponding equation for the ensemble-average root-mean-square velocity fluctuation is:

$$u'_{F,EA}(\bar{\theta}) = \left\{ \frac{1}{N_t} \sum_{i=1}^{N_c} \sum_{j=1}^{N_i} \left[u_{i,j} \left(\bar{\theta} \pm \frac{\Delta\theta}{2} \right) \right]^2 \right\}^{1/2} \quad (43)$$

where

$$u_{i,j} = U_{i,j} - \bar{U}_{EA} \quad (44)$$

As has already been explained, this definition of fluctuation intensity (the ensemble-average rms velocity fluctuation, equation (43)) includes cyclic variations in the mean flow as well as the turbulent fluctuations about each cycle's mean flow [1]. It is necessary to determine the mean and fluctuating velocities on an individual cycle basis to characterize the flow field more completely. The critical part of this process is defining the mean velocity at a specific crank angle (or within a small window centered about that crank-angle) in each cycle. Several methods have been used to determine this individual-cycle mean-velocity (e.g., moving window, low-pass filtering, data smoothing, conditional sampling; see [1] for a summary).

In this individual-cycle velocity analysis the individual-cycle time-averaged or mean velocity $\bar{U}(\bar{\theta}, i)$ is first determined [1] [72]. The ensemble-average of this mean velocity

$$\bar{U}_{EA}(\bar{\theta}) = \frac{1}{N_c} \sum_{i=1}^{N_c} \bar{U} \left(\bar{\theta} \pm \frac{\Delta\theta}{2}, i \right) \quad (45)$$

is identical to the ensemble-average value given by equation (42). The root-mean-square fluctuation in individual-cycle mean-velocity can then be determined from

$$U_{RMS}(\bar{\theta}) = \left\{ \frac{1}{N_c} \sum_{i=1}^{N_c} \left[\bar{U} \left(\bar{\theta} \pm \frac{\Delta\theta}{2}, i \right) - \bar{U}_{EA}(\bar{\theta}) \right]^2 \right\}^{1/2} \quad (46)$$

This indicates the magnitude of the cyclic fluctuations in the mean motion.

The instantaneous velocity fluctuation from the individual cycle mean velocity, within a specified window $\Delta\theta$ at a particular crank-angle $\bar{\theta}$, is obtained from equation (37). This instantaneous velocity fluctuation is ensemble averaged, because it varies substantially cycle-by-cycle and because the amount of data is usually insufficient to give reliable individual cycle results:

$$u'_{T,EA}(\bar{\theta}) = \left\{ \frac{1}{N_c} \sum_{i=1}^{N_c} \left[U \left(\bar{\theta} \pm \frac{\Delta\theta}{2}, i \right) - \bar{U} \left(\bar{\theta} \pm \frac{\Delta\theta}{2}, i \right) \right]^2 \right\}^{1/2} \quad (47)$$

This quantity is the ensemble-averaged turbulent intensity.

In turbulent flows, a number of length scales exist which characterize different aspects of the flow behavior. The largest eddies in the flow are limited in size by the system boundaries. The smallest scales of the turbulent motion are limited by molecular diffusion. In internal combustion engines, the eddies responsible for most of the turbulence production during intake are the large eddies in the conical inlet jet flow. These are roughly equal in size to the local jet thickness. This scale is the *integral scale*, l_I : it is a measure of the largest scale structures of the flow field. Velocity measurements made at two points separated by a distance x significantly less than l_I will correlate with each other; with $x \gg l_I$, no correlation will exist. The autocorrelation coefficient of the fluctuating velocity at two adjacent points in the flow with respect to the variable distance x between the points is

$$R_x = \frac{1}{N_m - 1} \sum_{i=1}^{N_m} \frac{u(x_0)u(x_0 + x)}{u'(x_0)u'(x_0 + x)} \quad (48)$$

where N_m is the number of measurements. The integral length scale, $l_{I,x}$, is then:

$$l_{I,x} = \int_0^\infty R_x dx \quad (49)$$

This technique for determining the integral scale requires simultaneous measurements at two points. Due to the difficulty of applying such a technique in engines it has only recently been attempted [73], and most efforts to determine length scales have first employed correlations to determine the *integral time scale*, τ_I . The integral time scale of turbulence is defined by the a correlation between two velocities at a fixed point in space, but separated in time:

$$\tau_I = \int_0^\infty R_t dt \quad (50)$$

where

$$R_t = \frac{1}{N_m - 1} \sum_{i=1}^{N_m} \frac{u(t_0)u(t_0 + t)}{(u')^2} \quad (51)$$

Under conditions where the turbulence pattern is convected past the observation point without significant distortion, and the turbulence is homogeneous and relatively weak, the integral length and time scales are related by

$$l_I = \bar{U} \tau_I \quad (52)$$

¹This need to ensemble average over a finite crank-angle window introduces an error called crank-angle broadening, due to change in the mean velocity across the window. This error depends on the velocity gradient, and can be made negligibly small by suitable choice of window size [69-71].

In engine flows these restrictions are not satisfied so the application of equation (52) is questionable [73].

Superposed on this large-scale flow is a range of eddies of smaller and smaller size, fed by the continual breakdown of larger eddies. Since the smaller eddies respond more rapidly to changes in local flow pattern, they are more likely to be isotropic (have no preferred direction) than are the large eddies, and have a structure like that of other turbulent flows. The dissipation of turbulence energy takes place in these smallest structures. At this smallest scale of the turbulent motion, called the *Kolmogorov scale*, molecular viscosity acts to dissipate small-scale kinetic energy into heat. The Kolmogorov length scale indicates the size of the smallest eddies. The Kolmogorov time scale characterizes the momentum-diffusion of these smallest structures.

A third scale is useful in characterizing a turbulent flow. It is called the *microscale* (or Taylor microscale). The micro length-scale l_M is defined by relating the fluctuating strain rate of the turbulent flow field to the turbulent intensity. It can be determined from the curvature of the autocorrelation curve at the origin [74]. More commonly, the micro time-scale τ_M is determined from the autocorrelation function of equation (51):

$$\tau_M^2 = -2/(\partial^2 R_i / \partial t^2) t_0 \quad (53)$$

For turbulence which is homogeneous (has no spatial gradients) and is isotropic (has no preferred direction), the microscales l_M and τ_M are related by:

$$l_M = \bar{U} \tau_M \quad (54)$$

A useful summary of the velocity and length scales defined in this section is given in Table 2.

5.2 Application to Engine Velocity Data. Several different techniques have been used to measure gas velocities within the engine cylinder (see [75] and [76] for brief reviews and references). The technique which provides most complete and accurate data is laser doppler anemometry. Sample results obtained with this technique will now be reviewed to illustrate the major turbulence features of the in-cylinder gas motion. The available results must be interpreted with caution since they have been obtained in special engines where the geometry and flow have been modified to make the experiments and their interpretation easier. Also, the flow within the cylinder is three-dimensional in nature. It takes measurements at many points

Table 2 Definition of velocities and length scales*

1. Velocity—local instantaneous gas velocity.
1. Bulk velocity—low frequency components (e.g., below appropriate cut-off frequency) of the gas velocity in each cycle.
3. Turbulence—high frequency components (e.g., above appropriate cut-off frequency) of the gas velocity in each cycle; i.e., the difference between the velocity and the bulk velocity at the same crankangle and in the same cycle.
4. Ensemble-averaged mean velocity—ensemble average of the velocity in small (e.g., one crankangle degree) windows.
5. Fluctuation—difference between the velocity and the ensemble-averaged mean velocity at the same crankangle.
6. Fluctuation intensity—Ensemble-averaged rms of the fluctuation in small (e.g., one crankangle degree) windows (this is the most common definition of non-cycle-resolved turbulence intensity).
7. Cyclic variation in the bulk velocity—ensemble-averaged rms fluctuation of the bulk velocity.
8. Turbulence intensity—ensemble averaged rms of the turbulence in small (e.g., one crankangle degree) windows (this is the cycle-resolved turbulence intensity).
9. Turbulence integral length scale—integral length scale based on the spatial correlation coefficient of turbulence.
10. Fluctuation integral length scales—integral length scale based on the spatial correlation coefficient of fluctuation (also referred to simply as the fluctuation length scale).

*Developed from [73].

within the flow field and the use of a flow visualization technique to characterize the flow adequately.

Figure 52 shows ensemble-averaged velocities throughout the engine cycle at two measurement locations in a special L-head engine designed to generate a swirling flow within the cylinder [71]. The engine was motored at 300 rev/min giving a mean piston speed of 0.76 m/s. Figure 52B shows the velocity in the path of the swirling intake flow within the clearance volume, in the swirl direction. Very high velocities are generated during the intake process, rising to a maximum and then decreasing in response to the piston motion (see Fig. 14). During the compression stroke, the velocity continues to decrease but at a much slower rate. This is a motored engine cycle. A comparison of intake and compression velocities with an equivalent firing cycle showed close agreement [77]. The expansion and exhaust stroke velocities are not typical of firing engine behavior, however.² Figure 52C shows the mean velocity in the clearance volume in the same direction, but on

²The increase in velocity when the exhaust valve opens is due to the flow of gas into the cylinder because, due to heat losses, the cylinder pressure is then below the exhaust system pressure.

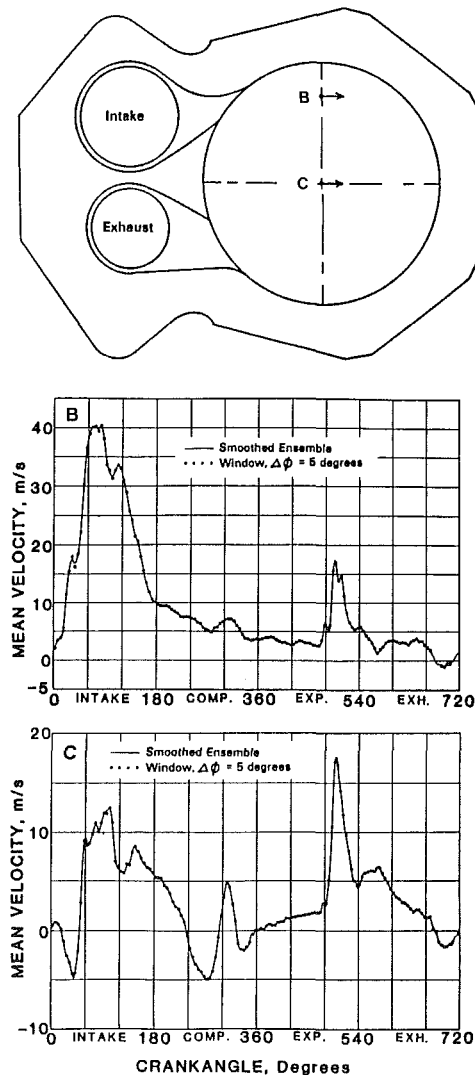


Fig. 52 Ensemble-averaged velocities measured with LDA throughout the engine cycle in motored 4-stroke L-head engine. 300 rev/min, mean piston speed 0.76 m/s. Top: engine schematic showing measurement locations and velocity directions. Middle: velocity at B in intake flow path. Bottom: velocity at C on cylinder axis where no ordered mean flow is apparent [71].

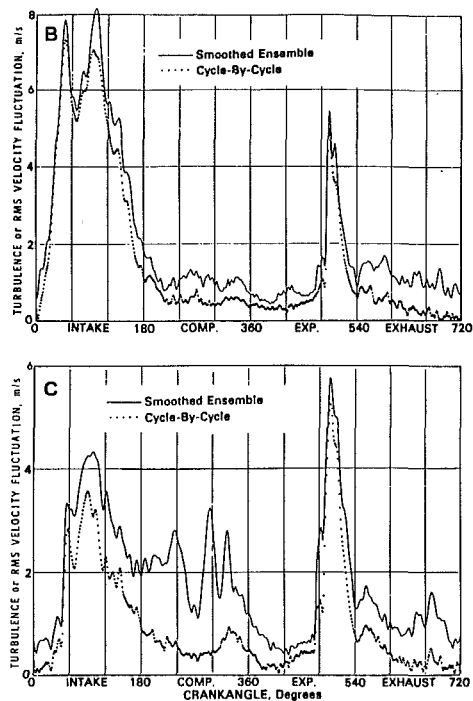


Fig. 53 Ensemble-average rms velocity fluctuation and ensemble-average individual-cycle turbulent intensity as a function of crank angle. Top: at location B in Fig. 52. Bottom: at location C in Fig. 52. The difference between these two velocities is substantial where no ordered mean flow exists [71].

the cylinder axis. At this location, positive and negative flow velocities were measured. Since this location is out of the path of the intake generated flow, velocities during the intake stroke are much lower. The non-homogeneous character of this particular ensemble-mean flow is evident.

Figure 53 shows the ensemble-average rms velocity fluctuation (which includes contributions from cycle-by-cycle variation in the mean flow and turbulence), and the ensemble-average individual cycle turbulent intensity at these same two locations and directions. The difference between the two curves in each graph is a measure of the cycle-by-cycle variation in the mean flow (equation (39)). During the intake process, within the directed intake flow pattern, the cycle-by-cycle variation in the mean flow is small in comparison to the high turbulence levels created by the intake flow. Out of this directed flow region, again during intake, this cycle-by-cycle contribution is more significant relative to the turbulence. During compression, the cycle-by-cycle mean flow variation is comparable in magnitude to the ensemble-average turbulent intensity. It is therefore highly significant.

Two important questions regarding the turbulence in the engine cylinder are whether it is homogeneous (i.e., uniform) and whether it is isotropic (i.e., independent of direction). The data already presented in Figs. 52 and 53 show that during intake the flow is far from homogeneous. Nor is it isotropic [71]. However, it is the character of the turbulence at the end of the compression process that is most important: that is what controls the fuel-air mixing and burning rates. Only limited data are available that relate to these questions. With open disk-shaped combustion chambers, measurements at different locations in the clearance volume around TC at the end of compression show the turbulence intensity is relatively homogeneous. In the absence of an intake generated swirling flow, the turbulent intensity was also essentially isotropic near TC [78]. These specific results support the more general conclusion that the inlet boundary conditions play the dominant role in the generation of the mean flow and turbulence fields during the intake stroke. However, in the absence of swirl, this

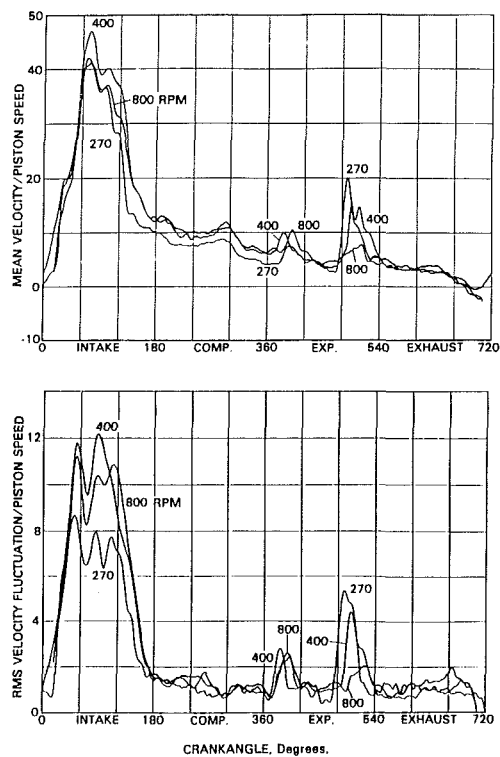


Fig. 54 Ensemble-averaged mean and rms velocity fluctuations, normalized by mean piston speed, throughout the engine cycle for three engine speeds. Location B in Fig. 52 [77].

intake generated flow structure has almost disappeared by the time the compression process commences. The turbulence levels follow this trend in the mean flow, with the rapid decay process lasting until intake valve closing. Later in the compression process the turbulence becomes essentially homogeneous [79].

When a swirling flow is generated during intake, an almost solid-body rotating flow develops which remains stable for much longer than the inlet jet generated rotating flows illustrated in Figs. 28 and 29. With simple disk-shaped chambers, the turbulence still appears to become almost homogeneous at the end of compression [79]. With swirl, and bowl-in-piston geometry chambers however, the flow is more complex.

The flow through the intake valve or port is responsible for many features of the in-cylinder motion. The flow velocity through the valve is proportional to the piston speed (see equation (7) which defines the pseudo valve flow-velocity). It would be expected therefore that in-cylinder flow velocities at different engine speeds would scale with mean piston speed. Figure 54 shows ensemble-average mean and rms velocity fluctuations, normalized by the mean piston speed, through the cycle, at three different engine speeds. The measurement location is in the path of the intake generated swirling flow (point B in Fig. 52). All the curves have approximately the same shape and magnitude indicating the appropriateness of this velocity scaling.³ Other results support this conclusion [80], though in the absence of an ordered mean motion such as swirl when the ensemble-average mean velocities at the end of compression are low, this scaling for the mean velocity does not always hold [78]. Figure 55 shows a compilation of ensemble-averaged rms fluctuation velocity and ensemble-averaged individual-cycle turbulent intensity results, at TC at the end of

³Note that because of the valve location and combustion chamber of this particular engine, the ratio of \bar{U} to \bar{S}_p is higher than is typical of normal engine geometries.

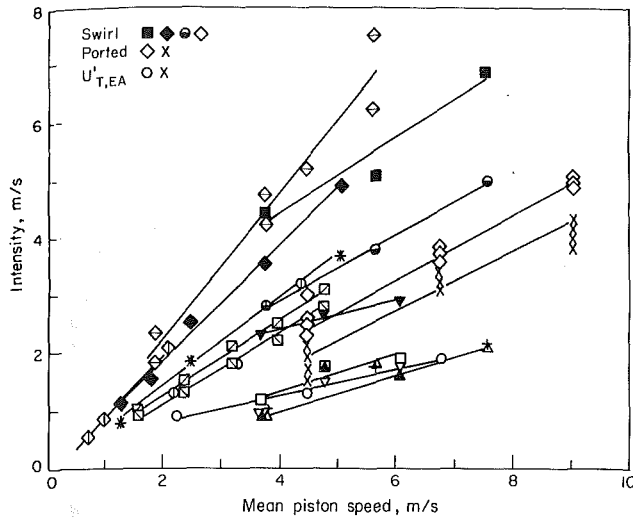


Fig. 55 Individual-cycle turbulent intensity $u'_{T,EA}$ (O,X), and ensemble-averaged rms fluctuation velocity (remaining symbols), at TC at the end of compression, for a number of different flow configurations and chamber geometries as a function of mean piston speed. Two data sets for two-stroke ported engines. Four data sets with intake-generated swirl [78].

compression, from thirteen different flow configurations and combustion chamber geometries. Two of these sets of results are from two-stroke cycle ported configurations. The measured fluctuating velocities or turbulent intensities are plotted against mean piston speed. The linear relationship holds well. There is a substantial variation in the proportionality constant, in part because in most of these studies (identified in the figure) the ensemble-average rms fluctuation velocity was the quantity measured. Since this includes the cycle-by-cycle fluctuation in the mean velocity, it is larger (by up to a factor of 2) than the average turbulent intensity $u'_{T,EA}$.

A consensus conclusion is emerging from these studies that the turbulent intensity at top center, with open combustion chambers in the absence of swirl, has a maximum value equal to about half the mean piston speed

$$u'_{T,EA}(\text{TC}) \approx 0.5 \bar{S}_p \quad (55)$$

When swirl is generated during intake, the turbulent intensity almost always increases [78], as shown by the four data sets with swirl in Fig. 55. The ensemble-averaged cyclic variation in individual-cycle mean-velocity at the end of compression also scales with mean piston speed. This quantity can be comparable in magnitude to the turbulent intensity. It decreases when a strong directed swirling flow is generated within the cylinder during the intake process [71, 78].

During the compression stroke, and also during combustion while the cylinder pressure continues to rise, the unburned mixture is compressed. Turbulent flow properties are changed significantly by the large and rapidly imposed distortions that result from this compression. Such distortions, in the absence of dissipation, would conserve the angular momentum of the flow: rapid compression would lead to an increase in vorticity and turbulent intensity. There is evidence that, with certain types of in-cylinder flow pattern, an increase in turbulence intensity resulting from piston motion and combustion does occur towards the end of the compression process. The compression of large scale rotating flows can cause this increase due to the increasing angular velocity required to conserve angular momentum resulting in a growth in turbulence generation by shear [81]. While the fundamental basis for applying such rapid distortion theories to engine flows is sound, it is unclear whether dissipative effects are small enough for any turbulence amplification due to compression to be apparent.

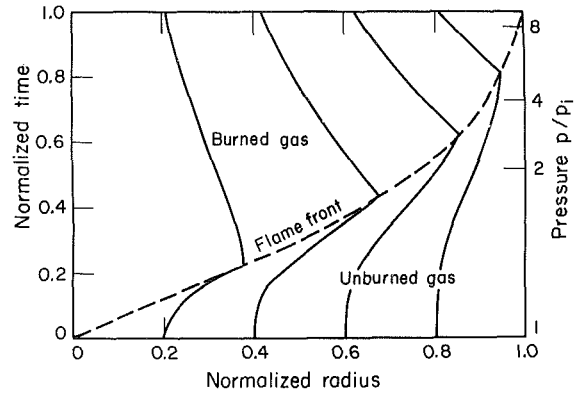


Fig. 56 Particle trajectories in unburned and burned gas as spherically symmetric thin flame propagates radially outward from center of spherical bomb. Stoichiometric hydrocarbon/air mixture

A few results are available which characterize turbulence length and time scales in automobile engine flows. During the intake process, the integral length scale is of the order of the intake jet diameter, which is of the order of the valve lift (≤ 10 mm in automobile size engines). During compression the flow relaxes to the shape of the combustion chamber. The integral time scale at the end of compression decreases with increasing engine speed. It is of order 1 ms at engine speeds of about 1000 rev/min. The integral length scale decreases to a minimum at the end of compression [73], is believed to scale with the clearance height, and varies little with engine speed. The limited results available indicate that the integral length scale at TC is of order 2–5 mm in automotive size engines. The micro time-scale at the end of compression is of order 0.1 ms at 1000 rev/min (again in automobile size engine cylinders), and decreases as engine speed increases. Estimates of the micro length-scales are of order 1 mm at the end of compression, and vary little with engine speed. Kolmogorov length scales at the end of compression are of order 10^{-2} mm [82–85].

5.3 Gas Velocities During Combustion. As stoichiometric mixture—the correct proportions of fuel and air for complete combustion—burns, its density decreases by about a factor of four. Thus burning within the engine cylinder causes gas expansion in the combustion region, which displaces and compresses both gases which have yet to burn and gases which have already burned. The combustion process itself creates additional fluid motion.

This combustion-produced gas motion is easiest to understand in spark-ignition engines where the fuel-air charge is premixed. As described above, the expansion of a gas element which occurs during combustion compresses the gas ahead of the flame and moves it away from the spark plug. At the same time, previously burned gas is compressed and moved back towards the spark plug. Defining this motion in an engine requires sophisticated flow models, because the combustion chamber shape is rarely symmetrical, the spark plug is not usually centrally located, and often there is a bulk gas motion at the time combustion is initiated. However, the gas motion in a spherical or cylindrical combustion bomb with central ignition can readily be computed and illustrates the features of the combustion-induced motion in an engine. Figure 56 shows calculated particle trajectories for a stoichiometric methane-air mixture, initially at ambient conditions, as a thin flame with a constant burning velocity propagates outwards from the center of the spherical container. Figure 57 shows how this gas model can be applied to the spark-ignition engine [86].

The flame propagating outward with an approximately spherical front from the flame center (which in the early stages of combustion can be convected away from the spark plug by

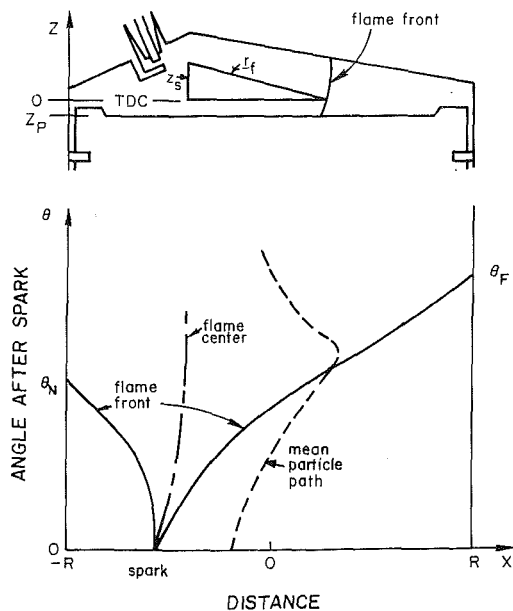


Fig. 57 Schematic showing equivalent particle trajectory in a premixed spark-ignition engine. With off-axis spark plug and non-symmetric chamber flow is more complex. Note flame center can be convected from plug by local flow in its initial growth period (from [86]).

the gas motion) causes the unburned gas ahead of the flame to be displaced and compressed away from the flame, and the gas behind the flame to be displaced and compressed back toward the spark plug as indicated by the dashed mean particle path.

The effect of flame propagation on the details of the turbulent flow field in the unburned mixture ahead of the premixed SI engine flame has been examined. This is an important topic, because it is the turbulence just ahead of the flame which determines the local burning velocity. Measurements of mean velocities and rms fluctuation velocities have been made using laser doppler anemometry, at different locations across the combustion chamber, as the flame approached each measurement location [87, 88]. Under normal engine conditions such data are difficult to interpret because the mean flow varies cycle-by-cycle, the turbulence is not homogeneous, and the flame motion and shape show substantial cyclic variations. The limited results available show that the mean unburned-mixture velocity normal to the front increases steadily from shortly after ignition, as the flame-produced gas expansion displaces unburned mixture towards the wall. This mean motion is greatest in the center of the chamber and decreases as the far wall is approached, as one expects from the idealized particle trajectory plot for a closed spherical vessel in Fig. 56. There was no significant mean gas motion parallel to the front. In one of these studies [87], the turbulent intensity normal to the front increased rapidly as the flame approached each measurement location to a value 1.5 to 1.9 times the value measured under motored engine conditions. The turbulent intensity tangential to the flame front did not increase significantly in the center of the chamber. In the second study [88], no significant change in turbulent intensity ahead of the flame was observed. Thus, whether the combustion produced compression of the unburned mixture ahead of the propagation of the spark-ignition engine flame produces significant turbulence amplification as predicted by rapid distortion theory has yet to be resolved.

Analogous gas motion is produced by the expansion of fuel-air mixture on combustion in the diesel or compression-ignition engine. However, both the nonuniform fuel distribution (from very rich mixture at the center of each jet or spray to air in regions where the fuel has yet to penetrate) and the initially very high energy-release rate introduce important dif-

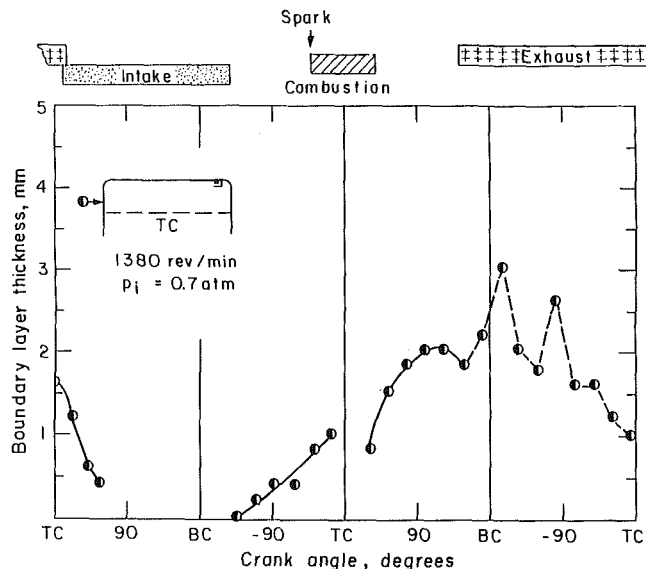


Fig. 58 Thickness of thermal boundary layer on the combustion chamber wall determined from schlieren photographs taken in a special flow-visualization spark-ignition engine, through the complete operating cycle [92]

ferences. Following spontaneous ignition, locally the rapid burning of a significant fraction of the fuel sets up strong pressure waves and substantial motion of the gas just ahead of the flame region away from the flame. Local velocities of the order of the sound speed have been predicted using a three-dimensional diesel engine flow code [89]. Similar high local outward gas velocities around the autoigniting region of a spark-ignition engine under knocking conditions have been predicted with a multidimensional model code [90].

6 Flows Near the Walls

The flow behavior adjacent to the walls of the cylinder can be substantially different from the bulk gas motion; it is important because it governs heat transfer to the chamber walls and, in spark-ignition engines, plays an important role in the unburned hydrocarbon emissions mechanism [91]. Boundary layers develop on the cylinder head, cylinder wall and piston crown. Then, because the piston slides along the cylinder wall and is sealed by piston rings, unusual corner flows develop and gas flows into and out of the regions around the piston rings.

6.1 Boundary Layer Flows. The bulk gas flows created by the intake and exhaust processes and the piston motion, create momentum and thermal boundary layers on the combustion chamber walls. Only limited information is available on boundary layer behavior during the engine's operating cycle. Measurements of thermal boundary layer thickness from schlieren photographs indicate that these regions are thinnest during intake, grow during compression and are thickest during the latter half of the expansion stroke. Figure 58 shows a set of such results. The layers are thickest (≤ 5 mm at moderate engine speeds) on the cylinder head and piston surfaces (where the displacing action of the piston does not create any significant flow) and of order half that thickness elsewhere. There is evidence that the cylinder-wall boundary-layer is a Rayleigh-type flow, growing as \sqrt{t} following the uncovering of the wall by the piston as it moves during the expansion stroke [92].

Note that the mass of gas in these boundary layer regions can be substantial. For an average thickness of 3 mm, at 90 degrees after TC, the boundary layer volume is some 20 percent of the cylinder volume and the boundary layer mass could

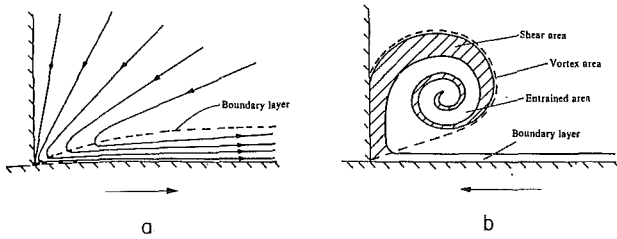


Fig. 59 Schematics of the flow pattern set up in the piston-face cylinder-wall corner, in piston-stationary coordinates, due to the boundary layer on the cylinder wall. (a) sink flow set up during intake and expansion; (b) vortex flow set up during compression and exhaust [93]. Arrow shows cylinder wall velocity relative to piston.

be 30–40 percent of the total charge since the boundary layer gas is more dense than the bulk gas.

6.2 Flows Generated by the Piston Cylinder-Wall Interaction. Because a boundary layer exists on the cylinder wall, the motion of the piston generates unusual flow patterns in the cylinder-liner piston-face corner. When the piston is moving away from top center a sink-type flow occurs. When the piston moves towards top center a vortex flow is generated. Figure 59 shows schematics of these flows (in a coordinate frame with the piston face at rest). The vortex flow has been studied because of its effect on gas motion at time of ignition, and because it has been suggested as a mechanism for removing unburned hydrocarbons off the cylinder wall during the exhaust stroke [94].

The vortex flow has been studied in cylinders with water as the fluid over the range of Reynolds numbers typical of engine operation [93] [95]. Laminar, transition and turbulent flow regimes have been identified. It has been shown that a quasi-steady flow assumption is valid, and that

$$A_V/L^2 = f(v_w L/\nu) \quad (48)$$

where A_V is the vortex area (area inside the dashed line in Fig. 59(b)), L is the stroke, v_w is the wall velocity in piston stationary coordinates ($v_w = S_p$ in the engine) and ν is the kinematic viscosity.

For the laminar flow regime, a good assumption is that A_V is proportional to the shear area in the vortex (shown cross-hatched) which equals the boundary-layer area; this can be estimated from boundary layer theory. In the turbulent flow regime, an entrainment theory was used, which assumed that the rate of change of vortex area was proportional to the product of the exposed perimeter of the vortex and the velocity difference between the vortex and the stationary fluid ($\approx v_w$). Figure 60 shows these two theories correlated against the hydraulic analog data:

$$\text{For } (v_w L/\nu) \leq 2 \times 10^4:$$

$$A_V/L^2 = (v_w L/\nu)^{-1/2} \quad (49)$$

$$\text{For } (v_w L/\nu) \geq 2 \times 10^4:$$

$$A_V/L^2 = 0.006 \quad (50)$$

These theories are for constant values of ν . During compression, ν decreases substantially as the gas temperature and pressure increase (ν decreases by a factor of 4 for a compression ratio of 8). This will decrease the size of the vortex until the turbulent regime is reached. During the exhaust stroke, following blowdown, ν will remain approximately constant as the pressure and temperature do not change significantly. Typical parameter values at 1500 rev/min are: $S_p = 5$ m/s, $L = 0.1$ m; average values of ν are 1.2×10^{-5} m²/s and 1.4×10^{-4} m²/s for compression and exhaust stroke respectively. Hence a Reynolds number for the compression stroke is 4×10^4 , $A_V/L^2 \approx 0.006$, and the vortex diameter $d_V \approx 0.09 L$. For the exhaust stroke, the Reynolds number is 4×10^3 , $A_V/L^2 \approx 0.015$ and $d_V \approx 0.14 L$. Thus the vortex dimensions

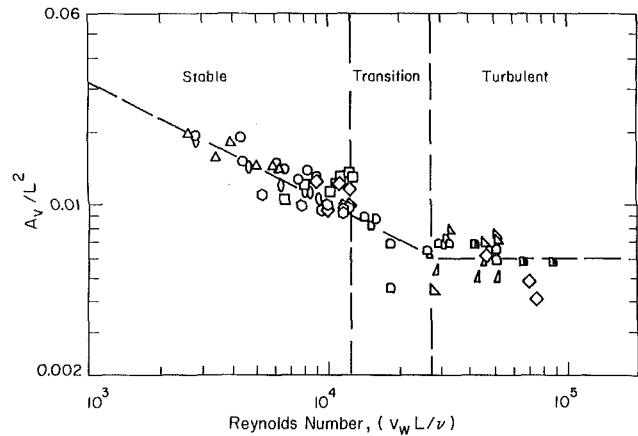


Fig. 60 Ratio of area of vortex in piston-face cylinder-wall corner to square of stroke, as a function of Reynolds number based on piston velocity, for piston moving toward the cylinder head [93]

at the end of the upward stroke of the piston are comparable to the engine clearance height.

This vortex flow has been observed in an operating engine. Figure 17 showed schlieren photographs taken during the exhaust stroke in a special square cross-section flow visualization spark-ignition engine. The accompanying schematic identifies the vortex structure which is visible in the photo because the cool boundary layer gas is being scraped off the cylinder wall by the upward moving piston and “rolled up.” The vortex diameter as the piston approaches TC is about 20 percent of the bore.

6.3 Crevice Flows and Blowby. The engine combustion chamber is connected to several small volumes usually called *crevices* because of their narrow entrances. Gas flows into and out of these volumes during the engine operating cycle, as the cylinder pressure changes.

The largest crevices are the volumes between the piston, piston rings and cylinder wall. Some gas flows out of these regions into the crankcase; it is called *blowby*. Other crevice volumes in production engines are the threads around the spark plug, the space around the plug center electrode, the gap around the fuel injector, crevices between the intake and exhaust valve heads and cylinder head, and the head gasket cutout. Total crevice volume is a few percent of the clearance volume, based on cold engine dimensions, and the piston and ring crevices are the dominant contributor [91]. When the engine is warmed up, dimensions and crevice volumes will change.

The important crevice processes occurring during the engine cycle are the following. As the cylinder pressure rises during compression, unburned mixture is forced into each crevice region. Since these volumes are thin they have a large surface to volume ratio; the gas flowing into the crevice cools by heat transfer to close to the wall temperature. During combustion, while the pressure continues to rise, unburned mixture or air, depending on engine type, continues to flow into the crevice volume. After flame arrival at the crevice entrance, burned gases will flow into the crevice until the cylinder pressure starts to decrease. Once the crevice gas pressure is higher than the cylinder pressure, gas flows back from the crevice into the cylinder.

The volumes between the piston, piston rings and cylinder wall are shown schematically in Fig. 61. These crevices consist of a series of volumes (numbered 1 to 5) connected by flow restrictions such as the ring side clearance and ring gap. The geometry changes as the ring moves up and down in the ring groove, sealing either at the top or bottom ring surface. The gas flow, pressure distribution and ring motion are therefore

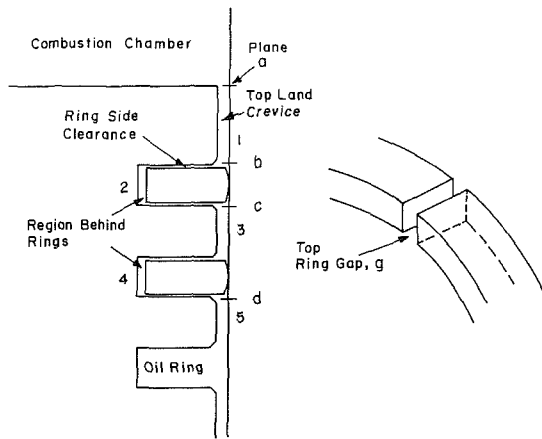


Fig. 61 Schematic of piston and ring assembly in automotive spark-ignition engine showing major crevice regions. Gas flows into and out of these regions across planes *a*, *b*, *c*, and *d*, and through ring gap *g*, during the compression and expansion strokes [91].

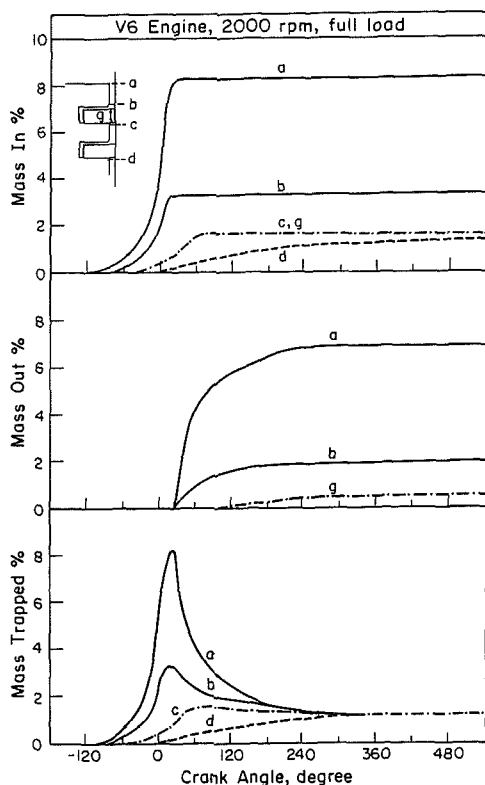


Fig. 62 Percentage of total cylinder mass that flows into, out of, and is trapped within the different crevice regions defined by planes *a*, *b*, *c*, and *d* in Fig. 61, as a function of crank angle. Automotive spark-ignition engine at wide-open-throttle and 2000 rev/min [91].

coupled. Figure 62 illustrates this behavior: mass flows of gas into and out of the regions defined by planes *a*, *b*, *c*, *d*, and through the ring gap *g*, are plotted versus crank angle through compression and expansion. These results come from an analysis of these regions as volumes connected by passageways, with a prescribed cylinder pressure versus crank angle profile, coupled with a dynamic model for ring motion, and assuming the gas temperature equals the wall temperature [91]. During compression and combustion, the rings are forced to the groove lower surfaces and mass flows *into* all the volumes in this total crevice region. The pressure above and behind the first ring is essentially the same as the cylinder pressure; there is a substantial pressure drop across each ring,

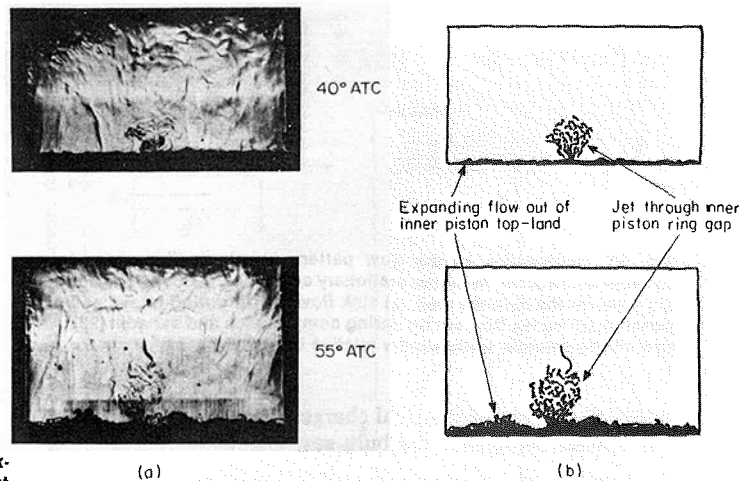


Fig. 63 Schlieren photographs of the flow out of the piston cylinder-wall crevices during the expansion stroke in square cross-section flow-visualization spark-ignition engine [91]. Standard circular cross-section piston-crown was inserted into square cross-section piston to simulate production engine ring crevice geometry. Gas flows at low velocity out of crevice entrance all around the piston circumference once the cylinder pressure starts decreasing early in the expansion stroke. Gas flows out of the ring gap as a jet, once the pressure above the ring falls below the pressure beneath the ring. Both the low velocity flow, and the jet flow, are visible in the photographs.

however. Once the cylinder pressure starts to decrease (after 15 deg ATC) gas flows out of regions 1 and 2 in Fig. 61 into the cylinder, but continues to flow *into* regions 3, 4 and 5 until the pressure in the cylinder falls below the pressure beneath the top ring. The top ring then shifts to seal with the upper groove surface and gas flows out of regions 2, 3, and 4 (which now have the same pressure), both into the cylinder and as blowby into the crankcase. Some 5–10 percent of the total cylinder charge is trapped in these regions at time of peak cylinder pressure. Most of this gas returns to the cylinder; about 1 percent goes to the crankcase as blowby. The gas flow back into the cylinder continues throughout the expansion process. In spark-ignition engines this gas is the major contributor to unburned hydrocarbon emissions. Since it removes air or fuel-air mixture from the primary combustion process, it also results in a loss of power and efficiency.

There is substantial experimental evidence to support the above description of flow in the piston-ring crevice region. In a special square cross-section flow-visualization engine both the low velocity gas expansion out of the volume above the first ring after time of peak pressure and the jet like flows through the top ring gap later in the expansion process when the pressure differences across the ring changes sign have been observed. Figure 63 shows these flows with explanatory schematics.

7 Conclusions

Contributions to our understanding of engine flows now come from many directions and sources: from both fundamental and more pragmatic studies of engine fluid flow behavior; from use of flow visualization techniques, detailed flow field measurements and predictions based on computer solutions of the flow conservation equations. The more sophisticated of these techniques—both experimental and computational—have developed rapidly over the last few years, and are now defining engine flow fields at a level of detail unimagined a few years ago. (However, we must acknowledge that key pioneers in this area of engine research such as Semenov [96] identified many major features of engine flows twenty-five or more years ago.)

These new tools are still largely focused on “understanding” the fundamentals of engine flows, and only to a limited

extent on development and design issues. There are several reasons for this. These measurement techniques are still mostly restricted to applications where the engine geometry and operating conditions have been simplified. The computational fluid dynamic analysis codes are limited by simplifying assumptions in some of their key sub-models, and the substantial computer time requirements of three-dimensional calculations with adequate spatial resolution. Thus, these tools have to date been primarily focused on understanding what is actually going on within the cylinder. There is still a large gap between what we are learning through use of these tools, and the practical flow-related knowledge required to implement improvements in engine development and design. While our increased understanding is having a substantial impact, it is largely indirect. Our ability to describe what flow pattern we want within the cylinder is still disappointingly inexact!

The desired in-cylinder flow is determined by the combustion requirements of the engine, within the constraints of minimizing the inlet and exit flow resistance. The key requirement is a repeatable combustion process, cycle-by-cycle, with a fuel-burning rate which is sufficiently fast to release the fuel's energy close to top center.

For spark-ignition engines this requires higher in-cylinder flow velocities than can be achieved with a simple inlet port and valve arrangement. Higher turbulence than has been the historical norm is required to give the fast burn rates that have recently been used to improve both fuel consumption and emission control. It is becoming clear that generating a swirling flow during the intake process is one of the more promising ways to achieve this fast burning rate; swirl is more stable than other large scale in-cylinder flows and therefore breaks up later in the cycle giving higher turbulence during combustion. This higher turbulence gives both faster flame front propagation and higher reactive flame surface area. It is also clear that excessive fluid motion and turbulence is undesirable since very fast burning rates are not required, and the higher than necessary heat transfer that occurs results in performance and efficiency losses. However, exactly what flow is needed—especially during the early stage of flame development which is critical to the cycle-by-cycle combustion variability—is not yet clear. Our knowledge of the flow field during the combustion process, and of the flow flame interactions, is not sufficient to resolve this question.

In compression-ignition engines, it is the interaction between the fuel jets and the airflow that controls the combustion process. It is well established that increasingly vigorous air motion is required as engine size decreases and maximum engine speed increases, to achieve sufficiently fast fuel-air mixing and combustion rates. Flow research tools are starting to show us how different types of inlet generated flows lead to different flows within the combustion chamber at time of injection. However, our knowledge of and ability to predict the behavior of the diesel liquid fuel spray in this air environment lags our understanding of the airflow. While the overall design goal is clear—achieving a fast enough mixing and burning rate in the latter half of the combustion process without making the early part much too fast, how best to achieve this in practice is not well defined. The flow combustion interaction in the diesel engine is an area where successful research would have a major impact on improving the engine's performance and emissions.

In closing, it is worth highlighting three technical areas where important basic questions have yet to be adequately answered. The first is in-cylinder turbulence. What is important here is how the flow affects the fuel burning rate through its influence on mixing and flame structure. Two critical questions are: How should turbulent fluctuations be separated from cyclic variations in the mean flow? What length scales are most important in determining the structure of the flame? Related important issues are the degree to which the tur-

bulence is homogeneous and isotropic during the period in which combustion occurs.

The second area relates to the in-cylinder bulk flow. What flow can we create by the intake process, and modify during compression through use of the most appropriate combustion chamber shape, to give the highest burning rates for the minimum breathing and wall heat loss penalties? It is unlikely that there is one single answer to this question; useful design input will come from continuing to develop our understanding of the behavior of in-cylinder bulk flows.

The third area is the application of computational fluid dynamic models to internal combustion engines. This review has indicated the promise of this type of analysis with many examples of model predictions. We do not yet know just how accurate these predictions are, in part because three-dimensional predictive capability has only recently become available, and also due to a lack of detailed experimental data against which to validate these predictions. The potential of these models for defining engine flow processes in their full detail is highly promising. However, how these flow models should be coupled to the combustion process is not nearly as well established as their flow behavior predictive capabilities. These are important areas for research.

Finally, the development of these sophisticated flow-defining tools is only the first stage. Detailed flow diagnostics such as laser doppler anemometry and computational fluid dynamic modeling produce enormous amounts of information which must be processed into a form where they can be assimilated and used by the practicing engineer. While much has indeed been accomplished, much more still remains to be done!

Acknowledgments

This review was made possible by the Freeman Scholar Program in Fluids Engineering of ASME. The author is grateful to the Program and to the Standing Committee of Dr. J. W. Daily, Prof. A. J. Acosta, and Dr. Jules Dussourd, for providing him this opportunity.

The author wishes to acknowledge the encouragement and support provided by colleagues at M.I.T. who have worked with him over many years on engine-related research: Prof. G. P. Beretta, Prof. W. K. Cheng, Dr. J. A. Ekchian, Prof. A. F. Ghoniem, Dr. D. P. Hoult, Prof. J. C. Keck, Dr. J. M. Rife. Their contributions have been many and generous. He is grateful to Ms. Karla A. Stryker for her expert and patient work on the manuscript.

References

- 1 Rask, R. B., "Laser Doppler Anemometer Measurements of Mean Velocity and Turbulence in Internal Combustion Engines," ICALCO '84 Conference Proceedings, Vols. 45 and 47, Inspection, Measurement and Control and Laser Diagnostics and Photochemistry, Laser Institute of America, Boston, Nov. 1984.
- 2 Butler, T. D., Cloutman, L. D., Dukowicz, J. K., and Ramshaw, J. D., "Multidimensional Numerical Simulation of Reactive Flow in Internal Combustion Engines," *Progr. in Energy and Combust. Sci.*, Vol. 7, 1981, pp. 293-315.
- 3 Gosman, A. D., "Multidimensional Modeling of Cold Flows and Turbulence in Reciprocating Engines," SAE Paper 850344, Soc. of Automotive Engineers, 1985.
- 4 Gosman, A. D., "Computer Modeling of Flow and Heat Transfer in Engines, Progress and Prospects," Proceedings of International Symposium on *Diagnostics and Modeling of Combustion in Reciprocating Engines*, COMODIA 85, JSME, Tokyo, Japan, Sept., 1985, pp. 15-26.
- 5 Bracco, F. V., "Modeling of Engine Sprays," SAE Paper 850394, in *Engine Combustion Analysis: New Approaches*, P-156, Soc. of Automotive Engineers, 1985.
- 6 Watkins, A. P., Gosman, A. D., and Tabrizi, B. S., "Calculations of Three Dimensional Spray Motion in Engines," SAE Paper 860468, Soc. of Automotive Engineers, 1986.
- 7 Gatowski, J. A., Heywood, J. B., and Deleplace, C., "Flame Photographs in a Spark-Ignition Engine," *Combustion & Flame*, Vol. 56, 1984, pp. 71-81.
- 8 Keck, J. C., "Turbulent Flame Structure and Speed in Spark-Ignition

- Engines," *Proceedings of Nineteenth Symposium (Int'l) on Combustion*, The Combustion Institute, 1982, pp. 1451-1466.
- 9 Witze, P. O., "The Effect of Spark Location on Combustion in a Variable-Swirl Engine," SAE Paper 820044, *SAE Trans.*, Vol. 91, 1982.
- 10 Taylor, C. F., *The Internal Combustion Engine in Theory and Practice*, Vol. II, *Combustion, Fuels, Materials, Design*, M.I.T. Press, 1968.
- 11 Abraham, J., Williams, F. A., and Bracco, F. V., "A Discussion of Turbulent Flame Structure in Premixed Charges," SAE Paper 850345, in *Engine Combustion Analysis: New Approaches*, P-156, Soc. of Automotive Engineers, 1985.
- 12 Heywood, J. B., "Combustion Chamber Design for Optimum Spark-Ignition Engine Performance," *Int. J. of Vehicle Design*, Vol. 5, No. 3, 1984, pp. 336-357.
- 13 Gruden, D. O., "Combustion Chamber Layout for Modern Otto Engines," SAE Paper 811231, Soc. of Automotive Engineers, 1981.
- 14 Barnes-Moss, H. W., "A Designers Viewpoint," *Passenger Car Engines*, Conference Proceedings, Institution of Mechanical Engineers, London, 1975, pp. 133-147.
- 15 Lyn, W. T., "Study of the Burning Rate and Nature of Combustion in Diesel Engines," 9th Symposium International on Combustion, The Combustion Institute, 1960, pp. 1069-1082.
- 16 Browne, K. R., Partridge, I. M., and Greeves, G., "Fuel Property Effects on Fuel/Air Mixing in an Experimental Diesel Engine," SAE Paper 860223, Soc. of Automotive Engineers, 1986.
- 17 Alcock, J. F., and Scott, W. M., "Some More Light on Diesel Combustion," *Proceedings of the Automobile Division*, No. 5, The Institution of Mechanical Engineers, 1962-1963.
- 18 Tabaczynski, R. J., "Effects of Inlet and Exhaust System Design on Engine Performance," SAE Paper 821577, Soc. of Automotive Engineers, 1985.
- 19 Asmus, T. W., "Valve Events and Engine Operation," SAE Paper 820749, *SAE Trans.*, Vol. 91, 1982.
- 20 Kastner, L. J., Williams, T. J., and White, J. B., "Poppet Inlet Valve Characteristics and Their Influence on the Induction Process," *Proceedings Institution of Mechanical Engineers*, Vol. 178, Part 1, No. 36, 1963-1964, pp. 955-978.
- 21 Taylor, C. F., *The Internal-Combustion Engine in Theory and Practice*, Vol. I, 2nd Edition, M.I.T. Press, Cambridge, Mass., 1966.
- 22 Woods, W. A., and Khan, S. R., "An Experimental Study of Flow Through Poppet Valves," *Proceedings of Institution of Mechanical Engineers*, Vol. 180, Part 3N, 1965-1966, pp. 32-41.
- 23 Annand, W. J. D., and Roe, G. E., *Gas Flow in the Internal Combustion Engine*, Haessner Publishing, Inc., Newfoundland, 1974.
- 24 Tanaka, K., "Air Flow Through Exhaust Valve of Conical Seat," *International Congress of Applied Mechanics*, Vol. 1, 1931, pp. 287-295.
- 25 Bicen, A. F., Vafidis, C., and Whitelaw, J. H., "Steady and Unsteady Air Flow Through an Intake Valve of a Reciprocating Engine," in *Flows in Internal Combustion Engines*, - II, FED Vol. 20, ASME, 1984, pp. 47-55.
- 26 Fukutani, I., and Watanabe, E., "An Analysis of the Volumetric Efficiency Characteristics of 4-Stroke Cycle Engines Using the Mean Inlet Mach Number Mim," SAE Paper 790484, *SAE Trans.*, Vol. 88, 1979.
- 27 Isshiki, Y., Shimamoto, Y., and Wakisaka, T., "Numerical Prediction of Effect of Intake Port Configurations on the Induction Swirl Intensity by Three-Dimensional Gas Flow Analysis," Proceedings of International Symposium on *Diagnostics and Modeling of Combustion in Reciprocating Engines*, COMODIA 85, JSME, Tokyo, Japan, Sept., 1985, pp. 295-304.
- 28 Namazian, M., Hansen, S., Lyford-Pike, E., Sanchez-Barsse, J., Heywood, J., and Rife, J., "Schlieren Visualization of the Flow and Density Fields in the Cylinder of a Spark-Ignition Engine," SAE Paper 800044, *SAE Trans.*, Vol. 89, 1980.
- 29 Wallace, W. B., "High-Output Medium-Speed Diesel Engine Air and Exhaust System Flow Losses," *Proceedings of Institution of Mechanical Engineers*, Vol. 182, Part 3D, 1967-1968, pp. 134-144.
- 30 Cole, B. N., and Mills, B., "The Theory of Sudden Enlargements Applied to Poppet Exhaust-Valve, with Special Reference to Exhaust-Pulse Scavenging," *Proceedings of Institution of Mechanical Engineers*, Part 1B, 1953, pp. 364-378.
- 31 Annand, W. J. D., "Compressible Flow Through Square-Edged Orifices: An Empirical Approximation for Computer Calculations," *J. Mech. Eng. Sci.*, Vol. 8, 1966, p. 448.
- 32 Jante, A., "Scavenging and Other Problems of Two-Stroke Cycle Spark-Ignition Engines," SAE Paper 680468, *SAE Trans.*, Vol. 77, 1968.
- 33 Benson, R. S., "Experiments on a Piston Controlled Port," *The Engineer*, Vol. 210, 1960, pp. 875-880.
- 34 Ekchian, A., and Hoult, D. P., "Flow Visualization Study of the Intake Process of an Internal Combustion Engine," SAE Paper 790095, *SAE Trans.*, Vol. 88, 1979.
- 35 Arcoumanis, C., Bicen, A. F., Vlachos, N. S., and Whitelaw, J. H., "Effects of Flow and Geometry Boundary Conditions on Fluid Motion in a Motored IC Model Engine," *Proc. Inst. Mech. Eng.*, Vol. 196, No. 4, 1982, pp. 1-10.
- 36 El-Tahry, S. H., "A Comparison of Three Turbulence Models in Engine-Like Geometries," Proceedings of International Symposium on *Diagnostics and Modeling of Combustion in Reciprocating Engines*, COMODIA 85, JSME, Tokyo, Japan, September, 1985, pp. 203-213.
- 37 Hirotsomi, T., Nagayama, I., Kobayashi, S., and Yamamasu, "Study of Induction Swirl in a Spark Ignition Engine," SAE Paper 810496, *SAE Trans.*, Vol. 90, 1981.
- 38 Wakisaka, T., Shimamoto, Y., and Isshiki, Y., "Three-Dimensional Numerical Analysis of In-Cylinder Flows in Reciprocating Engines," SAE Paper 860464, Soc. of Automotive Engineers, 1986.
- 39 Reynolds, W. C., "Modeling of Fluid Motions in Engines—An Introductory Overview," *Combustion Modeling in Reciprocating Engines*, eds. Mattavi, J. M., and Amann, C. A., Plenum Press, 1980, pp. 69-124.
- 40 Uzman, T., Borgnakke, C., and Morel, T., "Characterization of Flow Produced by a High-Swirl Inlet Port," SAE Paper 830266, Soc. of Automotive Engineers, 1983.
- 41 Monaghan, M. L., and Pettifer, H. F., "Air Motion and Its Effects on Diesel Performance and Emissions," SAE Paper 810255, in *Diesel Combustion and Emissions Part 2*, SP-484, *SAE Trans.*, Vol. 90, 1983.
- 42 Tindal, M. J., Williams, T. J., and Adloory, M., "The Effect of Inlet Port Design on Cylinder Gas Motion in Direct Injection Diesel Engines," in *Flows in Internal Combustion Engines*, ASME, New York, 1982.
- 43 Brandl, F., Reverencic, I., Cartellieri, W., and Dent, J. C., "Turbulent Air Flow in the Combustion Bowl of a D. I. Diesel Engine and Its Effect on Engine Performance," SAE Paper 790040, *SAE Trans.*, Vol. 88, 1979.
- 44 Brandstetter, W., Johns, R. J. R., and Wigley, G., "Calculation of the Flow Produced by a Tangential Inlet Port," *International Symposium on Flows in Internal Combustion Engines*, - III, FED - Vol. 28, ASME, 1985, pp. 135-148.
- 45 Brandstetter, W., Johns, R. J. R., and Wigley, G., "The Effect of Inlet Port Geometry on In-Cylinder Flow Structure," SAE Paper 850499, Soc. of Automotive Engineers, 1985.
- 46 Khalighi, B., El Tahry, S. H., and Kuziak, Jr., W. R., "Measured Steady Flow Velocity Distributions Around a Valve/Seat Annulus," SAE Paper 860462, Soc. of Automotive Engineers, 1986.
- 47 Davis, G. C., and Kent, J. C., "Comparison of Model Calculations and Experimental Measurements of the Bulk Cylinder Flow Processes in a Motored PROCO Engine," SAE Paper 790290, Soc. of Automotive Engineers, 1979.
- 48 Borgnakke, C., Davis, G. C., and Tabaczynski, R. J., "Predictions of In-Cylinder Swirl Velocity and Turbulence Intensity for an Open Chamber Cup in Piston Engine," SAE Paper 810224, *SAE Trans.*, Vol. 90, 1981.
- 49 Kondoh, T., Fukumoto, A., Ohsawa, K., and Ohkubo, Y., "An Assessment of a Multi-Dimensional Numerical Method to Predict the Flow in Internal Combustion Engines," SAE Paper 850500, Soc. of Automotive Engineers, 1985.
- 50 Arcoumanis, C., Bicen, A. F., and Whitelaw, J. H., "Squish and Swirl-Squish Interaction in Motored Model Engines," *ASME JOURNAL OF FLUIDS ENGINEERING*, Vol. 105, 1983, pp. 105-112.
- 51 Ikegami, M., Mitsuda, T., Kawatchi, K., and Fujikawa, T., "Air Motion and Combustion in Direct Injection Diesel Engines," JARI Technical Memorandum No. 2, 1971, pp. 231-245.
- 52 Fitzgeorge, D., and Allison, J. L., "Air Swirl in a Road-Vehicle Diesel Engine," *Proc. Instn. Mech. Engrs. (A.D.)*, No. 4, 1962-1963, pp. 151-168.
- 53 Lichty, L. C., *Combustion Engine Processes*, McGraw-Hill, 1967.
- 54 Shimamoto, Y., and Akiyama, K., "A Study of Squish in Open Combustion Chambers of a Diesel Engine," *Bull. JSME*, Vol. 13, No. 63, 1970, pp. 1096-1103.
- 55 Borman, G., and Nishiwaki, K., "A Review of Internal Combustion Engine Heat Transfer," to be published in *Progr. in Energy & Combust. & Sci.*, 1987.
- 56 Dent, J. C., and Derham, J. A., "Air Motion in a Four-Stroke Direct Injection Diesel Engine," *Proc. I. Mech. E.*, Vol. 188 21/74, 1974, pp. 269-280.
- 57 Asanuma, T., and Obokata, T., "Gas Velocity Measurements of a Motored and Firing Engine by Laser Anemometry," SAE Paper 790096, *SAE Trans.*, Vol. 88, 1979.
- 58 Schapertons, H., and Thiele, F., "Three-Dimensional Computations for Flowfields in DI Piston Bowls," SAE Paper 860463, Soc. of Automotive Engineers, 1986.
- 59 Turkish, M. C., "Prechamber and Valve Gear Design for 3-Valve Stratified-Charge Engines," SAE Paper 751004, *SAE Trans.*, Vol. 84, 1975.
- 60 Zimmerman, D. R., "Laser Anemometer Measurements of the Air Motion in the Prechamber of an Automotive Diesel Engine," SAE Paper 830452, Soc. of Automotive Engineers, 1983.
- 61 Meintjes, K., and Alkida, A. C., "An Experimental and Computational Investigation of the Flow in Diesel," SAE Paper 820275, *SAE Trans.*, Vol. 91, in *Diesel Engine Combustion, Emissions, & Particulates*, P-107, Soc. of Automotive Engineers, 1982.
- 62 Phatak, R. G., "A New Method of Analyzing Two-Stroke Cycle Engine Gas Flow Patterns," SAE Paper 790487, *SAE Trans.*, Vol. 88, 1979.
- 63 Rizk, W., "Experimental Studies of the Mixing Processes and Flow Configurations in Two-Cycle Engine Scavenging," *Proc. I. Mech. E.*, Vol. 172, 1958, pp. 417-437.
- 64 Dedeoglu, N., "Scavenging Model Solves Problems in Gas Burning Engine," SAE Paper 710579, *SAE Trans.*, Vol. 80, 1971.
- 65 Sher, E., "Investigating the Gas Exchange Process of a Two-Stroke Cycle Engine with a Flow Visualization Rig," *Israel Journal of Technology*, Vol. 20, 1982, pp. 127-136.
- 66 Adachi, T., Kato, S., and Tsujimura, H., "Numerical Analysis of Scavenging Flow in Two-Cycle Internal Combustion Engine," *Flows in Internal Combustion Engines*, ed. Uzman, T., ASME, 1982, pp. 29-34.
- 67 Diwakar, R., "Multidimensional Modeling of the Gas Exchange Processes in a Uniflow-Scavenged Two-Stroke Diesel Engine," *International Symposium on Flows in Internal Combustion Engines-III*, FED - Vol. 28, ed. Uzman, T., Tiederman, W. G., and Novak, J. M., ASME, 1985, pp. 125-134.

- 68 Johns, R. J. R., "A Unifuel Method for Calculating Engine Flows," Paper 84-DGP-18, presented at the 7th ASME Annual Energy-Sources Technology Conference and Exhibition, New Orleans, Feb., 12-16, 1984.
- 69 Witze, O., "A Critical Comparison of Hot-Wire Anemometry and Laser Doppler Velocimetry for I. C. Engine Applications," SAE Paper 800132, *SAE Trans.*, Vol. 89, 1980.
- 70 Witze, P. O., Martin, J. K., and Borgnakke, C., "Conditionally-Sampled Velocity and Turbulence Measurements in a Spark Ignition Engine," *Combustion Science and Technology*, Vol. 36, 1984, pp. 301-317.
- 71 Rask, R. B., "Comparison of Window, Smoothed-Ensemble, and Cycle-by-Cycle Data Reduction Techniques for Laser Doppler Anemometer Measurements of In-Cylinder Velocity," in *Fluid Mechanics of Combustion Systems*, edited by Morel, T., Lohmann, R. P., and Rackley, J. M., ASME, New York, 1981, pp. 11-20.
- 72 Liou, T.-M., and Santavica, D. A., "Cycle Resolved LDV Measurements in a Motored IC Engine," in *Engineering Applications of Laser Velocimetry*, ed. by Coleman, H. W., and Pfund, P. A., ASME, New York, 1982, pp. 33-37.
- 73 Fraser, R. A., Felton, P. G., and Bracco, F. V., "Preliminary Turbulence Length Scale Measurements in a Motored IC Engine," SAE Paper 860021, Soc. of Automotive Engineers, 1986.
- 74 Tennekes, H., and Lumley, J. L., *A First Course in Turbulence*, M.I.T. Press, 1972.
- 75 Amann, C. A., "Classical Combustion Diagnostics for Engine Research," SAE Paper 850395, in *Engine Combustion Analysis: New Approaches*, P-156, Soc. of Automotive Engineers, 1985.
- 76 Dyer, T. M., "New Experimental Techniques for In-Cylinder Engine Studies," SAE Paper 850396, in *Engine Combustion Analysis: New Approaches*, P-156, Soc. of Automotive Engineers, 1985.
- 77 Rask, R. B., "Laser Doppler Anemometer Measurements in an Internal Combustion Engine," SAE Paper 790094, *SAE Trans.*, Vol. 88, 1979.
- 78 Liou, T.-M., Hall, M., Santavica, D. A., and Bracco, F. V., "Laser Doppler Velocimetry Measurements in Valved and Ported Engines," SAE Paper 840375, *SAE Trans.*, Vol. 93, 1984.
- 79 Arcoumanis, C., Bicen, A. F., and Whitelaw, J. H., "Effect of Inlet Parameters on the Flow Characteristics in a Four-Stroke Model Engine," SAE Paper 820750, Soc. of Automotive Engineers, 1982.
- 80 Bopp, S., Vafidis, C., and Whitelaw, J. H., "The Effect of Engine Speed on the TDC Flowfield in a Motored Reciprocating Engine," SAE Paper 860023, Soc. of Automotive Engineers, 1986.
- 81 Wong, V. W., and Hoult, D. P., "Rapid Distortion Theory Applied to Turbulent Combustion," SAE Paper 790357, *SAE Trans.*, Vol. 88, 1979.
- 82 Tabaczynski, R. J., "Turbulence and Turbulent Combustion in Spark-Ignition Engines," *Progress in Energy and Combustion Science*, Vol. 2, 1976, pp. 143-165.
- 83 Dent, J. C., and Salama, N. S., "The Measurement of the Turbulence Characteristics in an Internal Combustion Engine Cylinder," SAE Paper 750886, Soc. of Automotive Engineers, 1975.
- 84 Lancaster, D. R., "Effects of Engine Variables on Turbulence in a Spark-Ignition Engine," SAE Paper 760159, *SAE Trans.*, Vol. 85, 1976.
- 85 Wakisaka, T., Hamamoto, Y., and Kinoshita, S., "The Measurement of Turbulent Flow in the Combustion Chamber of an I. C. Engine," *JSAE Review*, Vol. 3, 1980, pp. 9-16.
- 86 Beretta, G. P., Rashidi, M., and Keck, J. C., "Turbulent Flame Propagation and Combustion in Spark Ignition Engines," *Combustion & Flame*, Vol. 52, 1983, pp. 217-245.
- 87 Martin, J. K., Witze, P. O., and Borgnakke, C., "Combustion Effects on the Pre-flame Flow Field in a Research Engine," SAE Paper 850122, Soc. of Automotive Engineers, 1985.
- 88 Hall, M. J., Bracco, F. V., and Santavica, D. A., "Cycle-Resolved Velocity and Turbulence Measurements in an IC Engine With Combustion," SAE Paper 860320, Soc. of Automotive Engineers, 1986.
- 89 Theobald, M. A., "A Numerical Simulation of Diesel Autoignition," Ph.D. thesis, M.I.T., Department of Mechanical Engineering, Feb. 1986.
- 90 Schapertons, H., and Lee, W., "Multidimensional Modeling of Knocking Combustion in SI Engines," SAE Paper 850502, Soc. of Automotive Engineers, 1985.
- 91 Namazian, M., and Heywood, J. B., "Flow in the Piston-Cylinder-Ring Crevices of a Spark-Ignition Engine: Effect on Hydrocarbon Emissions, Efficiency and Power," SAE Paper 820088, *SAE Trans.*, Vol. 91, 1982.
- 92 Lyford-Pike, E. J., and Heywood, J. B., "Thermal Boundary Layer Thickness in the Cylinder of a Spark-Ignition Engine," *Int. J. Heat Mass Transfer*, Vol. 27, No. 10, 1984, pp. 1873-1878.
- 93 Tabaczynski, R. J., Hoult, D. P., and Keck, J. C., "High Reynolds Number Flow in a Moving Corner," *J. Fluid Mech.*, Vol. 42, 1970, pp. 249-255.
- 94 Tabaczynski, R. J., Heywood, J. B., and Keck, J. C., "Time-Resolved Measurements of Hydrocarbon Mass Flowrate in the Exhaust of a Spark-Ignition Engine," SAE Paper 720112, *SAE Trans.*, Vol. 81, 1972.
- 95 Daneshyar, H. F., Fuller, D. E., and Deckker, B. E. L., "Vortex Motion Induced by the Piston of an Internal Combustion Engine," *Int. J. Mech. Sci.*, Vol. 15, 1973, pp. 381-390.
- 96 Semenov, E. S., "Studies of Turbulent Gas Flow in Piston Engines," in *Combustion in Turbulent Flow*, Ed. Khitrin, L. N., translated from Russian and published by the Israel Program for Scientific Translations Ltd., OTS 62-11035, U.S. Dept. of Commerce, 1963.

Y. Miyake
Professor.

T. Inaba
Assistant Professor.

Department of Mechanical Engineering,
Osaka University,
Suita, Osaka, 565 Japan

T. Kato
Engineer,
FANUC Ltd.,
Oshino, Minami-Tsuru,
Yamanashi, 401-05 Japan

Improvement of Unstable Characteristics of an Axial Flow Fan by Air-Separator Equipment

The authors' previous papers demonstrated that an air-separator is the most effective equipment among various different types for the improvement of unstable characteristics of an axial-flow rotor. Further experiments revealed that this equipment could eliminate the unstable characteristics thoroughly even for a build which originally accompanied a heavy rotating stall. This paper describes the geometric conditions to realize this and discusses its performance mechanism on the basis of the experiments showing the discharge distribution of the bleeding flow from the blade tip to separator passage as well as the pressure distribution in a blade passage at the tip section of the rotor. It is suggested that the equipment is equally useful at any stage of a multistage rotor.

1 Introduction

A separator is one of the devices that improve unstable characteristics of an axial flow fan. It is a short ring with many fins on it and is installed coaxially in the casing just ahead of the rotor. The term "separator" is supposed to come from the fact that it divides the reverse flow from the ordinary flow in the inlet part to the rotor when the flow rate of the fan is small. So far, two different types of separator are known. One is installed in an ordinary casing and is referred to as a "blade separator," which was proposed by Ushakov [1]. Tanaka and Murata examined its working mechanism and showed that it was useful to moderately loaded blades [2]. The other is installed in a partly enlarged casing and is called an "air-separator." The prototype of this separator was proposed and patented by Ivanov [3]. But no details were given on its working mechanism. The present authors investigated air-separators and showed that an air-separator equipment was the most useful one to improve unstable characteristics among the devices of the same type [4]. Its working mechanism is discussed in [5]. Although the results in these papers [4, 5] showed a remarkable improvement by an air-separator over a fairly wide range of setting angle (the complement of stagger angle), a thoroughly smooth performance curve was not obtained as the setting angle became large. Later, much trial and error revealed that further improvement could be realized by this equipment even when the setting angle was unusually large. This paper presents the geometric conditions to realize this improvement on the basis of the measured results such as the velocity distribution of the outward (bleeding) flow from the blade tip to the enlarged part of the casing. Results are also presented of the experiments carried out to clarify why bleeding is necessary to improve the characteristics of a fan in small flow rate range.

Contributed by the Fluids Engineering Division for publication in the JOURNAL OF FLUIDS ENGINEERING. Manuscript received by the Fluids Engineering Division October 29, 1985.

With the intention of applying air-separators to multistage machines, all the separators used in the experiments had axial length limited within the extent of one stage (a set of rotor and stator). The results were very promising.

2 Experimental Setup

The rotor was of a free-vortex type with 12 blades of a constant chord length of 100 mm. The outer diameter was $2r_t = 500$ mm and the hub-tip ratio was 0.5. The setting angle of the blades was chosen at $\beta_t = 48.5$ deg (measured from circumferential direction) at the tip to realize a heavy dip on the performance curve in the middle flow rate range. (The design value was $\beta_t = 23.5$ deg and the corresponding diffusion factor was 0.188 at the tip.) The fan head was measured at location about 3 m downstream of the rotor and the losses between them were neglected in the characteristics. The stator vanes were removed in this experiment, since they hardly affected the performance of an air-separator. But this removal caused a larger loss than that in the previous experiments [4, 5]. The averaged inner diameter of the normal casing was 504 mm. The averaged tip clearance was, therefore 2 mm. Figure 1 shows the geometry of the air-separator and the enlarged casing. The part shown by broken lines is a ring which constitutes the extension part of the normal casing and enables to change the length l_c . The inner diameter of the ring was 506 mm, which made an average tip clearance of 3 mm.

The separator ring was made of sheet metal. The dimensions $l_d = 40$ mm, $l_r = 60$ mm, and $l_a = 6$ mm were chosen as the optimum values in the sense that the dip in the middle flow rate range of the performance curve could be perfectly removed, after much trial and error. These values were exclusively used in the following results. The axial length of the enlarged part of the casing ahead of the rotor was limited to an extent of the axial length of the stator. It, therefore, was

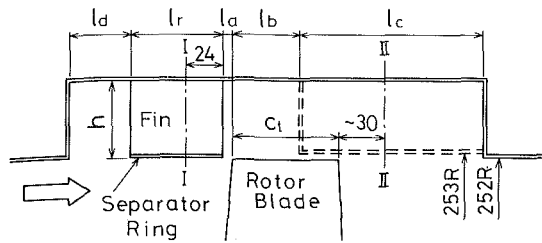


Fig. 1 Dimensions of air-separator (Uncertainty in radius = ± 0.6 mm)

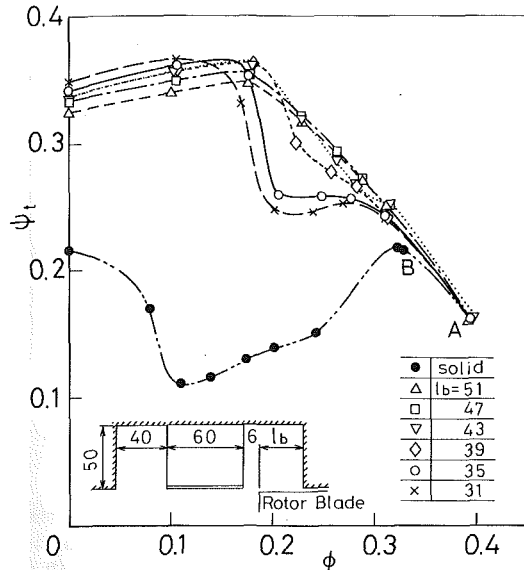


Fig. 2 Improvement of the characteristics by air-separator (effect of l_b)

shorter than the previous cases [4, 5]. In the following the flow passage between the enlarged casing and the separator ring will be called as separator passage.

3 Experimental Results and Discussions

3.1 Optimum Length of Open Part of Blade Tip, l_b . Experiments were carried out mainly on the case $l_b = 15$ mm in [4]. In [5], the working mechanism of an air-separator was discussed and it was shown that bleeding the fluid of low relative velocity from blade tip was essentially important. These results suggested that more extensive and careful investigation on the length l_b was needed to raise the bleeding effect. A series of experiments varying the values of l_d , l_a , and l_b yielded the results in Fig. 2. The total pressure coefficient ψ_t and the flow coefficient ϕ is defined as

$$\psi_t = H_t / (U_t^2 / 2g), \quad \phi = Q / (\pi r_t^2 U_t)$$

where H_t [m] is the total head of the fan, Q [m³/s], the flow rate, U_t [m/s], the tip velocity of the rotor ($= 33.6$ [m/s]) and g [m/s²], the acceleration due to gravity, and l_b [mm] is measured in axial length.

Fifteen axially directed straight fins of 60 mm long were attached on the separator ring within the separator passage. Figure 2 shows the most effective case with this separator. Modifications of fins enable a further improvement in the flow coefficient range smaller than that of the maximum pressure coefficient, as shown in Fig. 5.

The results in Fig. 2 show a more significant improvement by the air-separator than that obtained in the previous works [4, 5]. To realize this improvement, a length of l_b of more than 47 mm is required, which, therefore, extends over almost 2/3 chord length of rotor blades. A dip appears on the performance curve in the flow rate range larger than that of the maximum

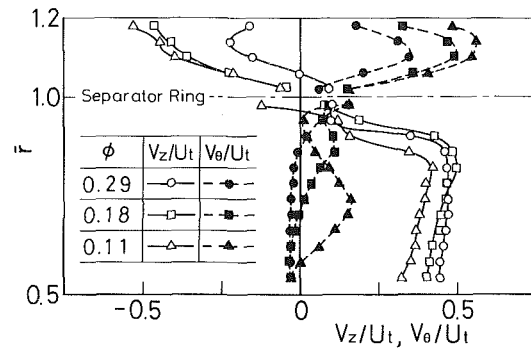


Fig. 3(a) Ahead of the rotor (section I-I of Fig. 2)

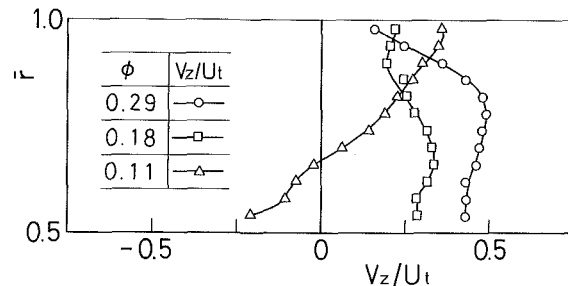


Fig. 3(b) Behind the rotor (section II-II of Fig. 2)

Fig. 3 Velocity distributions ahead of and behind the rotor. (Uncertainty in V_z/U_t and $V_\theta/U_t = 0.05$)

imum head when the value l_b is smaller than 47 mm, and the dip becomes deeper as the value of l_b decreases from 47 mm. Even the most effective air-separator in [4] did not have a sufficiently large value of l_b .

In the following, the cause of the difference in improvement due to variations of l_b is discussed.

Figure 3 shows velocity distributions (V_z : axial component, V_θ : circumferential component) measured by a three-hole Pitot tube; (a) and (b), respectively, show those ahead of (section I-I of Fig. 1) and behind (section II-II of Fig. 1) the rotor. The flow in the separator passage fluctuates intensively and the measured results there are less accurate. In an axial flow fan with a normal casing, a flow separation is often observed near the hub when the head rises again with decreasing flow rate. It usually corresponds to the change of the flow regime from the rotating stall to an axisymmetric one. In the present experiment, the performance curves in the range of flow rate smaller than that of maximum head ($\phi < 0.18$) are very similar regardless of the value of l_b , and so are the flow behind the rotor. However, the flow near the hub still has a margin till separation even at the flow rate of the maximum head as shown in Fig. 3(b). The steep head rise near the maximum head, therefore, does not come from the centrifuging effect due to the flow separation near the hub.

Figure 4 shows the radial velocity distributions (V_r/U_t) of the bleeding flow from the rotor measured using an "X" configuration hot wire and a regular "I" configuration one along with a phase locked averaging technique [6]: (a) is for the case of the smooth performance curve ($l_b = 47$ mm) and (b), for the case when a dip appears on the performance curve ($l_b = 31$ mm). Measurements were carried out in a cylindrical plane of 5 mm outside the blade tip. But the location of blades in Fig. 4 is not corrected for this discrepancy of 5 mm. V_z in the figure means the main flow (or axial) direction. The figures present: (i) when compared at similar flow rates, the amount of bleeding flow is larger when $l_b = 47$ mm, (ii) in the case of $l_b = 47$ mm, a circumferentially almost uniform outward flow occurs except for a small part of strong outward flow near the pressure side of blades, and the region of this uniform out-

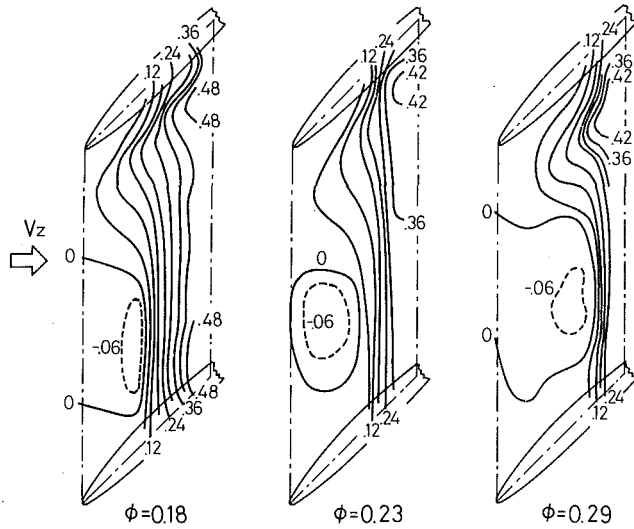


Fig. 4(a) $l_b = 47$ mm

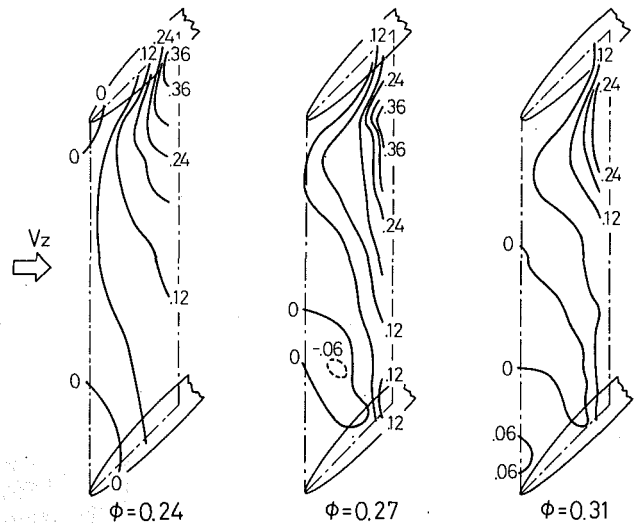


Fig. 4(b) $l_b = 31$ mm

Fig. 4 Contours of the bleeding flow from the blade tip to separator passage (V_z/U_t). (Uncertainty in $V_z/U_t = 0.03$)

ward flow moves upstream as the flow rate decreases, (iii) in the case of $l_b = 31$ mm, the outward flow is stronger near the pressure side. Although the flow rate of the bleeding increases as ϕ decreases, no significant difference is noticed between $\phi = 0.27$ and $\phi = 0.24$. This seems to correspond to the fact that the head is also very similar at both flow rates.

Along with the phase locked averaging, timewise variations of the output wave form were monitored during the experiment, and the circumferential uniformity of the outward flow was confirmed from the aperiodicity of the wave form. The above discussion leads to a conjecture that a dip appears on a performance curve when the amount of bleeding is insufficient. When the blade tip is exposed to open space, a flow occurs around the tip from the pressure side to the suction side to eliminate the pressure difference, and the flow due to the pressure difference between the pressure side of the blade and the outer space also occurs. They are considered to cause the outward flow. Figure 4 shows that the outward flow is strong in the latter half of the blade chord, although it expands upstream as the flow rate is decreased. In the case when the outward flow is strong near the pressure side as shown in Fig. 4(b), the part of the blade tip where a strong uniform outward flow should appear, is covered by the casing, and the outward flow is supposed to be mainly due to the forcing of the ac-

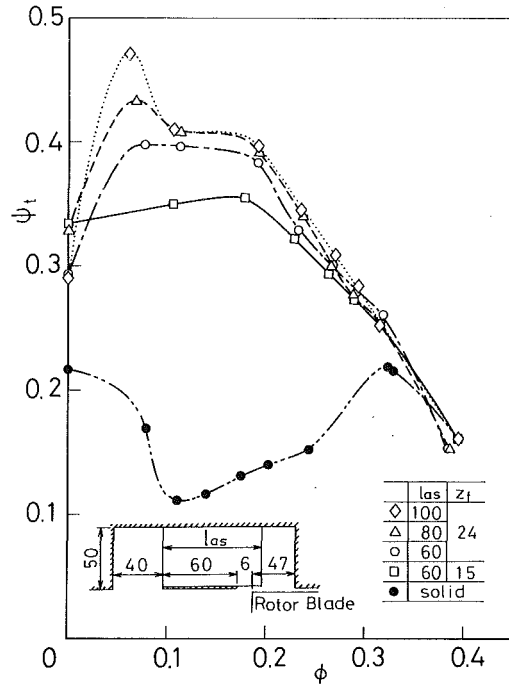


Fig. 5 Effect of separator fins

cumulated fluid near the casing which is scraped by blades. If the open part of the blade tip is sufficiently wide, the outward bleeding flow would be pronounced combined with the entrainment of the fluid near the casing. And in the part where the outward bleeding flow occurs, a spanwise flow from hub to tip would also occur along both surfaces of blades. A similar spanwise flow would occur in inter-blade passages, which is supposed to result in a circumferentially uniform bleeding flow in the open part of the tip.

A local and intermittent rotating stall was observed when the amount of bleeding flow was insufficient. Even in that case, the rotating stall did not reach the upstream region of the rotor as shown in Fig. 3(a), in which no swirl was observed in the velocity distribution ahead of the rotor.

3.2 Effect of Separator Fins. Separator fins are essential to promote the effect of an air-separator [4]. In the present experiments, the effect of fins was reexamined for the case when performance curves were improved to smooth ones in the range of middle flow rate. The results are shown in Fig. 5 for various axial lengths of fins of increased number. The characteristics in small flow rate range of $\phi < 0.18$ are further improved and preferable smooth characteristic curves are obtainable except for the range of very small flow rate of $\phi < 0.05$. The figure shows that an increase in number of fins and overhanging them over the rotor blades are effective to improve the characteristics in small flow rate range without spoiling the middle flow rate characteristics.

A maximum head point appears at $\phi = 0.08$ and a rotating stall occurs below that flow rate. This is supposed because, due to a large circumferential velocity of the bleeding flow, a large incidence angle at the leading edge of the axially directed straight fins prevents a smooth flow into the separator passage causing an overflow of the bleeding flow to the regular passage to the rotor. Bending fins near the rotor side end is effective [4] to solve this problem. Therefore, a further improvement would be expected by using fins of proper shape.

The unstable characteristics are thus dissolvable by selecting the value of l_b , the number of fins and their dimensions properly even if the setting angle is large.

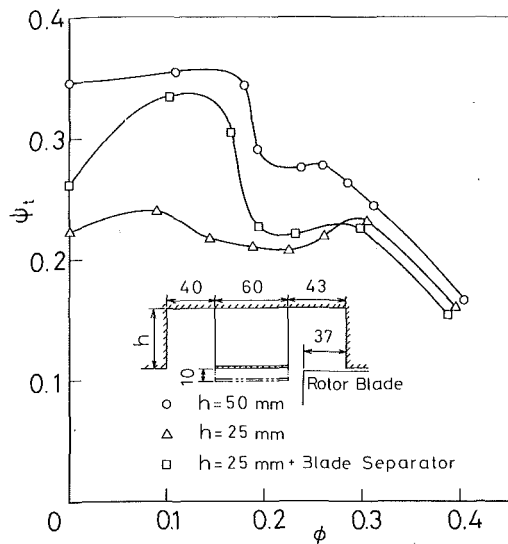


Fig. 6 Effect of the height of separator passage

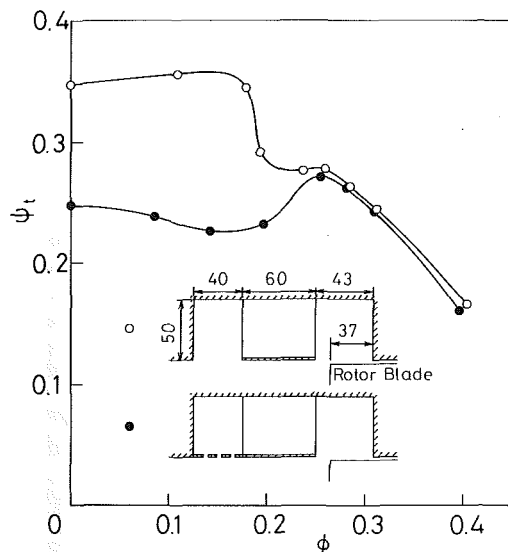


Fig. 7 Effect of the flow resistance of the separator passage

3.3 Effect of Height of Separator Passage. In Figs. 3(a) and 4(a), a part of the bleeding flow reverses the direction in the separator passage and flows into the rotor again through the separator passage. This seemed as if the separator passage was unnecessarily high, and an experiment was carried out decreasing the height to $h = 25$ mm which was half of the original height. The result in Fig. 6 shows that $h = 25$ mm is apparently too low and the improvement is insufficient. A rotating stall occurs at flow coefficient range $\phi < 0.3$ and the reverse flow due to the stall cell overflows the separator passage causing a swirl in the regular passage to the rotor. Installation of a blade separator of 10 mm high in addition to this air-separator improves the characteristics in the range $0.1 < \phi < 0.2$. In this range of flow rate, the reverse flow from the rotor is fully absorbed in the air-separator and the blade separator. Thus, there exists a minimum value in the height of an air-separator passage, and the addition of a blade separator is useful when a sufficient height is unable to take in the air-separator passage.

3.4 Effect of Flow Resistance in Separator Passage. The effect of l_b was investigated in [4] for the case of the setting angle $\beta_1 = 33.5$ deg. In the case when β_1 is much larger and the

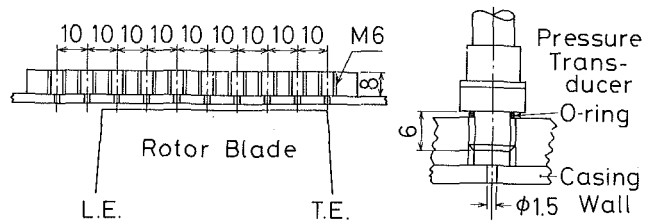


Fig. 8 Pressure taps on the casing wall

area of the open part of blade tip is wide, it is supposed that the flow rate in the separator passage is large and the flow resistance there is an important factor for the effectiveness of the separator. Figure 7 shows the result when the area of the opening of the upstream end of the separator passage is decreased to a half of the original one. Below the flow rate of the maximum head, the reverse flow from the rotor overflows to the regular passage to the rotor and intermittent rotating stalls occur deteriorating the effectiveness of the air-separator.

3.5 Pressure Distribution on Casing Wall. Rotating stalls can be prevented by partly bleeding the fluid near the blade tip as mentioned above. There is little experimental evidence that explains why the bleeding is necessary. Furthermore, the flow near the blade tip is supposed to vary from one fan to another according to its build. To provide such data for the present test fan, the pressure distributions at the rotor tip were measured at eight different axial locations shown in Fig. 8, and the flow near the tip was investigated using the normal casing for the case that a rotating stall occurs. The pressure on the casing wall was measured using a pressure transducer which had a flat characteristics below 2 kHz in the setting condition shown in Fig. 8. A hundred sets of data were phase-locked averaged to obtain an averaged pressure. Measurements were done at two different flow rates indicated by points A and B in Fig. 2. Point A is at a flow rate which still has a margin till stall, while point B is at a flow rate near the onset of stall.

Figures 9 and 10 show the pressure distributions at $\phi = 0.39$ (point A) and $\phi = 0.33$ (point B), respectively. The pressure is nondimensionalized as

$$c_p = (p - p_a) / (\rho U_t^2 / 2)$$

where p is the phase-locked average value of pressure, p_a , the atmospheric pressure. Figures 9 and 10 (a) show the contours of c_p and Figs. 9 and 10 (b), the pressure fluctuation intensity which is defined as

$$\sigma = [\Sigma (p - p_a)^2 / (\rho U_t^2 / 2) / N]^{1/2}$$

Figures in Figs. 9 and 10 (b) are the values of 100σ .

At both flow rates, a deep valley of low pressure is observed as the blade passes. Besides this deep valley, another valley is observed, which is indicated by a chain line in Figs. 9 and 10 (a). This valley is supposed to be the trace of a vortex core of the leakage flow through the tip clearance.

At $\phi = 0.39$, the vortex line can be seen as far as near the exit of the rotor blade row. The weak attenuation of the vortex suggests that there hardly exists complicated vortex flow other than this leakage vortex. This vortex is supposed to correspond to the part of low relative velocity in the vicinity of the casing wall in Fig. 7(a) in [5], which shows the relative velocity distribution behind the rotor.

At $\phi = 0.33$, the circumferential movement of the vortex is more rapid and the attenuation is quicker. The part of low pressure disappears in the middle of the inter-blade passage, and the fluid of low relative velocity which the leakage vortex makes, extends toward the pressure side of the blade before it reaches the exit of the rotor blade row.

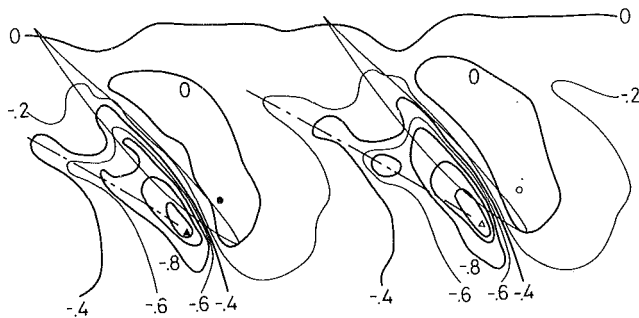


Fig. 9(a) Contours of averaged pressure (\circ ; 0.13, \bullet ; 0.12, Δ ; -1.84, Δ ; -1.77)

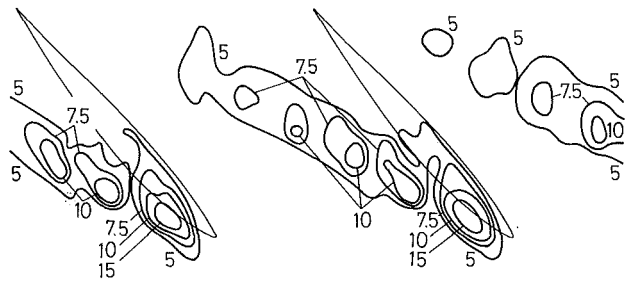


Fig. 9(b) Contours of pressure fluctuations

Fig. 9 Pressure distributions in the blade passage measured at the casing wall ($\phi = 0.39$). (Uncertainty in $c_p = \pm 0.01$, in $100\sigma = \pm 0.5$)

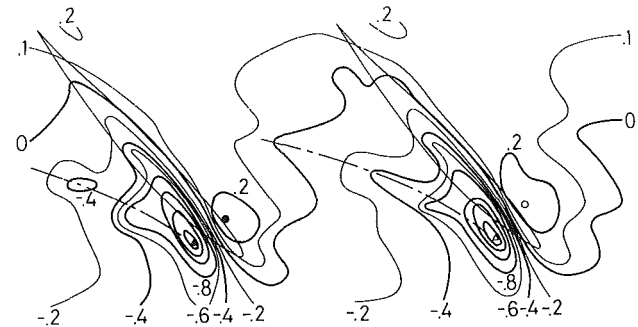


Fig. 10(a) Contours of averaged pressure (\circ ; 0.28, \bullet ; 0.28, Δ ; -2.17, Δ ; -2.18)

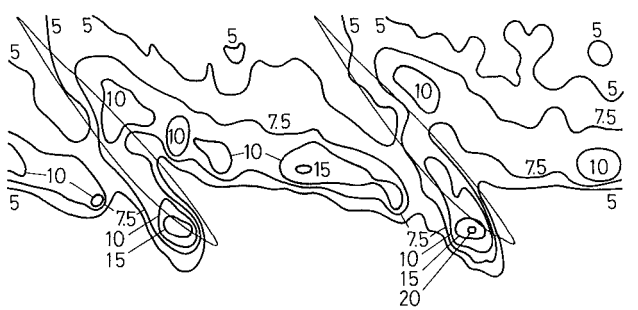


Fig. 10(b) Contours of pressure fluctuations

Fig. 10 Pressure distribution in the blade passage measured at the casing wall ($\phi = 0.33$). (Uncertainty in $c_p = \pm 0.01$, in $100\sigma = \pm 0.5$)

The distribution of pressure fluctuation in Figs. 9 and 10 (b) shows the trace of the vortex more clearly. At $\phi = 0.39$ where the flow still has a margin till stall, the pressure fluctuation also attenuates toward the downstream direction, and the vortex line fades out without disturbing the rest part of the flow field. At $\phi = 0.33$ of near stall point, although the pressure depression due to the vortex line vanishes also in the middle of the inter-blade passage, a band of strong fluctuation which the vortex line makes extends toward the pressure side of the blade and spreads over the region near the trailing edge. The pressure fluctuation does not vanish even near the downstream end of the vortex line, which suggests that the disturbances caused by the leakage vortex spread without attenuating. As mentioned before, the fluid which accompanies the leakage vortex has low relative velocities, and the highly turbulent fluid which accumulates toward the pressure side of the blade after the leakage vortex has faded out, is also considered as a part of low relative velocity fluid (low in the sense of chord-wise direction). Accordingly, the band of strong pressure fluctuation in Fig. 10(b) can be considered to act as a blockage in the flow field. It could be, therefore, concluded that the requirement for bleeding this highly fluctuating fluid is what necessitates the opening of a part of blade tip in an air-separator.

In the case of the present test fan, the leakage vortex is supposed to be the main cause of the unfavorable flow field in the tip region. But more experiments should be carried out for different machines such as axial-flow compressors in which the tip clearance is much smaller.

4 Concluding Remarks

An air-separator is an equipment to bleed a part of the fluid near the blade tip and return it to the regular flow passage to the rotor through the separator passage. The unstable characteristics of an axial flow fan can be almost perfectly

resolved by an air-separator which is designed to keep the amount of bleeding flow larger than a certain critical value.

The air-separator is useful even for a rotor which originally accompanies a heavy rotating stall. Since the axial length of the present air-separator is shorter than that of a set of rotor and stator, it can be applied to an arbitrary stage of a multistage machine.

The working mechanism of an air-separator has been discussed by measuring the radial velocity distribution of the bleeding flow. Furthermore, the reason to necessitate the bleeding, hence the cause of the onset of rotating stall, has been considered on the basis of the measured results of the pressure distribution on the casing wall at flow rates near the stall onset using a normal casing.

References

- 1 Ushakov, K. A., "Removal of Unstable Operation of Axial Flow Fan by Means of Separators," *Industrial Aerodynamics*, Vol. 24, 1962, p. 9.
- 2 Tanaka, S., and Murata, S., "On the Partial Flow Rate Performance of Axial-Flow Compressor and Rotating Stall (3rd Report, On the Devices for Improving the Unstable Performance and Stall Condition)," *Bull. JSME*, Vol. 18, No. 125, 1975, pp. 1277-1284.
- 3 Ivanov, S. G., U.S. Patent 3189260, 1965.
- 4 Miyake, Y., Nishikawa, Y., Noji, I., and Murata, S., "The Performance Characteristics of an Air-Separator of an Axial Flow Fan," *Bull. JSME*, Vol. 28, No. 242, 1984, pp. 1659-1666.
- 5 Miyake, Y., Inaba, T., Nishikawa, Y., Noji, I., and Kato, T., "A Study on the Flow within the Flow Passage of an Axial Flow Fan Equipped with Air-Separator," *Bull. JSME*, Vol. 29, No. 256, 1986, pp. 3394-3401.
- 6 Miyake, Y., Inaba, T., and Kato, T., "Three-Dimensional Measurements in an Axial-Flow Fan Using Hot-Wire Anemometers," *Proc. 2nd Osaka Symp. Flow Measuring-Techniques*, 1984, pp. 257-263.

Uncertainty

Unless otherwise specified in each figure caption, the uncertainty in lengths = ± 0.5 mm, in $\phi = \pm 0.005$, in $\psi_t = \pm 0.01$.

Calculation of Three-Dimensional Boundary Layers on Rotating Turbine Blades

O. L. Anderson

United Technologies Research Center,
East Hartford, Conn. 06108

An assessment has been made of the applicability of a three-dimensional boundary-layer analysis to the calculation of heat transfer and streamline flow patterns on the surfaces of both stationary and rotating turbine passages. In support of this effort, an analysis has been developed to calculate a general nonorthogonal surface coordinate system for arbitrary three-dimensional surfaces and also to calculate the boundary-layer edge conditions for compressible flow using the surface Euler equations and experimental pressure distributions. Using available experimental data to calibrate the method, calculations are presented for the endwall, and suction surfaces of a stationary cascade and for the pressure surface of a rotating turbine blade. The results strongly indicate that the three-dimensional boundary-layer analysis can give good predictions of the flow field and heat transfer on the pressure, suction, and endwall surfaces in a gas turbine passage.

Introduction

The prediction of the complete flow field in a turbine passage is an extremely difficult task due to the complex three-dimensional flow pattern which contains separation and attachment lines, a saddle point, and a horseshoe vortex. Whereas, in principle such a problem can be solved using the full Navier-Stokes equations, in reality methods based on a Navier-Stokes solution procedure encounter difficulty in accurately predicting surface quantities, such as heat transfer, due to grid limitations imposed by the speed and size of existing computers. On the other hand, the overall problem is strongly three dimensional and too complex to be analyzed by the current design methods based on inviscid and/or viscous strip theories. Thus there is a strong need to develop improved prediction techniques which are capable of providing a detailed resolution of three-dimensional viscous effects near the surface. A potentially simple and cost effective way to achieve this goal is to use a prediction method based on three-dimensional boundary layer (3-DBL) theory. The major objective of this paper is to assess the applicability of such a 3-DBL approach for the prediction of heat loads, boundary layer growth, pressure losses, and streamline skewing in critical areas of a turbine passage. For this purpose, the three dimensional boundary layer analysis developed by Vatsa [1, 2] and Anderson [3] has been selected to evaluate this approach as a means for calculating the local properties of the flow field.

In this approach zonal concepts are utilized to delineate regions of application of 3-DBL theory—these being the endwall surface, suction surface, and pressure surface of a turbine blade. The zonal concept employed in this paper implies that

there exists a thin region near the surface dominated by wall pressure forces, friction forces, and Coriolis forces so that boundary-layer theory is valid. Accurate solutions should be obtained provided that the proper inflow conditions and boundary layer edge conditions can be specified. This zonal approach requires three separate analyses: 1) an analysis to construct a general nonorthogonal surface coordinate system for twisted turbine blades, 2) an analysis to calculate the boundary layer edge conditions from a known static pressure distribution, and 3) a three-dimensional boundary-layer analysis which predicts the boundary-layer growth with prescribed inflow conditions. A review of the background literature on these three problems is given below.

Howarth [4] derived the three-dimensional boundary-layer equations in a general orthogonal coordinate system. However triply orthogonal coordinate systems are difficult to construct for arbitrary surfaces such as a twisted turbine blade. Squire [5] derived a more general set of boundary layer equations in a restricted nonorthogonal coordinate system. However this set of equations has certain coordinate curvature restrictions which make it difficult to apply in practical cases. If, however, one makes the assumption that the boundary layers are very thin compared to the radius of curvature of the surface, then the problem is greatly simplified. In this situation the third set of surfaces is approximated by the boundary surface and is called a surface coordinate system. In this surface coordinate system, two coordinates lie on the surface and the third is normal to the surface. In addition it should be noted that on the boundary surface, it is difficult to construct two orthogonal families of curves to describe the surface. Thus it is desirable to have a nonorthogonal coordinate system on the surface. The problem then reduces to the mapping of the three dimensional boundary surface to a plane surface to be described by two one parameter families of curves (coordinates). This map-

Contributed by the Fluids Engineering Division for publication in the JOURNAL OF FLUIDS ENGINEERING. Manuscript received by the Fluids Engineering Division February 5, 1986.

ping function has been developed by Gordon and Thiel [6] and the construction of a general nonorthogonal surface coordinate system for arbitrary surfaces is described in this paper. Since turbine blades are rotating, another requirement of the coordinate system is that it should be a rotating coordinate system so that the Coriolis, or apparent forces, appear explicitly in the boundary layer equations. Mager [7] has derived the boundary layer equations in a general orthogonal rotating coordinate system. However, as stated earlier, a nonorthogonal surface coordinate system is more useful. Vatsa [1, 2] has derived a set of boundary-layer equations in a nonorthogonal rotating surface coordinate system which meets all these requirements and therefore this analysis has been used to make the assessment presented in this paper.

The solution of the boundary-layer equations requires specification of the boundary layer edge conditions. These conditions are the two components of the edge velocity; the edge total enthalpy (rothalpy), and the thermodynamic variables of state. These edge conditions can be obtained directly from experimental data or they can be obtained from a solution of the Euler equations. Measurements of the vector velocity components in a three dimensional flow field are extremely difficult and costly to obtain. Difficulties are also encountered in the use of the Euler equations for the boundary layer edge conditions since these solutions do not produce secondary flows which are generated by viscous shear forces. An alternative approach is to obtain the edge conditions by solving the Euler equations evaluated at the surface (hereafter referred to as surface Euler equations) using a known (experimental) pressure distribution. Since static pressure distributions over the surface are relatively easy to obtain, this method is more straightforward and avoids the problems mentioned above. This method was outlined by Cebeci [8] for application to aircraft wings. Gleyzes and Cousteix [9] developed a similar method for incompressible flow over fusiform bodies. This paper extends this method to the prediction of the boundary layer edge velocities and thermodynamic quantities for compressible flow over general three-dimensional surfaces.

A detailed review of the development of three dimensional boundary layer theory is given by Vatsa [1, 2]. In this paper only a brief outline of the methods used by Vatsa shall be given. It has long been recognized that turbulent boundary-layer growth is governed by two length scales that have different properties. Near the wall the turbulence is affected by the presence of the wall and the inner length scale reflects this property of the turbulence. This flow is described by the well known law of the wall. Far from the wall, the turbulence is wakelike in behavior and an outer layer length scale describes the turbulence properties. For two dimensional laminar boundary layers, the Levy-Lees transformation, such as that used by Blottner [10], attempts to capture the growth of the boundary layer and thereby significantly simplifying the analysis. For turbulent boundary layers, Werle and Verdon [11] have generalized this concept by replacing the molecular

edge viscosity with an effective turbulent viscosity. Vatsa [1, 2] has generalized these concepts to three dimensional turbulent boundary layers and has successfully obtained solutions to a number of problems.

This paper presents an assessment of the applicability of three-dimensional boundary-layer theory to the calculation of heat transfer and streamline flow patterns on both stationary and rotating turbine passages. A method for calculating a general nonorthogonal surface coordinate system for arbitrary surfaces and for calculating boundary-layer edge conditions using the surface Euler equations and experimental surface pressure distributions is presented. Solutions for the three-dimensional boundary-layer flow over the endwall and suction surface of a stationary turbine cascade and for the pressure surface of a rotating turbine blade are presented and evaluated with experimental data.

Analysis

Surface Coordinate System. The three-dimensional boundary-layer equations are written in a surface coordinate system (x_1, x_2, x_3) in which x_1 and x_2 lie on the surface and x_3 is orthogonal to (x_1, x_2) and hence normal to the surface. The coordinate x_1 is generally in the streamwise direction and x_2 is generally in the crossflow direction. If the coordinates of the surface are written in Cartesian coordinates (y_1, y_2, y_3) , and the transformation

$$y_i = y_i(x_j) \quad (1)$$

is known, where the Jacobian

$$J = \left| \frac{\partial y_i}{\partial x_j} \right| \neq 0 \quad (2)$$

then the components of the covariant metric tensor are given by Warsi [12]

$$g_{ij} = \frac{\partial y_k}{\partial x_i} \frac{\partial y_k}{\partial x_j} \quad (3)$$

For the surface coordinates defined above, equation (3) reduces to

$$g_{11} = \left(\frac{\partial y_1}{\partial x_1} \right)^2 + \left(\frac{\partial y_2}{\partial x_1} \right)^2 + \left(\frac{\partial y_3}{\partial x_1} \right)^2 \quad (4)$$

$$g_{12} = \frac{\partial y_1}{\partial x_1} \frac{\partial y_1}{\partial x_2} + \frac{\partial y_2}{\partial x_1} \frac{\partial y_2}{\partial x_2} + \frac{\partial y_3}{\partial x_1} \frac{\partial y_3}{\partial x_2} \quad (5)$$

$$g_{13} = 0 \quad (6)$$

$$g_{21} = g_{12} \quad (7)$$

$$g_{22} = \left(\frac{\partial y_1}{\partial x_2} \right)^2 + \left(\frac{\partial y_2}{\partial x_2} \right)^2 + \left(\frac{\partial y_3}{\partial x_2} \right)^2 \quad (8)$$

$$g_{23} = 0 \quad (9)$$

$$g_{31} = 0 \quad (10)$$

Nomenclature

c_p = specific heat	k = thermal conductivity	γ_{ij} = direction cosines
C_p = pressure coefficient	\mathbf{n}_i = unit vectors surface coordinates	μ = molecular viscosity
\mathbf{e}_i = unit vectors Cartesian coordinates	p = static pressure	ρ = density
g_{ij} = covariant metric tensor components	\dot{q} = heat flux	τ_{ij} = stress
h_i = metric scale coefficients	S_1 = Stanton number	ω = rotor speed
H_i = total enthalpy	T = temperature	
I = rothalpy	u_i = velocity components	Subscripts
	v_B = rotor velocity	1,2 = streamwise, crossflow direction
	x_i = surface coordinates	e = boundary-layer edge
	y_i = Cartesian coordinates	

$$g_{32} = 0 \quad (11)$$

$$g_{33} = 1 \quad (12)$$

The determinant of the metric tensor is given by

$$|g| = g_{11}g_{22} - g_{12}^2 \quad (13)$$

and the metric scale coefficients are

$$h_1 = \sqrt{g_{11}} \quad (14)$$

$$h_2 = \sqrt{g_{22}} \quad (15)$$

$$h_3 = 1 \quad (16)$$

For surface coordinates, equation (1) takes the special form as shown by Anderson [3].

$$y_1 = y_1(x_1, x_2) \quad (17)$$

$$y_2 = y_2(x_1, x_2) \quad (18)$$

$$y_3 = y_3[y_1(x_1, x_2), y_2(x_1, x_2)] \quad (19)$$

It is noted that if the transformations of equations (17) and (18) are known, then the equation of the surface in the physical coordinates is known in terms of the computational coordinates by direct substitution via equation (19). The task then is to determine the transformations given by equations (17) and (18).

For a computational domain given by

$$\begin{aligned} 0.0 \leq x_1 \leq 1.0 \\ 0.0 \leq x_2 \leq 1.0 \end{aligned} \quad (20)$$

Gordon and Thiel [6], have developed a transfinite mapping for all interior points in the computational domain in terms of the boundary which is given by

$$\begin{aligned} y_i(x_1, x_2) = & (1-x_1)y_i(0, x_2) + x_1y_i(1, x_2) \\ & + (1-x_2)y_i(x_1, 0) + x_2y_i(x_1, 1) \\ & - (1-x_1)(1-x_2)y_i(0, 0) - (1-x_1)x_2y_i(0, 1) \\ & - x_1(1-x_2)y_i(1, 0) - x_1x_2y_i(1, 1) \end{aligned} \quad (21)$$

where $i=1, 2$. The boundary curves can easily be written in parametric form. Thus as an example (see reference [3]) $y_1(0, x_2)$, $y_2(0, x_2)$ may be written in parametric form for N boundary points in the following manner

$$\begin{aligned} y_1(0, x_2) &= y_1(I) \\ y_2(0, x_2) &= y_2(I) \\ x_2(I) &= (I-1)/(N-1) \end{aligned} \quad (22)$$

With all boundaries known in parametric form with either x_1 or x_2 as the appropriate variable, equations (21) provide the suitable transformations for equations (17) and (18) and hence equation (19) can be determined.

In addition to the metric tensor components g_{ij} , the boundary-layer equations require the components of the coordinate rotation vector ω . These components can be obtained using the direction cosines which have been derived by Anderson [3] from the unit vectors and are given by

$$\begin{aligned} \mathbf{n}_1 = & \frac{\mathbf{e}_1}{h_1} \frac{\partial y_1}{\partial x_1} + \frac{\mathbf{e}_2}{h_1} \frac{\partial y_2}{\partial x_1} \\ & + \frac{\mathbf{e}_3}{h_1} \left[\frac{\partial y_3}{\partial y_1} \frac{\partial y_1}{\partial x_1} + \frac{\partial y_3}{\partial y_2} \frac{\partial y_2}{\partial x_1} \right] \end{aligned} \quad (23)$$

$$\begin{aligned} \mathbf{n}_2 = & \frac{\mathbf{e}_1}{h_2} \frac{\partial y_1}{\partial x_2} + \frac{\mathbf{e}_2}{h_2} \frac{\partial y_2}{\partial x_2} \\ & + \frac{\mathbf{e}_3}{h_2} \left[\frac{\partial y_3}{\partial y_1} \frac{\partial y_1}{\partial x_2} + \frac{\partial y_3}{\partial y_2} \frac{\partial y_2}{\partial x_2} \right] \end{aligned}$$

$$\mathbf{n}_3 = \mathbf{n}_1 \times \mathbf{n}_2 / |\mathbf{n}_1 \times \mathbf{n}_2|$$

$$\gamma_{ij} = \mathbf{n}_i \cdot \mathbf{e}_j \quad (24)$$

Since the coordinates of the surface are known only in terms of numerical data, the boundary curves and their first and second derivatives are obtained using four point Lagrangian interpolation. Interpolation and differentiations of equation (19) is obtained using the surface spline developed by McCartin [13] and Spath [14].

Boundary Layer Analysis. A detailed review of the development of three-dimensional boundary layer theory is given by Vatsa [1, 2]. Details of the derivation of these equations are given by Vatsa [2] and Anderson [3]. These boundary-layer equations are derived in a nonorthogonal rotating coordinate system and include the Coriolis forces, complete energy equation, and the Reynolds stress terms. Thus these equations are valid for compressible turbulent flow on rotating turbine blades.

Continuity Equation

$$\frac{\partial}{\partial x_1} \left(\frac{\sqrt{g}}{h_1} \rho u_1 \right) + \frac{\partial}{\partial x_2} \left(\frac{\sqrt{g}}{h_2} \rho u_2 \right) + \frac{\partial}{\partial x_3} (\sqrt{g} \rho u_3) = 0 \quad (25)$$

x_1 Momentum Equation

$$\begin{aligned} & \frac{u_1}{h_1} \frac{\partial u_1}{\partial x_1} + \frac{u_2}{h_2} \frac{\partial u_1}{\partial x_2} + u_3 \frac{\partial u_1}{\partial x_3} \\ & + u_1 u_1 \left\{ \frac{g_{12}}{g} \frac{g_{12}}{h_1^2} \frac{\partial h_1}{\partial x_1} + \frac{\partial h_1}{\partial x_2} - \frac{1}{h_1} \frac{\partial g_{12}}{\partial x_1} \right\} \\ & + u_1 u_2 \frac{1}{g} \left\{ h_1 h_2 \left[1 + \left(\frac{g_{12}}{h_1 h_2} \right)^2 \frac{\partial h_1}{\partial x_2} \right] \right. \\ & \left. - 2g_{12} \frac{\partial h_2}{\partial x_1} \right\} \\ & + u_2 u_2 \frac{h_1}{g} \left\{ \frac{\partial g_{12}}{\partial x_2} - h_2 \frac{\partial h_2}{\partial x_1} - \frac{g_{12}}{h_2} \frac{\partial h_2}{\partial x_2} \right\} \\ & - 2 \frac{h_1 h_2}{\sqrt{g}} \omega_3 u_2 - 2 \frac{g_{12}}{\sqrt{g}} \omega_3 u_1 \\ & - \omega^2 r \frac{h_1 h_2^2}{g} \frac{\partial r}{\partial x_1} + \omega^2 r \frac{h_1 g_{12}}{g} \frac{\partial r}{\partial x_2} \\ & + \frac{h_1 h_2^2}{\rho g} \frac{\partial p}{\partial x_1} - \frac{h_1 g_{12}}{\rho g} \frac{\partial p}{\partial x_2} \\ & = \frac{1}{\rho} \frac{\partial}{\partial x_3} \left\{ \mu \frac{\partial u_1}{\partial x_3} - \rho \overline{u'_1 u'_3} \right\} \end{aligned} \quad (26)$$

x_2 Momentum Equation

$$\begin{aligned} & \frac{u_1}{h_1} \frac{\partial u_2}{\partial x_1} + \frac{u_2}{h_2} \frac{\partial u_2}{\partial x_2} + u_3 \frac{\partial u_2}{\partial x_3} \\ & + u_1 u_1 \frac{h_2}{g} \left\{ \frac{\partial g_{12}}{\partial x_1} - h_1 \frac{\partial h_1}{\partial x_2} - \frac{g_{12}}{h_1} \frac{\partial h_1}{\partial x_1} \right\} \\ & + \frac{u_1 u_2}{g} \left\{ h_1 h_2 \left[1 + \left(\frac{g_{12}}{h_1 h_2} \right)^2 \right] \frac{\partial h_2}{\partial x_1} - 2g_{12} \frac{\partial h_1}{\partial x_2} \right\} \end{aligned}$$

$$\begin{aligned}
& + u_2 u_2 \frac{g_{12}}{g} \frac{g_{12}}{h_2 h_2} \frac{\partial h_2}{\partial x_2} - \frac{1}{h_2} \frac{\partial g_{12}}{\partial x_2} + \frac{\partial h_2}{\partial x_1} \\
& + 2 \frac{g_{12}}{\sqrt{g}} \omega_3 u_2 + 2 \frac{h_1 h_2}{\sqrt{g}} \omega_3 u_1 \\
& + \omega^2 r \frac{h_2 g_{12}}{g} \frac{\partial r}{\partial x_1} - \omega^2 r \frac{h_1^2 h_2}{g} \frac{\partial r}{\partial x_2} \\
& - \frac{h_2 g_{12}}{\rho g} \frac{\partial p}{\partial x_1} + \frac{h_1^2 h_2}{\rho g} \frac{\partial p}{\partial x_2} \\
& = \frac{1}{\rho} \frac{\partial}{\partial x_3} \left\{ \mu \frac{\partial u_2}{\partial x_3} - \rho \overline{u_2' u_3'} \right\} \quad (27)
\end{aligned}$$

Energy Equation

$$\begin{aligned}
& \frac{u_1}{h_1} \frac{\partial H_t}{\partial x_1} + \frac{u_2}{h_2} \frac{\partial H_t}{\partial x_2} + u_3 \frac{\partial H_t}{\partial x_3} \\
& = \frac{1}{\rho} \frac{\partial}{\partial x_3} \left\{ \lambda \frac{\partial T}{\partial x_3} - \rho \overline{u_3' h_t'} + \mu \frac{\partial}{\partial x_3} \left(\frac{u_t'^2}{2} \right) \right\} \\
& + \frac{u_1}{2h_1} \frac{\partial}{\partial x_1} (\omega^2 r^2) + \frac{u_2}{2h_2} \frac{\partial}{\partial x_2} (\omega^2 r^2) \\
& + \frac{u_2}{2} \frac{\partial}{\partial x_3} (\omega^2 r^2) \quad (28)
\end{aligned}$$

In addition to the equations of motion, we have additional relations which are given below.

Equation of State

$$p = \rho R T \quad (29)$$

Stress/Strain Heat Flux Relations

$$\tau_{13} = \mu \frac{\partial u_1}{\partial x_3} - \rho \overline{u_1' u_3'} = (\mu + \epsilon_1) \frac{\partial u_1}{\partial x_3} \quad (30)$$

$$\tau_{23} = \mu \frac{\partial u_2}{\partial x_3} - \rho \overline{u_2' u_3'} = (\mu + \epsilon_2) \frac{\partial u_2}{\partial x_3} \quad (31)$$

$$\dot{q}_T = \lambda \frac{\partial T}{\partial x_3} - \rho \overline{u_3' H_t'} = \left(\frac{\mu}{Pr} + \frac{\epsilon_H}{Pr_t} \right) \frac{\partial H_t}{\partial x_3} - \frac{\mu}{Pr} \frac{\partial}{\partial x_3} \left(\frac{u_t'^2}{2} \right) \quad (32)$$

where ϵ_1 and ϵ_2 are the nonisotropic components of the eddy viscosity, ϵ_H is the eddy conductivity, and the turbulent Prandtl number is defined by,

$$Pr_t = C_p \epsilon_1 / \epsilon_H \quad (33)$$

Total Velocity

$$u_t'^2 = u_1'^2 + u_2'^2 + 2 u_1 u_2 \frac{g_{12}}{h_1 h_2} \quad (34)$$

where the third term is due to the nonorthogonality of the coordinates.

Total Enthalpy

$$H_t = C_p T + \frac{u_t'^2}{2} \quad (35)$$

Rothalpy

$$I = H_t - \frac{v_B^2}{2} \quad (36)$$

where the rotor speed is given by

$$v_B = r\omega \quad (37)$$

For stationary coordinates, $\omega = 0$ and the rothalpy is identical to the total enthalpy. On a rotating blade, rothalpy is conserved along a streamline. On a stationary blade, total enthalpy is conserved along a streamline. Except for very special cases, it cannot be assumed that the rothalpy is constant over the surface of a rotating blade.

Equations (25) through (32) are transformed to the Levy-Lees variables according to the method of Vatsa [15]. Details of this transformation are given in references [1, 2, and 3].

Properties of Equations. The set of equations derived above consist of four coupled partial differential equations; three of which are second order and one first order. The properties of these equations have been formally examined by Wang [16]. Wang's analysis shows that these equations are parabolic and therefore may be solved by a forward marching algorithm. However it is noted that there exist two sets of characteristics, a set of characteristics which consists of surfaces normal to the wall, and a set of surfaces consisting of the stream surfaces. These stream surfaces imply that the initial conditions for the problem are all the flow properties on a surface not a stream surface. These initial conditions are called inflow conditions because the solution can be obtained only downstream along stream surfaces. Thus, as pointed out by Blottner [17], a unique solution of the three dimensional boundary-layer equations requires specification of the inflow conditions along any inflow surface and specification of boundary conditions similar to those employed for the two dimensional boundary layer equations.

Boundary Conditions. The boundary conditions are the same as those for the two-dimensional boundary layer equations. Those take the form

$$\begin{aligned}
u_1(x_1, x_2, 0) &= 0 \\
u_2(x_1, x_2, 0) &= 0 \\
u_3(x_1, x_2, 0) &= u_w
\end{aligned} \quad (38)$$

where u_w is the surface injection velocity. For the energy equation,

$$T(x_1, x_2, 0) = T_w \quad (39)$$

or

$$\lambda \frac{\partial T}{\partial x_3} = \dot{q}_w$$

At the edge of the boundary layer

$$\begin{aligned}
\lim_{x_3 \rightarrow \infty} u_1 &= u_{1e} \\
\lim_{x_3 \rightarrow \infty} u_2 &= u_{2e} \\
\lim_{x_3 \rightarrow \infty} H_T &= H_{Te}
\end{aligned} \quad (40)$$

Inflow Conditions. The inflow conditions as well as the boundary conditions must be specified. These inflow condi-

tions include $u_1, u_2, P, T, \rho, H_i$ along any inflow plane. These properties may be specified as input data or constructed from analytic relations. An alternative approach is to construct the inflow conditions from degenerate solutions of the partial differential equations. These degenerate solutions are called similarity solutions and are of two types. The first type, called local similarity solutions, are obtained by reducing the partial differential equations in three independent variables to partial differential equations in two independent variables. The second type of degenerate solutions is obtained by reducing the partial differential equations to ordinary differential equations. A third special case also exists for a boundary which is a plane of symmetry for the flow field. In this last case, the plane of symmetry is a characteristic surface and requires special treatment as described by Blottner [18].

Turbulence Model. The turbulence model used to close the set of equations in this paper is that developed by Cebeci and Smith [19] which was developed for two dimensional boundary layers. This model was extended to three dimensional boundary layers, by Vatsa [1], by replacing the streamwise velocity with the total velocity. For transitional flow the forced transition model developed by Dhawan and Narasimha [20] is used.

Finite Difference Equations. The governing equations, described above, are a set of four coupled nonlinear partial differential equations. These equations are reduced to a set of four nonlinear finite difference equations (see reference [2]) and quasi-linearized to form a set of coupled equations which are solved in an iterative fashion with a block factorization algorithm described in detail by Vatsa [2].

Surface Euler Equations. The surface Euler equations can be obtained from the three dimensional boundary layer equations by taking the limit as $x_3 \rightarrow \infty$. Thus at the edge of the boundary layer normal derivatives vanish and the momentum and energy equations are written as follows:

X_1 Momentum

$$\frac{u_{1e}}{h_1} \frac{\partial u_{1e}}{\partial x_1} + \frac{u_{2e}}{h_2} \frac{\partial u_{1e}}{\partial x_2} + a_1 u_{1e}^2 + a_2 u_{1e} u_{2e} + a_3 u_{2e}^2 + C_1 u_{1e} + C_2 u_{2e} + C_3 = a_4 \frac{\partial C_p}{\partial x_1} + a_5 \frac{\partial C_p}{\partial x_2} \quad (41)$$

X_2 Momentum

$$\frac{u_{1e}}{h_1} \frac{\partial u_{2e}}{\partial x_1} + \frac{u_{2e}}{h_2} \frac{\partial u_{2e}}{\partial x_2} + a_6 u_{1e}^2 + a_7 u_{1e} u_{2e} + a_8 u_{2e}^2 + C_4 u_{1e} + C_5 u_{2e} + C_6 = a_9 \frac{\partial C_p}{\partial x_1} + a_{10} \frac{\partial C_p}{\partial x_2} \quad (42)$$

Energy

$$\frac{u_{1e}}{h_1} \frac{\partial I_e}{\partial x_1} + \frac{u_{2e}}{h_2} \frac{\partial I_e}{\partial x_2} = 0 \quad (43)$$

The coefficients in these equations are easily determined from equations (26) and (27).

Solution Algorithm. These equations are hyperbolic equations in which the characteristics are streamlines. Thus initial conditions (u_{1e}, u_{2e}, I_e, P_e) must be specified along the same inflow boundaries as the boundary layer equations. Equations (41), (42), and (43) are differenced in the x_1 and x_2 directions

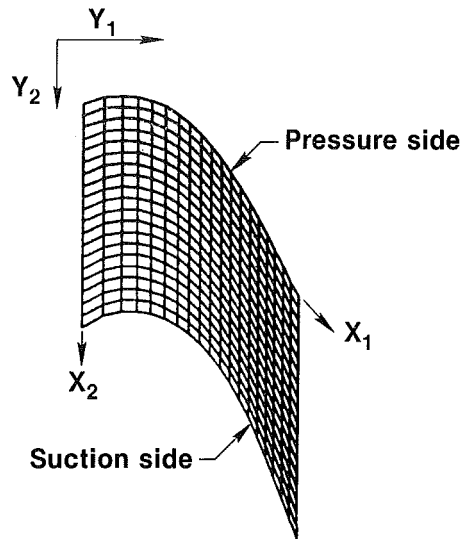


Fig. 1 Coordinate system for cascade endwall surface

in the same manner as the boundary-layer equations, (see reference [3]), resulting in a set of coupled quadratic algebraic equations are solved iteratively by successive substitution.

Results and Discussion

Introductory Discussion. In this assessment of the applicability of three dimensional boundary layer theory to predict the flow streamlines and heat transfer in a gas turbine passage, three regions of the flow field are examined. These regions are the turbine cascade endwall surface, the turbine cascade suction surface, and the rotor pressure surface. The first two cases test the analysis in a stationary coordinate system and the third in a rotating coordinate system. Experimental data for the endwall and suction surfaces were obtained by Graziani et al. [21] in a large gas turbine cascade which simulated a turbine rotor. Detailed wall static pressure distributions, three component velocity traverses, wall heat transfer, and wall limiting streamlines were presented. Data for the rotating blade case were obtained by Dring and Joslyn [22, 23]. These data include wall static pressure distributions and wall limiting streamlines. In addition, radial traverses of the total pressure and flow angle in the stationary reference frame upstream of the rotor were given.

Initial results using this three dimensional boundary layer analysis have been presented by Vatsa [1, 2] wherein the boundary layer edge conditions were obtained directly from the velocity traverses. In the assessment presented in this paper, the boundary layer edge conditions were obtained by integrating the surface Euler equations using the measured static pressure distributions. The overall analytical procedure was the same for all cases. Spline smoothed Cartesian coordinates of the turbine blade surface are used to calculate a coordinate system using the surface coordinate analysis. With the coordinates known, the experimental pressure distribution was used to calculate the boundary-layer edge conditions using the surface Euler analysis. Finally, the three-dimensional boundary-layer equations were solved. The inflow conditions were estimated using the local similarity approximation along all inflow planes that are not characteristic surfaces. Two components of the wall friction coefficient (streamwise and crossflow), heat transfer (Stanton number), and wall limiting streamline skew angles were calculated. The Stanton number was calculated in two steps. In the first step, the adiabatic wall temperature was calculated by assuming zero heat flux at the wall. In the second step, a constant heat flux equal to that ap-

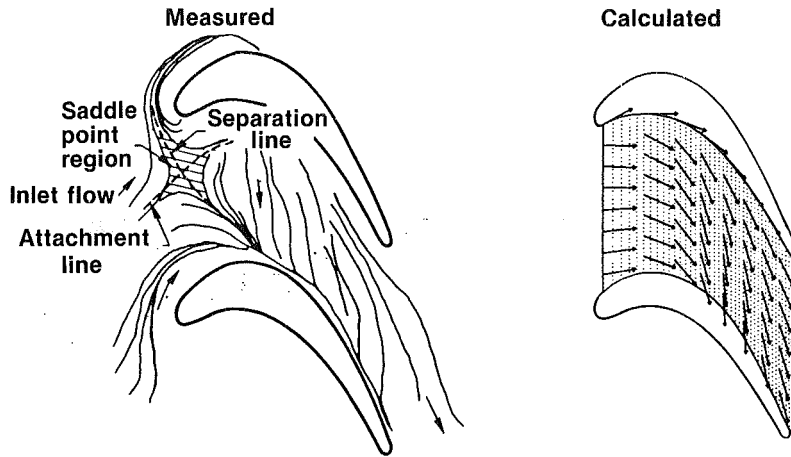


Fig. 2 Comparison of measured and calculated endwall limiting streamlines

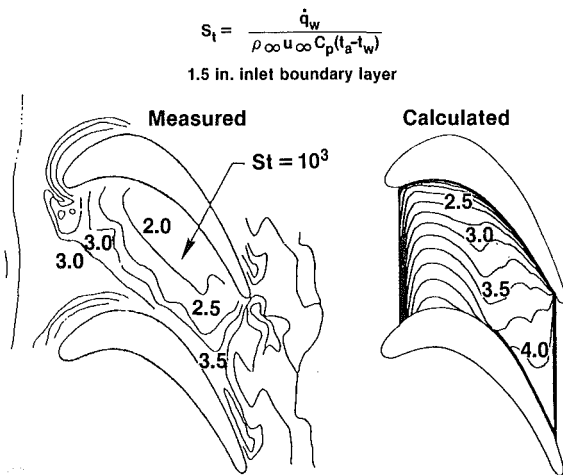


Fig. 3 Comparison of measured and calculated Stanton number distributions for end wall surface

plied experimentally was used, and the wall temperature calculated. Thus the calculation procedure used for determining the Stanton number was the same as that used experimentally in reference [21].

Turbine Cascade Endwall Surface. The endwall surface boundary layer has a large crossflow produced by the strong static pressure gradient from the pressure surface to the suction surface. In addition, this boundary layer has a complex pattern produced by a separation and attachment line and a saddle point. Downstream of this region the boundary layer is rapidly accelerated and the boundary layer growth is more systematic. In this downstream region it may be possible to use three-dimensional boundary-layer theory. The computational domain and skewed coordinate system used for this case is shown in Fig. 1. It consists of a 40 by 40 grid with 100 grid points normal to the surface grid which extends from a point just downstream from the saddle point to just upstream of the trailing edge. The boundary layer edge conditions were calculated using the wall static pressure distribution for the thick boundary layer case presented by Graziani et al. [21]. Along the inflow boundaries for the surface Euler calculation, it was assumed that the boundary layer edge flow was tangent to the x_1 coordinate line so that u_{2e} was assumed zero.

The boundary-layer calculation was started with inflow conditions obtained from local similarity solutions of the bound-

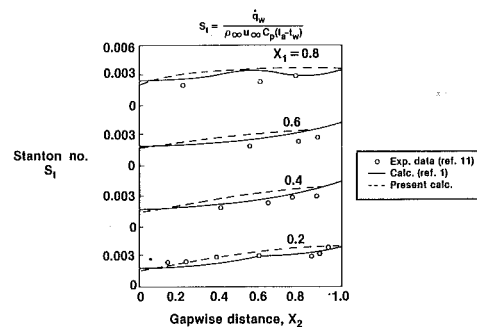


Fig. 4 Comparison of Stanton number distributions on endwall surface

ary layer equations. A comparison of the calculated wall shear vectors with the measured surface streamlines is shown in Fig. 2. As seen in this figure, the flow inclinations are in qualitative agreement with the measured data except in the neighborhood of the saddle point. It is also noted that the calculation presented here using the measured wall static pressures to derive the boundary layer edge conditions shows much better agreement for the predicted flow angle than the calculations of Vatsa [2] which used measured velocities for the edge conditions. This difference may be due to the difficulty in determining the edge of the boundary layer in a three dimensional flow field. Improved results perhaps may be obtained with better definition of the flow conditions along the upstream inflow plane. A comparison of the measured and calculated heat transfer (Stanton number) distributions is shown in Fig. 3 in the form of contour plots. Again qualitative agreement is obtained except in the region of the saddle point. The endwall case presented by Vatsa [1] is the same as that presented here except that the edge velocities were determined directly from three component velocity traverses whereas in the present case the edge velocities were calculated from the wall static pressure distribution using the surface Euler equations. Of interest then is a comparison of the predictions of heat transfer using the two methods. This is shown in Fig. 4 in the form of cross section plots of Stanton number versus spanwise distance at several axial stations. Good qualitative agreement is obtained between the two methods and the data where the difference between the results illustrates the difficulty in obtaining precise boundary layer edge conditions from measured data in a complex three-dimensional flow field.

Turbine Cascade Suction Surface. The suction surface boundary layer of a gas turbine blade develops strong three

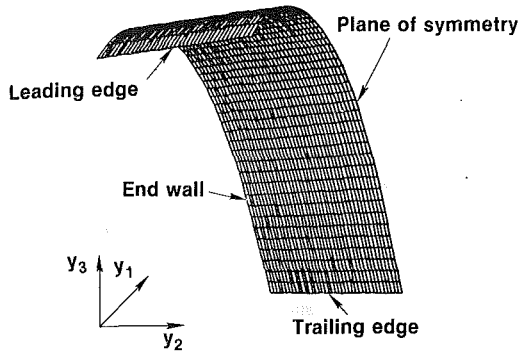


Fig. 5 Coordinate system calculated for cascade suction surface

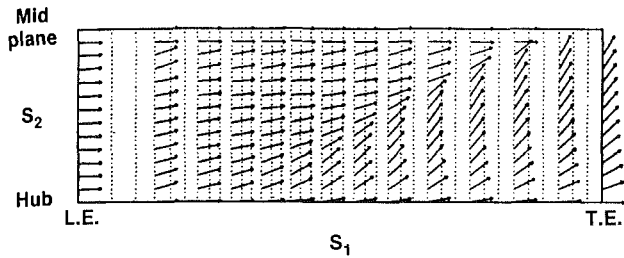


Fig. 6 Boundary layer edge velocity vectors calculated from experimental surface pressure distribution for cascade suction surface

dimensional effects due to the presence of the passage vortex which sweeps the flow up from the end wall surface. Since the boundary layer starts at the stagnation point near the leading edge of the blade, the leading edge inflow conditions are well established. However, the flow from the end wall inflow surface produces a separation line which divides the midspan flow from the end wall flow. This inflow is less well established. The computational domain and coordinate system for this case is shown in Fig. 5. It consists of a 40 by 40 grid with 100 grid points normal to the surface grid extending from just downstream from the leading edge of the blade to just upstream of the trailing edge of the blade and from the end wall to the mid plane or plane of symmetry. The boundary-layer edge conditions were calculated using the surface Euler equations assuming zero crossflow velocities at the leading edge inflow plane. Along the endwall inflow plane, the flow angle and hence crossflow u_{2e} velocity was estimated from the measured surface streamlines given by Graziani et al. [21]. A plot of the calculated edge velocity vectors is shown in Fig. 6. Since the cascade surface is a developable surface, the vector plot is shown using arc length as coordinates. This vector plot clearly shows the effect of the passage vortex on the flow at the boundary layer edge. Since the surface Euler equations are hyperbolic equations with streamlines as the characteristic lines, this case illustrates difficulties which may be encountered as the flow approaches the plane of symmetry. The overall flow direction is from the endwall to the plane of symmetry. Therefore the flow along the plane of symmetry is a result of the calculation, not an input boundary or inflow condition. Along this plane of symmetry the crossflow velocity is zero. Hence the static pressure must be such as to reduce the crossflow velocity to zero at the plane of symmetry. In general, without sufficient data, this may be difficult to achieve as was found in the present case near the blade trailing edge.

The three-dimensional boundary-layer equations were solved using local similarity inflow conditions. Since this is a transitional boundary layer, the beginning and end of transition must be estimated because the present analysis lacks a

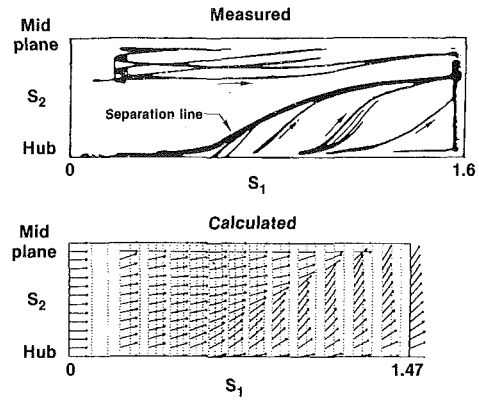


Fig. 7 Measured and calculated wall limiting streamline on cascade suction surface

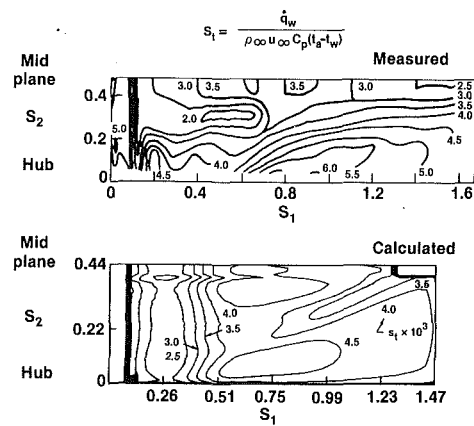


Fig. 8 Measured and calculated Stanton number on cascade suction surface

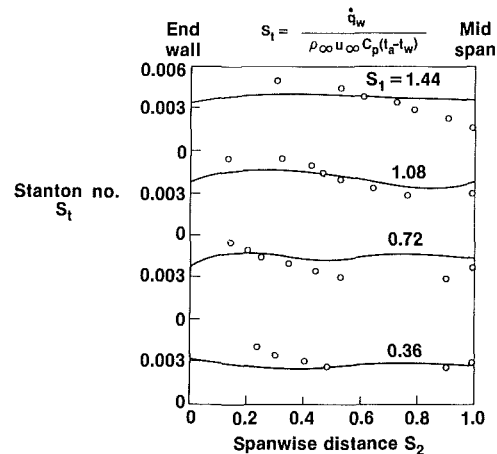


Fig. 9 Comparison of Stanton number distributions on cascade suction surface

transition model for three-dimensional boundary layers. The beginning and end of transition were obtained by calculating the quasi-two dimensional flow along the plane of symmetry using the intermittency function of Dhawan and Narashima [20] and comparing the results with the experimental data for heat transfer. These transition points were then held constant across the span of the blade. A comparison of the calculated wall shear vectors with the measured wall limiting streamlines is shown in Fig. 7. The flow direction at the wall is seen to be

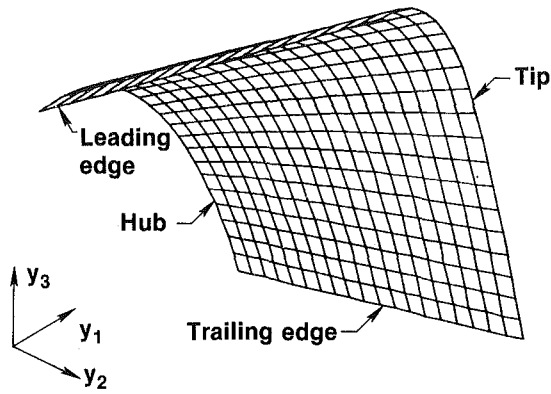


Fig. 10 Coordinate system calculated for turbine rotor

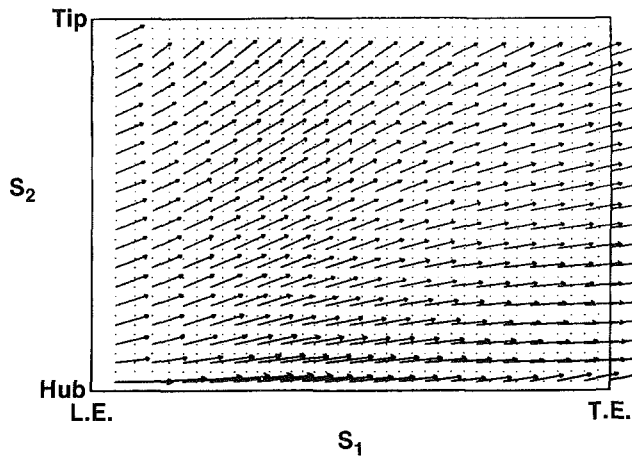


Fig. 11 Boundary layer edge velocity vectors calculated from the experimental pressure distribution for the pressure surface of a rotating turbine blade

calculated quite well and the separation line dividing the leading edge flow from the end wall flow is also predicted quite well. A comparison of the measured and calculated Stanton number distributions is shown in Fig. 8. Again encouraging agreement is obtained both as to magnitude and overall pattern. The calculation, however, appears to underpredict the peak heat transfer which occurs near the endwall inflow plane. Cross section plots of the Stanton number versus spanwise distance at different axial stations are shown in Fig. 9. These plots show that the average level of heat transfer across the span is predicted reasonably well, but that the high and low regions are underpredicted.

Turbine Rotor Pressure Surface. The flow over the rotor pressure surface is strongly influenced by the relative vorticity generated by rotation of coordinates. Thus the boundary-layer flow is driven by two applied forces; the pressure gradient, and the Coriolis force. Because of rotation, the pressure surface sees a strong radial pressure gradient which tends to drive the flow radially inward. The Coriolis force may tend to drive the flow radially inward or outward depending on the sign of the blade rotation vector normal to the surface ω_3 . The balance of these forces tends to drive the flow radially outward near the leading edge and axially near the trailing edge. The computational domain and coordinate grid for this problem is shown in Fig. 10. It consists of a 40 by 40 grid with 100 grid points normal to the surface grid extending from just downstream from the leading edge stagnation line to just upstream of the trailing edge and from the rotor hub to the rotor tip. The boundary-layer edge velocity vectors calculated

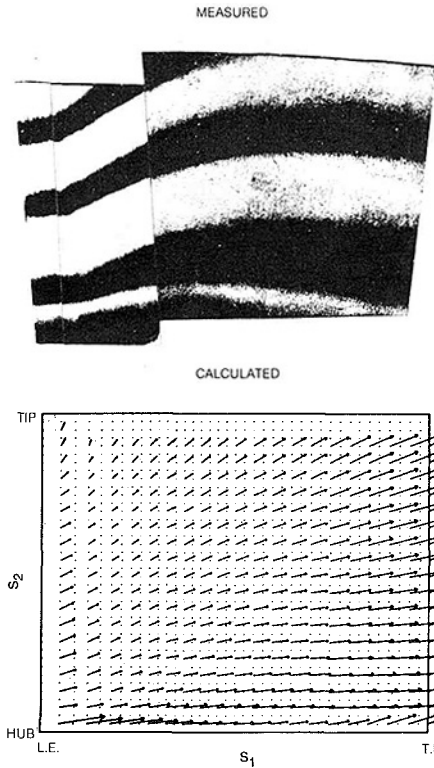


Fig. 12 Measured and calculated limiting streamlines on pressure surface of rotating turbine blade

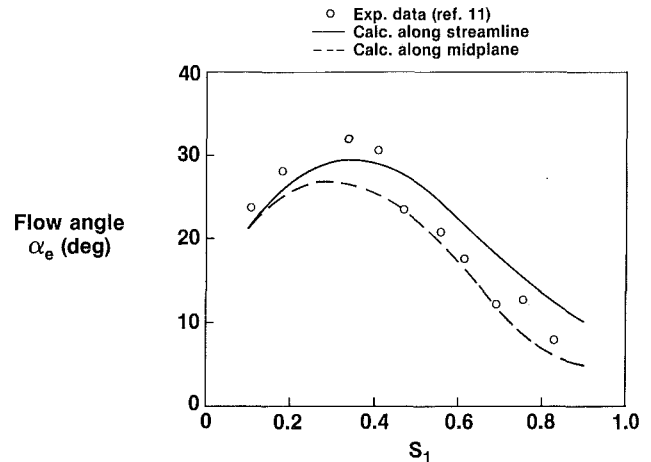


Fig. 13 Calculated and measured flow angle on a rotating rotor blade

from the surface Euler equations are shown in Fig. 11. It was found that no solution of the surface Euler equations exist along the leading edge inflow boundary for the crossflow velocity $U_{2e} = 0.0$. Therefore on both the leading edge and hub inflow boundaries, the crossflow edge velocity was estimated from the surface streamlines given by Dring and Joslyn [22, 23].

The boundary-layer equations were started with local similarity inflow conditions. A comparison of the calculated wall stress vectors with the wall streamlines obtained experimentally using the ammonia-ozalid process is shown in Fig. 12. The calculated vectors clearly show the general overall flow pattern quite well. Calculated flow angles are compared with the flow angles measured from the ozalid paper in Fig. 13. Two curves for surface streamline are shown. The first

curve (solid line) is the calculated flow angle at each point along the calculated streamline which started at the midplane. The second curve (dotted line) is the calculated flow angle along the midplane. A comparison of the edge velocity vectors with the wall vectors indicates that the flow skewing is up to about ten degrees. These figures clearly show that the flow streamlines are predicted reasonably accurately.

Concluding Remarks

An assessment has been made of the applicability of a three dimensional boundary-layer analysis for the calculation of heat transfer and streamline flow patterns on the surfaces of both stationary and rotating turbine passages. On the suction surface of a turbine cascade, the three-dimensional boundary-layer analysis along with the coordinate generator and surface Euler analysis produce predictions of heat transfer and surface streamline patterns which are in reasonably good agreement with available experimental data. Assessment of the three-dimensional boundary layer analysis for the predictions of the flow on a turbine endwall is complicated by the uncertainty in the inflow conditions downstream from the separation and attachment lines. However the results obtained in this study are encouraging as they indicate that the three-dimensional boundary-layer analysis is applicable to the endwall surface as well. On the pressure surface of a rotating turbine blade, prediction of the flow streamlines and flow skewing are in good agreement with available data.

Acknowledgments

This work was supported in part by NASA Lewis Research Center under Contract NAS3-23716.

The author also wishes to acknowledge the contributions of Dr. V. N. Vatsa of NASA Langley Research Center and D. J. E. Carter and B. Caplin of UTRC.

References

- 1 Vatsa, V. N., "A Three-Dimensional Boundary-Layer Analysis Including Heat Transfer and Blade Rotation Effects," Paper presented at the Third Symposium on Numerical and Physical Aspects of Aerodynamic Flows, Long Beach, Calif., Jan. 1985.
- 2 Vatsa, V. N., "A Three Dimensional Boundary Layer Analysis for Turbomachinery Applications," UTRC Report No. 84-44, 1984.
- 3 Anderson, O. L., and Caplin, B., "User's Manual for Three Dimensional Boundary Layer Code," UTRC Report R85-956834-1, Mar. 1985.
- 4 Howarth, L., "The Boundary Layer in Three-dimensional Flow Along a General Three Dimensional Surface," *Phil. Mag. Series 7*, Vol. 42, 1951, pp. 239-243.
- 5 Squire, L. C., "The Three-Dimensional Boundary Layer Equations and Some Power Series Solutions," ARC Tech. Rpt. R&M 3006, 1957.
- 6 Gordon, J. W., and Thiel, L. C., *Transfinite Mappings and Their Application to Grid Generation, Numerical Grid Generation*, F. Thompson Ed., Elsevier Science Publishing Co. Inc., 1982.
- 7 Mager, A., *Three Dimensional Laminar Boundary Layers, High Speed Aerodynamics and Jet Propulsion*, Ed. by F. K. Moore, Vol. IV, Princeton University Press, Princeton, N.J., 1964, pp. 286-394.
- 8 Cebeci, T., Kaups, K., and Ramsey, J. A., "A General Method For Calculating Three Dimensional Compressible Laminar and Turbulent Boundary Layers on Arbitrary Wings," NASA CR-2777, Jan. 1977.
- 9 Gleyzes, C., and Cousteix, J., "Calculation of Streamlines from Wall Pressures on a Fusiform Body," *Rech. Aerospace*, 1984-3.
- 10 Blottner, F. G., "Finite Difference Method of Solution of the Boundary Layer Equations," *IAAA Journal*, Vol. 18, Feb. 1970, pp. 193-205.
- 11 Werle, M. J., and Verdon, J. M., "Viscid/Inviscid Interaction Analysis for Symmetric Trailing Edges," UTRC Report R79-914493-5, Jan. 1980.
- 12 Warsi, Z. U. A., "Tensor and Differential Geometry Applied to Analytic and Numerical Coordinate Generation," Mississippi State University Report MSSU-EIRS-81-1, Dec. 1980.
- 13 McCartin, B. J., "Theory, Computation, and Application of Exponential Splines," Courant Mathematics and Computing Laboratories, Oct. 1981.
- 14 Spath, H., *Spline Algorithms for Curves and Surfaces*, Utilities Mathematica Publishing Co. Inc., Winnipeg, 1974.
- 15 Vatsa, V. N., and Davis, R. T., "The Use of Levy-Lees Variables in 3-D Boundary Layer Flows," NASA CR-112315, Jan. 1973.
- 16 Wang, K. C., "On the Determination of the Zones of Influence and Dependence for the Three-dimensional Boundary Layer Equations," *J. Fluid Mech.*, Vol. 8, 1971, pp. 397-404.

17 Blottner, F. G., "Computational Techniques for Boundary Layers," AGARD Lecture Series 73, presented at VKI, Feb. 1975

18 Blottner, F. G., and Ellis, M. A., "Finite Difference Solution of the Incompressible Three-Dimensional Boundary Layer Equations for a Blunt Body," *Int. J. of Computers and Fluids*, Vol. 1, 1973, pp. 133-158.

19 Cebeci, T., and Smith, A. M. O., *Analysis of Turbulent Boundary Layers*, Academic Press, New York, 1974.

20 Dhawan, S., and Narasimha, R., "Some Properties of Boundary Layer Flow During Transition from Laminar to Turbulent Motion," *J. of Fluid Mechanics*, Vol. 3, 1958, pp. 418-436.

21 Graziani, R. A., Blair, M. F., Taylor, J. R., and Mayle, R. D., "An Experimental Study of Endwall and Airfoil Surface Heat Transfer in a Large Scale Turbine Blade Cascade," *ASME Journal of Engineering for Power*, Vol. 102, No. 2, Apr. 1980, pp. 257-267.

22 Dring, R. P., and Joslyn, H. D., "Measurement of Turbine Rotor Blade Flows," *ASME Journal of Engineering for Power*, Vol. 103, No. 2, Apr. 1981, pp. 400-405.

23 Dring, R. P., and Joslyn, H. D., "The Relative Eddy in Axial Turbine Rotor Passages," *ASME Paper No. GT-22*, 1983.

24 Sharma, O. P., and Graziani, R. A., "Influence of Endwall Flow on Airfoil Suction Surface Midheight Boundary Layer Development in a Turbine Cascade," *ASME Journal of Engineering for Power*, Vol. 105, Jan. 1983, pp. 147-155.

curve (solid line) is the calculated flow angle at each point along the calculated streamline which started at the midplane. The second curve (dotted line) is the calculated flow angle along the midplane. A comparison of the edge velocity vectors with the wall vectors indicates that the flow skewing is up to about ten degrees. These figures clearly show that the flow streamlines are predicted reasonably accurately.

Concluding Remarks

An assessment has been made of the applicability of a three dimensional boundary-layer analysis for the calculation of heat transfer and streamline flow patterns on the surfaces of both stationary and rotating turbine passages. On the suction surface of a turbine cascade, the three-dimensional boundary-layer analysis along with the coordinate generator and surface Euler analysis produce predictions of heat transfer and surface streamline patterns which are in reasonably good agreement with available experimental data. Assessment of the three-dimensional boundary layer analysis for the predictions of the flow on a turbine endwall is complicated by the uncertainty in the inflow conditions downstream from the separation and attachment lines. However the results obtained in this study are encouraging as they indicate that the three-dimensional boundary-layer analysis is applicable to the endwall surface as well. On the pressure surface of a rotating turbine blade, prediction of the flow streamlines and flow skewing are in good agreement with available data.

Acknowledgments

This work was supported in part by NASA Lewis Research Center under Contract NAS3-23716.

The author also wishes to acknowledge the contributions of Dr. V. N. Vatsa of NASA Langley Research Center and D. J. E. Carter and B. Caplin of UTRC.

References

- 1 Vatsa, V. N., "A Three-Dimensional Boundary-Layer Analysis Including Heat Transfer and Blade Rotation Effects," Paper presented at the Third Symposium on Numerical and Physical Aspects of Aerodynamic Flows, Long Beach, Calif., Jan. 1985.
- 2 Vatsa, V. N., "A Three Dimensional Boundary Layer Analysis for Turbomachinery Applications," UTRC Report No. 84-44, 1984.
- 3 Anderson, O. L., and Caplin, B., "User's Manual for Three Dimensional Boundary Layer Code," UTRC Report R85-956834-1, Mar. 1985.
- 4 Howarth, L., "The Boundary Layer in Three-dimensional Flow Along a General Three Dimensional Surface," *Phil. Mag. Series 7*, Vol. 42, 1951, pp. 239-243.
- 5 Squire, L. C., "The Three-Dimensional Boundary Layer Equations and Some Power Series Solutions," ARC Tech. Rpt. R&M 3006, 1957.
- 6 Gordon, J. W., and Thiel, L. C., *Transfinite Mappings and Their Application to Grid Generation, Numerical Grid Generation*, F. Thompson Ed., Elsevier Science Publishing Co. Inc., 1982.
- 7 Mager, A., *Three Dimensional Laminar Boundary Layers, High Speed Aerodynamics and Jet Propulsion*, Ed. by F. K. Moore, Vol. IV, Princeton University Press, Princeton, N.J., 1964, pp. 286-394.
- 8 Cebeci, T., Kaups, K., and Ramsey, J. A., "A General Method For Calculating Three Dimensional Compressible Laminar and Turbulent Boundary Layers on Arbitrary Wings," NASA CR-2777, Jan. 1977.
- 9 Gleyzes, C., and Cousteix, J., "Calculation of Streamlines from Wall Pressures on a Fusiform Body," *Rech. Aerospace*, 1984-3.
- 10 Blottner, F. G., "Finite Difference Method of Solution of the Boundary Layer Equations," *IAAA Journal*, Vol. 18, Feb. 1970, pp. 193-205.
- 11 Werle, M. J., and Verdon, J. M., "Viscid/Inviscid Interaction Analysis for Symmetric Trailing Edges," UTRC Report R79-914493-5, Jan. 1980.
- 12 Warsi, Z. U. A., "Tensor and Differential Geometry Applied to Analytic and Numerical Coordinate Generation," Mississippi State University Report MSSU-EIRS-81-1, Dec. 1980.
- 13 McCartin, B. J., "Theory, Computation, and Application of Exponential Splines," Courant Mathematics and Computing Laboratories, Oct. 1981.
- 14 Spath, H., *Spline Algorithms for Curves and Surfaces*, Utilities Mathematica Publishing Co. Inc., Winnipeg, 1974.
- 15 Vatsa, V. N., and Davis, R. T., "The Use of Levy-Lees Variables in 3-D Boundary Layer Flows," NASA CR-112315, Jan. 1973.
- 16 Wang, K. C., "On the Determination of the Zones of Influence and Dependence for the Three-dimensional Boundary Layer Equations," *J. Fluid Mech.*, Vol. 8, 1971, pp. 397-404.

17 Blottner, F. G., "Computational Techniques for Boundary Layers," AGARD Lecture Series 73, presented at VKI, Feb. 1975

18 Blottner, F. G., and Ellis, M. A., "Finite Difference Solution of the Incompressible Three-Dimensional Boundary Layer Equations for a Blunt Body," *Int. J. of Computers and Fluids*, Vol. 1, 1973, pp. 133-158.

19 Cebeci, T., and Smith, A. M. O., *Analysis of Turbulent Boundary Layers*, Academic Press, New York, 1974.

20 Dhawan, S., and Narasimha, R., "Some Properties of Boundary Layer Flow During Transition from Laminar to Turbulent Motion," *J. of Fluid Mechanics*, Vol. 3, 1958, pp. 418-436.

21 Graziani, R. A., Blair, M. F., Taylor, J. R., and Mayle, R. D., "An Experimental Study of Endwall and Airfoil Surface Heat Transfer in a Large Scale Turbine Blade Cascade," *ASME Journal of Engineering for Power*, Vol. 102, No. 2, Apr. 1980, pp. 257-267.

22 Dring, R. P., and Joslyn, H. D., "Measurement of Turbine Rotor Blade Flows," *ASME Journal of Engineering for Power*, Vol. 103, No. 2, Apr. 1981, pp. 400-405.

23 Dring, R. P., and Joslyn, H. D., "The Relative Eddy in Axial Turbine Rotor Passages," *ASME Paper No. GT-22*, 1983.

24 Sharma, O. P., and Graziani, R. A., "Influence of Endwall Flow on Airfoil Suction Surface Midheight Boundary Layer Development in a Turbine Cascade," *ASME Journal of Engineering for Power*, Vol. 105, Jan. 1983, pp. 147-155.

DISCUSSION

F. G. Blottner¹

As the author points out, there is still a need to investigate the use of three-dimensional boundary layer theory to obtain numerical solutions to viscous flows. Perhaps besides being cost effective, it can also provide an insight into obtaining Navier-Stokes solutions. The author has advanced the techniques used for solving three-dimensional boundary layer flows and has evaluated the numerical predictions by comparison with experimental results. I believe that further work is required to show that the present solution procedure gives reasonable results.

It is not clear if the lack of good agreement with the experimental results is due to poor boundary layer edge conditions or to the turbulence and transition model used. Evaluation of the edge conditions is needed as progress on this part of the problem is easier to obtain. As the author points out, experimental results are insufficient to determine the edge conditions. An accurate numerical solution of the Navier-Stokes equations could be used to evaluate the edge conditions generated from the surface pressure. In addition, the flow field predicted from the three-dimensional boundary layer equations could be evaluated with a comparison to the Navier-Stokes solution.

The usefulness of boundary layer theory for three-dimensional flows is mainly limited by the ability to determine the inviscid edge flow conditions. The author has used experimental surface pressure to solve the Euler equations at the surface and obtain the complete edge flow conditions. The author appears to have developed a practical approach. Although this is useful and valid approach to assess the applicability of the three-dimensional boundary layer theory, it does not provide a truly predictive technique. This limits the usefulness of this approach in the long run.

A surface normal coordinate system with nonorthogonal coordinates on the surface is used in this paper with several references to company reports for further information. This approach is called a locally monocline coordinate system and has been developed in the book by Hirschel and Kordulla. This book might be a more readily available reference.

¹Computational Aerodynamics Division, Sandia National Laboratories, Albuquerque, NM 87185

Additional Reference

Hirschel, E. H., and Kordulla, W., "Shear Flow in Surface-Oriented Coordinates," *Notes on Numerical Fluid Mechanics*, Vol. 4, Friedr. Vieweg & Sohn, Braunschweig, 1981.

Authors' Closure

This author agrees with the main items considered by Dr. Blottner. Calculation of the three dimensional boundary layers on turbine passage walls is hindered by:

- 1) complexity of the flow field
- 2) unsteady flow
- 3) three dimensional transition

Of these problems, the first has been partially resolved when the boundary layer edge conditions are obtained from a solu-

tion of the surface Euler equations using a known static pressure distribution. As to the third problem, no satisfactory transition model is now available since it would require at a minimum a solution of the two equation model of turbulence.

For the long term using three dimensional boundary layer theory to truly predict skin friction and heat transfer, the author has suggested a method of local enhancement (see [1]) where the wall static pressure distribution is obtained on a relatively course mesh using a Navier-Stokes Solver, and the local skin friction and heat transfer is obtained on a refined mesh using the three dimensional boundary layer equations.

Additional Reference

Power, G. D., and Anderson, O. L., "Assessment of a Parabolic Analysis for Axisymmetric Internal Flows in Rocket and Turbomachinery Ducts," AIAA-86-1598, June 1986.

P. J. Roddy

Pratt and Whitney Co.,
West Palm Beach, Fl. 33403

R. Darby

Chemical Engineering Department.

G. L. Morrison

Mechanical Engineering Department.
Mem. ASME

Texas A&M University,
College Station, Texas 77843

P. E. Jenkins

Mechanical Engineering Department,
University of Nebraska,
Lincoln, Neb.,
Fellow ASME

Performance Characteristics of a Multiple-Disk Centrifugal Pump

Introduction

From the initial conceptual design about the turn of the century until the early 1960s, multiple-disk turbomachinery was viewed as a novelty. Since 1960, laminar flow multiple disk pumps, compressors, and turbines have been designed and tested as alternatives to standard turbomachines. Although some studies were conducted in the 1970s on turbulent flow between corotating disks, performance data and analyses on multiple disk turbomachines with turbulent flow are far from complete.

Disk pumps resemble conventional centrifugal pumps, except that the impeller consists of a set of closely spaced parallel smooth disks. The fluid enters through an opening in the center of the disks, which transfer angular momentum (and hence energy) to the fluid by means of shear forces. The advantages which have been claimed for such pumps relative to conventional vaned impeller pumps include greater stability, low sensitivity to cavitation, and the ability to operate with unusual fluids for which conventional pumps are unsuitable, such as highly viscous fluids, two phase gas-liquid mixtures, highly loaded slurries and suspensions, non-Newtonian fluids, etc. Although the efficiency of these pumps with ordinary fluids is less than that of conventional vaned rotor pumps, their ability to operate with unusual fluids for which conventional pumps fail makes them attractive for a variety of special purpose applications. This paper presents an analysis of the performance characteristics of multiple-disk centrifugal pumps operating with Newtonian liquids in the transition and turbulent flow regimes, from both an experimental and analytical point of view. The results are presented in terms of generalized dimensionless (affinity) relationships, which

should permit the prediction of performance of any geometrically similar pump, regardless of size, operating conditions, number of disks, etc., within reasonable limits. Future extension of this work to non-Newtonian fluids is planned.

Background

Several investigators [1-11] have been concerned with the analytical and experimental evaluation of disk pumps or compressors operating under laminar flow conditions since the original patent granted to Tesla [3] in 1913 for the concept of a disk turbine. Rice [4] performed both theoretical and experimental studies of a laminar flow disk pump. His assumption of a constant friction factor over the radius of the disk was shown to be inadequate. Breiter and Pohlhausen [5] analyzed the laminar flow between the disks using the Navier-Stokes equations, and compared their results with measured performance characteristics. A disk turbine configuration with radially inward laminar flow was analyzed by Boyack and Rice [6], and compared favorably with experimental results obtained by Adams and Rice [7] and Lawn and Rice [8]. Crawford [9] utilized numerical finite difference methods to solve the governing laminar flow equations, the results being in agreement with those of Breiter and Pohlhausen [5].

Byrne [10] analytically derived performance curves for laminar flow disk pumps for use in liquid fueled rockets, by expanding the equations of Breiter and Pohlhausen [5]. He concluded that the low flow and high head characteristics of the pumps were excellent for this application. Henry and Rae [11] studied a porous disk pump with low noise characteristics for submarine applications. Euler's equation was used to predict the pressure characteristics of the pump, and the results agreed reasonably well with experimental measurements.

Contributed by the Fluids Engineering Division for publication in the JOURNAL OF FLUIDS ENGINEERING. Manuscript received by the Fluids Engineering Division February 25, 1986.

Hasinger and Kehr [1] analyzed the performance of a laminar flow disk pump assuming a parabolic flow profile between the disks. Their predictions agreed to within 5 percent with the results of Breiter and Pohlhausen [5]. They found the pump operation to be stable, but showed a tendency to trap gas bubbles at low flow rates. Balje [12] applied the Hasinger and Kehr analysis to predict the performance of laminar flow pumps. He found the pumps to have a low sensitivity to cavitation, and recommended that the diffuser design be modified to improve performance because of the low discharge angle from the impeller.

Turbulent air flow between rotating disks was analyzed by Bakke and Kreidth [2]. They assumed the "1/7th power law" for the velocity profile and a constant friction factor based on experimental data, and integrated the momentum equation over the disks. No general correlation between friction factor and flow rate or disk speed was found.

In this paper, we present a general analysis for flow between disks of a disk pump, utilizing an expression for a local friction factor which is valid over the whole range of laminar and turbulent flow. The resulting predicted performance of the impeller is presented in dimensionless form, and illustrates the significant dimensionless groups or parameters which influence the pump performance. Experimental results are presented in terms of these same groups, and compared with the predicted performance characteristics. The results show, in a generalized form, how pump performance depends upon such properties as fluid viscosity, through a Reynolds number, the dimensionless disk spacing, etc.

Experimental Equipment

The pump which was evaluated in this study was a model 403 Discflow pump, provided by Discflow corporation. Figure 1 shows a schematic of the disk pack impeller. The impeller consists of 11 disks, the rear disk being connected to the pump shaft and the other 10 disks being supported by five 6.35 mm (0.25 inch) diameter pins. The disks are 356 mm (14 in.) in

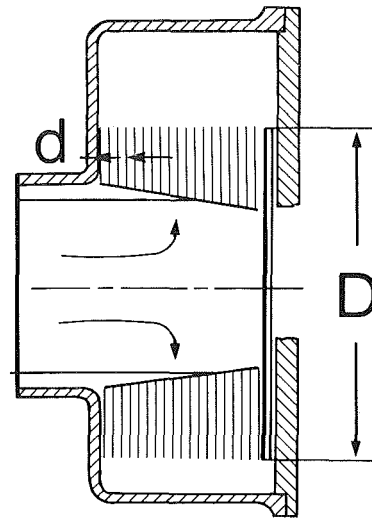


Fig. 1 Schematic of disk pump

diameter, 3.78 mm (0.1488 in.) thick, spaced 3.46 mm (0.136 in.) apart.

The pump was operated in an open loop system, consisting of a 36 m³ (9500 gallon) reservoir tank, a 10 cm (4 in.) suction line, and a 7.6 cm (3 in.) diameter discharge line. Shaft speeds of 890, 1227, 1790, and 2600 rpm were achieved by means of interchangeable belts and pulleys. The drive was a 112 kw (150 hp) electric motor.

Performance data were recorded in accordance with API pump testing standards, using water. Flow rate, suction pressure, discharge pressure, shaft torque, and shaft speed were measured. The pressure taps were 15 cm (6 in) upstream of the pump section and 117 cm (46 in) downstream from the discharge. At least twenty data points were obtained between shut off and maximum flow rate for each of the characteristic

Nomenclature

D = diameter of disks	N_{Ps} = dimensionless shaft power, $P_s/\rho D^5 \Omega^3$	v = local fluid velocity relative to the disk
d = gap spacing between disks	N_Q = dimensionless flow rate, $Q/\Omega D^3$	v_r = radial component of the absolute fluid velocity
e = roughness of disk surface	$N_{Re\omega}$ = rotational Reynolds number, $\Omega D^2/\nu$	v_θ = tangential component of the absolute fluid velocity
f = Fanning friction factor	P_d = power transmitted to fluid by disk	\bar{v} = dimensionless local relative velocity, $v/\Omega D$
g = acceleration due to gravity	P_h = hydraulic power delivered by the pump to the fluid, $\rho g H Q$	\bar{v}_r = dimensionless radial velocity component, $v_r/\Omega D$
H = pump discharge head, relative to suction conditions	P_i = net power acquired by fluid in the disk gap	\bar{v}_θ = dimensionless tangential velocity component, $v_\theta/\Omega D$
k = flow profile constant	P_s = shaft input power, $T_s \Omega$	ρ = fluid density
\dot{m} = mass flow rate between two disks	ΔP = net pump pressure rise, $\rho g H$	η_c = collector or discharge efficiency, P_h/P_i
n = number of gaps in disk pack (1 - no. of disks)	q = volumetric flow rate between two disks	η_d = disk suction efficiency, P_d/P_s
N_d = dimensionless disk spacing, d/D	Q = total volumetric flow rate	η_e = overall pump efficiency, P_h/P_s
N_H = dimensionless pump head, $gH/(D^2 \Omega^2)$	r = radial distance from center of disk	η_i = impeller or disk efficiency, P_i/P_d
N_{pd} = dimensionless power from disk to fluid, $P_d/\rho \Omega^3 D^5$	r_i = disk inlet radius	ν = fluid kinematic viscosity
N_{pf} = dimensionless power lost to friction in disk gap, $P_f/\rho \Omega^3 D^5$	r_o = disk outlet radius	τ_w = wall shear stress, exerted by disk on fluid
N_{ph} = dimensionless hydraulic power, $N_Q N_H$	\bar{r} = dimensionless radius, r/D	$\tau_{w\theta}$ = tangential component of wall shear stress
N_{pi} = dimensionless net power acquired by the fluid in the gap from angular momentum transfer, $P_i/\rho \Omega^3 D^5$	\bar{r}_i = dimensionless inlet radius, r_i/D	Ω = disk angular velocity
	\bar{r}_o = dimensionless outlet radius, r_o/D	
	T_s = shaft torque	

curves. Flow rate was measured by an orifice meter, and was varied by means of a valve in the discharge line. These data were used to determine the net developed pump head (exclusive of kinetic energy and gravity head changes), H , the input shaft power, P_s , and pump efficiency, η_e , for each point, where:

$$P_s = T_s \Omega, \quad \eta_e = \frac{\rho g H Q}{P_s}$$

Dimensional Analysis

A dimensional analysis may be performed on the variables and parameters which influence pump performance to determine the appropriate dimensionless groups which govern the system and which may be used to generalize relationships or to scale data. The parameters which are important in the operation of the disk pump are: D , Ω , Q , ΔP , d , T_s , μ , and ρ . There may also be additional ratios of geometric lengths which are of importance, such as casing diameter, casing to impeller clearance, etc. These eight parameters may be reduced to the following five dimensionless groups:

$$\text{Pressure: } N_p = \frac{\Delta P}{\rho D^2 \Omega^2} \quad \text{Flow: } N_Q = \frac{Q}{\Omega D^3}$$

$$\text{Torque: } N_T = \frac{T_s}{\rho D^5 \Omega^2} \quad \text{Gap: } N_d = \frac{d}{D}$$

$$\text{Reynolds: } N_{Re} = \frac{\Omega D^2}{\nu}$$

Alternate, but equivalent, sets of groups may also be deduced by utilizing various definitions. For example, the developed pump pressure is usually expressed in terms of fluid head, i.e., $\Delta P = \rho g H$. If this is used, the pressure group is replaced by the equivalent head group or coefficient:

$$\text{Head: } N_H = \frac{g H}{D^2 \Omega^2}$$

Also, the shaft torque on the impeller is related to the power delivered to the impeller by $P_s = T_s \Omega$, so that the dimensionless torque may be replaced by the corresponding dimensionless power number:

$$\text{Power: } N_{Ps} = \frac{P_s}{\rho D^5 \Omega^3}$$

Likewise, the hydraulic power delivered to the fluid is given by $P_h = \Delta P Q$, so that a corresponding hydraulic fluid power number may be defined as:

Hydraulic Fluid Power:

$$N_{Ph} = \frac{P_h}{\rho D^5 \Omega^3} = \frac{g H Q}{D^5 \Omega^3} = N_H N_Q$$

Furthermore, the total shaft input power, P_s , and the hydraulic fluid power are related by the definition of the pump efficiency:

$$\text{Efficiency: } \eta_e = \frac{P_h}{P_s} = \frac{N_H N_Q}{N_{Ps}}$$

The most common of these groups, and the ones which we shall use, are: N_H , N_Q , N_d , N_{Re} , N_{Ps} , and η_e . However, only five of these six groups are independent by virtue of the above definition of η_e .

For typical centrifugal pumps operating with low viscosity fluids, N_{Re} is not significant, and N_d does not apply, so that pump performance can be defined by only two functional relations, which are usually expressed as:

$$N_H = f_n(N_Q) \quad \text{and} \quad \eta_e = f_n(N_Q)$$

Although no fluid properties are involved in these groups, the

fluid density is needed to determine P_s from N_{Ps} , which is uniquely determined from known values of η_e , N_H , and N_Q . For the disk pump, however, all five independent groups are significant, and the pump characteristics can be defined by two functions of the form:

$$N_H = f_n(N_Q, N_{Re}, N_d) \quad \text{and} \quad \eta_e = f_n(N_Q, N_{Re}, N_d)$$

Because of a generality of dimensionless quantities, any functional relationship or affinity law for a given pump geometry expressed in terms of these groups should be valid, in principle, for any other geometrically similar pump of any size operating under any conditions within reason.

Theoretical Analysis

A theoretical analysis of the flow between two parallel rotating disks can be performed by applying the conservation of angular momentum principle to a differential element of fluid at a distance r from the center:

$$d(\dot{m} v_\theta r) = 2\tau_{w\theta} r dA = 4\tau_{w\theta} \pi r^2 dr \quad (1)$$

where $\tau_{w\theta}$ is the component of the shear stress exerted by the wall on the fluid in the tangential direction, and v_θ is the fluid tangential velocity. Equation (1) can be expanded and rearranged to give:

$$\frac{dv_\theta}{dr} = \frac{4\pi r \tau_{w\theta}}{\dot{m}} - \frac{v_\theta}{r} \quad (2)$$

The total wall shear stress may be expressed in terms of a local Fanning friction factor, f :

$$\tau_w = \frac{1}{2} \rho f v^2 \quad (3)$$

where v is the resultant local fluid velocity relative to the disk surface, and is related to the local tangential (v_θ) and radial (v_r) velocity components by:

$$v^2 = (v_\theta - \Omega r)^2 + v_r^2 \quad (4)$$

where $v_r = q/(2\pi r d)$ is the radial velocity component and q is the volumetric flow rate through the gap.

The Fanning friction factor may be obtained from the Moody diagram, or equivalently from the Churchill equation (13), which is valid for all values of Reynolds number including laminar as well as turbulent flow:

$$f = 2 \left[\left(\frac{8}{N_{Re}} \right)^{12} - \left(\frac{1}{A+B} \right)^{3/2} \right]^{1/12} \quad (5)$$

where

$$A = \left[2.57 \ln \left(\frac{1}{\left(\frac{7}{N_{Re}} \right)^{0.9} + \frac{0.27e}{D_h}} \right) \right]^{16}$$

$$B = \left(\frac{37,530}{N_{Re}} \right)^{16}$$

Although the Moody diagram (and the Churchill equation) was developed for pipe flows, it may be applied to noncircular conduits such as parallel plates if the pipe diameter in the Reynolds number is replaced by an equivalent diameter, kD_h , where $D_h = 2d$ for parallel plates, i.e.:

$$N_{Re} = \frac{kD_h v}{\nu} = \frac{2v}{\Omega D} k N_d N_{Rew}$$

where

$$N_{Rew} = \frac{\Omega D^2}{\nu}, \quad N_d = \frac{d}{D} \quad (6)$$

The factor e in equation (5) represents the equivalent roughness of the solid surface, which for the stainless steel disks in this study was assumed to be in the range $0 < e/D_h < 0.047$ mm (0.0018 in.). The parameter k is a factor which depends on the shape of the velocity profile, i.e., the geometry and the Reynolds number. For laminar flow between parallel plates, $k = 2/3$ and for turbulent flow it is in the range of $2/3$ to 1 .

The local angle between the tangential shear stress component ($\tau_{w\theta}$) and the total resultant stress (τ_w) is assumed to be the same as that between the velocity components v_θ and v , i.e.,

$$\tau_{w\theta} = \tau_w \left(\frac{\Omega r - v_\theta}{v} \right) \quad (7)$$

Equations (2), (3), and (7) can be combined to give:

$$\frac{dv_\theta}{dr} = \frac{2\pi\rho f r}{\dot{m}} (\Omega r - v_\theta) v - \frac{v_\theta}{r} \quad (8)$$

Equations (4), (5), and (8) can be solved simultaneously to determine local values of v_θ , v , and f at any distance, r , from the center of the disk. This was done numerically using a fourth-order Runge-Kutta technique.

It is informative to write the governing equations in dimensionless form, as follows:

$$\frac{d\tilde{v}_\theta}{d\tilde{r}} = \frac{2\pi\tilde{r}fn}{N_Q} (\tilde{r} - \tilde{v}_\theta) - \frac{\tilde{v}_\theta}{\tilde{r}} \quad (9)$$

$$\tilde{v} = \left[(\tilde{v}_\theta - \tilde{r})^2 + \left(\frac{N_Q}{2\pi\tilde{r}N_d n} \right)^2 \right]^{1/2} \quad (10)$$

and $f = fn(\tilde{v}, N_d, N_{Re_w}, k)$ from equation (5), where

$$\tilde{v}_\theta = v_\theta/\Omega D, \quad \tilde{v} = v/\Omega D, \quad \tilde{r} = r/D.$$

Equations (5), (9), and (10) can be solved simultaneously for f , \tilde{v} , and \tilde{v}_θ . It is evident that these solutions are of the form:

$$\tilde{v}, \tilde{v}_\theta, f = fn(N_Q/n, N_{Re_w}, N_d, k) \quad (11)$$

Power Distribution

The total power delivered to the pump can be divided into a number of components, with respective efficiencies, as illustrated below:

$$P_s \rightarrow \begin{cases} \rightarrow P_d = \eta_d P_s \\ \rightarrow P_b = (1 - \eta_d) P_s \end{cases} \rightarrow \begin{cases} \rightarrow P_i = \eta_i P_d \\ \rightarrow P_f = (1 - \eta_i) P_d \end{cases} \rightarrow \begin{cases} \rightarrow P_h = \eta_c P_i = \eta_e P_s \\ \rightarrow P_c = (1 - \eta_c) P_i \end{cases} \quad (12)$$

Here, P_s is the total input power from the shaft, P_b is the power lost in the bearings and suction, P_d is the total power transmitted to the fluid by the disks, P_f is the power lost by friction in the disk gap resulting from the radial and tangential fluid velocity components relative to the disk, P_i is the "ideal" or net power acquired by the fluid by means of the angular momentum transferred to the fluid in the gap, P_c is the power lost in the casing between the disk and the pump discharge, and P_h is the net pump hydraulic power as previously defined. The corresponding efficiencies η_d , η_i , and η_c represent losses in the bearings and disk suction, friction in the gap, and casing and discharge losses, respectively, and η_e is the overall pump efficiency as previously defined.

The total power transmitted by the disks to the fluid in the gap, P_d , is determined by integrating the product of the tangential component of the local wall stress and the local disk velocity over the total disk surface area:

$$P_d = 2n \int_A \tau_{w\theta} \Omega r dA = 4\pi n \int_{r_i}^{r_o} \tau_{w\theta} \Omega r^2 dr \quad (13)$$

In dimensionless form, this becomes:

$$N_{Pd} = 2\pi n \int_{r_i}^{r_o} f \tilde{v}^2 \tilde{r}^2 d\tilde{r} = \frac{P_d}{\rho \Omega^3 D^5} \quad (14)$$

Similarly, the power acquired by the fluid in the gap due to transfer of angular momentum is given by:

$$P_i = 2n \int_A \tau_{w\theta} v_\theta dA = 2\pi \rho n \int_{r_i}^{r_o} f v_\theta^2 v r dr \quad (15)$$

or:

$$N_{Pi} = \frac{P_i}{\rho \Omega^3 D^5} = 2\pi n \int_{r_i}^{r_o} f \tilde{v}_\theta^2 \tilde{v} \tilde{r} d\tilde{r} \quad (16)$$

where v_θ is the tangential component of the absolute fluid velocity in the gap. Likewise, the power dissipated by friction in the gap is given by

$$P_f = 2n \int_A \tau_{w\theta} (\Omega r - v_\theta) dA = 2\pi \rho n \int_{r_i}^{r_o} f v (\Omega r - v_\theta)^2 r dr \quad (17)$$

which is seen to be simply $P_d - P_i$, as expected. In dimensionless form, this is:

$$N_{Pf} = N_{Pd} - N_{Pi} \quad (18)$$

An overall angular momentum balance applied to the fluid in the gap can also be used to determine N_{Pi} :

$$N_{Pi} = N_Q (\tilde{r}_o \tilde{v}_o - \tilde{r}_i \tilde{v}_i) \quad (19)$$

which may be used as a check on the value of N_{Pi} as determined numerically from equation (15). The quantities \tilde{v}_o and \tilde{v}_i are the absolute tangential velocity components leaving and entering the disk, respectively, as determined from the numerical solution.

Equations (13)–(18) can be used to calculate theoretical values of N_{Pd} , N_{Pf} , and N_{Pi} as a function of the system parameters. Inspection of the equations shows that the relation will be of the form:

$$N_{Pd}, N_{Pf}, N_{Pi} = fn(N_Q, N_d, N_{Re_w}, k, e/d) \quad (20)$$

This result is consistent with the conclusions from dimensional analysis, with the addition of the two geometrical groups k and e/d . These calculated values can be used with the measured values of N_{Ps} and N_{Ph} to determine the suction and discharge power losses, N_{Pb} and N_{Pc} , by difference, and the corresponding efficiencies η_d , η_i , η_c , and η_e . The overall efficiency η_e can thus be decomposed into components representing losses in the suction, the disk gap, and the casing or discharge.

Experimental Results

Performance data were obtained for the eleven disk pump with water at speeds of 890, 1227, 1790, and 2600 rpm. Experimental measurements of performance variables were generally accurate to within ± 2 percent. The resulting uncertainties in the corresponding dimensionless parameters are shown in Table 1. The dimensionless head coefficient, N_H , is shown plotted versus the dimensionless flow coefficient, N_Q , in Fig. 2. Not only do all of the data points for all speeds fall on the same line when plotted in dimensionless terms, but the line is very nearly straight except for the points near shutoff conditions. At shutoff, virtually all of the fluid is being recir-

Table 1 Uncertainty estimates

N_d	$\pm 3 \times 10^{-4}$
N_H	$\pm 4 \times 10^{-4}$
N_{Ps}	$\pm 5 \times 10^{-6}$
N_{Ph}	$\pm 9 \times 10^{-4}$
N_Q	$\pm 8 \times 10^{-5}$
N_{Re}	$\pm 4 \times 10^{-4}$
η_e	$\pm 1 \times 10^{-7}$

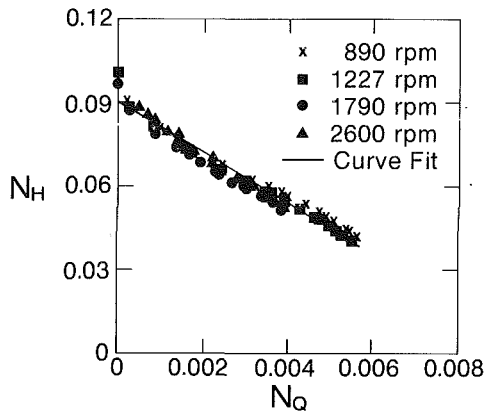


Fig. 2 Dimensionless pump head versus dimensionless flow coefficient

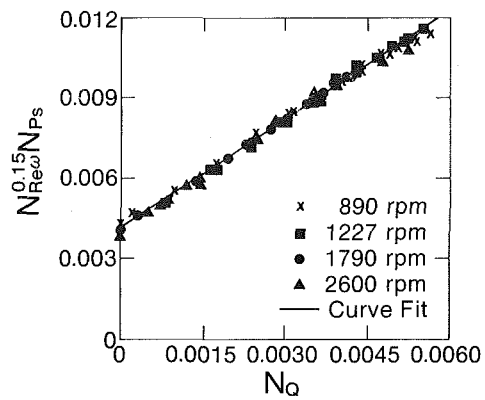


Fig. 5 Influence of rotational Reynolds number on power characteristic. The line represents equation (22).

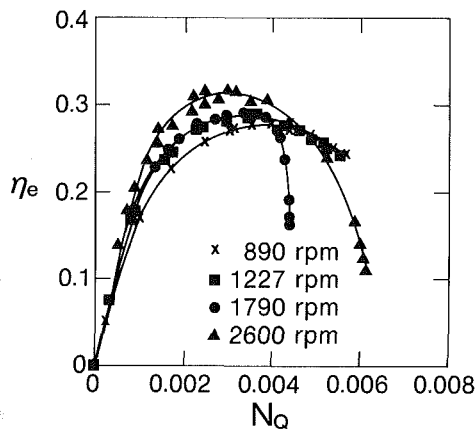


Fig. 3 Overall pump efficiency versus dimensionless flow coefficient

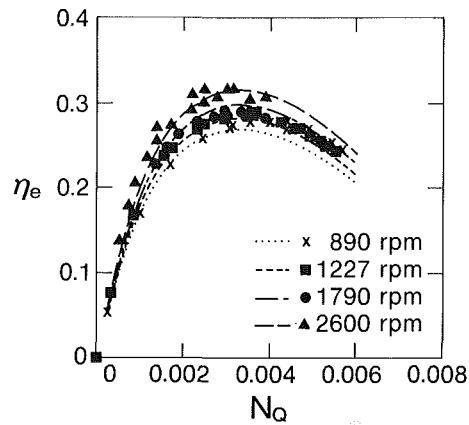


Fig. 6 Overall pump efficiency versus dimensionless flow coefficient for various speeds. The lines represent equation (23).

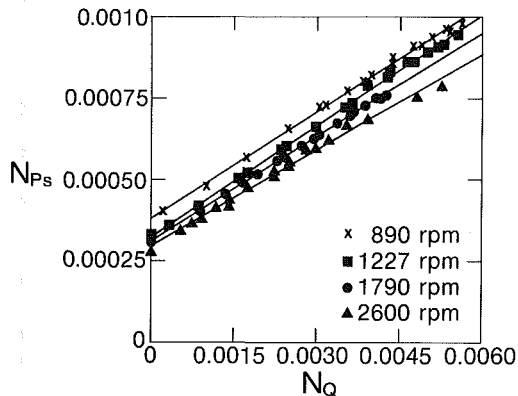


Fig. 4 Dimensionless shaft input power versus dimensionless flow coefficient

culated within the pump, and the efficiency is zero. The data of Fig. 2 can be represented by the following least-squares equation:

$$N_H = 0.09 - 9N_Q \quad (21)$$

The overall measured pump efficiency, η_e , is shown versus N_Q in Fig. 3. The peak efficiency increased with speed, ranging from 26 percent at 890 rpm to 32 percent at 2600 rpm. The sharp drop off in efficiency for the 1790 and 2600 rpm cases was due to cavitation in the orifice meter upstream of the pump, and therefore is probably not a true indication of the pump efficiency under these conditions. It is evident from Fig. 3 that the pump efficiency is dependent upon more than just

N_Q , since all of the data points do not fall on a single curve. Likewise, the data points for the dimensionless shaft input power, N_{Ps} , were found to fall on different lines for different pump speeds, as shown in Fig. 4, and these lines are very nearly straight. By cross-plotting these data, it was found that all points could be made to coincide on the same line if a dependence upon $N_{Re\omega}$ is included, in the form:

$$N_{Ps} = (0.0042 + 1.34N_Q) / N_{Re\omega}^{0.15} \quad (22)$$

The result is illustrated in Fig. 5, in which it is seen that all data points now collapse onto the same line.

As previously shown, the pump efficiency, total shaft power coefficient, hydraulic fluid power coefficient and head coefficient are related by $\eta_e = N_{ph} / N_{Ps} = N_H N_Q / N_{Ps}$. Therefore, an empirical expression for the overall pump efficiency can be obtained by combining equations (21) and (22), to give:

$$\eta_e = \frac{(0.09 - 9N_Q)N_Q N_{Re\omega}^{0.15}}{(0.0042 + 1.34N_Q)} \quad (23)$$

This expression compares favorably with the data points for the measured pump efficiency, as shown in Fig. 6.

Performance data were also made available from Discflow Corporation on geometrically similar model 403 Discflow pumps with 3, 5, and 8 disks in the disk pack and a comparable disk pack width (3.5 in., as compared with 3.0 inches for the 11 disk pump). These data were obtained by an independent pump test facility, not by the pump manufacturer. The disk gap for all pumps is shown in Table 2. Figure 7 shows the efficiency versus N_Q for each of these pumps, all at a speed of 2600 rpm. It is clear that the efficiency increases with decreasing disk gap. This is probably because the narrower the

Table 2 Gap dimensions for 14 in. diameter disk packs

No. Disks	No. Gaps	Gap Width, in.(mm)	N_d
11	10	0.136(3.45)	0.00971
8	7	0.330(8.38)	0.0236
5	4	0.689(17.5)	0.0492
3	2	1.527(38.8)	0.1090

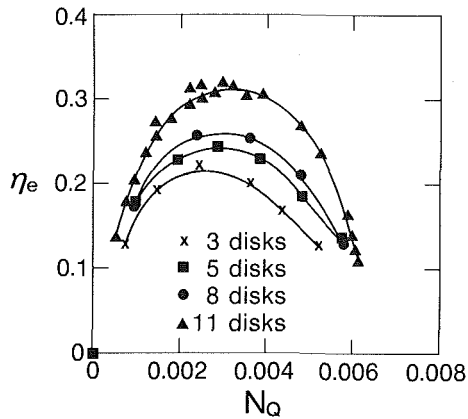


Fig. 7 Efficiency versus dimensionless flow coefficient for various size disk packs, 2600 rpm

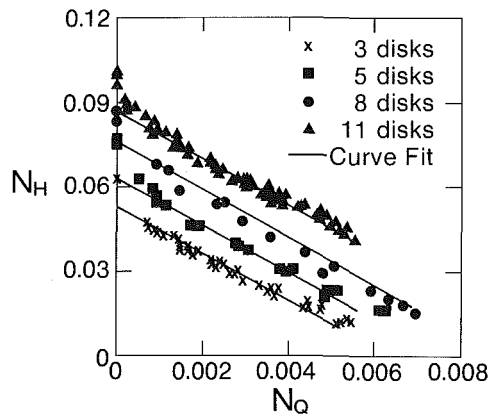


Fig. 8 Dimensionless pump head versus dimensionless flow coefficient for various size disk packs, 300 to 2750 rpm. The lines represent equation (24).

gap, the higher the disk surface area per unit volume of fluid, resulting in less "slippage" between the fluid and the disk, hence increasing the rate of momentum transferred to the fluid by wall shear.

The dimensionless head (N_H) versus flow (N_Q) characteristic for these pumps is shown in Fig. 8, which includes data for a range of pump speeds from 300 to 2750 rpm. As before, data for all speeds for a given pump fall on the same line. However, the lines for each of the disk packs are now distinct, although parallel, showing a definite dependence upon the disk gap. This dependence was determined again by linear least-squares regression to be of the form:

$$N_H = 0.095 - 0.92N_d + 4.93N_d^2 - 8.35N_Q \quad (24)$$

which is represented by the lines in Fig. 8. Thus the head versus flow rate characteristic for all disk packs is represented by this single expression.

The shaft input power number for all pumps is shown in Fig. 9, as $N_{Ps}N_{Re\omega}^{0.15}$ versus N_Q , which was shown before to collapse all data points for all speeds for the eleven disk pump to a single line. As before, data for all speeds for a given disk pack collapse to a single line, but there is an obvious

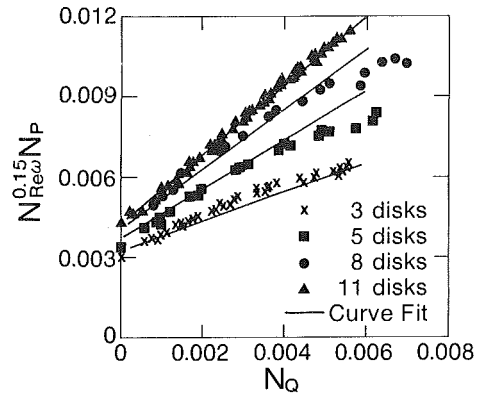


Fig. 9 The influence of rotational Reynolds number and disk spacing on the dimensionless shaft power coefficient. The lines represent equation (25).

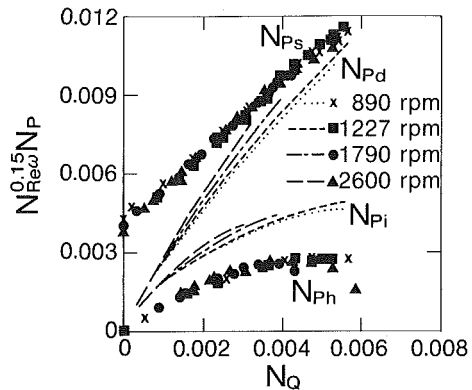


Fig. 10 Comparison of theoretically predicted disk power, N_{Pi} , with measured pump hydraulic power, N_{Ph} , and shaft power, N_{Ps}

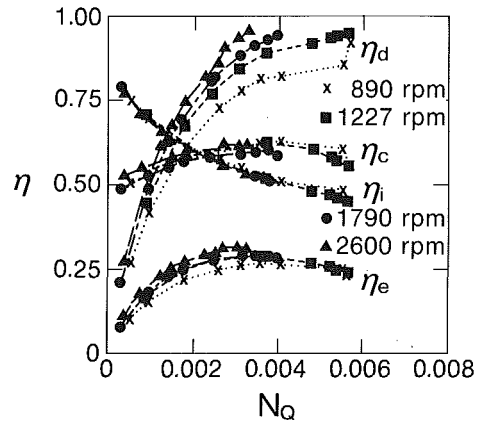


Fig. 11 Efficiency of suction (η_d), collector (η_c), impeller (η_i), and overall efficiency (η_e) versus dimensionless flow coefficient

dependence upon the disk gap, since a separate line results for each disk pack. Using linear regression methods, as before, the dependence upon disk spacing was found to be represented by the following expression:

$$N_{Ps}N_{Re\omega}^{0.15} = 0.00258 + (0.00071 + 0.54N_Q)^* \ln[(1.419 + \ln N_d)/(-0.294)] \quad (25)$$

Comparison With Theory

The values of N_{Pd} and N_{Pi} calculated from equations (14) and (16) are shown in Fig. 10, along with the measured values of N_{Ps} and N_{Ph} for the eleven disk pump. The data are

presented as $N_{P_i} N_{Re_w}^{0.15}$ versus N_Q , to reflect the previously observed dependence upon Reynolds number. The values of N_{P_i} computed from equation (16) were in agreement with those calculated from equation (19), which confirms the internal consistency of the numerical calculations. Because of the close grouping of the data points for different speeds on this plot, it is evident that the theoretical model predicts nearly the same dependence upon the Reynolds number as shown by the data.

The separate efficiencies of the suction, disk impeller, and casing discharge are shown in Fig. 11 as a function of N_Q . It is seen that the impeller efficiency (η_i) varies from about 45 to 80 percent, and decreases as the flow rate increases. This is as would be expected, because of the decreasing residence time in the gap with increasing flow rate. On the other hand, the suction efficiency (η_d) increases with increasing flow rate, and ranges from less than 30 to over 95 percent. This is also as expected, since bearing friction would contribute significantly to this loss at low flow rates, but would be increasingly less important as flow rate increases. Probably the most notable result, however, is the discharge or collector efficiency (η_c), which is of the order of 50–60 percent, with little variation with flow rate. This compares with typical values of 60–70 percent for conventional vaned pumps. In fact, the casing of the disk pump was originally designed for a vaned pump. Thus the lower collector efficiency is not unexpected, because of the higher tangential flow component leaving the disk compared with a typical vaned impeller.

The influence of impeller speed on the various efficiency components is also notable. It is evident from Fig. 11 that η_i and η_c are essentially independent of impeller speed, whereas η_d increases with increasing speed. Since η_d includes the efficiency of transfer of energy from the disk to the fluid in the gap, it is reasonable that this should increase with impeller speed because of the increasing ratio of angular momentum to radial momentum with increasing speed. However, because this efficiency is considerably higher than the others, it has a relatively small effect on the overall efficiency, η_e , which therefore is much less sensitive to impeller speed.

Conclusions

The generalized affinity laws, by which disk pump performance can be characterized in terms of groups of parameters representing the dimensionless head, power, efficiency, gap space, and Reynolds number have been confirmed by a theoretical analysis of flow between rotating disks based upon momentum transfer principles. It has been shown that the dimensionless pump power can be quantitatively related to a dimensionless flow rate, a dimensionless gap spacing, a rotational Reynolds number, a relative roughness of the disk surface, and a flow profile parameter. In addition, a theoretical analysis of the flow in the disk gap enabled separate calculation of the total power transferred from the disk to the fluid, the power acquired by the fluid by angular momentum transfer, and the friction loss in the gap. Combination of these quantities with the measured shaft power input to the pump and hydraulic power output enabled separate evaluation of power losses in the suction and in the discharge collector of the pump.

Performance data for disk pumps with 14 in. (35.6 cm) diameter impellers containing 3, 5, 8, and 11 disks have been correlated empirically in terms of the above dimensionless groups, and empirical equations have been proposed which relate the dimensionless pump head, fluid power, and efficiency to the dimensionless flow rate, a rotational Reynolds number, and gap spacing. These empirical correlations should

permit the prediction of the performance of geometrically similar pumps operating with Newtonian fluids over an extended range of operational conditions. The effect of disk diameter and gap spacing is included in the correlations, but geometric effects resulting from scaling up the casing and collector are not included.

Theoretical predictions of the disk performance characteristics agreed with the observed dependence upon Reynolds number and pump speed. It was shown that, over most of the operating range for which $N_Q > 0.0020$, the efficiency of the disk impeller is considerably greater than that of the total pump. That is, although the overall pump efficiency is only on the order of 20–25 percent over the operating range, the impeller itself was 45 to 80 percent efficient over this range. The suction efficiency varies from about 30 to 95 percent, but is highest at the higher flow rate operating range. On the other hand, the discharge or collector efficiency is of the order of 50–60 percent over the entire flow range. This is probably due to the fact that the discharge angle of the fluid leaving the impeller is very shallow (i.e., tangential) compared to that of a conventional vaned pump, and the casing is not designed for high efficiency conversion of the angular momentum in this flow to pressure head.

The only fluid used in this study was water. Since the effect of Reynolds number on the pump performance has been included in both the theoretical and empirical characterization of the pump performance, which are described in terms of generalized dimensionless quantities, it would be expected that these same relations could be used to predict the performance of similar pumps operating on other Newtonian fluids with viscosities greater than water, within reasonable limits. However, these limits cannot be determined without some experimental verification using viscous fluids. Likewise, since the apparent advantages of disk pumps are their claimed superiority when handling non-Newtonian fluids, such as highly loaded slurries and polymeric fluids, it would be of considerable interest to extend these studies, both experimental and analytical, to include such fluids.

References

- 1 Hasinger, S., and Kehrt, L., "Investigation of a Shear Force Pump," *ASME Journal of Engineering for Power*, Vol. 85, 1963, pp. 201–207.
- 2 Bakke, E., and Kreidth, F., "Disk Pump Performance in Turbulent Flow," *ASME Misc. Paper 77-WA/FE-26*, 1–8, 1977.
- 3 Tesla, N., "Turbine," U.S. Patent No. 1061206, May 6, 1913.
- 4 Rice, W., "An Analytical and Experimental Investigation of Multiple Disk Pumps and Compressors," *ASME Journal of Engineering for Power*, Vol. 85, 1963, pp. 191–200.
- 5 Breiter, M., and Pohlhausen, K., "Laminar Flow Between Two Rotating Disks," *ARL Report No. 62-218*, Wright-Patterson AFB, Dayton, Ohio, Mar. 1962.
- 6 Boyack, B., and Rice, W., "Integral Method for Flow Between Co-rotating Disks," *ASME Journal of Basic Engineering*, Vol. 93, 1971, pp. 350–354.
- 7 Adams, R., and Rice, W., "Experimental Investigation of the Flow Between Co-rotating Disks," *ASME Journal of Applied Mechanics*, Vol. 92, 1970, pp. 844–849.
- 8 Lawn, M., and Rice, W., "Calculated Design Data for the Multiple Disk Turbine Using Incompressible Fluid," *ASME JOURNAL OF FLUIDS ENGINEERING*, Vol. 96, 1974, pp. 252–258.
- 9 Crawford, M., "A Composite Solution Method for Analytical Design and Optimization Studies of a Multiple Disk Pump," M.S. thesis, Arizona State University, Feb. 1972.
- 10 Bryne, R., "Disk Pump Feasibility Investigation," Report No. RPL-TDR-64-119, AF Rocket Propulsion Laboratory, Edwards, CA, July 1964.
- 11 Henry, J., and Rae, S., "Development of a Quiet Vaneless Impeller Centrifugal Pump," MEL R&D Report No. 221/66, U.S. Navy Marine Engineering Laboratory, Annapolis, MD, Mar. 1967.
- 12 Balje, O., "A Study on the Performance Potential of Conventional and Shear Force Pumps," *ARL Report No. 65-118*, June 1965.
- 13 Churchill, S., "Friction Factor Equation Spans All Fluid Flow Regimes," *Chemical Engineering*, Nov. 1977, pp. 91–92.

Dynamics of Liquid Sloshing in Upright and Inverted Bladdered Tanks

F. T. Dodge

D. D. Kana

Southwest Research Institute,
San Antonio, Texas

The sloshing of liquids in tanks that use a flexible, inextensible bladder to contain the liquid is investigated experimentally and theoretically. The bladder affects both the configuration of the liquid in the tank and the sloshing frequencies and motion. The governing equations of liquid sloshing coupled to the structural dynamics of the bladder are formulated and examined to determine the interaction between the body forces of the liquid and the stiffness of the bladder and to show that the slosh dynamics can be represented by equivalent mechanical models. Tests are conducted to establish such mechanical models for normal and low-gravity conditions. For an inverted tank (liquid above the bladder), the sloshing is sufficiently different from conventional sloshing that the form of the equivalent mechanical model as well as the numerical values of the model parameters must be derived from the test results.

Introduction

The dynamic effects of liquid propellant sloshing (that is, free surface waves) on the stability and control of rockets and spacecraft are customarily assessed in system simulations by using a mechanical model of pendulous masses or spring-mass oscillators to represent the sloshing forces and torques. Such mechanical models can be rigorously shown to duplicate exactly the forces and torques produced by the potential flow motion of an ideal, inviscid, incompressible liquid that has small-amplitude standing waves on its free surface [1-3]. When required, the models can be modified to include linear dashpots to simulate a small amount of viscous-like damping. The damping is estimated from a separate boundary layer analysis, using the potential flow solution as the external flow, or from scale model tests [4, 5]. Because of this exact correspondence to potential flow sloshing, mechanical models are used even when the sloshing departs significantly from a potential flow. A tank that contains a flexible bladder, such as is used in some spacecraft to expel the propellant during periods of thrusting or to prevent a gross migration of propellant within the tank during periods of low-gravity, represents a case in which nonpotential flow effects are significant. Generally, the mechanical model for such situations must be shown by experiment to represent the sloshing dynamics satisfactorily.

As an example, the Tracking and Data Relay Satellite contains two bladdered tanks positioned along the spacecraft axis of symmetry, as sketched in Fig. 1. The bladders are flexible but nearly inextensible. In the upper tank, hereafter called the upright tank, the liquid is "below" the bladder during

thrusting. In the lower tank, the liquid is "above" the bladder, so this tank will be called the inverted tank. (This orientation of the liquid is desired for several reasons, including spacecraft center-of-mass control as the propellant is depleted from both tanks.) Sloshing in the upright tank is known from previous work to be qualitatively similar to a non-bladdered tank [6], but preliminary tests to study liquid motions in the inverted tank showed that (1) the configuration of the liquid at rest was significantly asymmetrical and (2) the sloshing did not resemble conventional sloshing in an unbladdered tank. Thus a test methodology was developed to examine the liquid motions in detail and to formulate a model that would reproduce the important dynamic effects.

Equations of Motion

The prototype tanks are identical ellipsoids with a vertical axis of symmetry (Fig. 1). As depicted in the sketch, the liquid in each tank was found to assume a static configuration that appeared to minimize the total potential energy of the system composed of the gravitational potential energy of the liquid (i.e., that due to body forces) and the bending strain energy of the bladder. The configuration is constrained by the fact that the total interface area between the liquid and the bladder must equal the fixed total area of the bladder. (The bladder is essentially inextensible and is just large enough so that the tank can be completely filled or emptied.) In mathematical form, the static interface configuration $z = F(x, y)$ is then the function that minimizes the total potential energy:

$$PE = \rho a \int \int z \, dz \, dA + \int \int h \, d \, dA \quad (1)$$

subject to the constraint that:

$$A = \int dA = \text{constant} \quad (2)$$

where the first term on the right of equation (1) is the potential energy of the liquid and the second is the strain energy of the

Contributed by the Fluids Engineering Division of the American Society of Mechanical Engineers and presented at the Winter Annual Meeting, Miami Beach, Florida, Nov. 17-22, 1985. Manuscript received by the Fluids Engineering Division October 7, 1986.

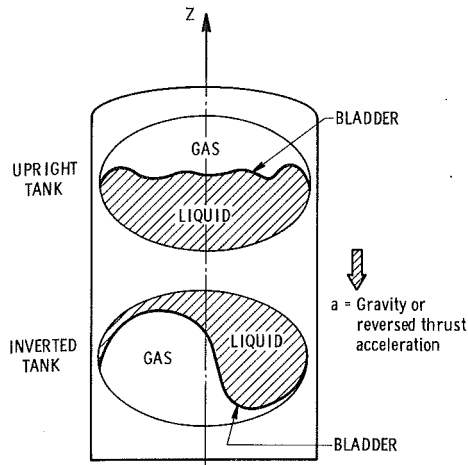


Fig. 1 Schematic of upright and inverted tanks showing typical static liquid configurations

bladder. Here, "a" is the effective gravitational acceleration (for example, the reversed axial thrust acceleration), ρ is the liquid density, A is the interface area, σ is the bending stress and ϵ the bending strain in the bladder, and h is the bladder thickness. In the laboratory, "a" is of course earth's gravitational acceleration, g .

Equations (1) and (2) are extremely difficult if not impossible to solve, so experimental testing was used to establish the interface configurations for both tanks as a function of fill level. (The experimental apparatus is described later.) The configuration at each fill level was also investigated as a function of effective gravity (body force) by conducting tests in which either water or various mixtures of zinc bromide (densities up to 2.5 times water) was used as the simulated propellant. (From equation (1), it can be seen that a change of liquid density is exactly equivalent to a change of effective gravity level.) It was found, for each fill level, that the interface configuration was independent of liquid density (i.e., effective gravity). The same configurations were also found when the tank was filled with zinc bromide or water on both sides of the bladder, which is equivalent to reducing the effective gravity to near zero since the potential energy of the liquid is near zero. The tests thus proved that the configuration is dominated by the liquid potential energy, which is always so large that the strain energy of the bladder is negligible, except at exactly zero-gravity. The liquid configurations observed in the laboratory tests are therefore the same that would occur under conditions of thrusting or low-gravity.

Figure 1 (upper part) shows a sketch of the symmetrical configuration found for the upright tank, in this case for a 45 per-

cent filling level by volume. The liquid configuration for the inverted tank for the same filling level was decidedly unsymmetrical, as is sketched in the lower part of Fig. 1. The liquid settled predominantly on one side of the tank and lower than would have a symmetrical configuration; this clearly minimizes the system potential energy. Further, as might be expected, the configuration was unstable and the liquid could be made to "flop" abruptly to the diametrically opposite side of the tank for a sufficiently large transverse acceleration or when the tank was tilted through a sufficiently large angle.

The bladder also was found to have a marked influence on the kinds of liquid-bladder interface waves created by small disturbances. In order to examine the influence analytically, an ideal, irrotational flow is assumed, for which a velocity potential Φ can be defined. The boundary conditions at the liquid-bladder interface for the potential flow are derived as follows. Bernoulli's equation written at the free surface, and for linearized motions, reduces to [1]:

$$\frac{\partial \Phi}{\partial t} + a\zeta + p/\rho = 0 \quad Z = F(x, y) \quad (3)$$

Here t is the time, ζ is the slosh wave amplitude, and p is the pressure acting on the liquid at the liquid-bladder interface. Equation (3) is evaluated at the static configuration surface, $z = F(x, y)$. The same interface pressure acts on the bladder, forcing it to conform to the liquid motion at the surface. Since the bladder thickness is small, the bladder inertia is negligible, and the bending of the bladder can be analyzed from statics [7]:

$$D \nabla^4 \zeta = p \quad (4)$$

where D is the flexural rigidity of the bladder. Note that the "del" operator is written in a coordinate system that conforms to the static shape of the bladder. Equations (3) and (4) can be combined to give:

$$\rho \frac{\partial \Phi}{\partial t} + (\rho a + D \nabla^4) \zeta = 0 \quad Z = F(x, y) \quad (5)$$

The condition that the component of liquid velocity normal to the interface and the surface wave amplitude match at the interface (i.e., the kinematic condition [1]) is written as:

$$\frac{\partial \zeta}{\partial t} = \frac{\partial \Phi}{\partial z} - \nabla F \cdot \nabla \Phi \quad Z = F(x, y) \quad (6)$$

Equations (5) and (6) can be combined to give:

$$\rho \frac{\partial^2 \Phi}{\partial t^2} + (\rho a + D \nabla^4) \left(\frac{\partial}{\partial z} - \nabla F \cdot \nabla \right) \Phi = 0 \quad Z = F(x, y) \quad (7)$$

Equation (7) can be compared to the corresponding equation for sloshing with surface tension [1, 3]:

$$\rho \frac{\partial^2 \Phi}{\partial t^2} + (\rho a - \tau \nabla^2) \left(\frac{\partial}{\partial Z} - \nabla F \cdot \nabla \right) \Phi = 0 \quad Z = F(x, y) \quad (8)$$

Nomenclature

a = effective gravitational acceleration	m_1, m_0 = slosh and immobile masses	$\zeta(x, y)$ = slosh wave amplitude
C_1, C_2, C_θ = viscous dashpot constants	m_{liq} = total liquid mass	θ = inverted pendulum tilt angle
D = bladder flexural rigidity	p = liquid pressure	ρ = liquid density
$F(x, y)$ = interface configuration function	R_{min} = minor (vertical) radius of ellipsoidal tank	$\Phi(x, y, z, t)$ = velocity potential
g = standard gravitational acceleration	t = time	ϕ_x, ϕ_y = rotational excitation amplitudes
h = bladder thickness	x, y, z = coordinate axes, z vertical	ω = frequency
$i = (-1)^{1/2}$	X_0, Y_0 = translation excitation amplitude	$\omega_1, \omega_2, \omega_n$ = natural frequencies
K_1, K_2, K = spring constants	$\beta_1, \beta_2, \beta_\theta$ = damping factors	$\Omega_1, \Omega_2, \Omega_n$ = ratios of excitation frequency to natural frequency
L_1 = pendulum length		

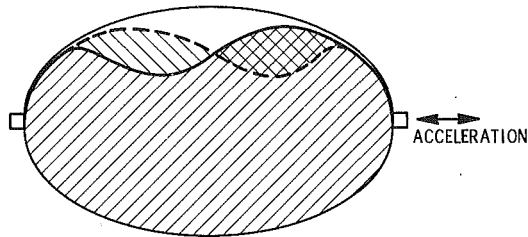


Fig. 2 Fundamental slosh mode for 93 percent full upright tank

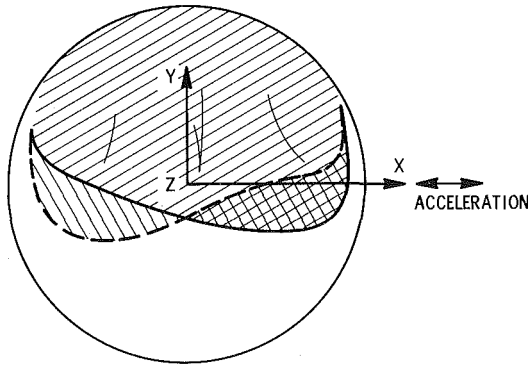


Fig. 3(a) Fundamental mode: X-Axial translation excitation

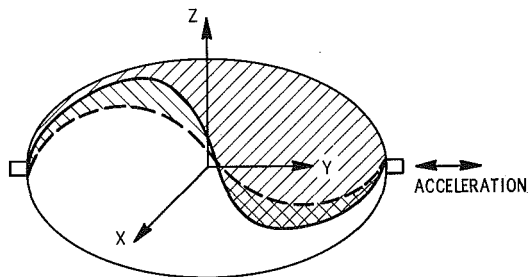


Fig. 3(b) Second mode: X-Axis rotational excitation

Fig. 3 Slosh modes for 46 percent full inverted tank

where τ is the surface tension. It can be seen that the membrane acts somewhat similarly to surface tension.

Because of the similarity of equations (7) and (8) and the observed stability of the interface for small disturbances, the potential flow solution for a bladdered tank would reduce to a familiar eigenvalue problem, from which the sloshing modes (wave shapes) could be extracted. For the purposes here, the analysis does not have to be carried further (and could not be in any event), since it is sufficient to know that normal modes exist to conclude that the dynamic effects of the sloshing can be represented by an equivalent, linear, mechanical model. A spring-mass oscillator or pendulous mass would need to be included for each slosh mode. By extension, it is justified to assume that a mechanical model will satisfactorily represent the actual nonpotential flow sloshing. Since no analytical solution is available, numerical values for the equivalent model must be determined empirically.

The parameters of the model depend on the static configuration, as shown by the presence of the function $z = F(x, y)$ in the equations, which explains why so much effort was exerted in the tests to demonstrate that the laboratory configuration was the same as that which would occur in practice. It is also evident from equation (7) that the sloshing frequencies, which are determined by the factors in equation (7) that multiply Φ , depend on a linear combination of body force and membrane stiffness effects; the test results verified this conclusion.

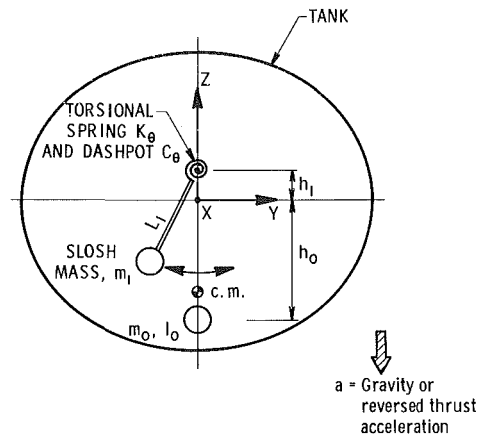


Fig. 4 Slosh model for upright tank

Sloshing Characteristics

All tests were conducted with a full-scale, plastic mockup of the actual tank. The major (horizontal) diameter of the tank was 101.6 cm (40 in.), and the minor (vertical) diameter was 76.2 cm (30 in.). A prototype bladder was used to ensure duplication of the bladder properties; it was attached along the major diameter (horizontal) circumference. Most of the tests were conducted by suspending the tank freely on long cables to support the dead weight. Electrohydraulic shakers were used to oscillate the tank and excite the various slosh modes. For some of the tests, the tank was supported directly in a load frame, so that rotational oscillation around the vertical (tank symmetry) axis could be obtained. Tank displacement, frequency, and acceleration, and liquid force, torque, damping, and phase angle comprised the test data. Displacements were measured to within 0.025 cm (.01 in.), frequency to within 0.015 Hz, and acceleration to within about 1 percent. The forces were measured to within 4 n (1 lb), torques to within 0.1 n-m (1 in-lb), and phase angles to within 2 degrees. The slosh resonant frequencies were identified to within 0.05 Hz.

For the upright tank, the fundamental slosh mode was found to be an "antisymmetrical" standing wave, in which the part of the liquid-membrane interface on one side of a diameter is "up" when the corresponding part on the other side is "down" and vice versa, as shown in Fig. 2. The wave was similar to a conventional sloshing mode, the main exception being that not all the liquid surface participated in the motion. Because of the symmetry of the tank and liquid configuration, the same modes were found for excitation in either the x or y direction. The similarity of these modes to conventional slosh modes implies that the form of the equivalent mechanical model will also be similar to a model of conventional sloshing.

For the inverted tank, two different modes were found, depending on the direction of the excitation. When the tank oscillation was x -axis translation or z -axis rotation, a low-frequency, antisymmetrical standing wave formed on the more-or-less vertical surface of the bladder; the wave resembled a standing wave on the surface of liquid in a conventional tank. Figure 3(a) shows a top view of the mode. When the tank oscillation was y -axis translation or x -axis rotation, a higher frequency standing wave, also antisymmetrical, was found; the mode is sketched in Fig. 3(b). Because of these unusual slosh modes and the instability of the static configuration, it is evident that, although an equivalent mechanical model can represent the slosh dynamics, a model of conventional form may not be a satisfactory representation of all the test observations.

Equivalent Mechanical Models

Upright Tank. Figure 4 shows the equivalent mechanical model developed to represent sloshing in the upright tank. A pendulous mass m_1 is used to represent the liquid mass that effectively participates in the fundamental mode, and an immobile mass m_0 is used to represent the rest of the liquid mass. (Only the fundamental mode exhibited large forces and torques, so that pendulums that would represent higher-order modes are not needed.) The immobile mass has a moment of inertia I_0 to duplicate the rotational inertia of the liquid. The primary difference between this model and a conventional model is that a torsional spring K_θ is attached to the pendulum pivot to simulate the bending stiffness of the bladder, in analogy to the appropriate term in equation (7). The natural frequency of the pendulum is:

$$\omega_n = (K_\theta/M_1 L_1^2 + a/L_1)^{1/2} \quad (9)$$

To determine K_θ and L_1 , either the effective gravity "a" or the slosh mass m_1 can be varied. Since it was not practical to use a centrifuge or a drop-tower to vary "a" on such a large tank, m_1 was varied by using liquids of various densities. (Recall that the liquid configuration, and therefore the slosh mode, was independent of the liquid density, i.e., the body force level. Likewise, from equation (7), the slosh frequencies can be varied by varying either ρ or "a", in agreement with the conclusion drawn from the model equation (9).)

The forces F_y and torques M_x predicted by the model for small lateral oscillations Y_0 and rotational oscillations ϕ_x are:

$$F_y = -\omega^2 Y_0 e^{i\omega t} \{ m_T + m_0 + m_1 + m_1 \Omega_n^2 / [1 - \Omega_n^2 + 2i\Omega_n \beta_n] \} \\ - \omega^2 \phi_x e^{i\omega t} \{ m_0 h_0 + m_1 (L_1 - h_1) \\ + m_1 (L_1 - h_1) [\Omega_n^2 + a / (L_1 - h_1) \omega_n^2] / \\ [1 - \Omega_n^2 + 2i\Omega_n \beta_n] \} \quad (10)$$

$$M_x = -\omega^2 Y_0 e^{i\omega t} \{ m_0 h_0 + m_1 (L_1 - h_1) + m_1 (L_1 - h_1) \\ \cdot [\Omega_n^2 + a / (L_1 - h_1) \omega_n^2] / [1 - \Omega_n^2 + 2i\Omega_n \beta_n] \} \\ - \omega^2 \phi_x e^{i\omega t} \{ I_T + I_0 + m_0 h_0^2 + m_1 (L_1 - h_1)^2 \\ + m_1 (L_1 - h_1)^2 [\Omega_n^2 + a^2 / (L_1 - h_1) \Omega_n^2 \omega_n^4 + 2a \\ / (L_1 - h_1) \omega_n^2] / [1 - \Omega_n^2 + 2i\Omega_n \beta_n] \} \quad (11)$$

A simple harmonic excitation $e^{i\omega t}$ is assumed, to correspond with the test conditions. The slosh damping is expressed by the damping factor β_n , defined as $C_\theta/2m_1\omega_1 L_1^2$ where C_θ is the pendulum damping, and $\Omega_n = \omega/\omega_n$ is the ratio of excitation frequency to pendulum natural frequency. (The mass m_T and moment of inertia I_T of the tank are included in the equations to help determine the model parameters from test data that included the dead weight of the tank.)

Inverted Tank. The slosh model postulated for the inverted tank is shown in Fig. 5. It represents both the static stability of the liquid and the two slosh modes found in the tests. The inverted pendulum of the model duplicates (1) the offset location of the liquid center of mass, (2) the effective mass of the liquid participating in the sloshing and (3) the ability of the liquid to change location for large transverse disturbances. It is clear that an inverted pendulum can be made to represent the instability of the liquid configuration at rest. But an inverted pendulum does not have an intrinsic natural frequency, so springs are included, as shown in the figure, to provide the restoring forces needed to allow the small oscillations that simulate the sloshing. The spring constants depend linearly on the effective gravity (i.e., the body forces) and the bladder bending stiffness. Spring K_1 and dashpot C_1 apply to the low-frequency mode, and K_2 and C_2 apply to the higher frequency mode found in the tests. The friction force, F_s , that restrains the pendulum support simulates the observed stability of the interface to small disturbances. When the disturbance is large enough, F_s is exceeded and the entire system of slosh mass and

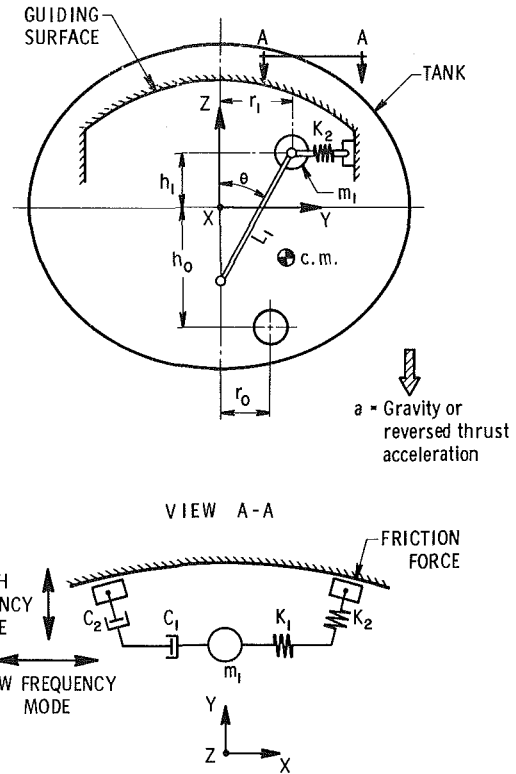


Fig. 5 Slosh model for inverted tank

immobile mass is assumed to move in concert to a new position. When the disturbance is even larger, the pendulum can swing abruptly to a new position. The friction force F_s and pendulum tilt angle θ are chosen to duplicate the observed static stability. Note that only one mass is used to represent both slosh modes; this assumption is not strictly valid but proved to be sufficiently accurate to make a workable model; the use of two slosh masses does not present any additional conceptual difficulty. The immobile mass is assumed to have distinct moments of inertia I_{0x} , I_{0y} , and I_{0z} .

The natural frequencies of the two slosh modes are:

$$\omega_1 = (K_1/m_1)^{1/2} \quad (12a)$$

$$\omega_2 = (K_2/m_1)^{1/2} \quad (12b)$$

Again, liquids of various densities were used in the tests to establish the separate dependencies of K_1 and K_2 on gravity and bladder bending stiffness.

Because of the asymmetry of the liquid configuration in the inverted tank about the vertical axis, x - and y - translational excitations and x -, y -, and z -axis rotational excitations were all tested. As examples of the model equations, the force F_x produced by x -axis lateral oscillation X_0 and the torque M_x produced by x -axis rotational oscillation ϕ_x are:

$$F_x = -\omega^2 X_0 e^{i\omega t} \{ m_T + m_0 + m_1 + m_1 \Omega_1^2 / [1 - \Omega_1^2 + 2i\Omega_1 \beta_1] \} \quad (13)$$

$$M_x = -\omega^2 \phi_x e^{i\omega t} \{ I_{Tx} + I_{0x} + m_0 (h_0^2 + r_0^2) + m_1 (h_1^2 + r_1^2) \\ + m_1 (h_1^2 + r_1^2) [\Omega_2^2 + a^2 / H_1^2 \Omega_2^2 \omega_2^4 + 2a / H_1 \omega_2^2] / \\ [1 - \Omega_2^2 + 2i\Omega_2 \beta_2] \} \quad (14)$$

Here $\Omega_1 = \omega/\omega_1$, $\Omega_2 = \omega/\omega_2$, $H_1^2 = h_1^2 + r_1^2$, $\beta_1 = C_1/2m_1\omega_1$, and $\beta_2 = C_2/2M_2\omega_2$. The empty tank properties are m_T , $I_{Tx} = I_{Ty}$, and I_{Tz} .

This combination model for the inverted tank is more complicated than would be a purely "slosh" model. In fact, the slosh dynamics alone could be represented, as always, by a suitable model of ordinary pendulums, similar to that for the upright tank (Fig. 4). But it is desirable in system simulations to represent by a single model both the forces and torques pro-

Table 1 Slosh model parameters for the upright Tank

93 Percent Fill Level		
m_1/m_{liq}	=	0.087
m_0/m_{liq}	=	0.913
L_1/R_{min}	=	0.327
K_θ/m_1gL_1	=	0.46
$C_\theta\omega_n/m_1gL_1$	=	0.30
$I_0/m_0R^2_{min}$	=	0.062
h_1/R_{min}	=	-0.33
45 Percent Fill Level		
m_1/m_{liq}	=	0.312
m_0/m_{liq}	=	0.688
L_1/R_{min}	=	0.43
K_θ/m_1gL_1	=	0.20
$C_\theta\omega_n/m_1gL_1$	=	0.21
$I_0/m_0R^2_{min}$	=	0.084
h_1/R_{min}	=	0
h_0/R_{min}	=	0.413

Note: R_{min} is one-half the vertical diameter.

Table 2 Slosh model parameters for 46 percent full inverted tank

m_1/m_{liq}	=	0.32
m_0/m_{liq}	=	0.68
r_1/R_{min}	=	0.133
r_0/R_{min}	=	0.407
h_1/R_{min}	=	0.567
h_0/R_{min}	=	0.113
L_1/R_{min}	=	0.390
K_1L_1/m_1g	=	0.388 + 1.34 (a/g)
$C_1\omega_1L_1/m_1g$	=	0.312
K_2L_1/m_1g	=	8.727 + 30.16 (a/g)
$C_2\omega_2L_1/m_1g$	=	5.865
$I_{0x}/m_0R^2_{min}$	=	0
$I_{0y}/m_0R^2_{min}$	=	0.236
$I_{0z}/m_0R^2_{min}$	=	0.275
θ	=	20°
F_s/m_1g	=	0.290 + 0.11 (a/g)

Note: R_{min} is one-half the vertical diameter.

duced by sloshing and the forces and torques produced by the instability, and this requires the use of an inverted pendulum.

Model Parameters and Comparison to Test Results

Values for all the model parameters were determined from the test results. Briefly, the observed resonant frequencies were matched to the model natural frequencies (after allowing for the large frequency shift due to the large damping) while simultaneously the forces and torques measured at the resonant frequencies were matched to the predicted forces and torques. The forces and torques for frequencies well above any resonance were used to establish the properties of the immobile mass. Although both the model and the actual liquid slosh are linear (i.e., response force and torque proportional to excitation acceleration), the large damping values made it difficult to isolate the effects of each model parameter on the measured responses. Generally, several iterations involving trial values of pendulum mass and natural frequency were needed to obtain satisfactory values for all the model parameters. The dependency of the torsional spring K_θ (Fig. 4) and the linear springs K_1 and K_2 (Fig. 5) on effective gravity and bladder stiffness was deduced by comparing equations (9) and (12) to the natural frequencies calculated from the observed resonant frequencies from tests that used the same fill level but different liquid densities.

Numerical values of the model parameters for typical tank filling percentages are presented in Tables 1 and 2 in non-dimensional form. Although they were derived from tests on a specific tank size, the nondimensional parameters apply to any geometrically-similar bladdered tank [1]. Those parameters

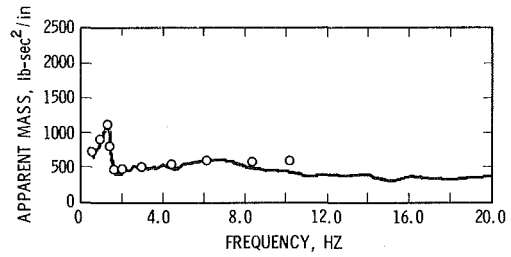


Fig. 6 Comparison of model and test slosh force for 45 percent full upright tank for X-Axis translation excitation. (Uncertainty in frequency = ± 0.015 Hz; uncertainty in apparent mass = ± 2.5 percent.)

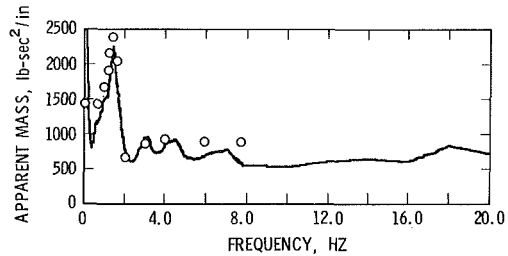


Fig. 7(a) Force for X-Axis translation acceleration

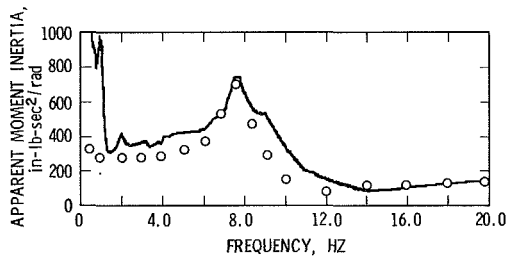


Fig. 7(b) Torque for X-Axis rotational excitation

Fig. 7 Comparison of model and tests for 46 percent full inverted tank. (Uncertainty in frequency = ± 0.015 Hz; uncertainty in apparent mass = ± 2.5 percent; uncertainty in apparent moment of inertia = ± 2.5 percent.)

that depend strongly on bladder stiffness no doubt vary with the bladder material, but the tabular values can probably be used to provide preliminary estimates for other types of bladders.

The nondimensional slosh mass parameter of the upright tank is slightly less than that for a similar unbladdered tank [1]; this agrees with the experimental observation that the slosh wave did not extend completely across the liquid-bladder interface (Fig. 2) and thus less liquid participated in the sloshing. On the other hand, the damping in the bladdered tank is extremely large compared to an unbladdered tank, which, since viscous damping is known to be small [1], indicates that most of the damping arises from the viscoelasticity of the bladder. For that reason, no attempt was made to separate the damping into parts due to the viscoelasticity and liquid viscosity.

For the 45 percent inverted tank (Table 2), it is interesting to note that the slosh mass parameter is about the same as for the upright tank with the same filling percentage [1]; it is doubtful, however, that such a result holds in general. The constant part of the K_1 and K_2 parameters represents the effects of bladder stiffness, while the part proportional to (a/g) represents the effects of body forces, where g is the standard acceleration of gravity. Although the tests showed a very slight dependence of the damping on body forces, the great bulk of the damping was due to bladder viscoelasticity; thus the damping parameter was taken to be independent of body forces.

The friction force, F_s , which "holds" the system of springs and inverted pendulum to the tank during sloshing, was, however, shown to depend on body forces, as indicated in Table 2.

Comparison of Models and Test Results

Figure 6 shows a comparison of the model predictions for the upright tank (the open circles) and typical test results for a 45 percent full tank of water. The excitation is along the x -axis. The force response is shown divided by the excitation amplitude (i.e., $X_0\omega^2$) to yield an apparent mass. The actual force at resonance for this test was 107 n (24.1 lb) for an excitation amplitude of 0.207 m/s² (0.021g's). The mass of the tank, test fixture, and the water was 325.2 kg (717 lb) which yields a dead weight load of 67.3 n (15.1 lb) at resonance, so the sloshing of the liquid contributed about 40 n (9 lb) to the force at resonance. The pendulum (slosh) mass is 52 kg for this configuration, so the resonant amplification is only $40/(52 \times 0.207) = 4$; thus, it evident that the damping is indeed large. The model and tests compared equally well for all liquid densities and fill levels.

Figure 7 show comparisons of the model predictions for the inverted tank (the open circles) and the test results for a 46 percent full tank of zinc bromide (specific gravity of 2.52). Figure 7(a) shows the apparent mass for x -axis horizontal excitation and Fig. 7(b) shows the apparent moment of inertia (torque divided by rotational acceleration amplitude) for X -axis rotational excitation. The resonance in Fig. 7(a) near zero-frequency is that of the entire test fixture as a pendulum, and should be ignored. As can be seen, the model and test compare well near the fundamental slosh resonance, although a number of smaller resonances are not predicted. The rotational excitation (Fig. 7(b)) excites the second mode shown previously in Fig. 3(b). The peak torque is predicted reasonably well by the model, but the width of the resonance peak is not. The resonance width depends on the damping, which was difficult to measure because of its high value. Overall, the model and the tests agree reasonably well for all the tested conditions.

Conclusions

These tests of sloshing in tanks fitted with flexible, inextensible bladders have shown that the interaction of the liquid with the flexible structure represented by the bladder has a strong influence on the configuration of the liquid, the static

stability of the configuration, and the slosh dynamics. The new testing procedure devised for this study, in which liquids of various densities were used, allowed the relative significance of bladder bending stiffness and body forces to be studied; by doing so, the results obtained in the laboratory could be interpreted in terms of both thrusting (high-g) and low-g conditions for the actual satellite.

The sloshing equations for a liquid in a bladdered tank were formulated and examined by analogy to sloshing in a non-bladder tank to show that the slosh dynamics could be represented by an equivalent mechanical model. For the upright tank, a conventional pendulum model was found to be an accurate representation. The primary new feature of the model is the torsional spring at the pendulum hinge point needed to simulate the effects of bladder bending stiffness. For the inverted tank, models of conventional form do not represent the test observations accurately. For example, the configuration of the liquid can change abruptly. The mechanical model that best represented all the test results of the inverted tank was an inverted pendulum, which is able to undergo small oscillations as well as large reorientations. Numerical values were established for all the model parameters for several tank filling percentages.

Acknowledgment

Part of this research was sponsored by NASA-Goddard Space Flight Center through Contracts NASA 5-25782 and 5-26482.

References

- 1 *The Dynamic Behavior of Liquids in Moving Containers*, NASA SP-106, 1966. (Reprinted by Southwest Research Institute, 1980).
- 2 Dodge, F. T., and Garza, L. R., "Experimental and Theoretical Studies of Liquid Sloshing at Simulated Low Gravity," *ASME Journal of Applied Mechanics*, Vol. 34, 1967, pp. 555-562.
- 3 Abramson, H. N., Chu, W. H., and Ransleben, G. E., "Representation of Fuel Sloshing in Cylindrical Tanks by an Equivalent Mechanical Model," *American Rocket Society Journal*, Vol. 31, 1961, pp. 1697-1705.
- 4 Case, K. M., "Damping of Surface Waves in an Incompressible Liquid," *Journal of Fluid Mechanics*, Vol. 2, Mar. 1957, pp. 172-184.
- 5 Stephens, D. G., Leonard, H. W., and Silveira, M. A., "An Experimental Investigation of Damping of Liquid Oscillations in an Oblate Spheroid Tank with and without Baffles," NASA TN D-808, 1961.
- 6 Ross, R. G., and Womack, J. R., "Slosh Testing of a Spherical Mercury Propellant Tank with Positive Expulsion Diaphragm," Tech. Memo. 33-632, Jet Propulsion Laboratory, Ca., 1973.
- 7 S. Timoshenko, *Theory of Plates and Shells*, McGraw-Hill, 1940.

Drop Size Distribution and Air Velocity Measurements in Air Assist Swirl Atomizer Sprays

C.-P. Mao

V. Oechsle

N. Chigier

Department of Mechanical Engineering,
Carnegie-Mellon University,
Pittsburgh, PA 15213

Detailed measurements of mean drop size (SMD) and size distribution parameters have been made using a Fraunhofer diffraction particle sizing instrument in a series of sprays generated by an air assist swirl atomizer. Thirty-six different combinations of fuel and air mass flow rates were examined with liquid flow rates up to 14 lbm/hr and atomizing air flow rates up to 10 lbm/hr. Linear relationships were found between SMD and liquid to air mass flow rate ratios. SMD increased with distance downstream along the center line and also with radial distance from the axis. Increase in obscuration with distance downstream was due to an increase in number density of particles as the result of deceleration of drops and an increase in the exposed path length of the laser beam. Velocity components of the atomizing air flow field measured by a laser anemometer show swirling jet air flow fields with solid body rotation in the core and free vortex flow in the outer regions.

Introduction

The process of liquid fuel atomization is of fundamental importance to the performance of spray combustion systems. In almost all liquid fuel combustion systems, fuel has to be atomized before the combustion process begins. The quality of atomization affects the combustion efficiency, emission of pollutants, chamber design, and stability limits. Research work on liquid fuel atomization has been carried out for many years and is still proceeding in order to develop an understanding of the physical processes and effects of various input parameters on atomization. Giffen and Muraszew [1], Chigier [2], and Lefebvre [3] have made comprehensive reviews of the processes of atomization of liquid fuels based on published theories and experimental results. Recent progress leading towards further understanding of the mechanisms of disintegration of liquid sheets, jet breakup, and transport phenomena for pressure jet, air blast, rotary and vibratory atomization was reported at ICLASS-82 [4]. Attention is being focused onto hydrodynamic instabilities, tearing, formation of perforations in liquid sheets, longitudinal vibrations of liquid jets, ligament formation, and their effects on drop formation. The effects of variation in nozzle geometry, liquid pressure, ambient pressure and temperature on initial size distribution are being studied by several investigators [4, 5]. There are still many unsolved problems and uncertainties about the fundamental physics of liquid fuel atomization. There is no comprehensive theory which allows accurate prediction of initial conditions for drop size, velocity and direction of flight in a spray based on input conditions to the nozzle. Yet study of liquid breakup is vital for determining the initial conditions of sprays. Recently, the gas turbine industry

and government funding agencies have been developing strong interests in studying the structures of sprays and spray flames as a function of initial conditions. Atomization characteristics have been shown to be strongly correlated with the characteristics of spray flames.

Liquid fuel requires breaking up into small drops in order to be effectively burned in combustion chambers. Atomization of liquid fuel in gas turbine combustion chambers is mostly carried out by using air-blast atomizers. The merits of the air-blast atomizer have led in recent years to its widespread application in practice and several experimental studies have been carried out. On the other hand, air-assist atomizers have drawn less attention from researchers. Air assist atomizers are not well suited for aircraft gas turbine engines since a separate atomizing air supply is required. However, they have been found to be particularly useful for obtaining good atomization at low fuel flows and pressures and for fuels with high viscosity. In air-assist atomizers, high velocity air is allowed to mix with fuel inside the atomizer with counter flow or concurrent flow interactions. This produces a fine spray which is particularly effective in atomizing fuels with high viscosity. Air-assist atomizer designs are presently the most effective method for atomizing cold and viscous fuels under engine light-up and low power conditions. Very few studies on the performance of air-assist atomizers have been reported in the literature. Simmons [5] derived an expression to predict the Sauter mean diameter as a function of mass flow rate, hypothetical film thickness, and fuel/air properties for air-assist atomizers. In fact, the spray characteristics of air-assist atomizers involve more complicated interactions between liquid and surrounding air. It is one of the most appropriate atomizers for studying the process of atomization in sprays. Therefore, an external-mixing type air-assist atomizer was selected for this investigation.

Contributed by the Fluids Engineering Division for publication in the JOURNAL OF FLUIDS ENGINEERING. Manuscript received by the Fluids Engineering Division May 20, 1984.

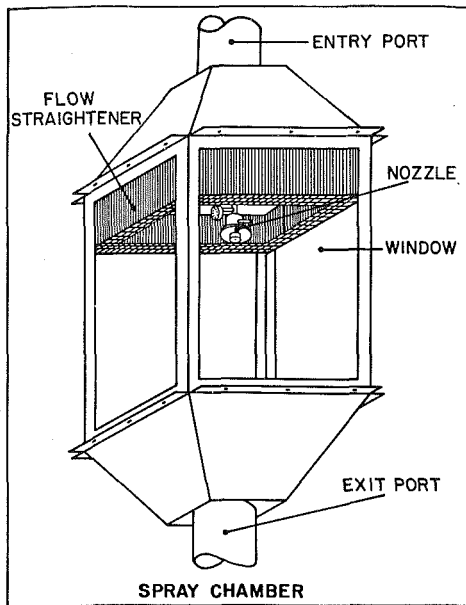


Fig. 1 Spray chamber

Detailed measurements have been made to study the aerodynamic structure of air-assist swirl atomizer sprays. The interaction between drops and surrounding air and the variation of mean drop size in the sprays are reported here. Correlations are sought between operating injection conditions and spray characteristics. A wide range of diagnostic techniques are used to characterize and make measurements in sprays including micro photography, laser diffraction particle sizing, and laser Doppler anemometry.

Experimental Apparatus

A schematic diagram of the chamber is shown in Fig. 1. The spray chamber has four windows large enough to view the entire spray and to allow both imaging and laser scattering instruments to be used for the measurements. The cross sectional area of the chamber measures 12×12 sq in. and the window height is 14 in. A top blower blows curtains of wash air through a $1\frac{1}{2}$ in. thick honeycomb flow straightener over the windows of the chamber to prevent window wetting. Another blower is located in the dump tank which creates a suction. The combination of blowing from the top and suction in the lower part of the chamber ensures that all droplets and mists are removed from the chamber. A demister is also installed at the exit of the dump tank to reduce the escape of small drops and prevent deposition on optical surfaces. This supply system was designed to accommodate a maximum liquid fuel flow rate of 20 lbm/hr. The pressure range for the injection system is 200 psig for fuel and 35 psig for atomizing air. Continuous and steady liquid fuel injection is supplied from a pressurized fuel tank compressed by high pressure water-pumped nitrogen. All flow meters and pressure transducers have been carefully tested and calibrated. A cocurrent swirling air-assist atomizer (fuel and air are swirling in the same direction) designed by Parker Hannifin for use in basic research was selected for testing. This research nozzle can be operated as an air-assist swirl atomizer and also as a fuel pressurized swirl atomizer. The direction and degree of swirl in the air can be controlled by using different air swirlers and different injection pressures. The materials used for construction of the nozzle make it very rugged and nozzle vibrations have been eliminated. A specially designed nozzle mount and a 2-dimensional traversing system were constructed for accurate traversing of the nozzle in both axial and radial directions. Measurements can be made easily at various stations in the spray without moving the diagnostic systems.

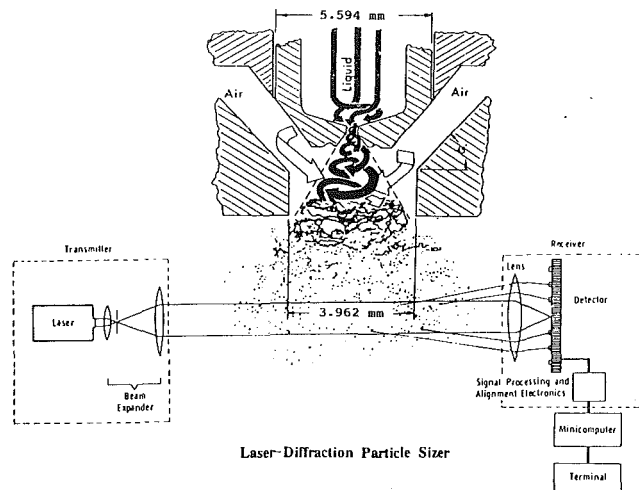


Fig. 2 Schematics illustrating the experimental setup

Figure 2 shows the nozzle geometry at the exit and the experimental set-up of the laser diffraction particle sizer. Throughout the study, a standard military calibration oil MIL-C-7024 type II was used as the test fluid.

Measurement Techniques

Still microphotography is used to assess the global structure of the spray. It is considered the most accurate, reliable, and least expensive particle sizing technique. Two photographic camera systems are employed: a 35-mm camera and a 4×5 in. format camera with a 10 ft bellows extension. The 35-mm camera is used to study the variation of spray cone angles as a function of input mass flow rates. A near-forward lighting technique is used in order to obtain the best contrast of the spray image. The 4×5 format camera is used to provide close-up views at the nozzle exit so that liquid sheet breakup and size information can be analyzed. It was found that light source alignment was extremely crucial for the 4×5 camera to produce good quality, high contrast spray pictures. With the 10 foot bellows, the magnification can be brought up to about 12 times life size at the film plane. The entire area that is examined is about 9×9 mm square. A high-speed, high intensity EG&G 549 microflash with a $0.5 \mu\text{s}$ pulse duration light source is used to freeze the moving drops. For taking high magnification 4×5 photographs, the back lighting technique is found to be the most effective lighting arrangement for obtaining high contrast spray images. Single photographs provide direct drop size, spray shape, and drop collision and coalescence information which are extremely useful for evaluating different nozzle designs. This information is also important for determining which optical components should be used for obtaining the most accurate results in size distribution by using the laser diffraction particle sizer.

For a rapid analysis of the global and local characteristics of a spray, the laser diffraction particle sizer (Malvern) is considered to be the most efficient instrument. This instrument consists of a transmitter, receiver, signal processing units, and a mini-computer. The transmitter produces a collimated 9-mm diameter laser beam. The receiver has a Fourier transform lens which focuses the scattered light intensity onto 31 semiannular ring detectors. The size distribution can be calculated based on the measured scattered light intensity. A size distribution model has to be preselected so that the mini-computer can perform a least-square analysis to find the appropriate size distribution parameters. A Rosin-Rammler size distribution model was chosen to represent the size distribution in the spray. The Malvern 2200 instrument has several limitations which affect measurement accuracy. Extensive studies have

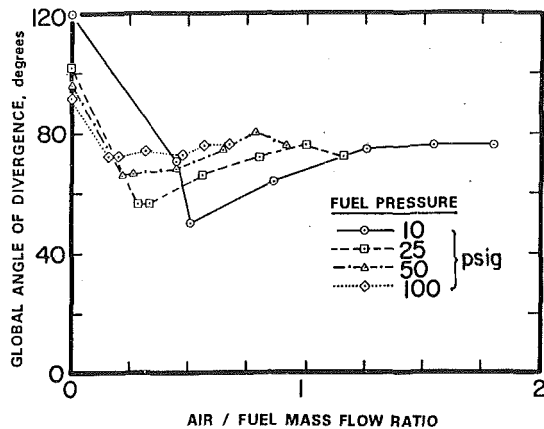


Fig. 3 Variation of spray angle as a function of air/fuel mass flow rate ratios

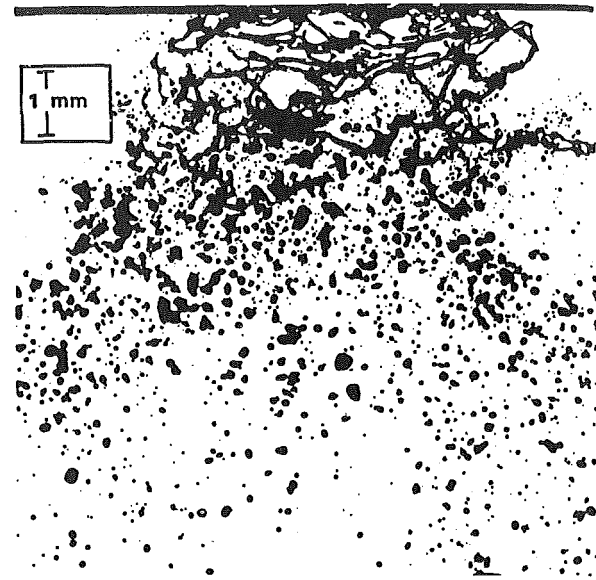
been made at CMU using a calibration reticle with known size distribution produced by Laser-Electro Optics Ltd. The following factors were proven to be crucial for determining accurate size distribution in sprays: the distance between the spray and receiver lens, focal length of the receiver lens, the angle between the position of the receiver optics and transmitting beam direction [6], and the responsivity of the ring detectors [7]. Based upon Fraunhofer diffraction theory, the drop positions in the laser beam do not affect the intensity distribution on the photo diode detectors. However, the transform lens can only refract the light which crosses the lens plane within its aperture. This introduces inherent differential biasing against small drops at distances longer than the lens focal length since smaller drops produce larger scattering angles which are truncated by the transform lens aperture. The critical distances between the receiver lens and the scattering medium are obtained by measurements using a calibration reticle traversed along the direction of the laser beam. The measured critical distances were also verified by diffraction theory. It was found that for 300 mm, 100 mm, and 63 mm focal length lenses, the critical distances are 336 mm, 122 mm, and 55 mm, respectively. Obscuration is a multidiffraction phenomenon which also needs to be considered during the measurements. On the basis of the measurements made with stacked calibration reticles and suspended latex spheres in a liquid cell, obscuration should be limited to less than 50 percent. For obscuration of more than 50 percent, empirical corrections must be made for the multiple scattering effects.

Throughout the study, a 300-mm focal length lens was used and the distance from the center of the spray to the receiver lens was 10 in. The spray chamber was tilted about 3 deg from the optical axis so that interference of the laser light due to window reflection can be prevented and background signal noise is reduced to a minimum. Corrections were made by using the same calibration procedure suggested by Dodge [7] to calibrate the responsivity of each detector.

Measurements were made using the calibrated Malvern instrument at various axial and radial locations in the spray for a wide range of operating injection conditions. Variation of mean drop size (SMD), size distribution, obscuration, and contour maps of spray patterns are presented and discussed.

Experimental Results and Discussion

The effect of air and fuel mass flow rate on the variation of spray cone angle is examined by taking 35-mm photographs. The variation of spray angle as a function of air/fuel mass flow rate ratios is shown in Fig. 3. The measured spray cone angle is defined as the angle between the tangents to the spray envelope at the atomizer exit. For a fixed fuel injection



Fuel Pressure: 10 psig, Air Pressure: 0.18 psig
Fuel/air mass flow ratio: 2.29

Fig. 4 Close-up look at breakup region

pressure, the increase of air flow rate causes a reduction in spray cone angle. Since the conical shape of the spray is due to the radial velocity components in the flow, it is expected that the relative value of axial to radial velocities is increased.

After the spray angle reaches a minimum value at a certain air/fuel ratio, it starts to increase slightly.

The spray cone angle approaches a constant value of 80 deg when the air/fuel mass flow rate ratio is larger than 1 for the range of testing conditions. For fuel injection pressures greater than 10 psig, the breakup length decreases with increase in fuel injection pressure while air injection pressures are maintained constant. For fuel injection pressures less than 10 psig, the liquid sheet recedes to the inside of the nozzle and the breakup length cannot be measured.

The 4 × 5 format camera provides microscopic details of the local structure of the spray. Figure 4 is an example taken at the liquid sheet breakup region. Clusters of drops are formed due to nonuniform breakup of the liquid sheet. In spray combustion, the collection of drops into clusters can cause locally fuel rich mixtures which can result in reduced combustion efficiency. The instantaneous grouping phenomena of drops could be due to the concurrent mixing of fuel and air inside the atomizer. The spitting and streaking of liquid fuels are commonly observed in atomization when viewed with high-speed cameras. These phenomena are related to the upstream mixing processes inside the atomizer and instabilities developed during break up. In the present study fluctuations of injection pressures have been carefully eliminated from the supply system.

Detailed Malvern measurements were made at several centerline downstream stations with 36 different combinations of fuel and air mass flow rates. Figure 5 shows the variation of SMD versus the ratio of fuel and air mass flow rates at 1.5 cm centerline downstream from the nozzle exit. For a fixed fuel injection pressure, the increase of air flow rates normally causes a decrease in SMD. The rate of decrease in SMD is greatly reduced at high air flow rates so that beyond a certain air flow rate, further increase of the air flow rate does not produce better atomization. For a fixed air flow rate, the higher the fuel injection pressure, the smaller the SMD. This feature

1.5 cm CENTERLINE DOWNSTREAM

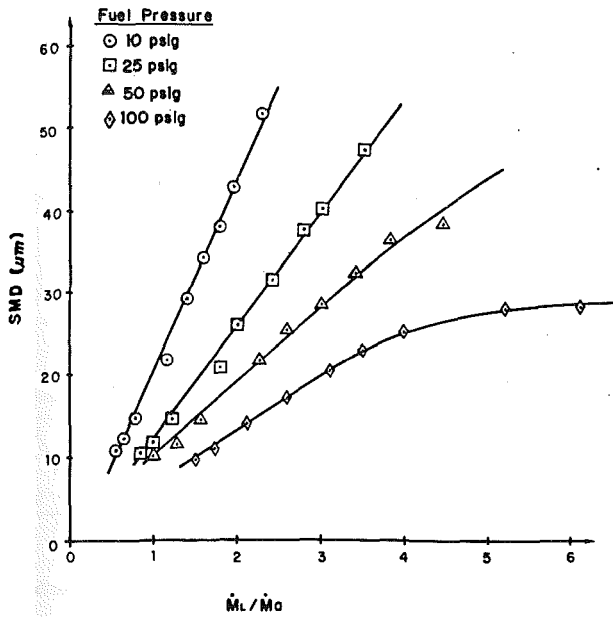


Fig. 5 Mean drop size as function of liquid/air mass flow rate ratio at 1.5 cm downstream

is quite opposite to what is observed in pressure atomizers. In air-assist swirl atomizers, the thickness of the liquid sheet decreases as the injection pressure increases due to the generation of higher degrees of swirl. Figure 5 also shows that SMD varies linearly with the increase of fuel to air mass flow rate for most of the test conditions. However, this linear correlation seems valid only for fuel to air mass flow rate ratios ranging from 0.5 to 4.

Figure 6 shows the variation of SMD versus the fuel to air mass flow rate ratios at 3 cm centerline downstream from the atomizer exit. The variation of SMD at 3 cm is found to be very similar to that at 1.5 cm. The linear correlation between SMD and fuel to air mass flow rate ratios is still valid for all of the test conditions. The slope of the straight lines at the upstream station (1.5 cm) is larger than at the downstream station (3.0 cm) for corresponding fuel injection conditions. At 5 cm centerline downstream from the atomizer, Fig. 7 shows that this linear proportionality disappears. By comparing the results shown in Figs. 5 through 7 a recommendation can be made to nozzle manufacturers that spray characterization for air-assist atomizers should be performed at regions closer to the nozzle where the atomization has just been completed, because there is a simple linear relation between line-of-sight SMD and fuel to air mass flow rate ratio. Measurements made in the flow field near the orifice not only provide the ease of finding simple relations for correlation equations, but also provide more representative locations for detecting the entire spray drop size spectra (see Fig. 8 N variation). It is also noted that there are two types of SMD variation with centerline downstream distance, depending on the ratio of fuel to air mass flow rates. For low values of fuel to air mass flow rate ratios, SMD increases progressively along the center line downstream distance. For higher values of mass flow rate ratios, SMD first decreases with increase in downstream distance, and then, after reaching a minimum value, increases progressively with increase in downstream distance x . Figure 8 shows the variation of SMD, Rosin-Rammler mean drop size parameter \bar{X} and size distribution parameter N at a fuel injection pressure of 50 psig and air injection pressure of 0.5 psig. The variations of N show that broadest size distributions are at the region close to the nozzle, becoming narrower with in-

3.0 cm CENTERLINE DOWNSTREAM

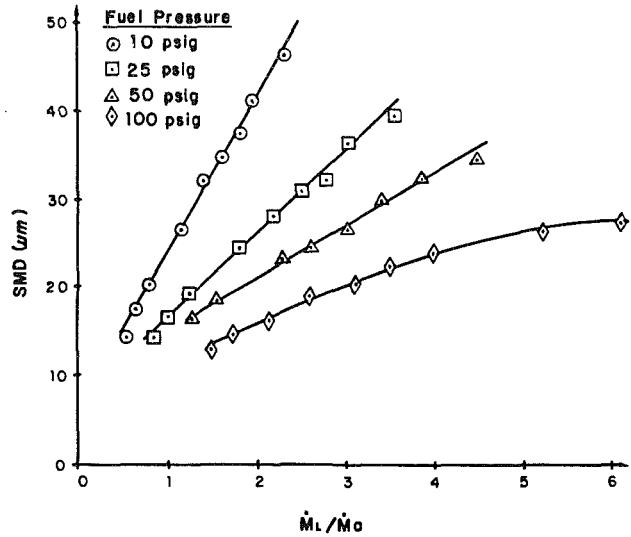


Fig. 6 Mean drop size as function of liquid/air mass flow rate ratio at 3.0 cm downstream

5.0 cm CENTERLINE DOWNSTREAM

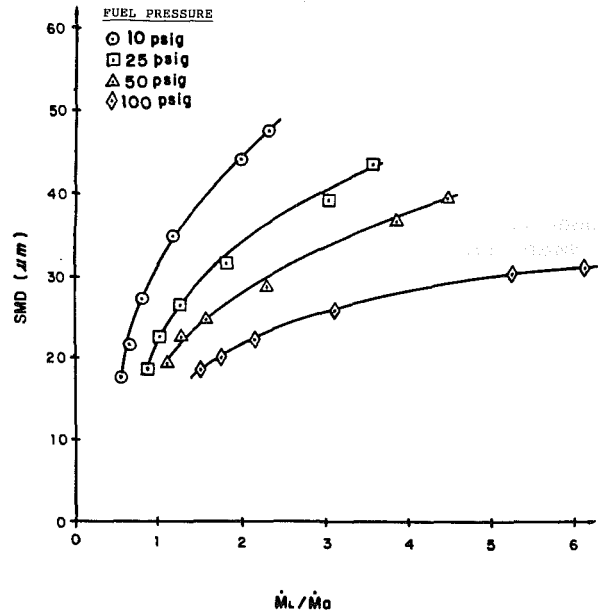


Fig. 7 Mean drop size as function of liquid/air mass flow rate ratio at 5.0 cm downstream

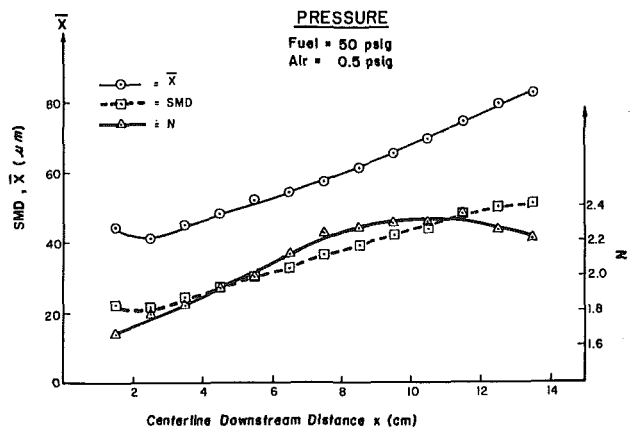


Fig. 8 Mean drop size and size distribution parameters as function of downstream distance

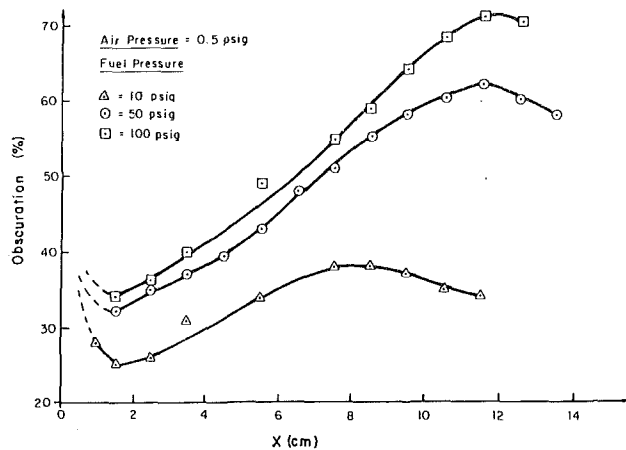


Fig. 9 Obscuration as function of downstream distance

crease in downstream distance until at a certain distance from the nozzle, the size distribution becomes broader again.

It indicates that a complete size spectrum has been determined after breakup. The effect of downstream distances only causes the redistribution of drop sizes. The explanation of this variation is related to the acceleration of drops and the consequent change in number density. When drops are injected at velocities lower than that of the air flow, the drops will be accelerated, depending on drop size and relative velocity. After a short distance of drop acceleration, all drops start to decelerate since the velocity of assist air decays rapidly. The effects of acceleration/deceleration trigger the drop collision and coalescence which causes the drop size spectrum to shift to a narrow range. The measurements of obscuration provide additional evidence about the changes in spray structure.

Obscuration, as measured by the center ring detector on the Malvern receiver, is a measure of the amount of incident laser intensity that can directly pass through the spray. The measured obscuration for three different fuel injection pressures at various center line downstream stations is shown in Fig. 9. Contrary to some previous expectations that obscuration should decrease as the spray becomes more dilute with downstream distance, the measurements show clearly that obscuration increases with increase in downstream distance and also with increase in fuel injection pressure. The increase in obscuration with increased fuel pressure can be explained by the decrease in mean drop size (SMD) and the increase in liquid volume concentration for higher fuel injection pressures. In the liquid sheet and ligament breakup regions, the obscuration is, obviously, very high. Obscuration drops quickly and reaches a minimum at the downstream distance where atomization processes are complete. Then obscuration starts to increase despite the fact that the spray becomes more dilute with downstream distance. It is believed that there are two factors which contribute to the increase in obscuration as downstream distance increases. One is the number density and the other is the length of the laser beam that passes through the spray. Because the spray is diverging, obscured path length increases with downstream distance, and this could result in an increase in laser attenuation by light scattering. However, change in number density depends upon whether the drops are accelerating or decelerating along the atomizing air flow especially in the region near the nozzle. For the case of drop acceleration, the number density decreases with downstream distance and this should result in a decrease in obscuration. But, if the effect of increase of exposed path length becomes more dominant, the net result can be an increase of obscuration in these cases. As drops eventually decelerate towards the main stream air flow, this causes a "compression" effect as number density increases. Number densities become large

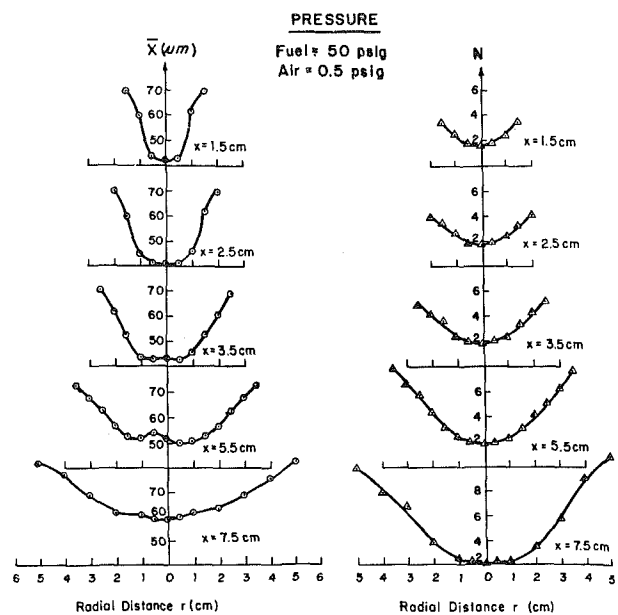


Fig. 10 Radial distribution of mean drop size and size distribution parameters at several axial stations

enough to produce a maximum obscuration at a certain distance from the nozzle. From there on downstream, the spray dispersion and evaporation come into play, resulting in a decline in obscuration towards zero when all drops are finally evaporated. The effect of evaporation on the variation of SMD was evaluated using the d^2 -law for single droplet evaporation with the Ranz-Marshall [8] correction. It was found that the effect of evaporation on the variation of SMD was negligibly small over the 8 cm distance from the nozzle exit where measurements were made.

Detailed line-of-sight measurements in the radial direction, at several axial stations, were also made for several combinations of fuel and air injection pressures. The measured Rosin-Rammler parameters \bar{X} and N for fuel injection pressure 50 psig and air injection pressure 0.5 psig is shown in Fig. 10. The plots of \bar{X} and N show variations in the local drop size distribution. The results show that the sprays are symmetric about the spray axis, and the width of the spray variation determined from the Malvern measurements agreed very well with those determined by photography. All the measurements were made within 8 cm distance from the nozzle and measured obscurations were all less than 50 percent. On the basis of previous calibration of the instrument, the measurement accuracy was within 5 percent for this range of conditions. For all the sprays that were tested, the spray structures were found to be similar. In the radial direction, smaller drops are mostly concentrated in the center region of the spray while larger drops are mostly concentrated in the outer regions of the spray. The broadest size bands are in the center area becoming more monosized towards the outer layer. From the data shown in Fig. 9, a contour map with constant SMD lines can be constructed by calculating the SMD's from \bar{X} and N , revealing a picture of the spray structure. A contour map for fuel injection pressure 50 psig and air injection pressure 0.5 psig is shown in Fig. 11. For the higher fuel injection pressures, the smaller drops have higher inertia allowing them to penetrate farther and to wider distances from the nozzle.

The variations of mean drop size and size distribution in the spray cannot be fully analyzed without knowing the velocity field. Since the liquid fuel is injected co-currently with the atomizing air flow, a separate study was made of the aerodynamic structure of air flow without fuel injection. Measurements of local air velocity were made using a single

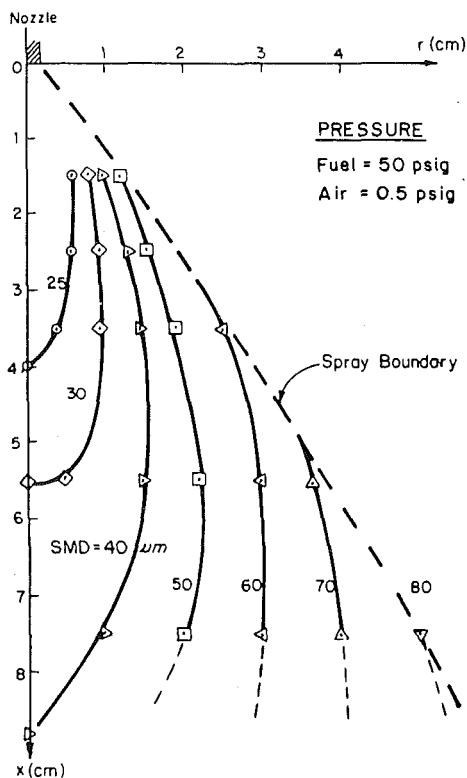


Fig. 11 Isolines of mean drop size

component He-Ne laser anemometer system, utilizing a Bragg cell as a beam shifter to frequency shift the first deflected beam. The measured velocity component was in the plane of the two incident beams and perpendicular to their bisector. The forward scatter system was used to detect signals from seeding particles in the air flow. All three components of the velocity were obtained sequentially by rotating the plane of the incident beams and angles. Single particle, time-domain, signal processing was used to build up the velocity probability density functions from which both mean and RMS velocities were obtained.

The measured axial and tangential velocity components at various axial stations for air injection pressure 0.5 psig is shown in Fig. 12. The upstream axial velocity profiles are different from those at the downstream stations. For the first 5 cm region from the nozzle, the maximum axial velocity component is at a distance away from the axis. The tangential velocity profiles have similar forms at the various axial stations. In the inner region, the flow corresponds to that of a forced vortex motion. In the outer region, the flow character is close to that of free vortex motion. The air flow is generally very symmetric for the mean axial flow velocities. However, air core distortion does occur especially for high air injection pressures. Detailed drop size-velocity correlation and air flow velocity measurements will be made using the newly developed phase/Doppler analyzer. This will allow a more comprehensive analysis of the drop/air interactions, slip effects, and mixing processes.

Summary

Detailed measurements have been made of mean drop size (SMD) and size distribution parameters as well as air flow velocity components for a concurrent swirl mixing air-assist

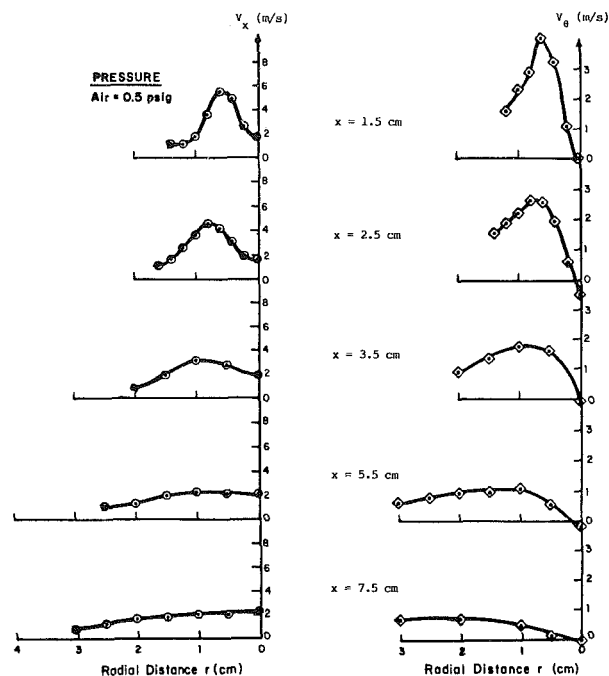


Fig. 12 Velocity distributions in atomizing air jet

atomizer spray. Several interesting phenomena about the aerodynamic structure of air-assist swirl atomizer sprays were observed and analyzed. These phenomena include: the non-uniform grouping of drops, variation of SMD along center line downstream distance, air core distortion, and effects of obscuration, drop acceleration/deceleration and evaporation. The process of liquid fuel atomization is closely related to all these phenomena. The ultimate understanding of spray combustion requires detailed investigations of the fundamental physics of liquid fuel atomization. The results reported in this study are the first stage of an extensive series of measurements in sprays that are being made at Carnegie-Mellon University.

Acknowledgments

The authors wish to thank Geng Wang and John Feeney for support in making the measurements. Financial support was provided by grants from Parker Hannifin and NASA-Lewis, Cleveland.

References

- 1 Giffen, E., and Muraszew, A., *The Atomization of Liquid Fuels*, Wiley, New York, 1953.
- 2 Chigier, N., *Energy, Combustion and Environment*, McGraw-Hill, 1981.
- 3 Lefebvre, A. W., *Gas Turbine Combustion*, McGraw-Hill, 1983.
- 4 ICLASS-82, The 2nd International Conference on Liquid Atomization and Spray Systems, Proceeding, Madison, Wis., June 1982.
- 5 Simmons, H. C., "The Prediction of Sauter Mean Diameter for Gas Turbine Fuel Nozzles of Different Type," *ASME Journal of Engineering for Power*, Vol. 102, July 1980, pp. 646-652.
- 6 Hirtleman, E. D., Oechsle, V., and Chigier, N. A., "Response Characteristics of Laser Diffraction Particle Size Analyzers: Optical Sample Volume Extent and Lens Effects," *Optical Engineering*, Vol. 23, No. 5, 1984, pp. 610-619.
- 7 Dodge, L. G., "Calibration of Malvern Particle Sizer," *Applied Optics*, Vol. 23, 1984, p. 2415.
- 8 Ranz, W. E., and Marshall, W. R., Jr., *Chemical Engr. Prog.*, Vol. 48, 1952, pp. 141-173.

Hiroharu Kato
 Hajime Yamaguchi
 Shinzo Okada¹
 Kohei Kikuchi²
 Masaru Miyanaga

Department of Naval Architecture,
 Faculty of Engineering, University of Tokyo,
 Hongo, 7-3-1, Bunkyo, Tokyo 113, Japan

Suppression of Sheet Cavitation Inception by Water Discharge Through Slit

This paper studies experimentally the suppression effect of water discharge on incipient and developed sheet cavitation on a hemispherical headform. The water is discharged tangentially from a slit upstream of a cavitating region into the boundary layer on the headform. Increasing the discharge rate, the length of the sheet cavity becomes shorter and then the cavity is suppressed completely. Flow visualization test shows the generation of wavy motion in the boundary layer which disturbs the separated zone, resulting in disappearance of the sheet cavitation.

Introduction

It is well-known that cavitation inception depends on the characteristics of boundary layer [1]. When the Reynolds number is lower than a critical value, laminar separation occurs at the adverse pressure region of a body. Lowering static pressure, cavitation originates at the reattachment region of the separated boundary layer and the cavity grows to fill the separation bubble, resulting in a steady sheet type cavitation. It can therefore be conceived that the control of sheet cavitation inception can be made by controlling the laminar separation. From this idea boundary layer tripping techniques using a strip of small roughness particles [2-6] or a tripping wire [7,8] have been developed for the control of cavitation. Blowing and suction are other effective techniques for the control of the boundary layer. These techniques have been studied widely in the field of aeronautics. However, the effect on cavitation has not been studied deeply until now.

This paper treats the suppression effect of water discharge on incipient and developed sheet cavitation on a hemispherical headform. Water was discharged tangentially from an axisymmetric slit upstream of separation region into the boundary layer on the headform. The effect of discharge rate, cavitation number, and Reynolds number on suppression were investigated experimentally.

Flow visualization experiments were performed at non-cavitating conditions to investigate the mechanism. Oil film method and ink tracer method were used. Characteristics of the boundary layer were also calculated using multistrip method [9]. The mechanism of cavitation suppression will be discussed with reference to these observations and calculations.

¹Presently Hiratsuka Research Laboratory, Sumitomo Heavy Industries Ltd., Hiratsuka, Japan.

²Presently Nippon Kokan Co. Ltd., Yokohama, Japan.

Contributed by the Fluids Engineering Division for publication in the JOURNAL OF FLUIDS ENGINEERING. Manuscript received by the Fluids Engineering Division October 15, 1986.

Experimental Setup

The tested headform is shown in Fig. 1. Its head shape is a hemisphere of 15 mm in radius when the width of slit is set at 1.5 mm. The width can be adjusted in the range of 0-5 mm. Detail of the slit is shown in Fig. 2. Position of the slit was decided by compromising between two conflicting requirements. Firstly cavitation should not generate at the slit, that means, the position should be upstream enough from the low pressure zone. Secondly discharged water should have considerable effect on the separated zone, that means, the position should be as close as possible to the lower pressure zone. The headform with the slit was installed in the TE type cavitation tunnel at the University of Tokyo. Details of the tunnel were given elsewhere [10]. It was set at the center of the section with a supporting strut as seen in Fig. 1. Discharged water was supplied through a hole inside the strut.

The cross section of the tunnel is 80 mm × 80 mm and the

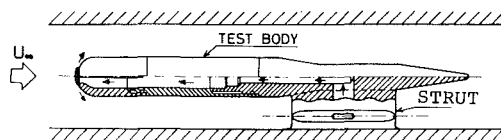


Fig. 1 Headform with slit

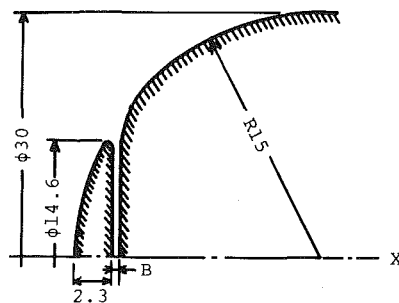


Fig. 2 Detail of the slit

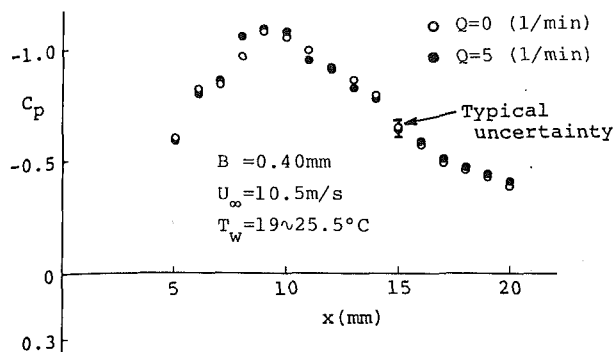


Fig. 3 Pressure distribution along headform with and without discharge

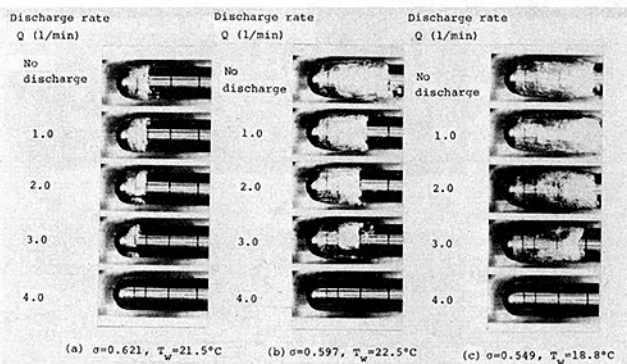


Fig. 4 Effect of discharge ($B = 0.30$ mm, $U_\infty = 12.0$ m/s)

headform is 30 mm in diameter. Therefore, side wall effects cannot be neglected. Velocity distribution at the outer edge of the boundary layer was measured along the headform surface using a laser doppler velocimeter. The pressure distribution was estimated using Bernoulli's equation as shown in Fig. 3. The difference in pressure distributions with and without water discharge is within the range of experimental uncertainty. The water was bypassed at the top of the settling tank in the loop and discharged by the pressure difference between the tank and the slit. No pump or other feeding devices were used to eliminate the generation of small air nuclei that was inevitable in a pump. Therefore, no discharge can be made when the main flow does not circulate in the tunnel. The flow rate was controlled with a valve and measured by a Rotameter whose accuracy was ± 0.1 l/min. The maximum discharge flow rate varied with the tunnel mean flow velocity. The range of maximum flow rate was 4–6 l/min with the main flow velocity varying between 8–15 m/s.

After preliminary tests, three slit widths of 0.25, 0.30, and 0.42 mm were selected. It was measured with a thickness gauge whose accuracy was better than ± 0.01 mm.

Experiments of Cavitation Suppression

A series of photographs of cavitation suppression caused by water discharge are shown in Figs. 4(a)–(c). The cavitation was typical sheet type cavitation at no discharge condition. It was stable, axisymmetric, and transparent at its fore part. The ap-

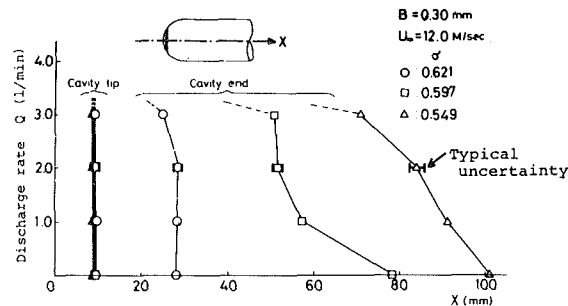


Fig. 5 Change of cavity leading and trailing edges with discharge rate

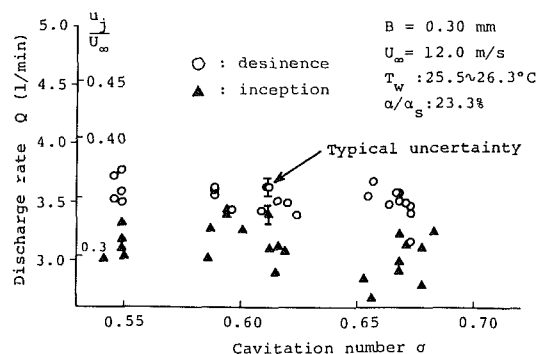


Fig. 6 Suppression discharge rate versus cavitation number

pearance and the length were uniform circumferentially. At low discharge rates of 1–2 l/min, the length of cavity became shorter and the cavity end moved upstream. The cavity leading edge, however, did not move by the discharge. It is clearly shown in Fig. 5 which was measured from photographs shown in Fig. 4.

Increasing discharge rate, the cavity no longer remained uniform circumferentially. As seen in the photograph of $Q = 3$ l/min in Fig. 4(a), the cavity pattern became patch type at the lower part of the body. Cavitation was completely suppressed at a discharge rate between 3 and 4 l/min. At a lower cavitation number, the length of cavity became longer, though the necessary discharge rate for complete suppression did not change.

Parameters affecting the suppression were also examined. They were cavitation number, discharge rate, velocity and Reynolds number. Figure 6 shows the effect of cavitation number on the suppression discharge rate. The nondimensional discharge water velocity at the slit, u_j/U_∞ is also shown as the ordinate. Open circles are the critical suppression discharge rate which was measured by increasing the discharge rate. Desinence of cavitation was judged by the inception interval of the last cavity patch. When the interval became more than a few seconds, it was defined as desinence. Solid triangles are the critical incipient discharge rate which was measured by decreasing flow rate from the completely suppressed condition. When a stable cavity existed more than a few seconds, it was defined as inception. The critical discharge rate was almost constant regardless of the cavitation number, though

Nomenclature

B = width of slit
 C_p = pressure coefficient
 D = diameter of headform
 Q = water discharge rate
 Re = Reynolds number $\equiv UD/\nu$
 T = temperature
 U, u = velocity

x = axial distance from nose
 y = coordinate across boundary layer
 α/α_s = relative air content to saturated condition
 ν = kinematic viscosity
 σ = cavitation number

Subscripts

c = critical
 e = external
 j = slit
 w = water
 ∞ = infinity

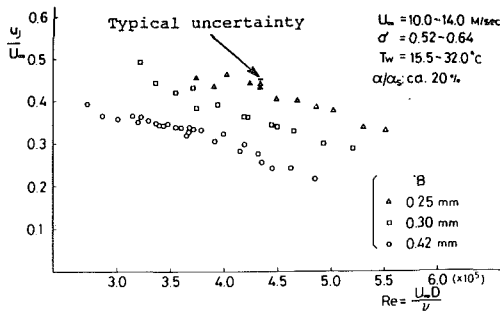


Fig. 7 Effect of Reynolds number

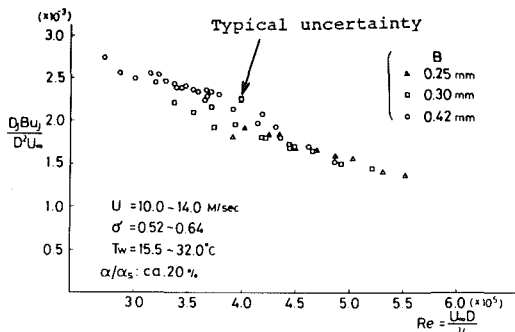


Fig. 8 Nondimensional discharge rate versus Reynolds number

there were a few very low points for the inception. There was hysteresis between incipient and desinent conditions. That is, the discharge rate was less at inception than that at desinence. The desinent discharge rate was more stable than the incipient rate as seen in the figure. Therefore, hereafter only the desinent condition will be discussed.

It is worth noting that the discharge velocity is relatively low compared to the main flow velocity. The value of u_j/U_∞ is in the range of 0.2-0.5, where u_j and U_∞ are discharge velocity at the outlet of the slit and main flow velocity, respectively. Therefore, this phenomenon is not similar to the boundary layer blowing where u_j is usually larger than U_∞ .

The effect of Reynolds number was examined by changing the main flow velocity as well as the water temperature. The static pressure in the system was set to get the cavity length of 20-50 mm at the no discharge condition and five measurements of desinence were repeated at one condition. Averaged data of the five measurements are shown in Figs. 7 and 8. Figure 7 shows the nondimensional critical velocity at the outlet of the slit. Whereas, Fig. 8 is the nondimensional discharge rate against Reynolds number.

For a decreasing Reynolds number, the discharge rate for the complete suppression increased and it seems that there is a critical Reynolds number below which the water discharge does not have any effect. The critical Reynolds number differed with the width of slit, B . For example, $Re_c \approx 2.5 \times 10^5$ and 3×10^5 at $B = 0.42$ mm and 0.30 mm, respectively. Comparing Figs. 7 and 8, it seems that the governing parameter is not the discharge velocity but the volumetric discharge rate.

Flow Visualization

Two kinds of flow visualization techniques were used for the experiment with no cavitation. These were oil film method and ink tracer method. Separated zone on the headform surface was visualized with the oil film method. A typical result after a one minute test is shown in Fig. 9. The oil used was transmission oil with carbon black powder. Separation and reattachment points judged from the oil film test are shown in Fig. 10. The behavior of the separated zone agreed well with that of the sheet cavity. Leading edge of the separated zone

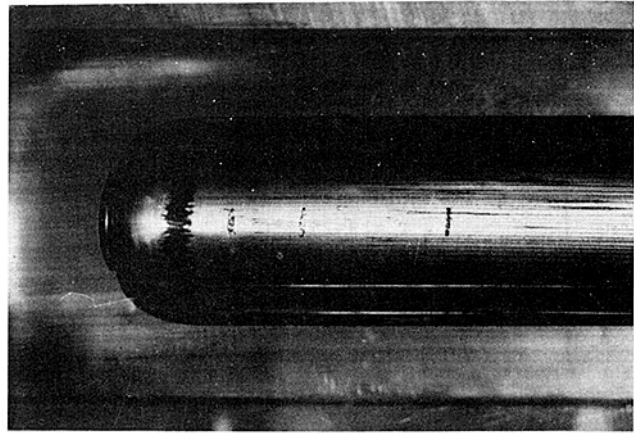


Fig. 9 Oil film method

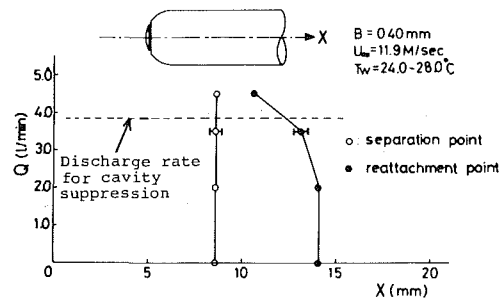


Fig. 10 Variation of separation bubbles by discharge (oil film method)

did not move by changing the discharge rate. Whereas, its trailing edge moved upstream which was quite similar to the case of cavity. The vanishing flow rate also agreed well with that of cavity desinence.

Flow inside of the boundary layer was examined by the ink tracer method, where ink-colored water was discharged from the slit as seen in Fig. 11. In the figure the main flow is from right to left.

As seen in the photographs, the flow is smooth and has no disturbance at the low discharge rates. On the contrary, wavy motion can be seen at higher discharge rate. It starts just downstream of the slit. The wave length is about 2.2 mm. Its amplitude increases downstream and finally the wave breaks into turbulent flow. The wavy motion could also be seen in circumferential direction whose wave length was almost the same as that of the longitudinal wave. The separated flow at the shoulder of the headform couldn't be observed by the ink tracer technique, although it was clearly seen by the oil film method. This may be due to the very thin boundary layer thickness of less than 0.2 mm. Discussions of these flow observations will be made in detail later.

Boundary Layer Calculation

The analysis of the boundary layer along the hemispherical headform with discharge was made using the multi-strip method [9]. The complicated boundary layer with discharge was divided into several strips, whose velocity profiles were assumed to be of polynomial form for each strip. Applying the momentum equation of boundary layer to each strip, coupled differential equations of momentum were derived which could be solved using the Runge-Kutta method. Details of the analysis are given elsewhere [11].

A typical result is shown in Fig. 12, where the boundary layer is assumed to be laminar and $u_j/U_\infty = 0.307$. The thickness of the boundary layer becomes thinner at first because of acceleration of the outer flow. Then it becomes

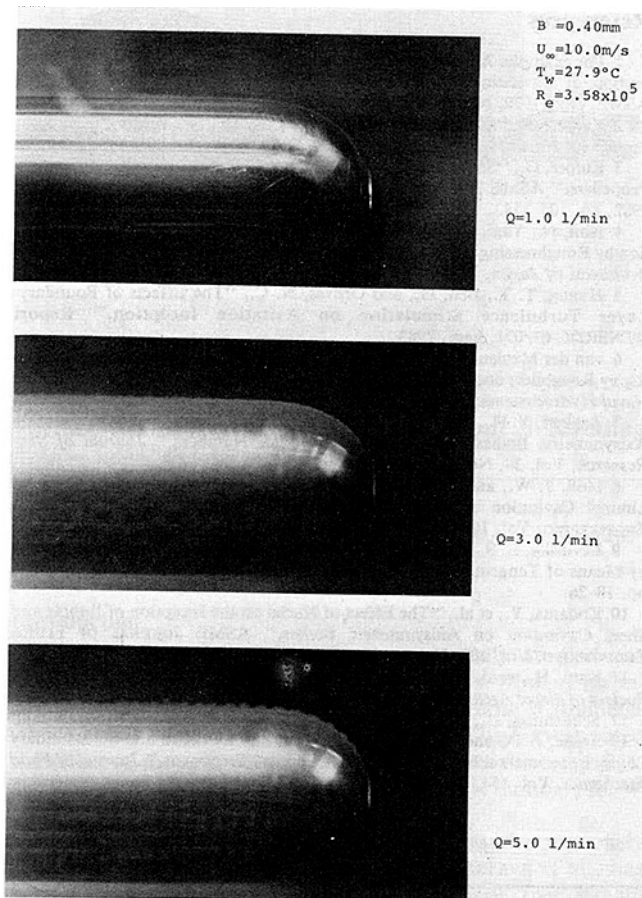


Fig. 11 Flow observation by ink tracer method

thicker again and the velocity gradient at the wall becomes smaller. Finally the boundary layer separates from the wall. The assumed uniform velocity profile at the outlet of the discharge flow becomes narrower and finally the uniform region vanishes at $x/D=0.228$. Downstream of that point the velocity profile becomes gradually similar in shape to that of no discharge. An important result is the existence of a "point of inflexion" of the velocity profile caused by water discharge. According to the stability theory [12] the existence of "point of inflexion" is the necessary and sufficient conditions for the amplification of disturbances. It usually arises in a boundary layer at a decelerating flow condition. But in the present case it arises even in the accelerating boundary layer because of the discharged flow.

Discussion

Blowing is an effective technique of boundary layer control. In such a case the blowing velocity is usually larger than the main flow velocity and the effect is the prevention of separation by supplying energy to the flow inside the boundary layer. However, the present flow mechanism is not the same as that of blowing. The most significant effect of discharge is the generation of wavy motion. This wave has a wave length of about 2 mm which is much larger than the boundary layer thickness.

The mechanism of cavity suppression can be explained as follows. First, the existence of the slit itself does not give any disturbance at no discharge condition, because it exists in the accelerating flow region (see Fig. 11). Therefore the characteristics of the boundary layer are almost same as that without the slit. The critical Reynolds number of turbulent transition is about 5×10^6 for a hemispherical headform. In

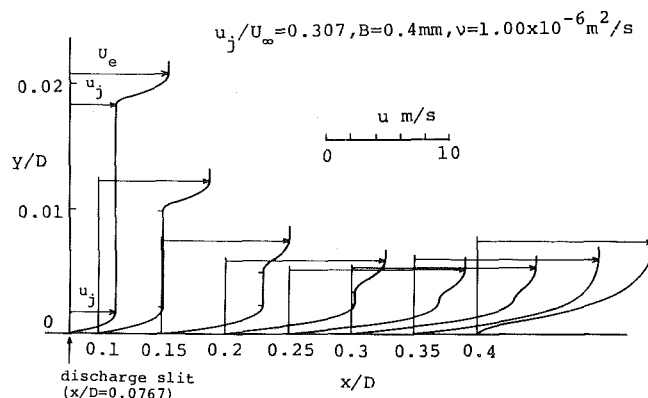


Fig. 12 Boundary layer calculation (laminar case)

the present experiment the Reynolds number is less than 5×10^5 . Therefore, laminar separation occurs at the deceleration region on the headform surface, and this leads to the occurrence of sheet cavitation.

When some amount of discharged water flows into bottom of the boundary layer, a point of inflexion is incorporated into the velocity profile. Because of it, the boundary layer becomes unstable and small disturbances are amplified even in the accelerated flow region. Then, finally the flow becomes turbulent which prevents laminar separation. Recently Franc and Michel [13] found that sheet (attached) cavitation could be suppressed by transition to turbulent flow. The present finding is thought to be similar phenomenon as their observation.

The discharge velocity should be less than that of the local main flow velocity to realize the point of inflexion in the boundary layer. On the other hand, the discharge rate should be enough to keep the inflected velocity profile intact. That is, the discharge velocity and width are both important to get cavitation suppression. This might be the reason why the data become consistent when they are plotted against the discharge rate as seen in Fig. 8. It should be emphasized that this type of cavitation suppression mechanism is effective only for sheet (attached) cavitation. At the present experiment bubble cavitation was sometimes observed when sheet cavitation was completely suppressed by discharge.

As mentioned before, there is a critical Reynolds number below which the discharge rate does not affect the suppression of cavitation. The reason is that the small disturbances cannot amplify under a critical Reynolds number. The observed critical Reynolds number based on displacement thickness was about 600 at $B=0.4$ mm. Whereas critical Reynolds number calculated using Orr-Sommerfeld equation is 520 for a flat plate [12].

The length of the cavity or that of the separation bubble becomes shorter when the discharge rate becomes more. This phenomenon is not fully understood. The water discharge changes the pressure distribution little as shown in Fig. 3. The discharge velocity is also much less than the external flow velocity, so that the jet momentum effect seems insignificant. It is verified by the fact that the leading edge of the cavity does not move by the discharge. One possible explanation is the disturbance effect of the amplified wavy motion. In the case of cavity flow, the increased disturbance on the cavity surface might prevent the existence of a stable cavity at its rear part.

Conclusions

The suppression effect of water discharge on incipient and developed sheet cavitation on a hemispherical headform was investigated. The water was discharged tangentially from a slit upstream of cavitation region into the boundary layer on the headform. The following conclusions have been reached:

1. A sheet cavity can be suppressed completely by the water discharge. The discharge velocity required is lower than the main flow velocity.

2. The water discharge is effective even at a low cavitation number where a long cavity should develop in the case of no discharge.

3. There is a critical Reynolds number below which the water discharge does not have any effect.

4. Flow visualizations showed generation of wavy motion in the boundary layer due to the water discharge even in the accelerating flow region. The boundary layer calculation also suggested the generation of a "point of inflexion" of the velocity profile due to water discharge which introduced instability of the boundary layer.

5. The wavy motion, or in other words, the transitional flow motion disturbs the separation bubble or the sheet cavity, resulting in a shorter bubble length or a shorter cavity leading finally to disappearance of either.

Acknowledgments

The authors wish to thank Mr. M. Maeda, and other staff at the highspeed laboratory, Department of Naval Architecture, University of Tokyo, for their assistance in conducting the experiment. The authors also thank Mr. T. Komura, Ms. K. Nishida, and Mr. S. Chattopadhyay for their sincere help during preparation of the paper.

References

- 1 For example: Arakeri, V. H., and Acosta, A., "Viscous Effects in the Inception of Cavitation," *International Symposium on Cavitation Inception*, ASME, Dec. 1979, New York, pp. 1-9.
- 2 Kuiper, G., "Scale Effects on Propeller Cavitation Inception," *12th Symposium on Naval Hydrodynamics*, Wash., D.C., 1979, pp. 401-429.
- 3 Kuiper, G., "Some Experiments with Specific Types of Cavitation on Ship Propellers," *ASME JOURNAL OF FLUIDS ENGINEERING*, Vol. 104, No. 1, Mar. 1982, pp. 105-114.
- 4 Ishii, N., Yagi, H., and Yuasa, H., "Model Testing of Propeller Cavitation by Roughnessing the Leading-Edge of Blades," *Journal of Society of Naval Architects of Japan*, Vol. 153, June 1983, pp. 106-116.
- 5 Huang, T. T., Belt, G., and Groves, N. C., "The Effects of Boundary-Layer Turbulence Stimulation on Cavitation Inception," Report DTNSRDC-83/071, Sept. 1983.
- 6 van der Meulen, J. H. J., and Ye, Yuan-Pei, "Cavitation Inception Scaling by Roughness and Nuclei Generation," *Proceedings of 14th Symposium on Naval Hydrodynamics*, 1983, pp. 507-545.
- 7 Arakeri, V. H., and Acosta, A. J., "Cavitation Inception Observations on Axisymmetric Bodies at Supercritical Reynolds Numbers," *Journal of Ship Research*, Vol. 20, No. 1, Mar. 1976, pp. 40-50.
- 8 Holl, J. W., and Carroll, J. A., "Observations of the Various Types of Limited Cavitation on Axisymmetric Bodies," *ASME JOURNAL OF FLUIDS ENGINEERING*, Vol. 103, No. 3, Sept. 1981, pp. 415-423.
- 9 Levinsky, E. S., and Schappeller, R. H., "Analysis of Separation Control by Means of Tangential Blowing," *Journal of Aircraft*, Vol. 12, No. 1, 1975, pp. 18-26.
- 10 Kodama, Y., et al., "The Effect of Nuclei on the Inception of Bubble and Sheet Cavitation on Axisymmetric Bodies," *ASME JOURNAL OF FLUIDS ENGINEERING*, Vol. 103, No. 4, 1981, pp. 557-563.
- 11 Kato, H., et al., "Control of Sheet Cavitation by Injection," *Journal of Society of Naval Architects of Japan*, Vol. 150, 1981, pp. 140-147 (in Japanese).
- 12 Schlichting, H., *Boundary-Layer Theory*, Seventh Edition, McGraw-Hill.
- 13 Franc, J. P., and Michel, J. M., "Attached Cavitation and the Boundary Layer: Experimental Investigation and Numerical Treatment," *Journal of Fluid Mechanics*, Vol. 154, 1985, pp. 63-90.

Further Studies on Laminar Flow About a Rotating Sphere in an Axial Stream

M. A. I. El-Shaarawi,¹ M. M. Kemry,¹ and S. A. El-Bedeawi¹

Introduction

El-Shaarawi et al. (1985) have numerically studied the steady laminar boundary layer produced by a flow of an incompressible fluid over a sphere rotating about a diameter whose axis is aligned with the free stream. They investigated the effect of the spin parameter, Ta/Re^2 ,² over the range $0 \leq Ta/Ra^2 \leq 10,000$ at a fixed value of Reynolds number, $Re = 10,000$.

In the present paper a numerical study, using the previously developed finite difference scheme of El-Shaarawi et al., has been carried out to investigate the effect of free stream Reynolds number. Results are presented for the range $5000 \leq Re \leq 300,000$ for values of $Ta/Re^2 = 0$ and 1.

Results and Conclusions

Effect of Reynolds Number on Separation Angle. Table 1 reports the effect of Re on θ_s , the separation angle, for both $Ta/Re^2 = 0$ and 1. As seen in this table, in the range $5000 \leq Re \leq 300,000$ and for a given Ta/Re^2 , there is a shift in the position of the laminar separation line by at most 2 deg. This indicates that Reynolds number has a negligible effect on the separation angle. This conclusion is in good agreement with the work of other investigators (see, for example, Fage, 1937 and Schlichting, 1953). Hence it may be assumed that the separation angle is a function of Ta/Re^2 only, and the curve given by El-Shaarawi et al. (1985) for the variation of θ_s with Ta/Re^2 may be considered a universal curve for any value of Re .

Effect of Re on C_D and C_M . Figures 1 and 2 illustrate the effect of Re on the variation of the nondimensional meridional and azimuthal wall shear stresses, (T_x and T_y , respectively), with the meridional angle θ . As seen from these figures, increasing Re decreases slightly the values of T_x and T_y . This is because both the U -profiles and the V -profiles become steeper with increasing Re . This means that both $(\partial U/\partial Z)_0$ and

$(\partial V/\partial Z)_0$, and consequently the dimensional shear stresses, t_x and t_y , increase as Re increases. However, since $T_x = (\sqrt{2}/Re)(\partial U/\partial Z)_0$ and

$$T_y = \sqrt{\frac{Ta}{Re^2}} \sqrt{\frac{2}{Re}} (\partial V/\partial Z)_0,$$

it may be concluded from Figs. 1 and 2 that each of the products $\sqrt{Re}/(\partial U/\partial Z)_0$ and $\sqrt{Re}/(\partial V/\partial Z)_0$ is, for a given value of Ta/Re^2 , approximately constant, regardless of the value of Re .

Table 2 illustrates the effect of Re on C_D and C_M ; both C_D and C_M decrease considerably as Re increases. This is expected since, as was mentioned by El-Shaarawi et al. (1985), for a given Ta/Re^2 , each of C_D and C_M is, for the first approximation, proportional to \sqrt{Re} . To check the accuracy of this statement the values of C_D and C_M in Table 2 show that, over the range $5000 \leq Re \leq 300,000$, $C_D\sqrt{Re}$ is nearly constant with maximum deviations of 4.3 percent and 7.1 percent for $Ta/Re^2 = 0$ and 1, respectively, while for $Ta/Re^2 = 1$ the value of $C_M\sqrt{Re}$ is constant within 0.63 percent.

Correlations for C_D and C_M . As pointed out, there are two important parameters which affect the solution. These

Table 1 Effect of Re on the separation angle, θ_s

Re	Ta/Re ²	θ_s , in degrees	
		0	1
300,000		109.0	106.3
200,000		108.3	106.2
100,000		108.0	105.4
50,000		107.3	-
10,000		107.0	104.5
5,000		107.1	105.0

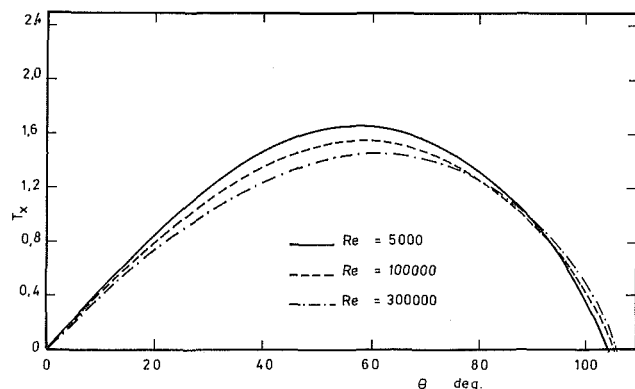


Fig. 1 Effect of Re on dimensionless azimuthal wall shear stress, $Ta/Re^2 = 1$

¹ Associate Professors and Lecturer, respectively, Department of Mechanical Engineering, Al Azhar University, Nasr City, Cairo, Egypt.

² $Ta = \text{Taylor number } 4 \Omega^2 a^4 / \gamma^2$
 $Re = \text{Reynolds number } 2U_\infty a / \gamma$
 $U_\infty = \text{free stream velocity}$
 $\Omega = \text{rotational velocity}$
 $a = \text{radius}$
 $\gamma = \text{kinematic viscosity}$

Contributed by the Fluids Engineering Division of THE AMERICAN SOCIETY OF MECHANICAL ENGINEERS. Manuscript received by the Fluids Engineering Division, June 2, 1986.

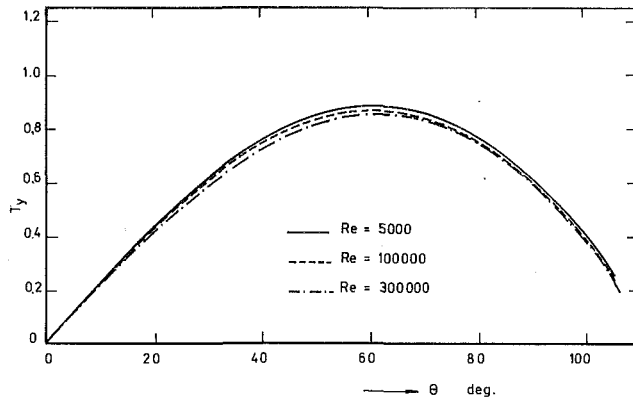


Fig. 2 Effect of Re on dimensionless meridional wall shear stress, $Ta/Re^2 = 1$

Table 2 Effect of Re on C_D and C_M

Re	Ta/Re^2	C_D		C_M
		0	1	1
300,000		0.01186	0.0120771	0.0231643
200,000		0.01465	0.0149970	0.0283864
100,000		0.020961	0.021587	0.0398974
50,000		0.029824	-	-
10,000		0.067164	0.0701300	0.1258300
5,000		0.095827	0.1001102	0.1806209

parameters are the free stream Reynolds number, Re, and the spin parameter, Ta/Re^2 . The effect of the latter was investigated separately (El-Shaarawi et al., 1985) while the effect of the former is studied in the present paper. This was done by keeping one parameter fixed at a constant value while the other parameter was varied. However an important question arises: is it possible to estimate the values of important quantities, such as C_D and C_M , for different combined values of the controlling parameters (Re and Ta/Re^2) other than those values investigated in the present work? An attempt to answer this question has been made and is concerned with the two coefficients C_D and C_M , of particular interest to engineers.

The results presented in Table 2 show that, for a given value of Ta/Re^2 , C_D is inversely proportional to \sqrt{Re} . On the other hand, the results presented by El-Shaarawi et al. (1985) show that, at a constant value of Re, C_D increases with increasing Ta/Re^2 . Plotting the variation of C_D with Ta/Re^2 on a log-log scale shows that, for Re = 10,000 and for $25 \leq Ta/Re^2 \leq 10,000$, C_D can be given within about 4 percent by the following equation:

$$C_D = 0.0165(Ta/Re^2)^{0.65} \quad (1)$$

Combining the effects of Re and Ta/Re^2 in one equation gives the following correlation, for any value of Re and $25 \leq Ta/Re^2 \leq 10,000$:

$$C_D \sqrt{Re} = 1.65(Ta/Re^2)^{0.65} \quad (2)$$

For values of $0 \leq Ta/Re^2 < 25$ we may assume that, for a given Re, C_D is proportional to Ta/Re^2 and hence for the simultaneous effect of the two controlling parameters we have

$$C_D \propto \frac{Ta/Re^2}{\sqrt{Re}} \quad (3)$$

To put this proportionality relation in an appropriate form, the value of C_D must be known at some reference values of Re and Ta/Re^2 . Let these reference values be subscripted by the symbol r , then the above proportionality relationship can be presented in the following form

$$C_D \sqrt{Re} = (C_D \sqrt{Re})_r \left\{ 1 + k[(Ta/Re^2) - (Ta/Re^2)_r] \right\}, \quad (4)$$

in which $k(C_D \sqrt{Re})_r$ is a constant of proportionality for the relation (3).

Considering Re = 10,000 and $Ta/Re^2 = 1$ as the reference values and using the computed value of C_D at these reference values, 0.07013, we have $(C_D \sqrt{Re})_r = 7.01$. A curve fit of the present numerical data showed that the value of k , which appears in equation (4) is 0.045. Therefore, equation (4), after substitution of these constants, reduces to the following correlation which fits the numerical data, over the range $0 \leq Ta/Re^2 < 25$, within about 2 percent.

$$C_D \sqrt{Re} = 7.01 \left[1 + 0.045 \left(\frac{Ta}{Re^2} - 1 \right) \right] \quad (5)$$

For Re = 10,000, plotting C_M against Ta/Re^2 on a log-log scale showed that over the range $25 \leq Ta/Re^2 \leq 10,000$, C_M can be represented within about 5 percent, by the following equation

$$C_M = 0.06279(Ta/Re^2)^{-0.284} \quad (6)$$

Introducing the combined effect of Re and Ta/Re^2 into equation (6) gives the following correlation, for any value of Re, over the range $25 \leq Ta/Re^2 \leq 10^5$

$$C_M \sqrt{Re} = 6.279(Ta/Re^2)^{-0.284} \quad (7)$$

Similarly, for values of $0 \leq Ta/Re^2 < 25$ the following correlation for C_M , within about 4 percent, is obtained

$$C_M \sqrt{Re} \sqrt{Ta/Re^2} = 12.583 \quad (8)$$

Correlations for θ_s and T_y at the Separation Point. An attempt was made to find a correlation for θ_s . By curve fitting θ_s versus Ta/Re^2 the correlation was found to obey the following form within 2 percent over the range $1 \leq Ta/Re^2 \leq 100$:

$$\theta_s = 1.833 - \frac{1}{9} \log(Ta/Re^2) \quad (9)$$

Finally, it is important to mention that the nondimensional azimuthal wall shear stress does not vanish at the separation point. Investigation of the values of T_y at θ_s showed that the following equation is in excellent agreement with the numerical data over the range $0 \leq Ta/Re^2 \leq 10,000$:

$$T_{y \text{ at } \theta_s} = 0.24(Ta/Re^2)^{0.64} \quad (10)$$

Numerical Accuracy

Following the procedures described by Carnahan et al. (1969), it was shown by El-Bedeawi (1985) that the truncation error due to the approximation of each of the three governing equations (continuity, x -momentum and y -momentum equations) by its corresponding finite-difference representation is proportional to ΔX and $(\Delta Z)^2$. As a result, such a truncation error tends to zero as the mesh sizes tend to zero. This means that the finite-difference equations are consistent with their original partial differential equations.

The results presented in the present paper were obtained by using mesh sizes in the meridional and radial directions such that $\Delta \theta \leq 1$ deg and $\Delta Z \leq 0.001$. The largest meridional mesh size (ΔX) was associated with the lowest investigated Reynolds number (Re = 5,000). The largest mesh sizes used were $\Delta X = 0.698 \times 10^{-5}$ and $\Delta Z = 10^{-3}$. Taking into consideration that the truncation error of any of the three equations is proportional to $\Delta X = 0.698 \times 10^{-5}$ and $(\Delta Z)^2 = 10^{-6}$, it is clear that using smaller mesh sizes than those employed here would only affect the numerical solutions in the fifth decimal digit.

Acknowledgments

The financial support of Alazhar University and the encouragement of Professor M. E. El-Refaie are acknowledged.

References

Carnahan, B., Luther, H. A., and Wilkes, J. O., 1969, *Applied Numerical Methods*, Wiley, New York, pp. 429-453.

Fage, A., 1937, "Experiments on a Sphere at Critical Reynolds Numbers," Aeronaut. Res. Council Reports and Memoranda No. 1766.

El-Bedeawi, S. A., 1985, "The Boundary Layer Flow On A Rotating Body," Ph.D. thesis, Dept. of Mechanical Engineering, Alazhar University, Cairo, Egypt, pp. 204-211.

El-Shaarawi, M. A. I., El-Refaie, M. F., and El-Bedeawi, S. A., 1985, "Numerical Solution of Laminar Boundary Layer Flow About a Rotating Sphere in an Axial Stream," ASME JOURNAL OF FLUIDS ENGINEERING, Vol. 107, No. 1, pp. 97-104.

Schlichting, H., 1953, "Laminar Flow About a Rotating Body of Revolution in an Axial Airstream," NACA TM 1415.

Critical Condition of Cavitation Occurrence in Various Liquids

D. H. Fruman.² The paper by Professors Kamiyama and Yamasaki deals with a subject which is receiving much attention from the scientific community and presents some interesting results which deserve few comments.

I would appreciate very much if the authors can clarify the following questions:

1) The authors do not give any indication on the method used to determine cavitation desinence. Was visual inspection or noise measurements used?

2) Can the authors be more explicit on what kind of "actual measurements" were conducted to determine the "apparent vapour pressure"?

3) Why a sharp edge orifice has been selected to perform the experiments? Indeed, since in the case of Freon 12 cavitation occurred downstream of the orifice exit it seems to me that no comparison can be established between the results obtained with the other three fluids for which cavitation occurs near the entrance.

4) Why cavitation occurred downstream of the orifice entrance in the case of Freon 12? Is this effect a result of the hydrodynamics of the flow (such as much larger Reynolds numbers in the case of Freon, absence of separation, etc.) or of some thermodynamics peculiarities of this fluid? These questions are directly related to question 2 since the use of a sharp edged orifice would have eliminated the difficulty of interpreting the results. It is my belief that cavitation near the entrance results from a separation of the flow and the consecutive decrease of the local pressure while cavitation downstream the exit is due to local pressure reductions within the vortices in the free shear layer.

5) In equation (12) the orifice has been assumed to operate in the laminar regime but the Reynolds number values indicated in Figs. 5-8 are well above the transition. Can the authors comment on this question?

6) In Fig. 5 the authors seem to have used equation (10) in their comparison of the experimental results. This looks very improbable since this equation does not incorporate any two phase flow effect. Is this a misprint or a misunderstanding of the author's computations?

7) A quick inspection of Figs. 5-7 seems to indicate that the pressure ratio is rather well correlated by the Reynolds number (instead of the mean flow velocity in the orifice) regardless of the fluid. Have the authors attempted such a correlation?

8) In Fig. 8 the authors indicate results obtained "without gas." How should these results be interpreted? My own interpretation is that the Nitrogen cover has not been used to

pressurize the Freon. If this is so, how the large Nitrogen pressure (10^3 kPa) effect the nuclei in this fluid? Finally, why using Celsius and Kelvin degrees in the same figure?

9) In Fig. 5 the experimental results are compared with equation (10) (?) in Fig. 6 and 7 with equation (12) and in Fig. 8 with equation (8) and the authors state "equations (9) or (12) show good correlation with the present experimental results." Can the authors comment on this apparent contradiction?

10) Is a factor of three "a little modification in p_s values" for kerosene? Is cavitation occurrence being advanced or retarded in this fluid?

Authors' Closure

The authors are grateful to Professor Fruman for his useful discussion of our paper.

(1) These data of the desinent conditions were observed directly by visual inspection.

(2) Equilibrium pressure of the liquids evacuated with vacuum pump are estimated as the apparent vapour pressure.

(3) and (4) The pressure distribution in a long orifice with square edge depend strongly on the friction loss in the throat portion and expansion loss at the outlet. It is therefore the purpose of the paper to confirm the applicability of the authors' prediction method [10] to such orifice configuration. The orifice with square edge can be easily made and used widely as a flow regulator. This is the second reason why the authors used the orifice. In the case of Freon 12 with $l/d = 34.0$ (differing from $l/d = 14.9$ in the case of other liquids), cavitation occurs at the exit of throat due to a large friction loss in the throat which causes larger pressure drop than the local pressure drop at the inlet.

(5) The additional loss coefficient ξ is empirically determined by equation (13) as (total loss factor) $-(64/Re)(l/d)$ even in the case of turbulent flow regime.

(6) There are a few misprints. Please see the errata shown below.

(7) The main object of the test is to clarify the velocity effect on desinent cavitation in various liquids for comparison with the prediction based on the authors previous work [10]. Therefore, the scale of velocity is taken as a abscissa, though the Reynolds number are also plotted above the figures as a standard scale.

(8) In this case, "without gas" means "without Nitrogen gas as so-called inert gas." Originally Freon has only a little solubility so that the desinent cavitation without gas means vaporous cavitation.

In Fig. 8, authors try to show the thermodynamic effect as the difference from the room temperature in Celsius degree.

(9) Experimental results are compared with equation (12) in all cases except for Freon 12.

In the case of Freon 12, the critical σ_d values are calculated from equation (9). However, the calculated σ_d values shown in

¹By S. Kamiyama and T. Yamasaki, published in the December 1986 issue of the JOURNAL OF FLUIDS ENGINEERING, Vol. 108, pp. 428-432.

²Professor, Ecole National Supérieure de Techniques Avancées, Laboratoire de Mécanique et Energetique Chemin de la Huniere, 91120 Palaiseau, France.

Fig. 8 are obtained by using two methods of calculation for sonic velocity C .

One is based on a simple expression of equation (8) and the other is more complicated expression by taking into account the thermodynamic effect [11].

(10) It is necessary to modify the measured vapour pressure p_s for the prediction of p_2^*/p_1 only in the case of kerosene because of the uncertainty of the measured vapour pressure.

Experimental results of desinent condition in kerosene advances in comparison with the prediction with equilibrium pressure p_s without modification.

Errata

in equation (8)	$= -\frac{1}{\rho_l} \left(\frac{d\alpha}{dp_l} \right)^{-1} = -\frac{1}{\rho_l} \left(\frac{d\alpha}{dr} \frac{dr}{dp_l} \right)^{-1}$	$\rightarrow = \left(-\rho_l \frac{d\alpha}{dp_l} \right)^{-1/2} = \left(-\rho_l \frac{d\alpha}{dr} \frac{dr}{dp_l} \right)^{-1/2}$
in equation (12)	41Re^*	$\rightarrow 4/\text{Re}^*$
	$\xi \frac{\text{Re}^*}{16}$	$\rightarrow \xi \frac{\text{Re}^*}{16\pi}$
in Fig. 5	equation (10)	\rightarrow equation (12)
upper abscissa in Fig. 6	$11, \dots, 18 \times 10^3$	$\rightarrow 1.1, \dots, 1.8 \times 10^3$

Scrutinizing the k - ϵ Turbulence Model Under Adverse Pressure Gradient Conditions¹

P. Bradshaw.² This useful paper incidentally reminds us that the standard model of the dissipation (ϵ) equation is based on a subtle interpretation of the terms in the equation, originally derived by Professor Rodi in unpublished work.

Most turbulence models are arranged to reproduce the mixing-length formula, rather than the logarithmic law as such, in the inner layer: that is, they reduce to turbulent energy production $P_k = \epsilon$, with $L \equiv k^{3/2}/\epsilon = (\kappa/c_\mu^{3/4})y$ as in equation (9) of the paper, leading to $\partial U/\partial y = (-uv)^{1/2}/(\kappa y)$. If we use these "local equilibrium" assumptions in Rodi and Scheuerer's analysis, their equation (10) is replaced by

$$c_{e1} = c_{e2} - \frac{\kappa^2}{\sigma_\epsilon \sqrt{c_\mu}} \left(1 - \frac{\alpha y}{\tau} + \frac{3}{2} \left(\frac{\alpha y}{\tau} \right)^2 \right) \quad (1)$$

where $\tau \equiv -\overline{uv}$ and $\alpha \equiv \partial\tau/\partial y$ (assumed independent of y). If $\alpha = 0$ (zero pressure gradient) this of course reduces to equation (8) of Rodi and Scheuerer. This formula is somewhat simpler than equation (10) which follows from assuming the logarithmic law, and it avoids the quite unphysical result that a turbulence parameter (c_{e1}) depends on the mean pressure gradient. In principle the shear-stress gradient α is an extra unknown but in any numerical method it can be evaluated, as an average over the inner layer $0 < y/\delta < 0.1$ say, within the iterative loop needed to solve the main set of nonlinear equations.

Authors' Closure

The authors are grateful to Professor Bradshaw for his stimulating discussion in which he suggests to replace equation (10) in the paper by his equation (1). This is certainly a possi-

ble and useful alternative. The basic difference is that, in the derivation of the equation, Professor Bradshaw puts more emphasis on the assumption of local equilibrium while the authors assume the logarithmic velocity law to prevail in the inner layer. In both derivations, the length scale is assumed to vary linearly as in the mixing-length model. It is not entirely clear to the authors which of the two assumptions holds better under increasing adverse pressure gradients. There is, however, more experimental information available on the logarithmic law, which appears to hold quite well even for boundary layers approaching separation. It is for this reason

that the authors prefer their derivation. Also, in a real calculation, the shear stress gradient α appearing in Professor Bradshaw's formula would have to be obtained from a straight-line approximation over the inner layer. This is probably not always easy to achieve, especially not for situations where the pressure gradient changes rapidly in the streamwise direction, causing relaxation phenomena in the boundary layer. It should be pointed out in this connection that equation (10) is also impractical for use in calculations and was not suggested for this purpose. Rather, the equation was presented in the paper to show qualitatively how the constant c_{e1} should change with increasing adverse pressure gradient.

Automatic Remeshing Scheme for Modeling Hot Forming Process¹

Bruce Caswell.² This paper gives a concise account of how the finite element method can be applied on a mesh which moves with a fluid domain undergoing large changes. In the forming process described, a gob of molten glass is squeezed between mold and die with large changes in the free surface position. Furthermore, free surface elements eventually come into contact with the solid surfaces, and this gives rise to acute difficulties in the control of the moving mesh. The usual Galerkin formulation is altered by the introduction of time derivatives localized in the moving mesh. The main features of the problem are discussed as follows. At every time step, a new configuration of the boundary is computed from the velocity data on the boundary. In order for the interior domain to be reasonably discretized the interior nodes are recalculated on the basis of the updated boundary by means of algorithms described in the paper. Advancement to the next time step requires the most recently determined fields to be re-interpolated relative to the new nodal positions. This is a crucial step for er-

¹By W. Rodi and G. Scheuerer, published in the June 1986 issue of the JOURNAL OF FLUIDS ENGINEERING, Vol. 108, pp. 174-179.

²Department of Aeronautics, Imperial College, London, SW7 2BY England.

¹By H. P. Wang and R. T. McLay, published in the December 1986 issue of the JOURNAL OF FLUIDS ENGINEERING, Vol. 108, No. 4, pp. 465-469.

²Division of Engineering, Brown University, Providence, R.I. 02912.

Fig. 8 are obtained by using two methods of calculation for sonic velocity C .

One is based on a simple expression of equation (8) and the other is more complicated expression by taking into account the thermodynamic effect [11].

(10) It is necessary to modify the measured vapour pressure p_s for the prediction of p_2^*/p_1 only in the case of kerosene because of the uncertainty of the measured vapour pressure.

Experimental results of desinent condition in kerosene advances in comparison with the prediction with equilibrium pressure p_s without modification.

Errata

in equation (8)	$= -\frac{1}{\rho_l} \left(\frac{d\alpha}{dp_l} \right)^{-1} = -\frac{1}{\rho_l} \left(\frac{d\alpha}{dr} \frac{dr}{dp_l} \right)^{-1}$	$\rightarrow = \left(-\rho_l \frac{d\alpha}{dp_l} \right)^{-1/2} = \left(-\rho_l \frac{d\alpha}{dr} \frac{dr}{dp_l} \right)^{-1/2}$
in equation (12)	41Re^*	$\rightarrow 4/\text{Re}^*$
	$\xi \frac{\text{Re}^*}{16}$	$\rightarrow \xi \frac{\text{Re}^*}{16\pi}$
in Fig. 5	equation (10)	\rightarrow equation (12)
upper abscissa in Fig. 6	$11, \dots, 18 \times 10^3$	$\rightarrow 1.1, \dots, 1.8 \times 10^3$

Scrutinizing the k - ϵ Turbulence Model Under Adverse Pressure Gradient Conditions¹

P. Bradshaw.² This useful paper incidentally reminds us that the standard model of the dissipation (ϵ) equation is based on a subtle interpretation of the terms in the equation, originally derived by Professor Rodi in unpublished work.

Most turbulence models are arranged to reproduce the mixing-length formula, rather than the logarithmic law as such, in the inner layer: that is, they reduce to turbulent energy production $P_k = \epsilon$, with $L \equiv k^{3/2}/\epsilon = (\kappa/c_\mu^{3/4})y$ as in equation (9) of the paper, leading to $\partial U/\partial y = (-uv)^{1/2}/(\kappa y)$. If we use these "local equilibrium" assumptions in Rodi and Scheuerer's analysis, their equation (10) is replaced by

$$c_{e1} = c_{e2} - \frac{\kappa^2}{\sigma_\epsilon \sqrt{c_\mu}} \left(1 - \frac{\alpha y}{\tau} + \frac{3}{2} \left(\frac{\alpha y}{\tau} \right)^2 \right) \quad (1)$$

where $\tau \equiv -\overline{uv}$ and $\alpha \equiv \partial\tau/\partial y$ (assumed independent of y). If $\alpha = 0$ (zero pressure gradient) this of course reduces to equation (8) of Rodi and Scheuerer. This formula is somewhat simpler than equation (10) which follows from assuming the logarithmic law, and it avoids the quite unphysical result that a turbulence parameter (c_{e1}) depends on the mean pressure gradient. In principle the shear-stress gradient α is an extra unknown but in any numerical method it can be evaluated, as an average over the inner layer $0 < y/\delta < 0.1$ say, within the iterative loop needed to solve the main set of nonlinear equations.

Authors' Closure

The authors are grateful to Professor Bradshaw for his stimulating discussion in which he suggests to replace equation (10) in the paper by his equation (1). This is certainly a possi-

ble and useful alternative. The basic difference is that, in the derivation of the equation, Professor Bradshaw puts more emphasis on the assumption of local equilibrium while the authors assume the logarithmic velocity law to prevail in the inner layer. In both derivations, the length scale is assumed to vary linearly as in the mixing-length model. It is not entirely clear to the authors which of the two assumptions holds better under increasing adverse pressure gradients. There is, however, more experimental information available on the logarithmic law, which appears to hold quite well even for boundary layers approaching separation. It is for this reason

that the authors prefer their derivation. Also, in a real calculation, the shear stress gradient α appearing in Professor Bradshaw's formula would have to be obtained from a straight-line approximation over the inner layer. This is probably not always easy to achieve, especially not for situations where the pressure gradient changes rapidly in the streamwise direction, causing relaxation phenomena in the boundary layer. It should be pointed out in this connection that equation (10) is also impractical for use in calculations and was not suggested for this purpose. Rather, the equation was presented in the paper to show qualitatively how the constant c_{e1} should change with increasing adverse pressure gradient.

Automatic Remeshing Scheme for Modeling Hot Forming Process¹

Bruce Caswell.² This paper gives a concise account of how the finite element method can be applied on a mesh which moves with a fluid domain undergoing large changes. In the forming process described, a gob of molten glass is squeezed between mold and die with large changes in the free surface position. Furthermore, free surface elements eventually come into contact with the solid surfaces, and this gives rise to acute difficulties in the control of the moving mesh. The usual Galerkin formulation is altered by the introduction of time derivatives localized in the moving mesh. The main features of the problem are discussed as follows. At every time step, a new configuration of the boundary is computed from the velocity data on the boundary. In order for the interior domain to be reasonably discretized the interior nodes are recalculated on the basis of the updated boundary by means of algorithms described in the paper. Advancement to the next time step requires the most recently determined fields to be re-interpolated relative to the new nodal positions. This is a crucial step for er-

¹By W. Rodi and G. Scheuerer, published in the June 1986 issue of the JOURNAL OF FLUIDS ENGINEERING, Vol. 108, pp. 174-179.

²Department of Aeronautics, Imperial College, London, SW7 2BY England.

¹By H. P. Wang and R. T. McLay, published in the December 1986 issue of the JOURNAL OF FLUIDS ENGINEERING, Vol. 108, No. 4, pp. 465-469.

²Division of Engineering, Brown University, Providence, R.I. 02912.

CONFERENCE REPORT
International Conference on
Laser Anemometry: Advances and Application
16th–18th December 1985, Manchester, U.K.

The UK LDA Users Group held its first International Conference on Laser Anemometry at the University of Manchester in December, 1985. The conference was organized by the UK LDA Users Group, sponsored by the University of Manchester and co-sponsored by the Institution of Mechanical Engineers, the Royal Aeronautical Society, and the British Hydromechanics Research Association. A large field of papers of a high standard had been received and of the thirty-eight papers presented at the conference sixteen were by overseas authors, with a similar proportion of overseas delegates. There were no parallel sessions and the quality of the papers and enthusiasm of the delegates could be judged by the high attendance levels at all sessions. The atmosphere of the conference was amicable and workman-like and the local organizers must be congratulated both on the quality of the social and domestic arrangements and on running the proceedings to time!

The technical sessions of the conference were structured around five invited papers by internationally recognized authorities who had each been asked to address a particular aspect of laser anemometry. Mike Fingerson's introduction to fibre optics in LDA applications was the springboard for a group of papers demonstrating the considerable potential of fibre optics in radically altering our concept of optical systems design in terms of both miniaturization and the use of fibre optic phase modulators. Two authors described multipoint measurements using fibre optics to deliver and collect light at many points in the flow simultaneously. Preben Buchhave considered the design of 3D measurement systems and described the often conflicting requirements of a real example. A number of papers addressed the problems of making measurements in 3D and rotating flows and presented results from a variety of rotating flow structures. Les Drain discussed laser anemometry and particle sizing, providing an overview of the combined field of size and velocity measurement and describing the range of techniques that have been developed. LDA measurements in two phase flows were presented by various authors who had examined water sprays in air, solid particles in a spouted bed and wet steam flows. Franz Durst's paper on turbulence quantities and Reynolds stresses in a pipe flow of polymer solutions discussed measurements in turbulent boundary layer flows and described the use of refractive index matching techniques to permit detailed study of the near wall region. This paper acted as the focus for a group of papers which considered a wide range of special applications varying from turbulent confined jets with recirculation to natural convection flows, from bluff body wakes to ribbed wall channel flow. Jim Whitelaw described a wide range of ap-

plications of laser anemometry to engine flows, both combustion studies for gas turbines and in-cylinder measurements in reciprocating IC engines. He also addressed the difficulties of making measurements of fuel droplet size in such flows. Other authors presented measurements made in furnaces and in motored reciprocating engines.

The LDA Users Group has broadened its field of interest, dropping the word Counter from its title and this was demonstrated by the large number of papers presenting aspects of instrumentation, signal processing and interpretation using frequency trackers, transient recorders, photon correlators and filter banks. The emphasis of this conference was on advances and application and the papers presented show the wide front of the advance. Although three papers were presented specifically on the topic of comparison between theoretical prediction and experimental measurement it does still seem that there is no general feedback into computational modelling of data obtained from turbulent flows using LDA. Perhaps this is a topic that will be addressed by authors at the next conference in this series.

The quality of the technical sessions was repeated in the excellent exhibition of instrumentation and equipment which included displays by the major manufacturers. The exhibitors had obviously taken a great deal of trouble to present the current state of their art and the stands were manned with the standard of erudition one has come to expect.

Copies of the Conference volume containing the five invited papers and twenty eight contributed papers may be obtained from Publications Sales, BHRA, Cranfield, Bedford, MK43 0AJ, U.K., at a price of £44.00 UK and EEC-£47.00 elsewhere.

Encouraged by the success of this first international conference, and the previous national symposium in 1983, the LDA Users Group has decided to hold the second international conference at the University of Strathclyde between 21st and 23rd September 1987. A preliminary announcement has been made and a call for papers will follow very soon. The UK LDA Users Group continues to hold meetings several times yearly, acting as a forum for researchers concerned with the application of LDA. Further details can be obtained from UK LDA Users Group, c/o Department of Engineering, University of Manchester, Oxford Road, Manchester.

Dr. C. F. King
School of Engineering and Applied Science,
University of Durham,
Durham,
U.K.